Investigations of dynamic stall and dynamic stall control on helicopter airfoils

A cumulative habilitation thesis

Dr. Anthony D. Gardner, BSc(Hons), Msc, PhD.

2015

Investigations of dynamic stall and dynamic stall control on helicopter airfoils

Kumulative Habilitationsschrift zur Erlangung der Lehrbefugnis für das Fachgebiet Strömungsmechanik

Vorgelegt von
Dr. Anthony D. Gardner, BSc(Hons), Msc, PhD.
aus Göttingen

Wissenschaftler am Institut für Aerodynamik und Strömungstechnik des Deutschen Zentrums für Luft- und Raumfahrt (DLR) in Göttingen

Bei der

Fakultät für Mathematik/Informatik und Maschinenbau
der Technischen Universität Clausthal

2015

Abstract

Investigations into dynamic stall and dynamic stall control on airfoils are detailed using pitching airfoil experiments and numerical investigations at Mach 0.3, 0.4 and 0.5 on the airfoils EDI-M109, EDI-M112 and OA209. Two-dimensional dynamic stall was investigated, and the effects of the wind tunnel interference, rotation and the finite wing on the three-dimensional stall process were described. The curvature of the stall vortex and its effect in reducing the strength of the dynamic stall compared to a two-dimensional treatment was investigated using CFD and experiments with high-speed pressure sensitive paint (PSP) and pressure transducers. Stall control was designed based on its ability to increase the lift in CFD simulations of static stall and implemented by using constant and pulsed blowing with high-pressure air jets in the vertical direction, and the stall was demonstrated to be significantly reduced at all Mach numbers investigated. Optimal mass flux and jet spacing were found for Mach 0.3 and Mach 0.5, and depended on the test case investigated. Optima for deep stall were around C_μ=0.12 for M=0.3 and C_μ=0.02 for M=0.5. Pulsed blowing was found to be at best as effective as constant blowing with the same mass flux, for the jet configuration and test cases investigated. Flow control by blowing reduced drag for separated flow, but the energy required in compressed air to achieve this was more than the savings in drag, and no cases were found in which flow control resulted in a reduction in total power used.

Zusammenfassung

Die vorliegende Arbeit beschreibt experimentelle und numerische Untersuchungen des dynamischen Strömungsabrisses und dessen Beeinflussung bei Mach 0,3, 0,4 und 0,5 an den Profilen EDI-M109, EDI-M112 und OA209. Untersucht wurde hauptsächlich der zweidimensionale dynamische Strömungsabriss. Ebenso wurden die Einflüsse der Windkanalinterferenz, der Rotation und der Blattspitze auf den dreidimensionalen Ablauf des dynamischen Abrisses untersucht. Die dreidimensionale Krümmung der Ablösewirbel bewirkte eine Verringerung der Stärke des dynamischen Strömungsabrisses im Vergleich zum zweidimensionalen Ansatz. Diese Verringerung wurde durch Experimente mit schnell reagierender drucksensitiver Farbe (PSP) sowie Drucksensoren und mit CFD untersucht. Methoden zur Beeinflussung des dynamischen Strömungsabrisses wurden unter anderem aufgrund ihrer Fähigkeit ausgewählt, den Auftrieb in CFD-Simulationen mit statischer Strömungsablösung zu erhöhen. Die Beeinflussung des dynamischen Strömungsabrisses ist durch die Verwendung von konstantem und gepulstem Ausblasen mit Hochdruckluftdüsen in der vertikalen Richtung umgesetzt worden. Die negativen Effekte des Strömungsabrisses wurden bei allen Machzahlen deutlich reduziert. Für die Machzahlen 0,3 und 0,5 wurden optimale Werte für den reduzierten Massenstrom C_μ und den Düsenabstand bestimmt. Für Testfälle mit starkem dynamischen Strömungsabriss ergaben sich Werte im Bereich von C_μ=0,12 (M=0,3) bis C_μ=0,02 (M=0,5). Für die untersuchten Luftstrahlkonfigurationen und Testfälle war gepulstes Ausblasen nicht effektiver als konstantes Ausblasen mit dem gleichen Massenfluss. Strömungssteuerung durch Ausblasen reduzierte den Luftwiderstand für abgelöste Strömung, aber die für die Druckluft benötigte Energie war immer größer als der energetische Gewinn durch Reduktion des Widerstandes. Es gab keine Testfälle bei denen Strömungssteuerung zu einer Verringerung der Gesamtleistung führte.

Foreword

This habilitation thesis contains a summary of my work in the field of the flow control of dynamic stall between 2008 and 2014 at the Institute of Aerodynamics and Flow Technology at the German Aerospace center (DLR), in Göttingen, Germany. The work has been published in both the refereed and unrefereed literature, and where the work has been otherwise published, this is indicated in the text. A full list of my publications can be found after the bibliography. The relevant publications are referenced in the text and listed together with other references in the bibliography.

Between 2008 and 2014, a range of experimental and numerical investigations were carried out at the DLR. The experimental work concentrated on pitching airfoil experiments, that is a wing of constant cross-section spanned the whole width of the wind tunnel and was moved with forced, sinusoidal pitching oscillations of large amplitude around the quarter-chord axis. The experiments took place in the transonic wind tunnel Göttingen (TWG) at Mach numbers between 0.3 and 0.85, and total pressures between 0.3 bar and 1.2 bar. My own contributions included investigations of two new helicopter airfoils, the EDI-M109 and EDI-M112 for their dynamic stall performance, and the flow-control model OA209-FCD.

The control of dynamic stall was investigated using high pressure constant and pulsed blowing of air on an OA209 pitching airfoil model in the TWG. The model design and jet layout was performed using CFD and the experiment was performed with two wind tunnel entries in 2011 and 2012. A large number of new results regarding 2D and 3D dynamic stall and dynamic stall control resulted from these experiments and are detailed in this habilitation thesis. The results included the first use of fast response pressure-sensitive paint for the investigation of dynamic stall and a large amount of high-quality pressure sensor data.

In addition, the effect of 3D stall in rotating and nonrotating systems was investigated numerically, showing that both systems show significant differences to 2D dynamic stall. Further, the effect of the model-wall connection was investigated both numerically and experimentally showing that the connection method can significantly influence the local aerodynamics of the airfoil while not being directly detectable on the airfoil centerline.

All of these results are presented in this document, and are connected to an overview of the state of aerodynamic investigations on dynamic stall.

Acknowledgments

The work presented in this document is, to the best of my knowledge and belief, original, except as acknowledged in the text. This material has not been submitted, either in whole or part, for a degree at any university. Parts of the text have been previously published in journals, at conferences and in internal reports, as noted in the text.

For each of the papers presented in this habilitation thesis, I was the primary author. This involved the planning, design and management of the experiments, and the execution of all of the computations presented in this work, as well as the analysis of the experimental and numerical data and writing each of the papers presented. However, large wind tunnel campaigns are always the result of a large team, and I am very grateful to the scientific and technical staff at the German-Dutch Wind tunnel association (DNW), the DLR workshops (SHT) and my colleagues at the DLR Institute of Aerodynamics and Flow Technology and the DLR Institute of Aeroelastics.

Many of my colleagues are co-authors on the papers, and have the following inputs:

- Altmikus, A.R.M., Klein, A. and Rohardt, C.-H.: EDI-M109 and EDI-M112 airfoil design team
- Klein, C., Sachs, W., Henne, U.: Pressure sensitive paint team
- Knopp, T.: Implementation of the pulsing jet boundary condition in the TAU CFD code
- Mai, H.: Leader of the experimental team controlling the pitching motion test stand and the data recording in the TWG wind tunnel
- Neuhaus, D.: Design and manufacture of miniature valves for the FCD wind tunnel model
- Richter, K.: Project planning and management for the DLR projects SIMCOS and STELAR and the LUFO project ECO-HC, scientific support
- Rosemann, H.: Project planning and management

A.D. Gardner, Göttingen, 2015

Nomenclature

Symbols

A	Jet area for 1 m of airfoil (m^2)
A_{Ref}	Airfoil reference area (m^2)
a	Acceleration (m/s^2)
α	Angle of attack ($^\circ$)
$\alpha_{C_{L_{max}},static}$	Angle of attack at maximum lift for a static polar ($^\circ$)
α_{max}	Sinusoidal motion maximum angle ($^\circ$)
α_{min}	Sinusoidal motion minimal angle ($^\circ$)
$\alpha_{\pm}$	Sinusoidal motion amplitude ($^\circ$)
$\overline{\alpha}$	Mean angle of attack ($^\circ$)
$\overline{\alpha'}$	Mean angular velocity ($^\circ$/s)
$\overline{\alpha'_{norm}}$	Normalised mean angular velocity($^\circ$/s)
b	Breadth of airfoil considered (m)
β	Vortex rotation angle ($^\circ$)
C	Heat capacity. For air C=1004 J/K/kg.
C_D	Drag coefficient
$\overline{C_D}$	Mean drag coefficient
C_{D_p}	Peak drag coefficient
$C_{D_{rake}}$	Drag coefficient as measured by the wake rake
C_L	Lift coefficient
$\overline{C_L}$	Mean lift coefficient
$C_{L_{max}}$	Maximum lift coefficient
C_{L_p}	Lift coefficient peak
C_M	Pitching moment coefficient
$\overline{C_M}$	Mean pitching moment coefficient
C_{M_p}	Negative pitching moment coefficient peak
C_μ	Momentum ratio jets/freestream: $C_\mu = \frac{2}{cL_{act}} \frac{\dot{m}_m v_j}{\rho_\infty v_\infty^2}$
C_q	Mass flux ratio jets/freestream; $C_q = \frac{\dot{m}_m}{\rho_\infty v_\infty c L_{act}}$
C_P	Pressure coefficient
C_{P-crit}	Critical pressure coefficient
C_{P_0}	C_P at minimum angle of attack
c	Length of the airfoil chord (0.3 m)
Δ	Difference in variable
ΔC_L, ΔC_M	Lift/drag correction for jet impulse
D	Aerodynamic damping
d	Jet diameter (m)
d_a	Airfoil thickness (m)
F	Force due to the jet impulse (N): $F = \dot{m}v = \dot{m}/L_{act}\sqrt{\frac{2\gamma RT_0}{\gamma+1}}$

F^+	Dimensionless pulsing frequency: $F^+ = f_{pulse} x_{te}/v_\infty$
f	Frequency (Hz)
f_{pulse}	Jet pulsing frequency (Hz)
γ	Ratio of specific heats
h	Slot height (m)
h_{Ri}	Reference length for Ri (m)
K	Calibration constant for $\dot{m}_{inst}$ (kg/s/Pa)
k	Reduced frequency: $k = \omega^*/2 = \pi f c/v_\infty$
k_ν	Turbulent kinetic energy
L	Integration length for wake rake (m)
L_{act}	Breadth of model with actuation (m)
L_S	Stack spacing of 2D planes along the blade (% chord)
λ_2	Vortex and curvature criterion [51]
M	Mach number
$\dot{m}$	Mass flux (kg/s)
$\dot{m}_{inst}$	Instantaneous mass flux (kg/s)
$\dot{m}_j$	Mass flux out of the injectors over 1 meter of wing section (kg/s/m) (=$\dot{m}/b$)
$\dot{m}_m$	Mean mass flux (kg/s)
μ	Advance ratio = Helicopter flight speed/rotor tip speed
ν_t	Eddy viscosity
ω	Rotation rate of the blade (radians/s)
ω^*	Reduced frequency: $\omega^* = 2k = 2\pi f c/v_\infty$
P	Pressure (Pa)
P_∞	Freestream pressure (Pa)
P_0	Total pressure (Pa)
P_{0_∞}	Freestream total pressure (Pa)
P_4	Pressure after valve (Pa)
P_j	Total pressure of the jet air (bar)
P_{t2}	Pitot pressure (Pa)
ϕ	Phase of 1/rev blowing compared to optimal (°)
ψ	Azimuthal coordinate system of rotation (°)
R	Gas constant (R=287 J/kg/K for air)
R_{max}	Position of blade tip (m)
R_{min}	Position of blade root (m)
R_{ref}	Position of reference section (=2.75 m)
r	Radial position (m)
Re	Reynolds number (based on c)
Ri	Richardson number: $Ri = \frac{a h_{Ri}}{v_{Ri}^2}$
ρ_∞	Freestream density (kg/m^3)
ρ_0	Total density (kg/m^3)
s	Jet spacing in y-direction (m)
σ	Standard deviation of variable
T	Period $T = 1/f$ (s)
T_∞	Freestream temperature (K)
T_0	Total temperature (K)
t	Time (s)
Tu	Turbulence intensity
$U_{\max}$	Maximum inflow velocity (m/s)
v_∞	Freestream velocity (m/s)

v_j	Speed of the jet at the injector exit (M=1) (m/s)
v_{Ri}	Reference velocity for Ri (m/s)
W_D	Power required to offset drag on 1 m of airfoil $W_D = \frac{1}{2} C_D A_{Ref} \rho_\infty v_\infty^3$ (W/m)
W_{D_p}	Power required to offset peak drag on 1 m of airfoil (kW/m)
$\overline{W_D}$	Power required to offset average drag on 1 m of airfoil (kW/m)
W_j	Power required to drive air jets $W_j = ln\left(\frac{P_{0_j}}{P_\infty}\right) \frac{RT_\infty \dot{m}}{2b}$ (W/m)
W_T	Total power $W_T = W_D + W_j$ (kW/m)
X	Refers to a value C_L, C_D, C_{my} or D
x	Streamwise co-ordinate (m)
x_{te}	Distance from actuator to trailing edge (m)
y	Co-ordinate across the width (m)
y^+	Dimensionless wall distance for the first structured grid layer
z	Co-ordinate in height (m)

Acronyms and Trademarks

2D	Two-dimensional
3D	Three-dimensional
BL	Boundary Layer
Centaur	A grid generation program
CFD	Computational Fluid Dynamics
CFL	Courant-Friedrichs-Lewy number (dimensionless timestep size)
CPUh	Central Processing Unit hours of operation
DC	Duty cycle
DE	Discretisation error
DLR	German Aerospace Center
DNW	German-Dutch Wind tunnels
DS	Dynamic Stall
DS2	SIMCOS Dynamic Stall test case 2 OA209, c=300 mm, M=0.31, Re=1.16e6, α=12.87$\pm$7.13°, ω^*=0.101, T_∞=313 K.
ECD	The firm Eurocopter Deutschland, now Airbus Helicopters
EDI-M109	A 9% thickness helicopter airfoil
EDI-M112	A 12% thickness helicopter airfoil
EDIRHE	ONERA project on helicopter dynamic stall
FCD	Fluidic Control Device
INROS	DLR/ECD project on helicopter dynamic stall
LEVoG	Leading Edge Vortex Generator of cylinder type used by Mai *et al*
LUSGS	Lower Upper Symmetric Gauss Seidel implicit solver scheme
MUSCL	Monotone Upstream-centered Schemes for Conservation Laws
OA209	A 9% thickness helicopter airfoil
ONERA	French Aerospace Center
ONERA-F2	ONERA low-speed wind tunnel
PIV	Particle Image Velocimetry
PSP	Pressure Sensitive Paint
RANS	Reynolds-averaged Navier-Stokes CFD
SAE	Spalart-Allmaras turbulence model with Edwards modification
SBR	Single-Blade Rotor
SIMCOS	DLR-ONERA project on helicopter dynamic stall
SJA	Synthetic Jet Actuator
STELAR	DLR project on helicopter dynamic stall
TAU	DLR unstructured CFD code
TCXX	Denotes a test case number for an injector configuration
TR-PIV	Time-Resolved PIV
TWG	Transonic Wind tunnel Göttingen
URANS	Unsteady (time accurate) Reynolds-averaged Navier-Stokes CFD
VR7	A helicopter airfoil
ZMF	Zero Mass Flux jet

Contents

Chapter 1

Introduction

The helicopter is a fascinating flying machine, not least because of its fundamentally unsteady aerodynamics and complex system of aerodynamic surfaces moving relative to each other. The main rotor of a conventional helicopter consists of a number of helicopter blades connected in their center to a rotating hub. The blades have a large aspect ratio and long regions of constant cross-section, and so the aerodynamics of blade sections can be approximated by the two-dimensional airfoil problem for the estimation of qualitative and quantitative performance at many relevant flight conditions.

A conventional helicopter consists of a single main rotor, which provides the lift and thrust, and a tail rotor as an anti-rotation measure, as seen in Fig. 1.1a. The aerodynamic limits on the helicopter are given by the limits on the main rotor, and it is this configuration which is mainly investigated

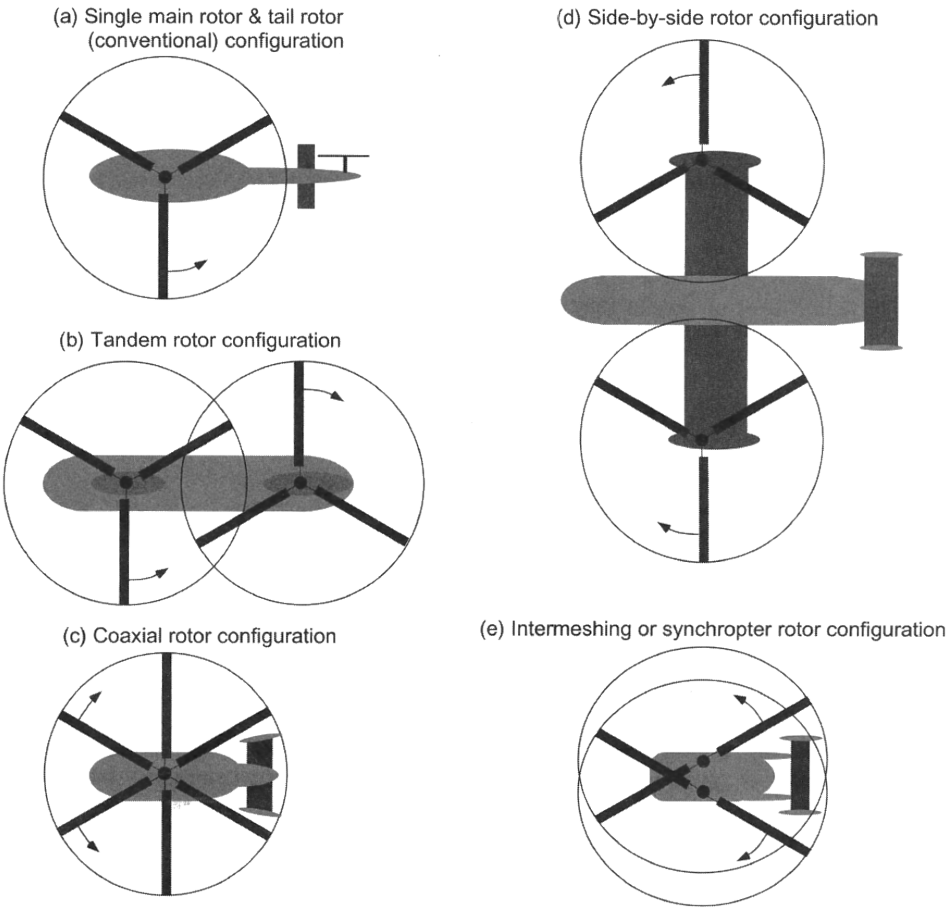

Figure 1.1: Types of helicopter, from [65]

in this habilitation thesis. Alternative configurations using two rotors (Fig. 1.1b-e) do not require a tail rotor, and have advantages for particular flight conditions, but the simplicity of the single rotor configuration has ensured its continued popularity.

For a helicopter in forward flight, the main rotor blades experience a varying Mach number as they rotate. The azimuthal coordinate system of rotation starts over the tailboom with ψ=0° (Figure 1.2). As the blades rotate toward the front of the helicopter, the airfoil sections see an onflow faster than the rotational speed, and this is a maximum at ψ=90°. As seen in Fig. 1.3, the forward flight speed and the rotational speed of the rotor are superimposed, so that at ψ=90° the local airfoils on the rotor see the sum of the rotational and forward flight speeds. Starting at ψ=180°, over the nose of the aircraft, the airfoil sees an onflow slower than the flight speed of the aircraft, and the onflow speed is a minimum at ψ=270°. Since the Mach number over the rotor is also a function of radius, with the rotational Mach number decreasing in the direction of the rotor hub, the addition of the forward speed of the aircraft to the rotational speed of the rotor results in a region where the rotor blade experiences a negative flow velocity, i.e. the sharp rear of the rotor blade airfoils sees the flow first. This is the circular region to the left of the centerline in Fig. 1.3. On the rim of the circle the flow speed is zero, and thus in this region no lift is produced.

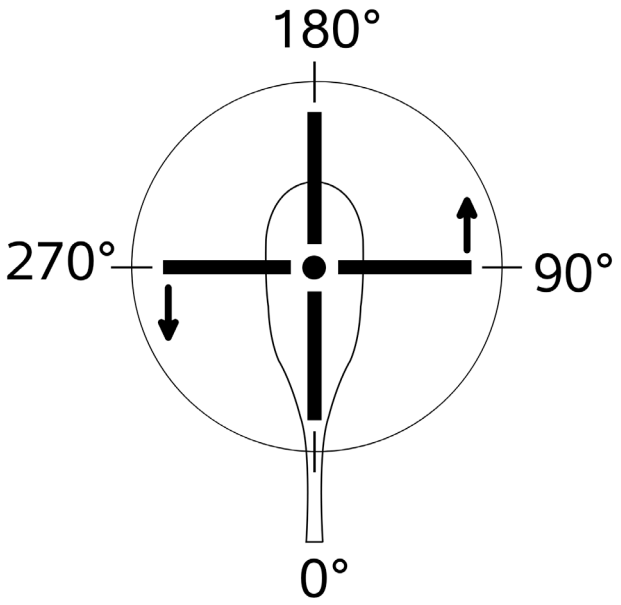

Figure 1.2: Simple diagram of a helicopter blade reference system

In order to balance the forces on the helicopter, the main rotor blades can be controlled by *collective pitch* controls, which vary the pitch angle (α) of all blades equally to increase thrust, or by *cyclic pitch* controls, which vary the pitch angle (α) as a function of the azimuthal position (ψ). In this way α is low at ψ=90° for low-drag, medium lift conditions at high Mach number and α is high at ψ=270° for high lift to balance the forces during low-Mach number flow (Figure 1.4). Since the pitch varies with the azimuthal angle, this means that each airfoil section sees a pitching motion with the same frequency as the rotor rotation frequency, which is usually of the order of 3-8 Hz. At the same time, each airfoil sees a Mach number variation with 180° phase change to the pitching variation (i.e. high Mach number is seen at low angle, and vice-versa).

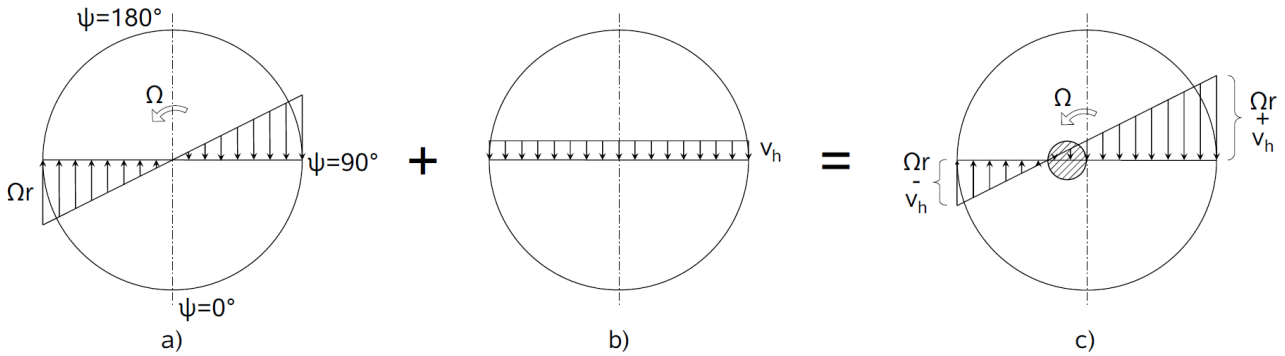

Figure 1.3: Mach number variation over a rotor. (Figure 1.1 from [46])

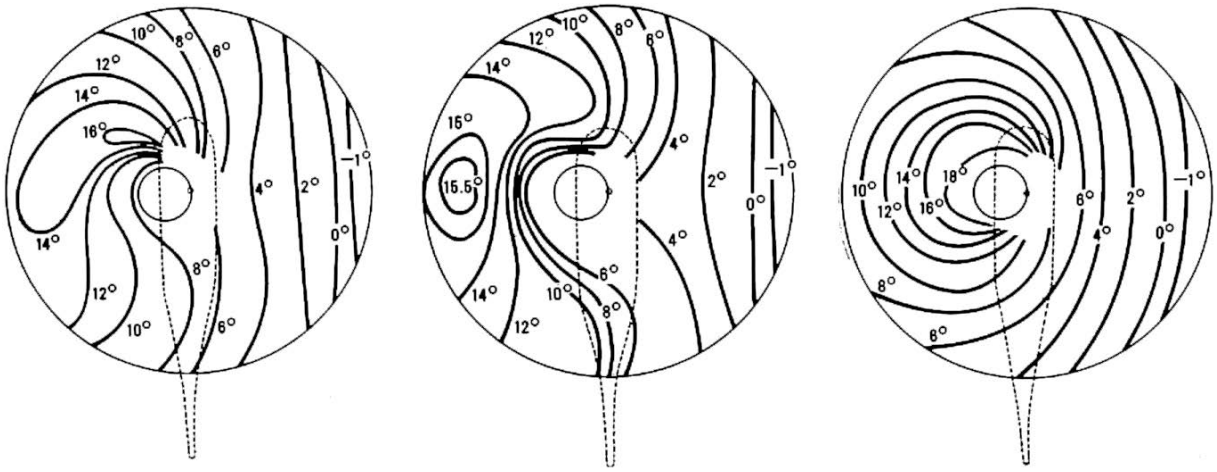

Figure 1.4: Blade airfoil aerodynamic angle of attack at a) Horizontal flight, b) Ascent at 5.1 m/s, c) Autorotation. (From [98])

(a)

(b)

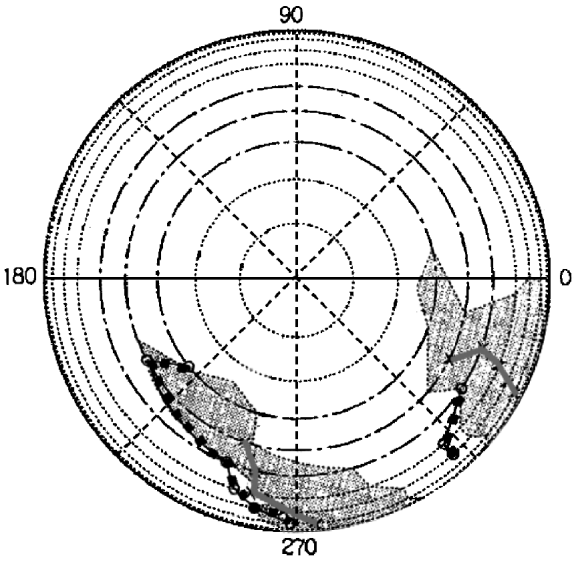

Figure 1.5: (a) UH-60 helicopter (from Wikimedia commons), (b) Stall map for the UH-60 flight test from [96]. Grey areas indicate separated flow.

The thrust of older helicopters, which often used reciprocating engines or low-power turbine engines, was primarily limited by the power available to the rotor from the engines. Modern advances in engine and transmission technology mean that the engines can provide more power than can be effectively used by the rotor. In this case the thrust of a helicopter at a particular speed is limited by the stall of the blades on the retreating side. When airfoil sections of the blades are stalled, then lift is significantly reduced, as known from fixed-wing aircraft. However, the transient stall causes the formation of vortices which cause a high transient pitching moment. The combination of this high transient pitching moment and fast loss of lift in sections causes high vibratory loads on the helicopter, and can cause structural damage, particularly to the pitch-links (rods which control the blade pitch angle). This process is known as “dynamic stall”, and is the topic of this habilitation thesis.

In the extreme case that significant sections of the rotor blade stall, then lift is lost in this region. The effect is experienced with a delay of ψ=30-90° depending on the flexibility of the rotor system, due to the effect of the rotating rotor system. A fully articulated rotor will experience “high-speed pitch-up”, whereas stiffer rotors will experience a mixture of roll and pitch-up. Figure 1.5a, shows a

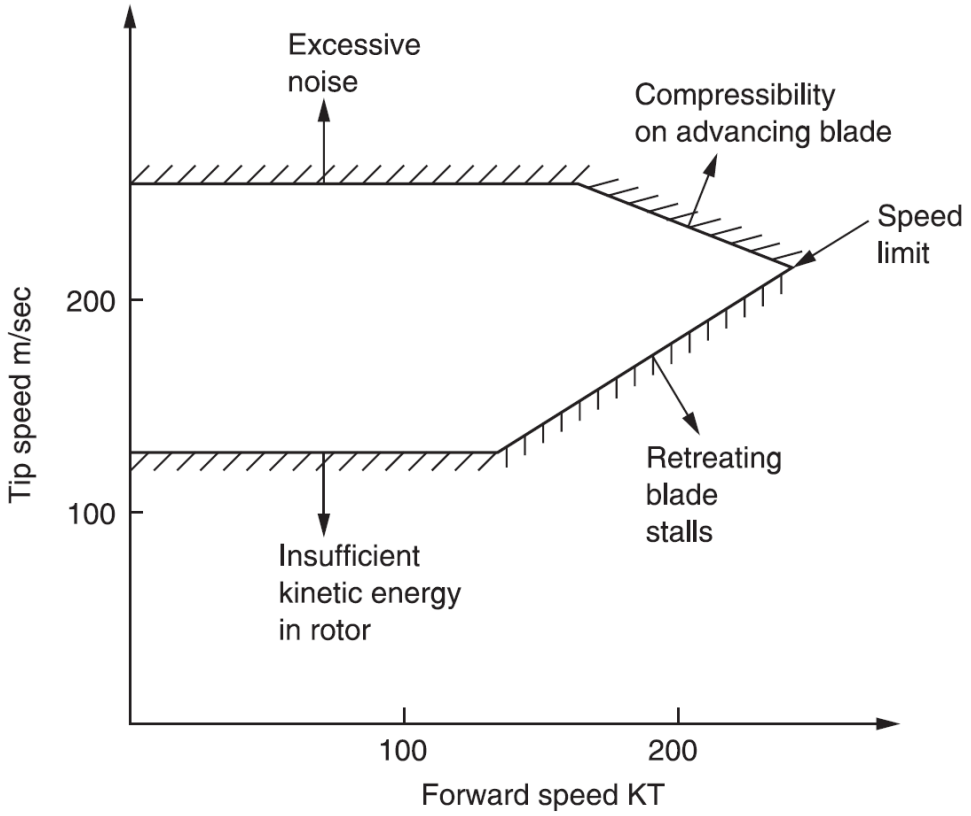

Figure 1.6: Limits on the helicopter flight envelope, from [120].

common a 5 tonne military helicopter, the UH-60 black hawk. Figure 1.5b shows a stall map for the rotor of a UH-60 helicopter at an advance ratio μ=0.24. The advance ratio is defined as the helicopter flight speed divided by the rotor tip speed, and this flight point is thus a highly loaded fast forward flight case. In the diagram the helicopter is flying toward the left of the picture and the rotor is turning anticlockwise. A large stall region is seen for the retreating blade, starting at ψ=200° in the middle of the rotor blade, and moving outward toward the blade tip with increasing ψ. At the point of minimum local flow velocity, at ψ=270°, the outer 25% of the rotor blade is stalled, and the size of the stalled region then reduces until ψ=300°. This region is the classical dynamic stall area due to low-speed flow. The second stall region in Fig. 1.5b, at ψ=320-360° often occurs due to the torsional elasticity of the rotor blade. The stall causes a strong pitch-down torsion, which twists the rotor blade to reduce the angle of attack. This causes an early end to the dynamic stall region. When the stall ends, the pitch-down torsion stops and the rotor elastically recoils to have a higher angle of attack than would be expected for a stiff blade, and this causes the blade to stall for a second time. The increasing Mach number in this region means that the stall is prolonged past where it would be expected from a rigid blade.

The flight envelope of a helicopter has four basic limits, as shown in Fig. 1.6. At low forward flight speed, the rotor speed must be fast enough so that it contains enough rotational kinetic energy to allow transition to autorotation in the case of an engine failure. At the upper limit, the rotor should avoid transonic effects which cause high noise, but also increases drag and vibration. On the advancing rotor at high forward flight speeds, the appearance of strong shocks causes high drag and vibration which limits the maximum flight speed of the helicopter. This line can be shifted to higher speeds by the use of high-performance transonic airfoils in the outer part of the rotor blade, but these airfoils are generally thin, and the structural requirements of the rotor blade limit their application. A second method of avoiding this area is to slow the rotor rotation speed at high speed forward flight, however the technical difficulty of achieving a variable-speed transmission for a constant-speed turbine is

considerable.

The dynamic stall limit, seen at the bottom right in Fig. 1.6, appears on the retreating side for flight speeds where the rotor rotation rate is not high enough to cause transonic stall problems first. Lower rotor rotation rates cause earlier dynamic stall, and there is thus an optimum rotor rotation rate where both effects can be avoided. The line denoting dynamic stall can be easily moved to the left or right, and its location depends on the blade design and the load on the rotor (or thrust produced by the rotor), as a function of the flight altitude. A highly loaded rotor can be produced either by a heavily loaded helicopter, or by additional loading in turning flight. Additionally, the maximum thrust a rotor can produce without stalling is a function of the flight altitude and other factors including the air temperature and humidity. Thus the dynamic stall limits on a helicopter are often stated as HHH: Hot, High and Heavy. For a given forward flight speed and rotor rotation rate, a helicopter will fly into dynamic stall earlier if it is heavily loaded, undergoing turning maneuvers with increased positive g-loading, flying at high altitude, or on a hot day. Since the most basic parameters of an aircraft are the load it can carry, flight speed, turn rate and service ceiling, it can be seen that dynamic stall is a serious limitation on the flight envelope of helicopters

Airfoil design for rotor blades is complicated by the requirement to meet a range of design targets, both for the different flow conditions encountered during the rotor cycle for a constant flight condition, and for different flight conditions. The optimum performance (L/D) of most airfoils is reached shortly before stall, and thus stall diagrams, as seen in Fig. 1.7 illustrate how the different aims limit the rotor performance at different points. In Fig. 1.7a, the local sectional lift of the airfoil lift is plotted against the Mach number seen by the airfoil. At low Mach number and high angle of attack the airfoil stalls, and this is most commonly seen on the retreating blade. At high Mach number and high angle of attack, or with increasing angle of attack at constant Mach number, the airfoil experiences shock-induced stall. In Fig. 1.7a, the path followed by a single airfoil for high advance ratio and low blade loading is shown, and this section of the rotor would experience shock-induced stall. Of course parts of the rotor which are closer to the root have a lower Mach number and higher load, as seen in Fig. 1.7b, which can result in dynamic stall. To avoid these problems, modern rotors are designed with multiple airfoils, including thicker airfoils with higher lift before stall nearer to the hub, and thinner airfoils with a higher drag divergence Mach number near the rotor tip. Each airfoil is optimised for its maximum lift coefficient and drag divergence Mach number, and is optimised to produce a good L/D over a wide range of operating conditions. Additionally, the airfoils are required to have a low pitching moment to help reduce the blade control loads. Rotor blades are twisted to improve their efficiency, with higher angles of attack near the rotor hub, reducing toward the rotor blade tip, and this twist is also modified to reduce the effects of dynamic stall and shock-induced stall. The twist is visible in Fig. 1.4, especially on the high-speed side of the rotor (at ψ=90°), and it can be seen that even slightly negative angles of attack are achieved near the rotor blade tip at this position.

Thus it can be seen that dynamic stall is an interesting effect, and a practical problem which it would be advantageous to control. Improving our knowledge of dynamic stall allows improved helicopter design to avoid stall, an improved prediction of the helicopter flight envelope, and possibilities of reducing or eliminating dynamic stall. One method of approaching this problem is to study the effect of dynamic stall on a helicopter airfoil.

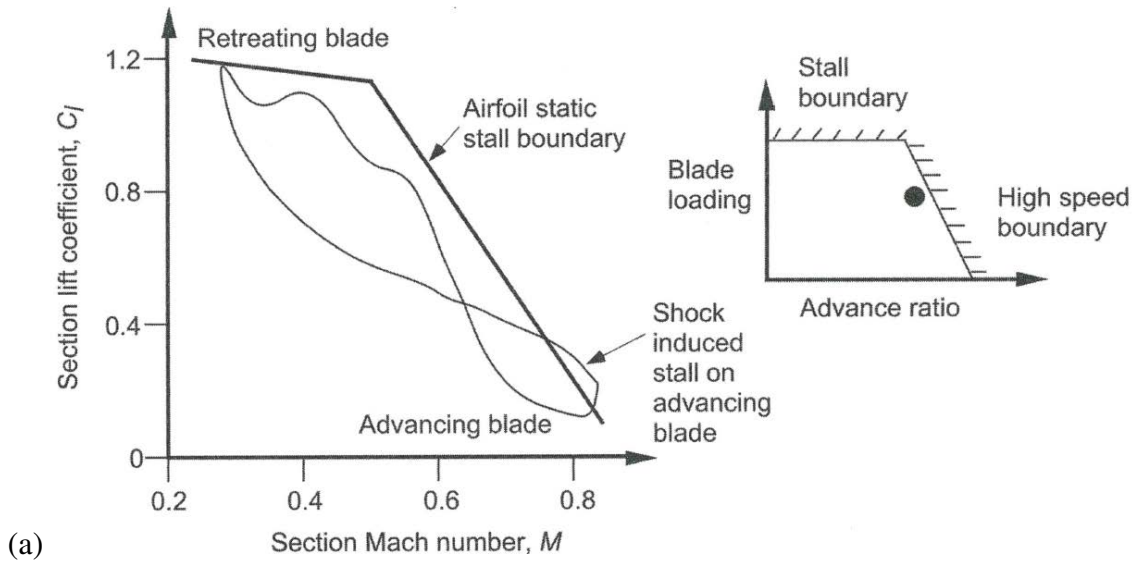

(a)

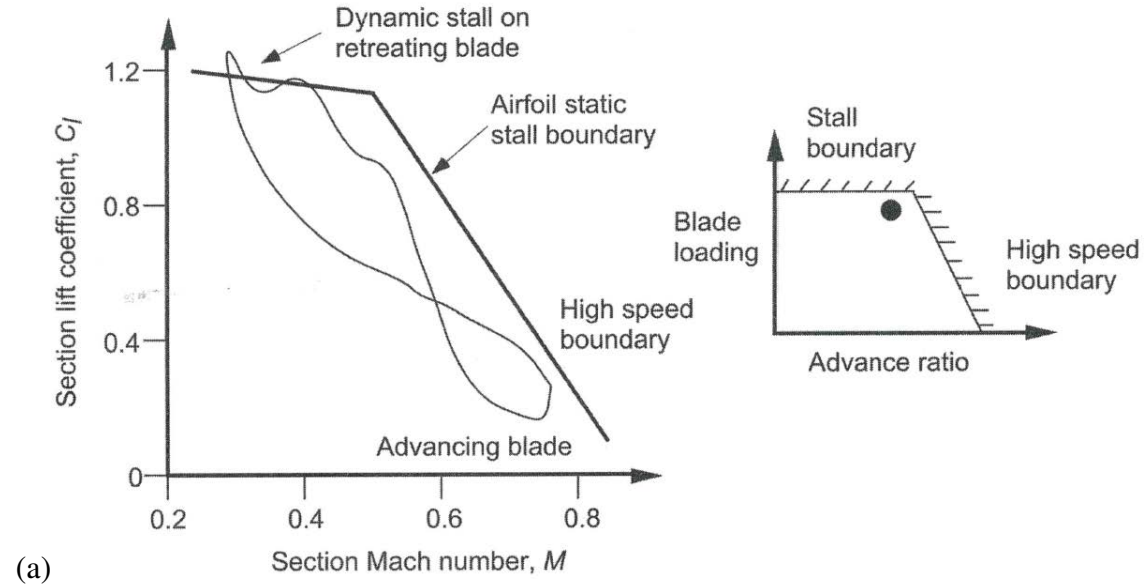

(a)

Figure 1.7: Example of operating limits on an airfoil at different flight conditions for a helicopter rotor airfoil. The limits may be determined by (a) Performance limitation my compressibility effects (b) Performance limitation by retreating blade dynamic stall (from [65]).

1.1 Dynamic stall on a helicopter airfoil

Dynamic stall is a well-known effect, which occurs when a pitching airfoil stalls [5, 9, 64] leading to a rapid change in pitching moment. Static airfoil stall is characterised by a transition from high lift attached flow to lower lift separated flow with increasing angle of attack. Between these two states is an intermediate region which contains a mix of the two conditions. In contrast, dynamic stall is characterised by large peaks in the forces and moments during the stall process which exceed the forces during any other flow condition.

Dynamic stall is a complex phenomenon, which is still not easily predictable or well understood. For low Mach number leading-edge stall, the most commonly studied variant, separated flow rolls up to form a coherent vortical structure: the dynamic stall vortex. The low pressure region in the center of the vortex acts on the airfoil to increase lift, which is a desirable effect also used by the flapping wings

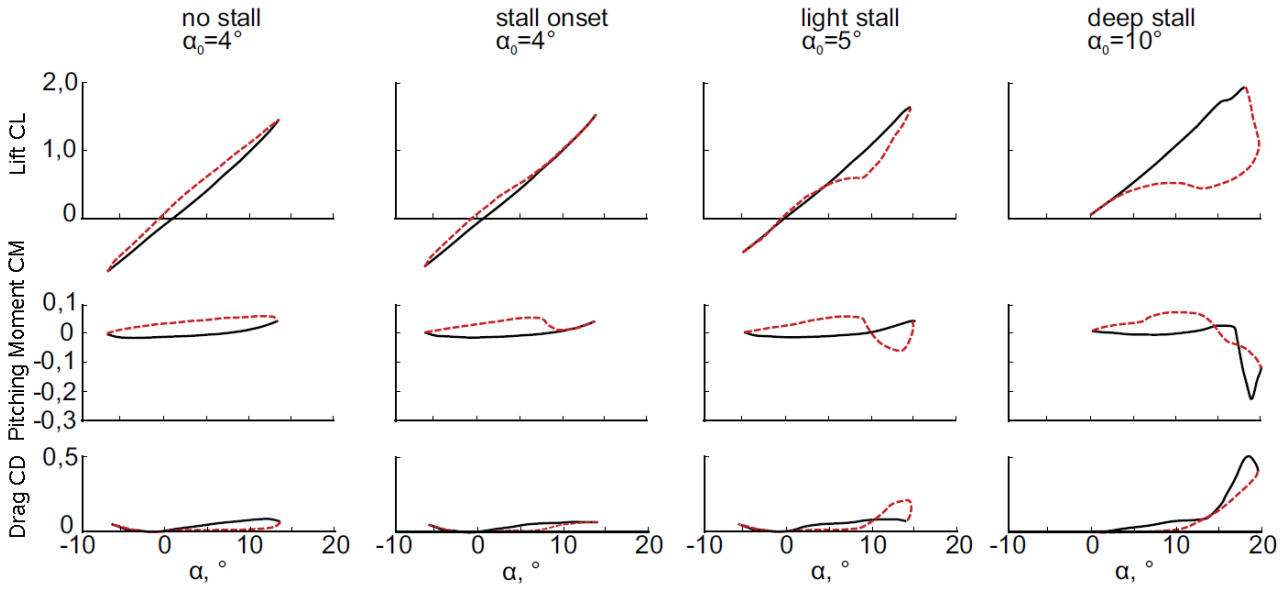

Figure 1.8: Dynamic stall variation with mean angle of attack on pitching airfoils. Red lines indicate downstroke. (from [79] via [46])

of insects. The dynamic stall vortex is convected downstream by the flow. As the point of application of the localised suction from the vortex moves toward the airfoil trailing edge a large negative pitching moment is seen in addition to the lift increase. As the vortex moves away from the airfoil, a rapid drop in lift is observed, as well as a return of the pitching moment to smaller negative levels, similar to those seen in static stall. The torsional impulse from the pitching moment peak is often a load-limiting case for the pitch links of the helicopter rotor blades, and high drag is experienced compared to attached flow. Control of dynamic stall concentrates on reducing the pitching moment peak while retaining high lift, and normally this will also result in a reduction of drag.

The dynamic stall vortex forms at the leading edge of the airfoil and is first indicated by leading edge separation, as for the OA209 [84], or by trailing edge separation, as for the VR-7 [77]. Depending on the airfoil, a leading edge separation vortex may be induced by the bursting of a laminar separation bubble or the action of a shock [9]. Particularly in the case where no large regions of supersonic flow are present around the airfoil, regarding the boundary layer as fully turbulent appears to often match the experimentally observed dynamic stall behaviour of the OA209 well [103].

With a few notable exceptions [50], most wind tunnels operate at constant Mach number over a period of seconds or longer. Thus the periodic variation of Mach number, as experienced by a helicopter airfoil cannot be directly studied except by installing a full rotor system into a wind tunnel. The experimental study of full rotor systems is technically challenging since the wind tunnel rotors have a high mechanical complexity, need to be driven by a motor and require trimming to the flight conditions. The high aspect ratio of the blades means that the wind tunnel model cannot be assumed to be stiff, and the elastic properties of the rotor blades must be known, and the true position and deformation of the rotor blades must be measured during the experiment to provide high-quality aerodynamic data. Due to the requirement to scale down a full rotor to the space available in a wind tunnel, the chord length of the rotor blades is generally small, with the limited space restricting the amount of instrumentation which can be included. Additionally, the extraction of data from the rotating frame requires a telemetry system which is costly and often very limited in the number of channels which can be broadcasted. The common simplification of the three-dimensional rotor is to use an airfoil pitching at a constant Mach number, where the Mach number is selected to be correct at the moment of stall.

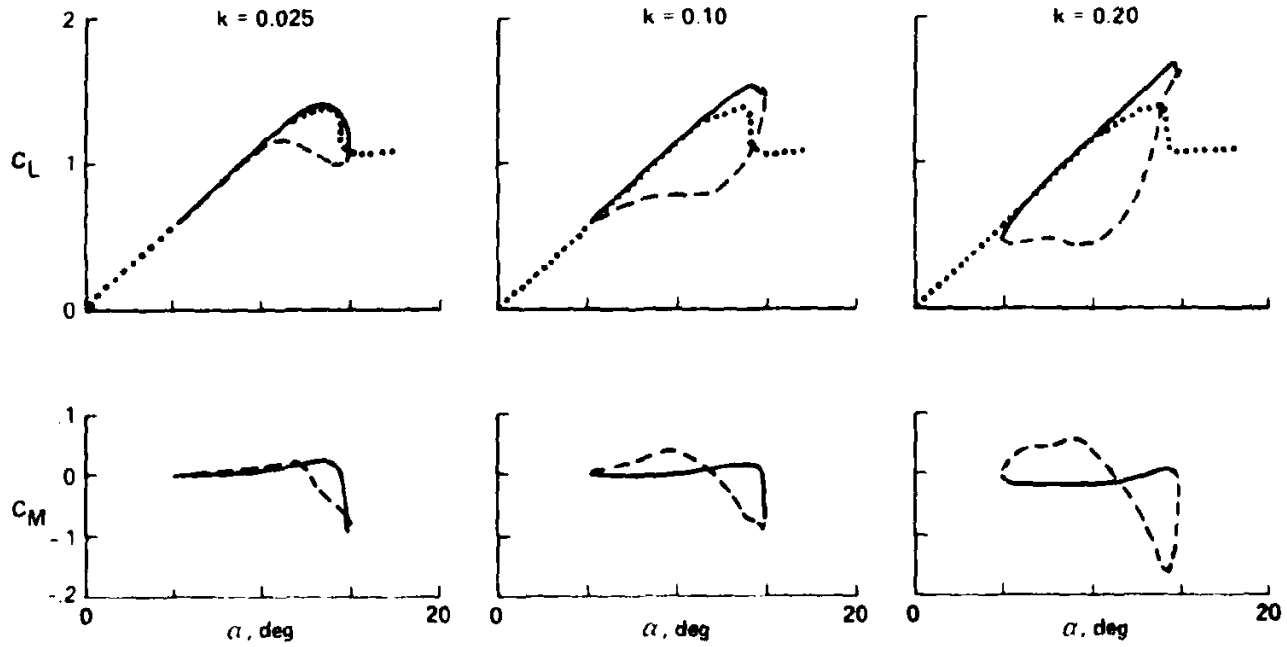

Figure 1.9: Dynamic stall variation with pitching frequency on pitching airfoils, from [79]

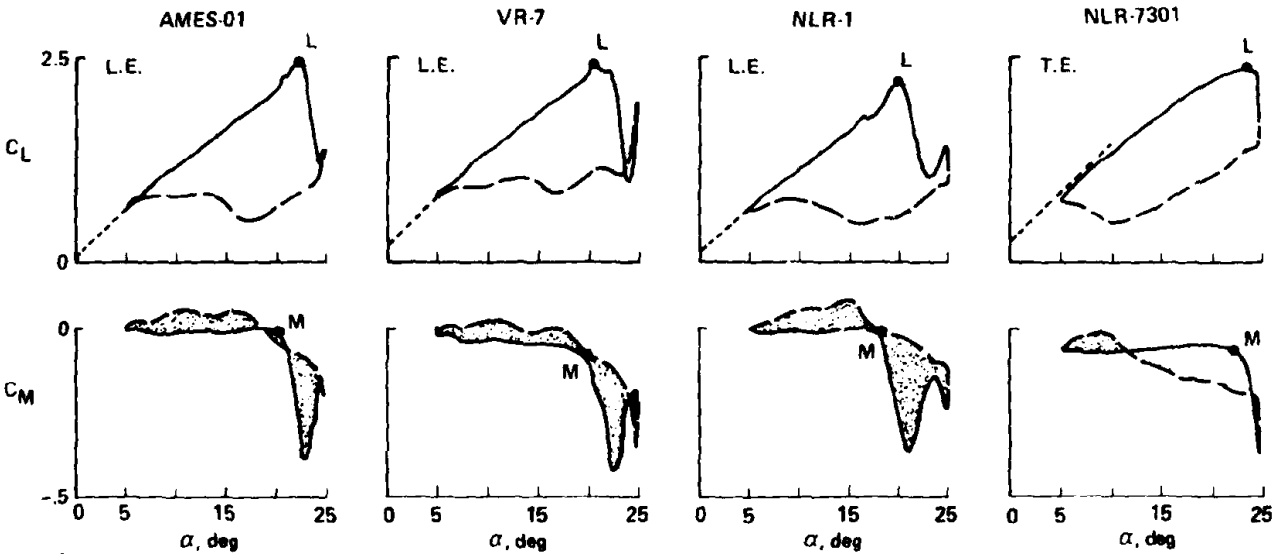

Figure 1.10: Dynamic stall variation with different airfoil types, from [79]

The most common aerodynamic simplification of the helicopter dynamic stall problem is seen in the sinusoidally pitching airfoil. Figure 1.8 shows the effect of raising the mean angle of attack of a pitching airfoil. At low mean angles of attack, the flow is linear and attached, and the resulting force curves show a damped, linear hysteresis around the static polar values, as suggested by Theordorsen's thin airfoil theory. As the mean angle is increased, then the oval hysteresis curve at lower angle turns into an "8", since at the high angle of attack nonlinearities due to the thickening of the boundary layer appear. Continuing to higher mean angles of attack results in stalled flow, by dynamic stall. The pitching moment coefficients show a large a negative pitching moment peak and this is concurrent with a large positive drag peak. Thus dynamic stall causes high transient loads in pitching moment, drag and lift, which lead to vibration and fatigue on an aircraft.

In addition to the mean angle of attack, the reduced frequency $\omega^* = 2k = 2\pi fc/v_\infty$ affects the severity of the dynamic stall, as seen in Fig. 1.9. At one extreme, the static stall (at zero reduced

frequency) does not cause a peak in the pitching moment. When dynamic pitching is used, increasing the pitching frequency increases the hysteresis of the lift curve, and increases the size of the pitching moment peak, leading to more severe dynamic stall with increasing pitching frequency. It can be shown that the severity of the dynamic stall is related to the *pitching rate* of the airfoil at stall, and thus increasing the pitching amplitude causes more severe dynamic stall, as a combination of the increased maximum angle of attack and the increased pitching rate at stall. Each of the results for the variation of mean angle and pitching rate in Figs. 1.8 and 1.9 are for a single airfoil. The selection of the airfoil tested at a particular flow and pitching condition has a strong effect on the severity of the dynamic stall, and on the behaviour at stall, as seen in Fig. 1.10. In Fig. 1.10 the AMES-01 and VR-7 airfoils have similar pitching moment peaks, but the VR-7 has a double peak in the lift at maximum lift, and a strong second peak is seen in the pitching moment. In comparison, the NLR-1 has a similar size of the pitching moment peak, but the earlier stall means both that the maximum lift is lower, and the time with a large negative pitching moment is greater than both of the airfoils to its left. Again the double pitching moment peak is seen for the NLR-1. In contrast the NLR-7301, which is a transonic supercritical airfoil, shows late stall with a very high maximum lift. When the NLR-7301 stalls, the pitching moment peak is as large as for the other airfoils, but the negative pitching moment remains low for much longer than the other airfoils. The clockwise middle loop in the pitching moment indicates a negative aerodynamic damping, and this airfoil will tend to extract energy from the air into the structure, and be prone to flutter under these conditions. Thus it can be seen that the airfoil selected can have a large effect on dynamic stall.

A pitching airfoil in a wind tunnel at constant Mach number can be used to estimate the dynamic stall properties of an airfoil [69, 77], as seen in the example in Fig. 1.11. Here an airfoil is mounted across the width or height of a wind tunnel test section, or more rarely between splitter plates, and the airfoil is moved in a forced, sinusoidal pitching motion by motors outside the wind tunnel. The dynamic pitching airfoil is a standard wind-tunnel technique used since at least the mid-1950s [76]. The best known experiments with this method come from McCroskey et al. [77]. Dynamic pitching airfoil rigs are used by a large number of universities [43, 64, 105, 108, 125] and research institutions [22, 56, 73, 99], although only NASA's Dynamic Stall Testing and Research Facility (DSTAR) [74], DLR's Transonic Wind Tunnel Göttingen (DNW-TWG) [32], and Notre Dame's Whitefield Laboratory [4] have recently published results for $M_\infty \geq 0.5$.

Airfoil testing in adaptive-wall test sections has been extensively studied for static cases showing that minimal interference with wind tunnel walls and good correction of the data is possible [100]. Figure 1.12 shows a sketch of an adaptive-wall test section where the top and bottom wind tunnel walls are deformed to follow the streamlines of an airfoil. An additional deformation compensates the blockage due to the growth of the boundary layers on the wind tunnel side-walls. The advantage of adaptive-wall test sections is that models with large blockages (10% or more) can be tested without the large wind tunnel interference which would be seen for a static-wall wind tunnel. Additionally, since the shape of the walls is recorded, the Reynolds-averaged Navier-Stokes (RANS) computation of the full three-dimensional wind tunnel installation is easier than for perforated walls or a free-jet.

It is generally assumed that the difference in static stall behaviour between two airfoils tested in the same wind tunnel is more reliable than predictions by Reynolds-Averages Navier-Stokes (RANS) codes, and can be used as a predictive tool when corrected and used as input into a correctly calibrated comprehensive code (for example as [52]) where dynamic stall models estimate the dynamic stall performance of the airfoils. The dynamic flow on a finite-span airfoil must be treated with some caution as a predictor for three dimensional (3D) rotor dynamic stall. Experimental results [5] suggest that the dynamic stall results are similar except near the blade tip, even though three-dimensional stall [14] exhibits the development of far more complex structures than two dimensional (2D) stall [84]. Despite these potential problems, pitching motion on a finite-span airfoil is usually the best available dynamic stall data available before flight testing.

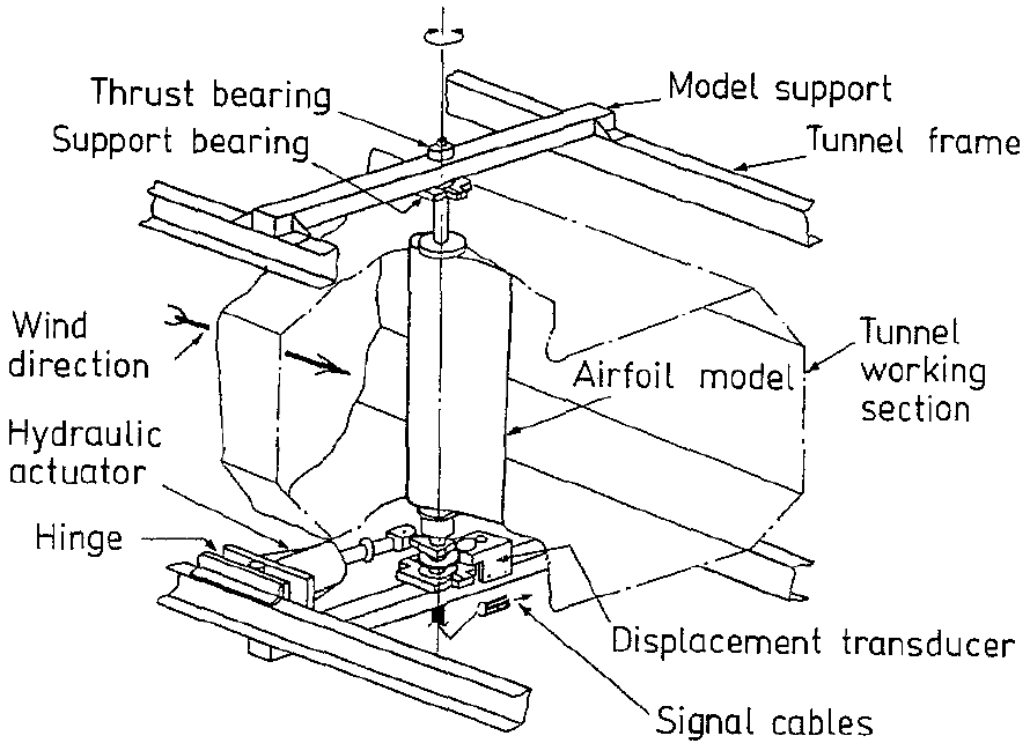

Figure 1.11: Pitching motion device in a wind tunnel showing mounting and actuation (from [64])

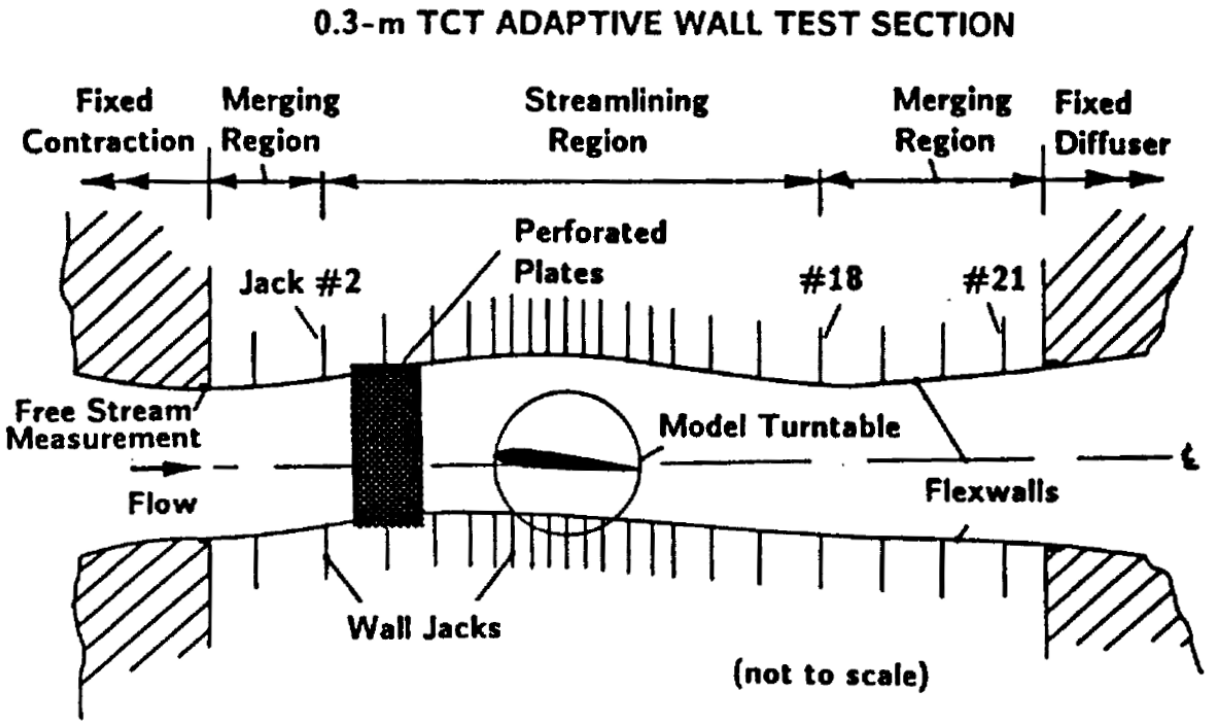

Figure 1.12: Diagram of the adaptive wall test section of the Langley 0.3 m Transonic Cryogenic Tunnel (TCT) (from [100])

The Mach numbers and Reynolds numbers of interest for the study of dynamic stall depend on the assumption about the condition in which stall occurs. If stall due to exceeding the maximum flight speed is assumed, then the dynamic stall occurs at Mach numbers $M < 0.3$. However a common case for dynamic stall is aircraft operation at high altitude with heavy loads (or under maneuver loads $>$1g), and in this case stall occurs at much slower forward flight speeds, leading to stall at Mach numbers $M < 0.5$.

Figure 1.13 illustrates a typical low-Mach-number leading edge dynamic stall and the comparison with static stall. At point 1, the airfoil is at low angle of attack, pitching up. Flow is attached in both the static and dynamic cases, and the aerodynamics are comparable. At point 2, the static stall angle has been reached, and the static case begins to separate. The dynamic case has attached flow, but a thickening of the boundary layer. Point 3 sees the start of the dynamic stall process, with the development of a small dynamic stall vortex near the airfoil leading edge. At this point the rest of the flow on the airfoil is still attached, and the stall is visible as the start of the negative pitching moment peak, and a reduction in the slope of the lift curve. As the dynamic stall vortex moves downstream,

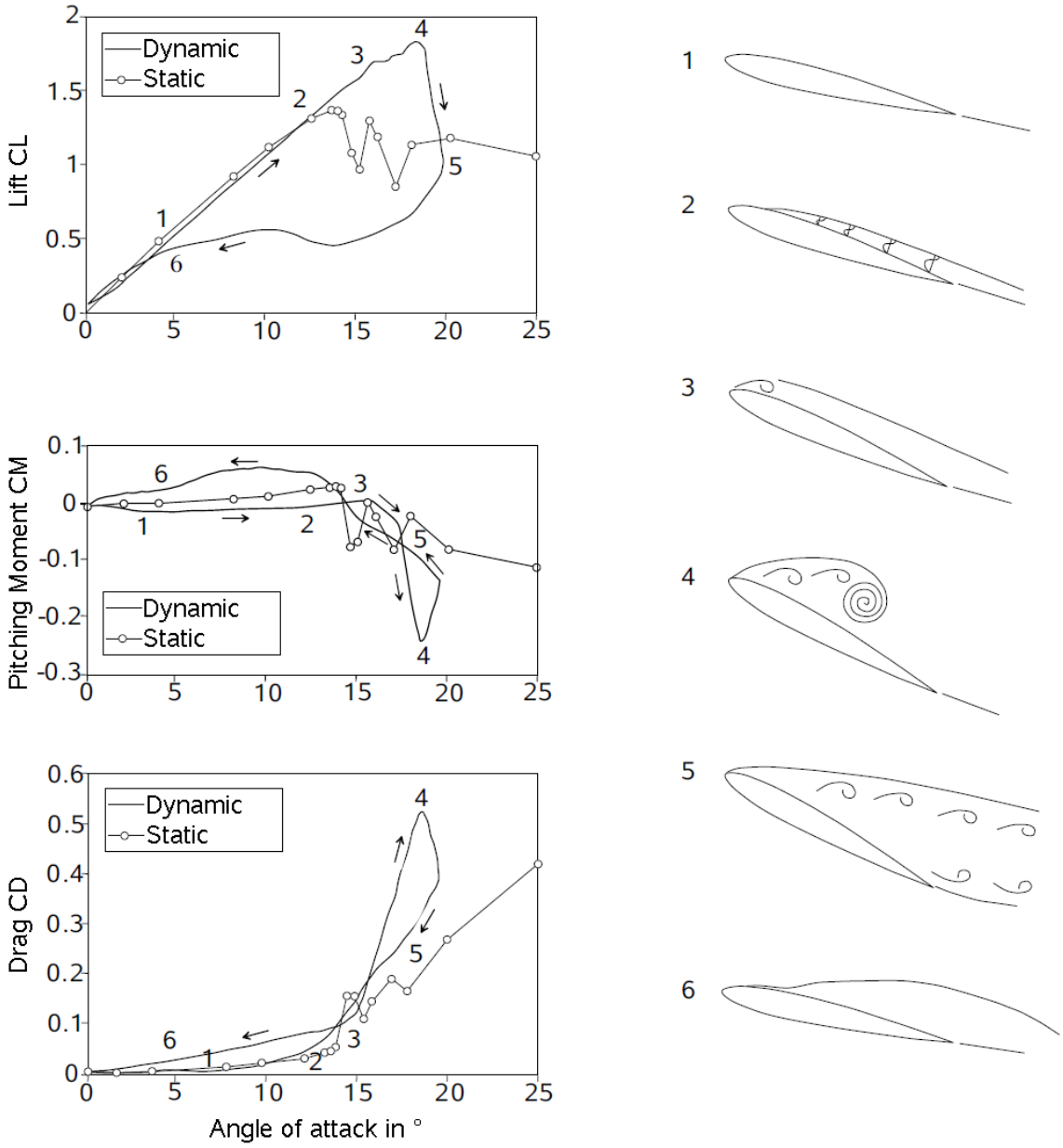

Figure 1.13: Low Mach number, leading edge dynamic stall (from [65])

the vorticity in the airfoil boundary layer is entrained into the vortex. The rotating vortex has a low pressure region at its core, which acts on the airfoil. By point 4 the effect of the low pressure region of the vortex is at a maximum, causing a peak in the lift. Since the vortex is near the airfoil trailing edge at this point, the effect is to suck the trailing edge upward, causing a negative peak in the pitching moment. The separated flow on much of the airfoil and the high angle of attack mean that point 4 is also associated with a peak in the airfoil drag. After this, the vortex moves off from the airfoil, causing a rapid drop in lift and a rise in the pitching moment, as the airfoil transitions to fully separated flow at point 5. As the airfoil pitches down, then the flow reattaches from the leading edge to the trailing edge around point 6, and the cycle restarts.

The idea for the control of dynamic stall is that transitioning from point 2 to point 5 in Figure 1.13 by no means requires the appearance of high pitching moments or a dynamic stall vortex. Since the lift is lower in stalled flow, the circulation of the airfoil must be transported away somehow. This is already the case for some well-known natural cases, such as for shock-induced separation, where the transport of circulation away from the airfoil occurs by the formation of a thick, separated shear layer downstream of the shock which does not form a dynamic stall vortex. Likewise, many airfoils exhibit trailing edge stall at low Mach number, and here most of the circulation is bled away in a slow expansion of the separated region from the trailing edge to the leading edge before a dynamic stall vortex is formed, and these test cases show lower peaks in pitching moment and drag. Additionally, if the lift after stall remains relatively high then the circulation available for the formation of the dynamic stall vortex is reduced.

Although the convection of circulation (or vorticity) away from the airfoil explains the reduction in lift associated with dynamic stall, this does not explain why two airfoils might have similar lifts before and after stall but a different dynamic stall process. The movement of the separation point, either from trailing edge to leading edge, or from a midpoint on the airfoil towards the leading edge accounts for much of the difference between airfoils. Likewise, trailing edge separation cases result in less of the pre-separation shear-layer being rolled up into the dynamic stall vortex, and in a slower stall process, both of which are clearly advantageous in reducing the peak forces and moment associated with dynamic stall.

1.2 Visualisation of dynamic stall in the literature

Experiments in dynamic stall have a long history, with the first "modern" pitching airfoil experiments taking place in the 1950s [76]. Wind tunnel experiments primarily used pressure measurements with tubes attached to a scanning pressure system. As seen in [77], the time-scale of these measurements was limited to, at best, a few hundred Hertz, due to the length of the tubes and the limitations of the scanning system. Modern experiments, such as those described in this habilitation thesis, use miniature pressure sensors mounted close under the surface of the airfoil, and this results in reliable measurements up to a frequency of 1-5 kHz, depending on the details of the sensor mounting. Additional measurements using force balances can also be used, but tend to be avoided since airfoil measurements are nearly impossible to make without a significant effect of the end connections of the airfoil, which can lead to systematic errors as high as 30% of the force measured.

Modern flow visualisation has resulted in a significant understanding of the dynamic stall process, and has improved on the classic visualisations of the flow using hot-wire anemometry and distributed

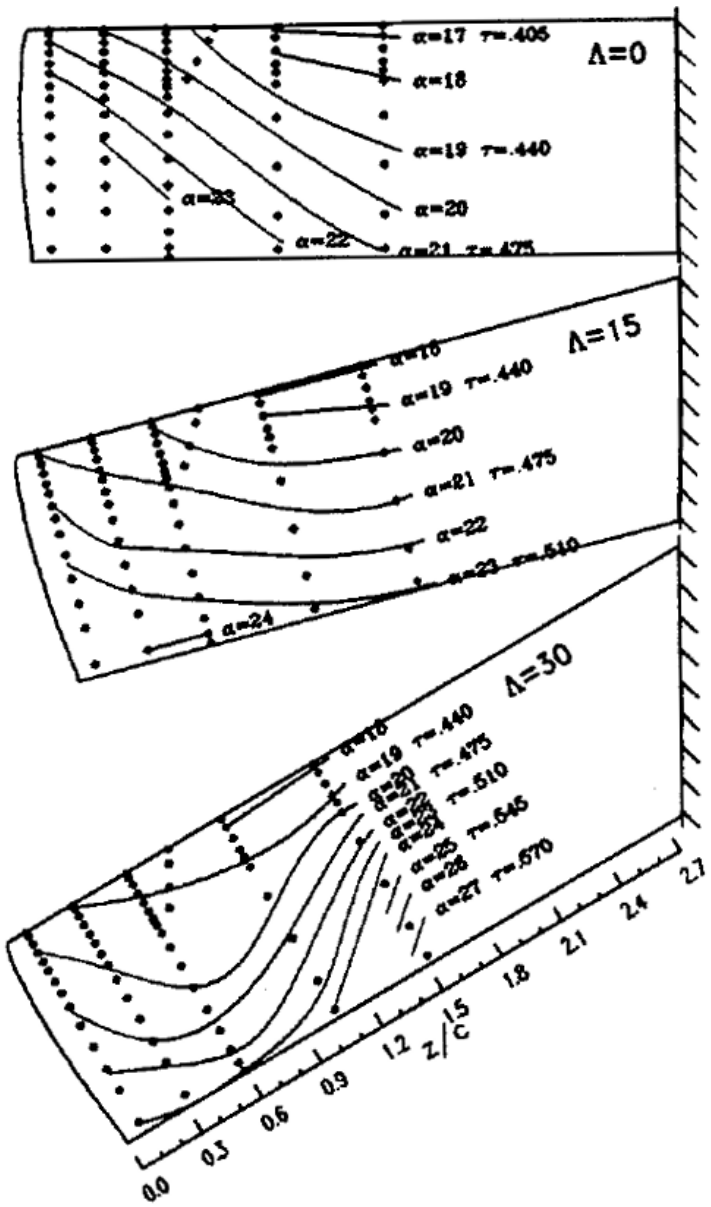

Figure 1.14: Visualisation of the propagation of dynamic stall over a three dimensional wing by the analysis of hot film and pressure signals (from [71])

pressure sensors. Figure 1.14 shows an analysis of pressure and hot-film signals to find the three-dimensional footprint of the dynamic stall vortex on the surface of a three-dimensional wingtip during dynamic stall for different sweep angles of the wing. This is a particularly interesting problem for rotorcraft, since the rotor blade only has a nonzero sweep at ψ=90° and ψ=270°, and the rest of the time the blade has a sweep angle which may approach 90° for areas on the blade which have a low onflow velocity. In Fig. 1.14, the point of initial stall moves toward the wing tip for increasing sweep angle. The dynamic stall vortex becomes bowed as it moves downstream, and this bowing is more pronounced for higher sweep angles, where the stall vortex propagates towards the wing tip and starts to interact with the wing tip vortex. Similar surface visualisations can be gained by liquid crystals, or by using Pressure Sensitive Paint (PSP), as seen in Chapter 3 of this habilitation thesis.

A sensitive Schlieren system (see Fig. 1.15) can visualise the density gradients produced when the dynamic stall vortex is formed. In Fig. 1.15, the formation of a classic low-speed dynamic stall vortex

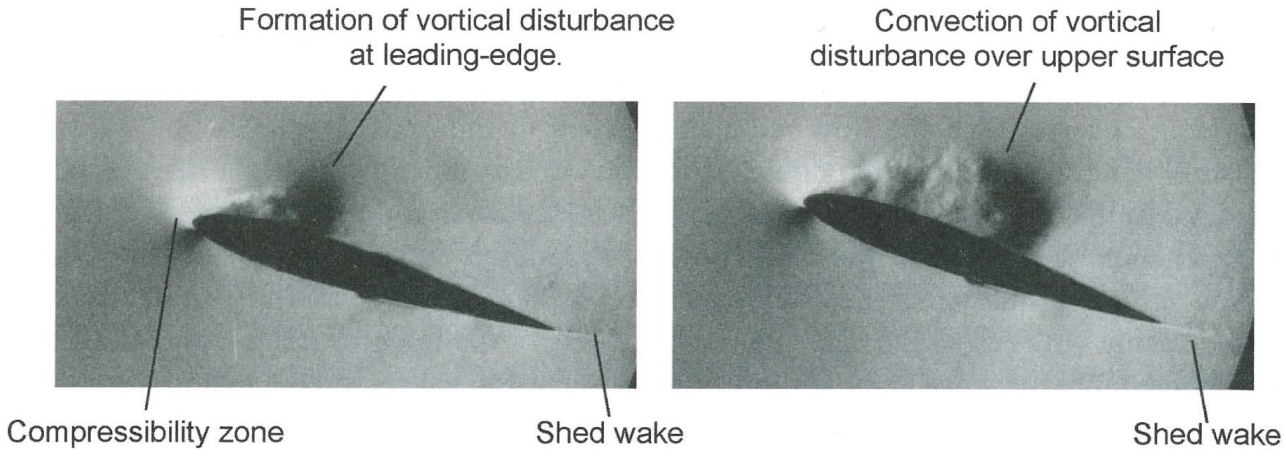

Figure 1.15: Schlieren visualisation of dynamic stall on pitch-up. Left: α=15.9°, Right: α=17.1° (from [10], via [65])

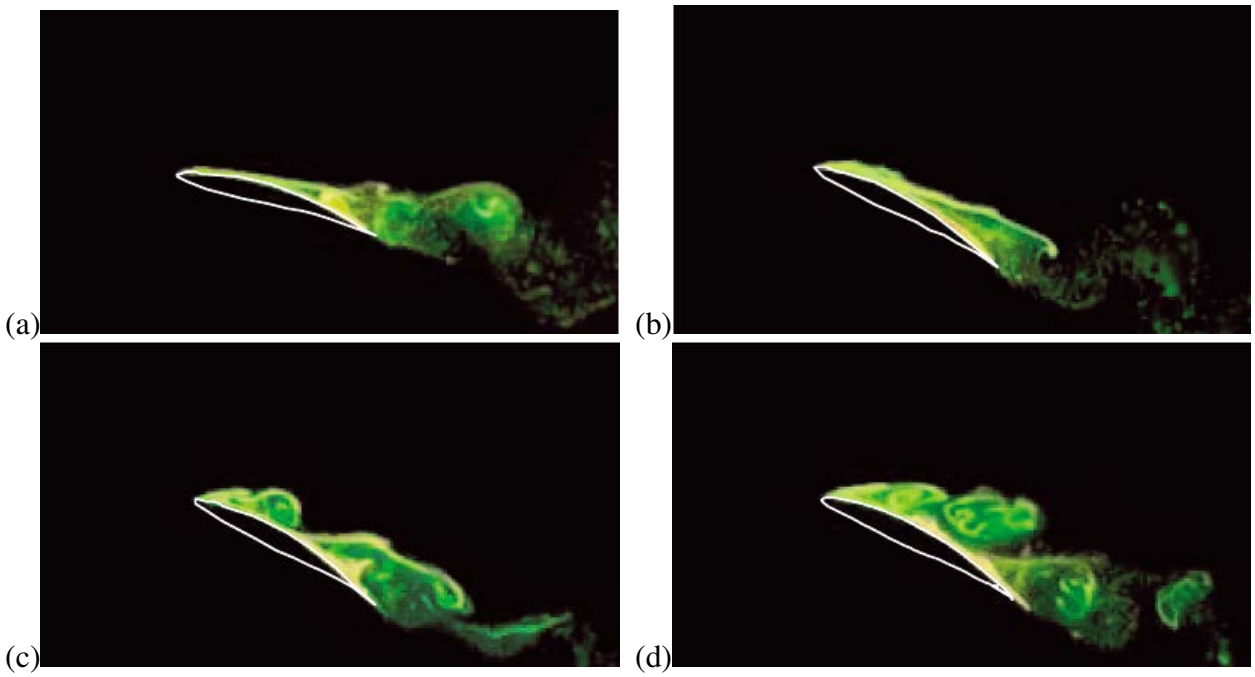

Figure 1.16: Dye visualisation of the progression of a dynamic stall vortex in a water tunnel (a)-(d): Generation of the main dynamic stall vortex (from [21])

is shown, with the vortex forming near the leading edge of the airfoil and afterwards being convected downstream by the external flow. The small initial vortex rolls up the turbulence from the boundary layer on the suction side of the airfoil, and the turbulent structure of the flow within the dynamic stall vortex can be clearly seen in Fig. 1.15, Right. The Schlieren system can also detect the boundary layer and wake of the airfoil, with sufficient sensitivity. Alternative systems to Schlieren, including shadowgraphy and Background Oriented Schlieren (BOS) will provide similar data to those seen for the schlieren system.

The concentrated nature of the vortex and the low density gradients mean that visualisation in water tunnels using bubbles or dye (see Fig. 1.16) can be used for an improved visualisation of the dynamic stall process. The dye visualisation in Fig. 1.16 shows the generation of dynamic stall in more detail. A trailing edge separation extends forward from the trailing to the leading edge, and then a dynamic stall vortex is formed. More fine detail can be seen here than in the Schlieren visualisation, and the generation of multiple vortices can be seen in a shedding stream, with some similarity to blunt body flow. The laminated structure of the young vortices due to the entrainment of the boundary layer flow, and the turbulent nature of the vortices is apparent due to the rapid mixing of the dye. This visualisation shows a typical trailing edge stall, as seen for stall with relatively thick airfoils, or for lower reduced frequency. Using smoke trails, bubbles or other tracer methods result in similar visualisations.

Unfortunately, many dynamic stall phenomena, even at moderate Mach numbers are the result of transonic effects [74], so that water tunnel experiments are only suitable for qualitative comparisons, or for very low Mach number comparisons. The effects of compressibility on dynamic stall are effectively illustrated at Mach 0.3 by the interferograms in Fig. 1.17. Interferometry produces fringe diagrams, where the fringe shift is a linear function of the refractive index, and for subsonic flows is approximately a function of the density. In Fig. 1.17a it can be seen that the leading edge stall is preceded by the formation of a series of weak shocks. In this case the shocks do not cause separation

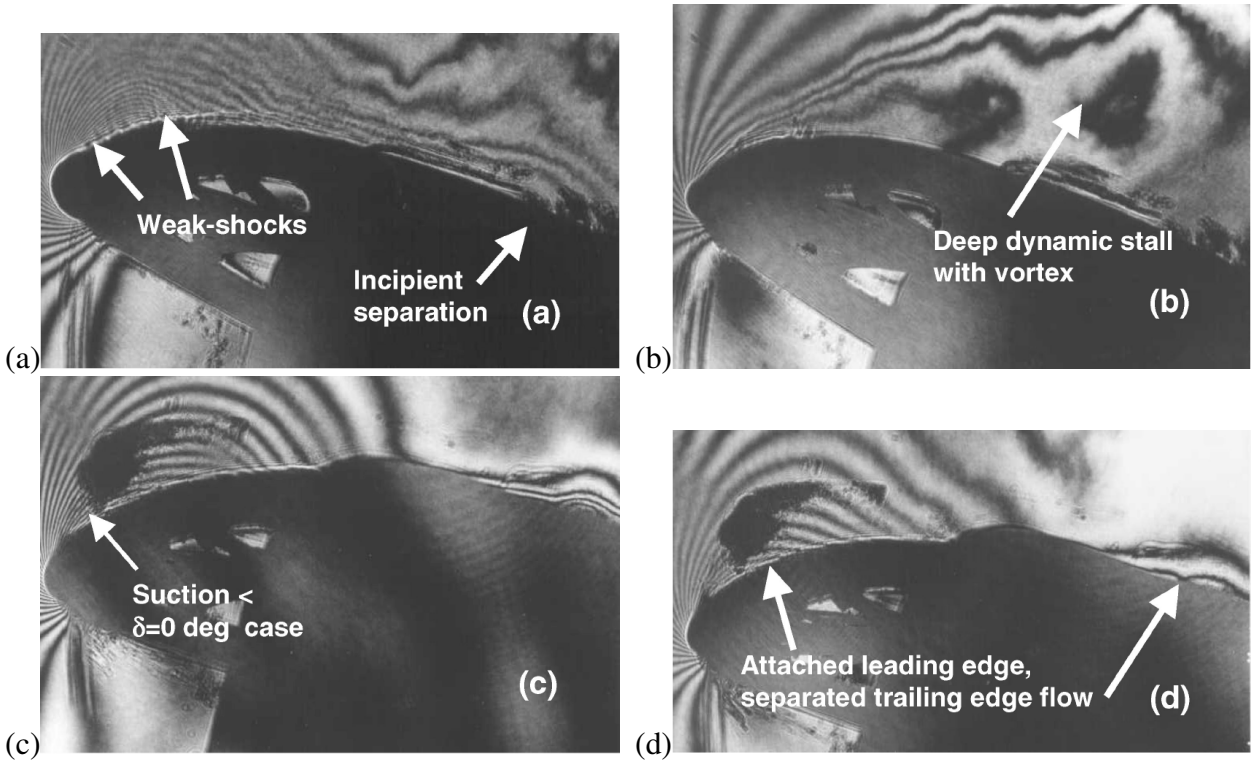

Figure 1.17: Point diffraction interferogram visualisation of the progression of a dynamic stall vortex at Mach 0.3 (a)-(d): Generation of the main dynamic stall vortex (from [8])

directly, and the separation is triggered by the advance of the trailing edge separation towards the leading edge. The dynamic stall vortex is visible as a density ring in Fig. 1.17b, due to the low pressure region in the middle of the vortex. The reattachment starts from the leading edge with the re-formation of the suction peak in Fig. 1.17c, and then the attached flow expands toward the trailing edge. Like Schlieren, interferograms give qualitative integral data on the flow field, and although they can be calibrated to give absolute density data, this is technically challenging and not usually done.

Although the visualisation of the flow via Schlieren or tracers is important qualitatively, quantitative analysis of the flow requires improved measurement techniques. The oldest of the quantitative optical methods currently in use is Laser Doppler Velocimetry (LDV), also known as Laser Doppler Anemometry (LDA). In this method the velocity at a single point is measured using a particle counting method at the intersection of two laser beams. Multiple velocity components can be measured by using multiple pairs of laser beams, and data rates of tens of kilohertz are typical. If the beam is scanned across a volume, then an image can be produced, but this image is averaged both over both over a range of time (or angle of attack), and phase-averaged. Moreover, due to the scanning process, different parts of the images are taken at different times. Figure 1.18 shows an LDV measurement of dynamic stall on the suction side of a finite wing, where the colour contours are of normalised velocity. The attached flow in Fig. 1.18a gives way to progressively more separated flow in Fig. 1.18b and 1.18c, and then the separated flow starts to reduce in Fig. 1.18d. The time and spatial averaging in the LDV measurements mean that no concentrated dynamic stall vortex is visible, but the velocity values are absolute.

An improvement on this situation is given by using Particle Image Velocimetry (PIV), where the entire two-dimensional field is taken my measuring the movement of particle groups between two images. The images are taken by illuminating the flow using a thin laser sheet, with the small seeding particles visible as points on the images. Many PIV measurements are phase-averaged to improve the signal-to-noise ratio of the signals, and this results in data such as that in Fig. 1.19. The fast laser pulses and known measurement times results in a well-defined time of the images, and the thin laser sheet mean that a defined two-dimensional slice of the field is observed. Similar to the dye results, Fig. 1.19a and b show a trailing edge separation which advances to the leading edge. Figures 1.19c and d show the generation of a single, large dynamic stall vortex, with some smaller vortices surrounding it, and this single large vortex propagates downstream. We know, for

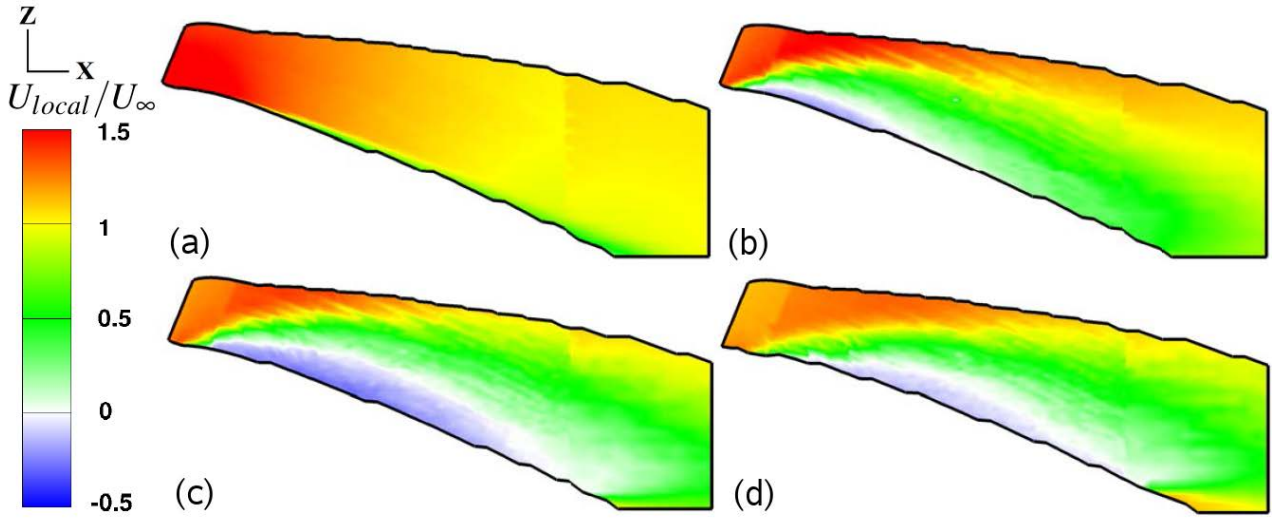

Figure 1.18: LDV visualisation of the progression of a dynamic stall vortex with contours of velocity. the flow is from left to right and the airfoil top surface is at the bottom of each image. (a)-(d): Generation of the dynamic stall vortex (from [58])

example from the dye visualisation, that the main vortex is an agglomeration of smaller vortices, but the phase averaging causes the resulting image to appear to have only a single vortex in the results. This description of the dynamic stall vortex is sufficient to describe the amount of energy in the vortex, and the low pressure region in the center of the vortex region. Many CFD codes using one and two-equation turbulence models, as seen in Fig. 1.20, also predict the generation of a few large vortices, rather than the smaller vortices seen in experiments, although sufficiently complex turbulence models also generate smaller vortices. The counter-rotating vortex generated at the airfoil trailing edge is visible both in the experiment and the PIV, and it is this vortex which works to convect the dynamic stall vortex upward away from the airfoil, and eventually to separate it from the airfoil.

High speed particle image velocimetry functions similarly to standard PIV, but the laser pulse rate is high, usually 1-10 kHz, and cameras are available which take a picture for each laser pulse. This results in a series of images with direct correlation to the instantaneous flow. The camera data rate, total amount of data and laser power required are technically challenging, but high-speed PIV systems are currently commercially available. The results of the high-speed PIV analysis is a series of fields which follow each other directly, and thus individual vortices can be followed. The correlation of the

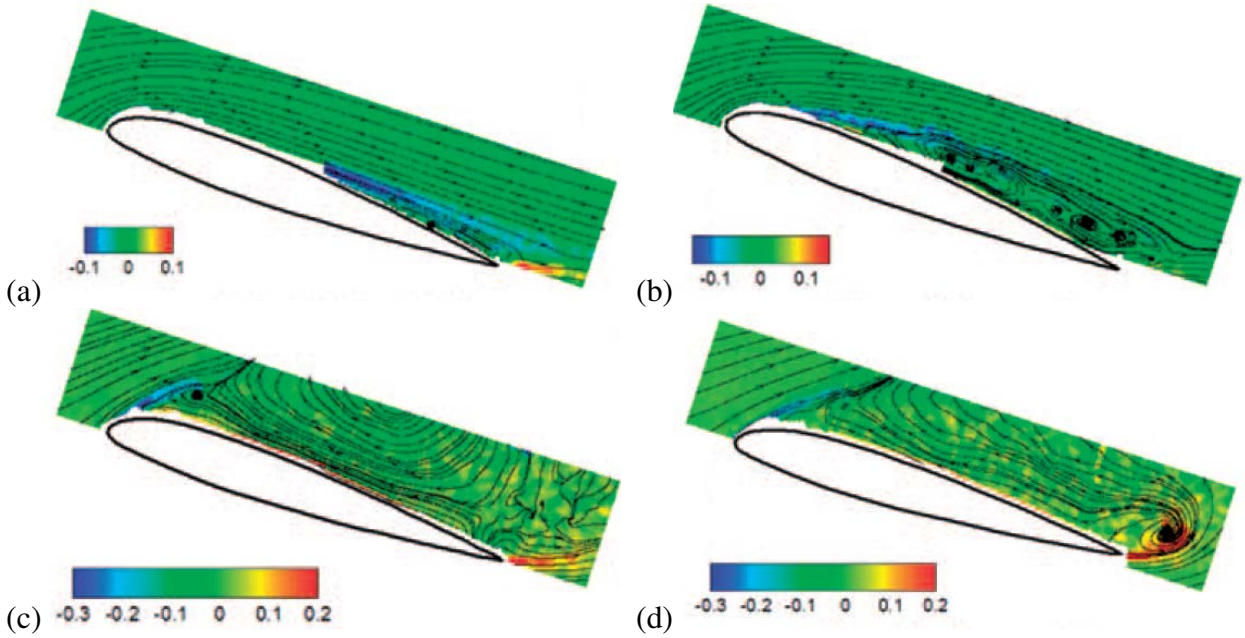

Figure 1.19: Phase-averaged PIV visualisation of the progression of a dynamic stall vortex (a)-(d): Generation of the dynamic stall vortex (from [125])

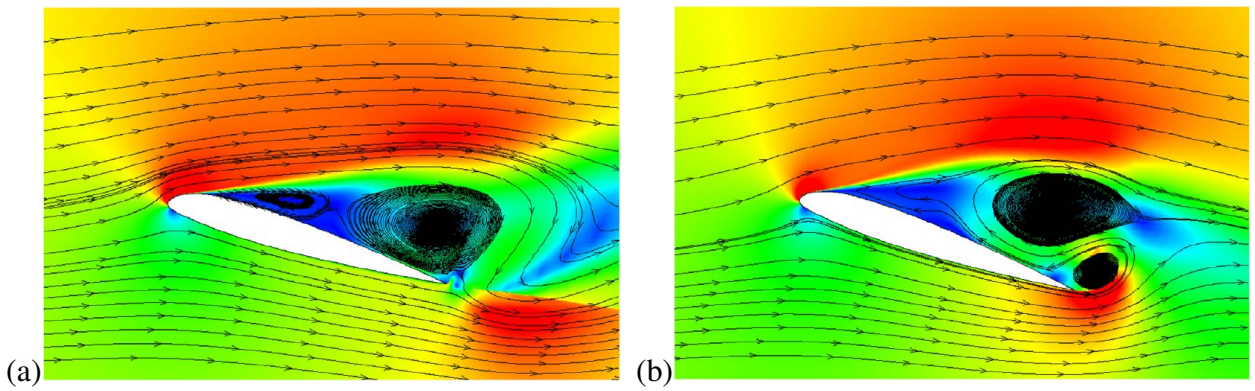

Figure 1.20: Two-dimensional CFD of low speed dynamic stall (a)-(b): Propagation of the main vortex downstream (from [126])

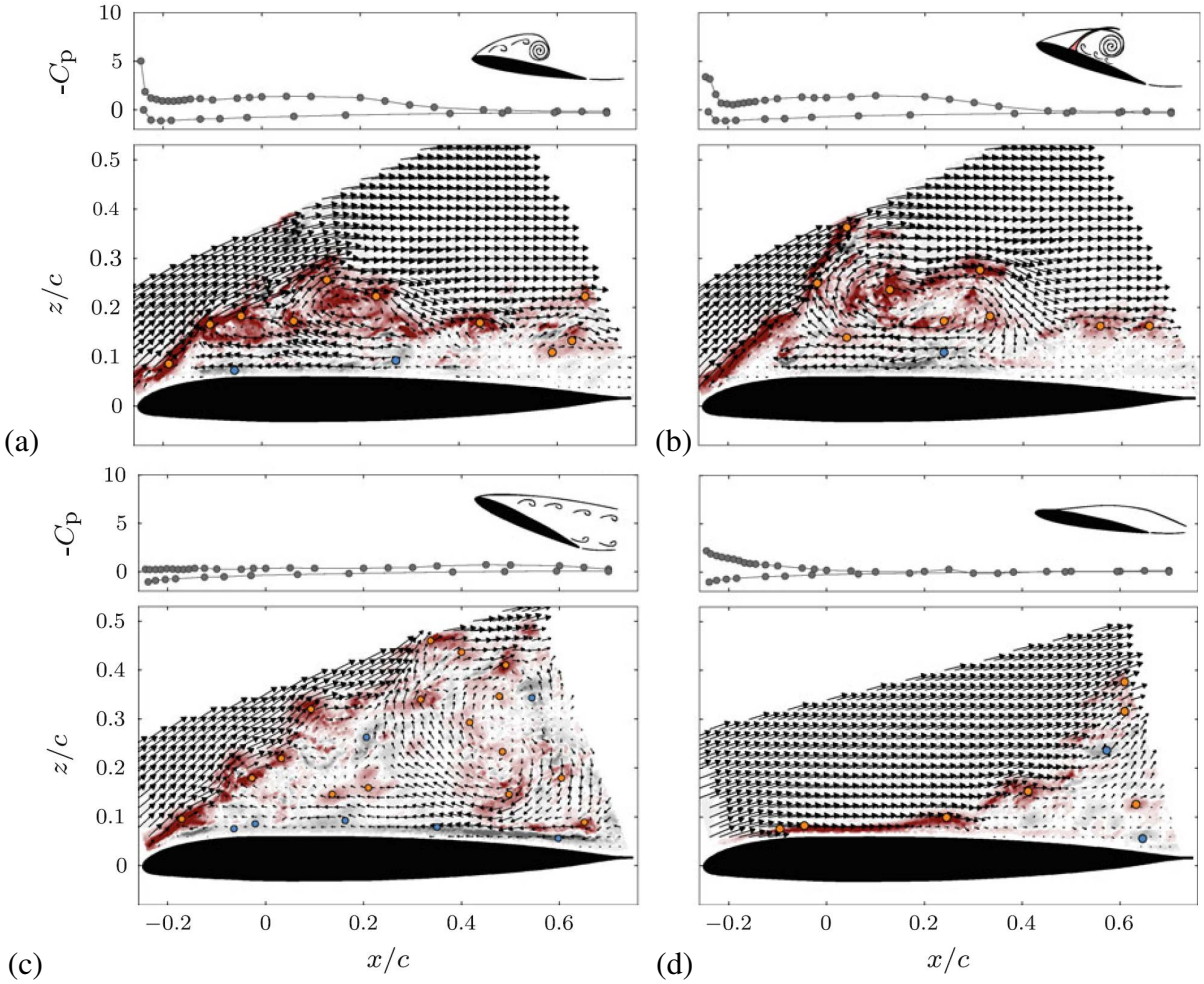

Figure 1.21: Instantaneous PIV visualisation of the progression of a dynamic stall vortex, with simultaneous pressure measurements (a)-(d): Propagation of the main vortex downstream and reattachment (from [85])

PIV images with pressure data aids in understanding the pressure signals for other cases where PIV is not available. Figure 1.21 shows four high speed PIV images, together with their corresponding pressure distributions for an airfoil undergoing dynamic stall. The out-of plane vorticity is coloured, and the in-plane components are denoted by the vectors. The vortex cores were detected using an Euler method and are illustrated using orange dots for clockwise vortices and blue dots for counterclockwise vortices. The newly generated dynamic stall vortex is shown in Fig. 1.21a, and in Fig. 1.21b and Fig. 1.21c it is convected downstream, leaving a fully separated, turbulent flow in its wake. In Fig. 1.21d the flow reattaches from the leading edge, and this image is immediately followed by fully attached flow. It can be seen in the vectors that a single dynamic stall vortex is formed, but the colour contours show that this vortex is highly turbulent, with high local out-of-plane velocities. The vortex detection method yields multiple vortex cores, showing that the large vortex actually agglomerates several smaller vortices. The counter-rotating trailing edge vortex is not seen in this view, although it must be present.

1.3 Similarity parameters for dynamic stall

The forces on a pitching airfoil are affected by the same similarity parameters as for non-pitching airfoils: Mach number M and Reynolds number Re computed using the airfoil chord. When we consider the force coefficients C_L, C_D and C_M, then the direct effect of Mach number is to define whether the flow will separate due to the presence of recompression shocks. Depending on the airfoil, this first occurs around Mach 0.4-0.5. Since the typical Reynolds numbers at which helicopter airfoils are operated are of the order of 1 Million, then the Reynolds number has two effects: Firstly, a thickening of the boundary layer at low Reynolds numbers increases the amount of vorticity in the shear layer which can be entrained into a dynamic stall vortex, resulting in higher forces, as seen in section 4.3. Secondly, the boundary layer transition interacts with the separation and reattachment in unexpected ways. The transition has been shown to have a large effect in some test cases and absolutely no effect in others [103].

For a sinusoidal pitching of the type:

$$\alpha = \overline{\alpha} + \alpha_{\pm} \sin(2\pi f t), \tag{1.1}$$

the reduced frequency:

$$\omega^* = 2k = 2\pi f c / v_{\infty}, \tag{1.2}$$

is used to find a similarity between different test cases. The two reduced frequencies ω^* and k differ by a factor of 2 and are used by different research groups. Increasing the reduced frequency increases the hysteresis of attached flow, and increases the strength of the dynamic forces due to dynamic stall during separated flow, as shown further in section 2.2. Increasing the pitching amplitude $\alpha_{\pm}$ or the mean angle of attack $\overline{\alpha}$ results in an increase in the maximum angle of attack α_{max}, and this correlates with an increase in the dynamic stall forces, see section 2.2. Similarly, increasing the pitching rate of the airfoil α' at the moment of stall results in increased forces, although since the instantaneous pitching rate α' is often not known (due to variation in the separation angle), the mean pitching rate $\overline{\alpha'}$ can be used as a substitute.

The aerodynamic damping:

$$D = [-\oint C_M \, d\alpha (\alpha_{\pm})^2 \pi^3 c f] / [2 v_{\infty}], \tag{1.3}$$

is used as a measure of the energy transfer between the flow and structure, and is used particularly for the pitching moment to identify flows which can be aeroelastically unstable, as shown in sections 4.3.7 and 2.2. Particularly when flow control by blowing is used, then the damping is an important parameter. For flow control, the blowing constants:

$$C_{\mu} = \frac{2}{bc} \frac{\dot{m}_j v_j}{\rho_{\infty} v_{\infty}^2}, \tag{1.4}$$

(jet momentum ratio) and:

$$C_q = \frac{\dot{m}_j}{\rho_{\infty} v_{\infty} bc}, \tag{1.5}$$

(jet mass ratio) can be used to normalise the blowing rates. C_{μ} is well defined for incompressible flows, but can provide some unexpected results for compressible flows, and thus C_q is provided additionally. For pulsed blowing, the pulsation rate is normalised as:

$$F^+ = f_{pulse} x_{te} / v_{\infty}, \tag{1.6}$$

where x_{te} is the distance between the flow control and the airfoil trailing edge, effectively providing a Strouhal number for the pulsation.

1.4 Dynamic stall control in the literature

A large number of groups have investigated devices for the control of dynamic stall. Passive methods, including slotted airfoils [6, 7] and perforated airfoils [97], use the energy in the oncoming flow and do not require any actuation in the rotor blade. The example perforated airfoil in Fig. 1.22 has a pipe installed to use air from the airfoil pressure side to control the flow on the airfoil suction side. This is an example of low pressure blowing, with the advantage that the pressure difference between the pressure and suction sides of the airfoil increases with increasing angle of attack, meaning that the blowing is most effective near stall. Equally, since the pressure difference between the pressure and suction sides is small at low angle of attack, the negative effect on the flow is reduced. Prince et al. showed experimentally and numerically that this configuration could control static stall on an airfoil, while having the same or less drag as the airfoil without flow control.

Camber-changing devices including the active droop nose [37], which can also be combined with a flap [8, 53] use the energy of the incoming flow, but require actuation to change the camber of the airfoil between the retreating and advancing sides of the rotor. The droop nose airfoil in Fig. 1.23 could be actively actuated once per pitching cycle to change the camber of the airfoil. Statically, the droop nose acts similarly to a slat or a flap, but is more mechanically stable. Statically the maximum lift is increased and the stall delayed, but once the airfoil stalls, the stall behaviour is not significantly changed. For the pitching airfoil, since camber-changing devices increase the maximum lift before stall, the droop nose could delay stall and significantly decrease the height of the pitching moment peak. The active actuation was necessary to avoid adverse transonic effects at high Mach number

The relatively low actuation frequencies of the droop nose, due to its relatively large size, mean that a smaller device would be more suitable if higher harmonic control is of interest in addition to dynamic stall control. Smaller devices also can be actuated with less power and smaller actuators. The active Gurney flap, shown in Fig. 1.24, is a small, vertical flap which extends from the underside of an airfoil near the trailing edge. In the example shown, the Gurney flap is not precisely at the trailing edge due to the space required to retract the Gurney flap at low angles of attack and high Mach numbers. The low weight of the Gurney flap meant that it could be fully actuated at up to

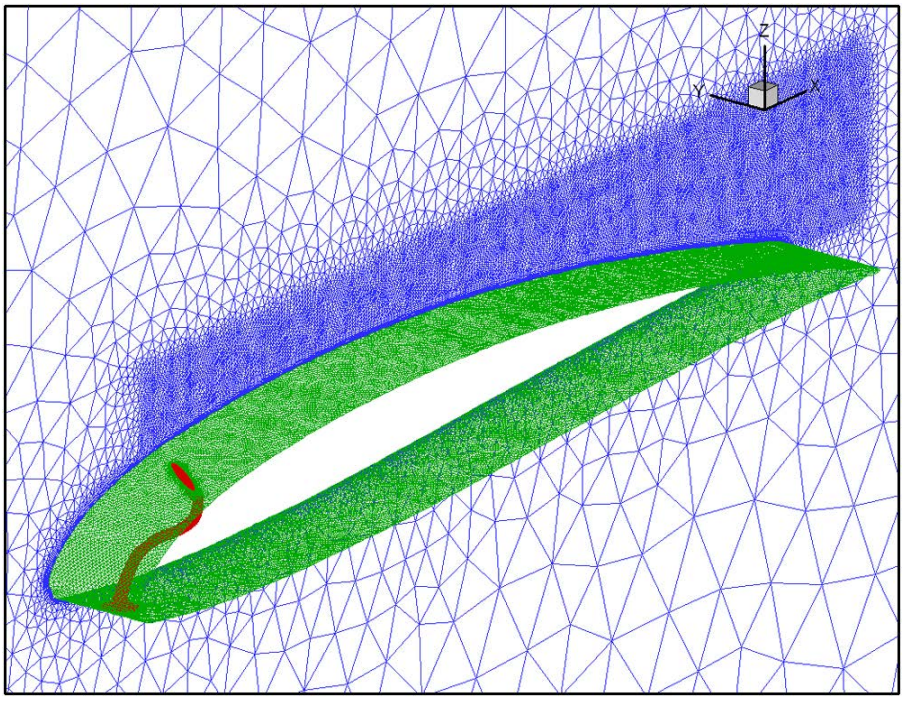

Figure 1.22: Perforated airfoil geometry for dynamic stall control (from [97])

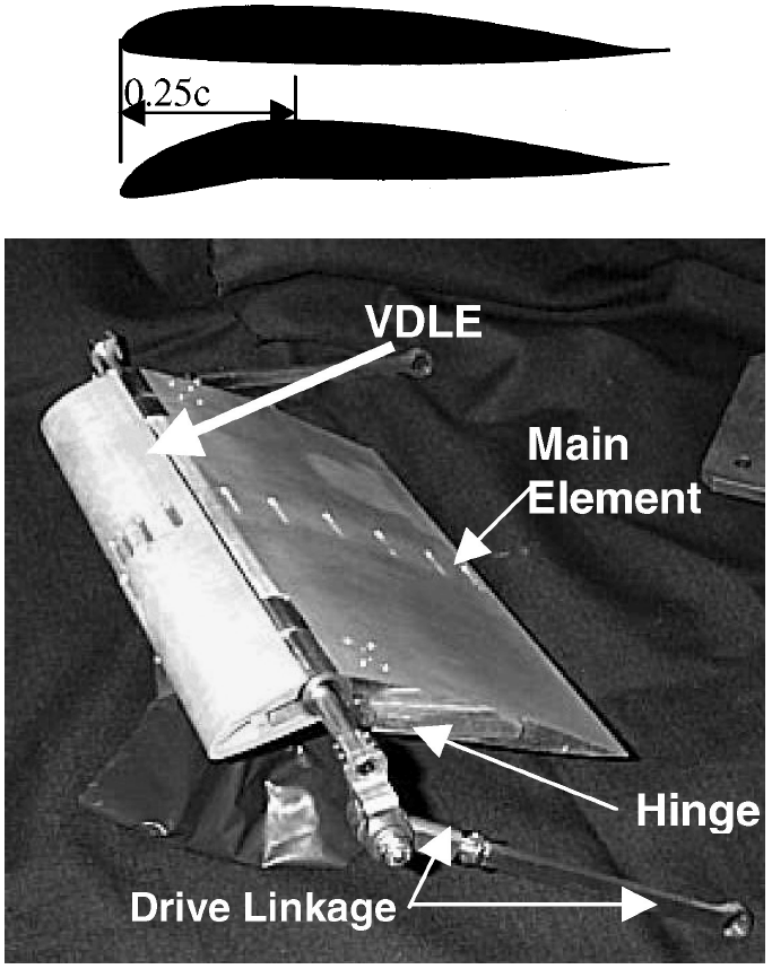

Figure 1.23: Active droop nose airfoil for dynamic stall control (from [8])

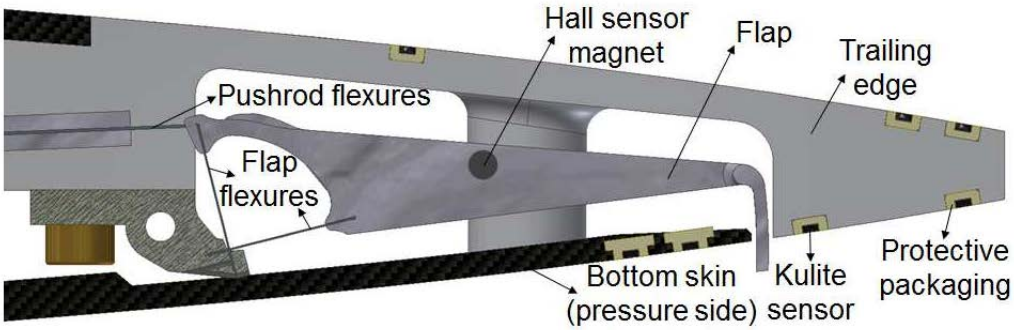

Figure 1.24: Active Gurney flap for dynamic stall control (from [66])

35 Hz, 5-7 times the rotational frequency of most helicopter rotors. These active Gurney flaps are robust enough to be installed on a rotor. Investigations of a number of different rotor flight conditions indicate that Gurney flaps have great potential to improve the efficiency and expand the flight envelope of helicopter rotors [81].

Passive devices for dynamic stall control on the OA209 airfoil [23] have shown promising results, with Leading Edge Vortex Generators (LEVoGs) showing a 50% reduction in the pitching moment peak (C_{M_P}) at M=0.14 [48], and around 25% reduction in C_{M_P} at M=0.3 and 0.4 [73]. These small disturbance generators are cylinders or discs attached to the leading edge of an airfoil (Fig. 1.25) and

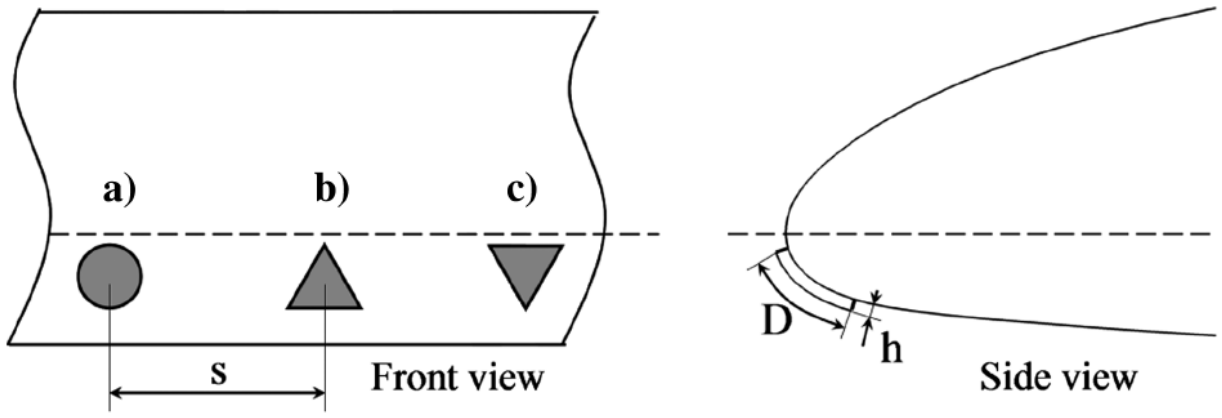

Figure 1.25: Leading Edge Vortex Generators (LEVoGs) (from [48])

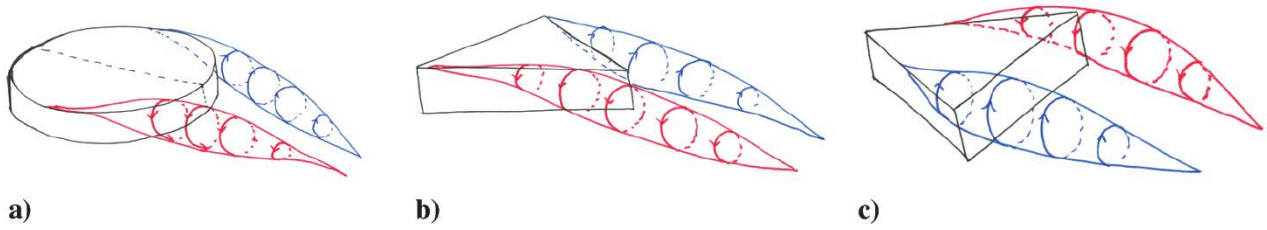

Figure 1.26: Vortex wakes from different LEVoGs, from from [48]

are at the stagnation point when the airfoil is at low angle of attack. At high angle of attack, the stagnation point moves so that the suction side streamlines flow over the LEVoGs, energising the flow and delaying the flow separation. It appears that, despite the name, the discrete vortices produced by the LEVoGs do not persist in the flow, but that the increased level of turbulence shifts the point of initial separation further downstream, and introduces three-dimensional disturbances into the flow, on the scale of 1/4 to 1/2 of the chord length, which result in a weakening of the dynamic stall vortex. Despite the disappearance of the discrete vortices, the direction of the vortices was shown to have an effect on the effectiveness of the LEVoGs. As seen in Fig. 1.26, three shapes were tested. The disc and backward triangle in Fig. 1.26a and b caused an upwash in the middle of the wake, and the forward triangle in Fig. 1.26c caused a downwash in the middle of the wake. Only the configurations which caused an upwash in the middle of the wake were effective in reducing the pitching moment peak, and the triangle with downwash in the middle of the wake even caused earlier stall. Experiments with forcing boundary layer transition using roughness elements showed that the effect of the LEVoGs is not caused by forcing earlier boundary layer transition. From the LEVoGs it is clear that moving the initial separation point rearward and creating three-dimensional structures in the separated flow are effective strategies to reduce the size of the pitching moment peak without a negative effect on the lift of an airfoil.

Deployable Vortex Generators (DVGs), standard corotating vortex generators which were retracted at low angle of attack and extended at high angle of attack, reduced C_{M_P} by up to 55% at M=0.16 [67], see Figure 1.27. The vortex generators caused the initial point of separation to be moved rearward, and for the dynamic stall vortex to be considerably weaker than without the vortex generators. The retraction was necessary to avoid high drag at low angles of attack, and the airfoil with the retracted vortex generators was not significantly different in its aerodynamic performance to the airfoil without the vortex generators. The retraction mechanism is, however, a significant technical challenge due to its mechanical complexity. Similar experiments by Martin et al. using vane vortex generators [74], showed a strong control effect at M=0.3. As shown in Fig. 1.28, Martin et al.

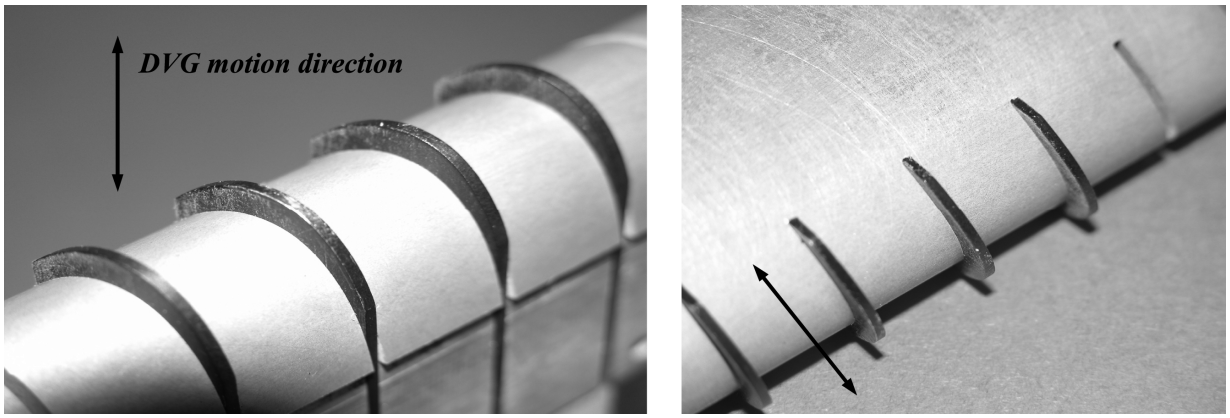

Figure 1.27: Deployable vortex generators for dynamic stall control (from [67])

Figure 1.28: Vane-type vortex generators on a glove for dynamic stall control (from [74])

changed the airfoil leading edge contour using a glove manufactured by a rapid prototyping process to separately investigate the effect of the change in airfoil contour and of the vortex generators, which were moulded as part of the glove. Both the change in airfoil shape and the vane vortex generators were extremely effective in reducing the pitching moment peak and the lift hysteresis from dynamic stall. In contrast to most other experiments, which investigated only low Mach numbers, Martin et al. investigated increased Mach numbers including flow separation dominated by a strong shock, and in this case the stall was worsened by the addition of the vane vortex generators, due to their tendency to generate additional local shocks on the airfoil. This tendency would have been countered if the vanes had been retractable. From this experiment we can see that effective flow control for dynamic stall must be effective from M=0.1 to 0.5, and have no critical M or α dependence.

In contrast to passive control devices, which use energy from the oncoming flow, active control devices have an external energy source, increasing the maximum possible control of the flow. Active methods include suction [57, 2], which removes energy from the flow, and pulsed blowing [44] or synthetic jets [101], which add energy to the flow. One type of active control device is constant blowing by jets out of the surface of the airfoil. Blowing by air jets can be used to control separated flow, and has been used on rotor blades since at least the 1950s [5]. Early experiments with low

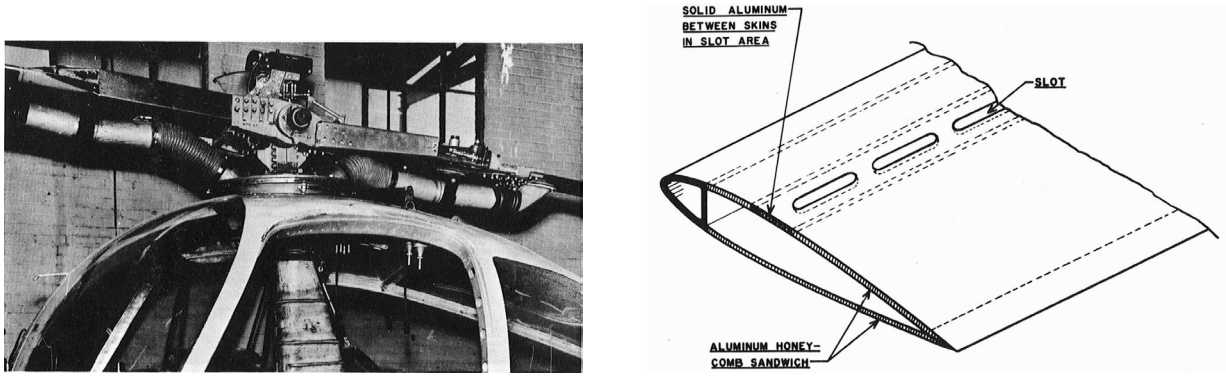

Figure 1.29: "Boundary layer control" system installed on a Cessna CH1 helicopter in the 1950s (from [49])

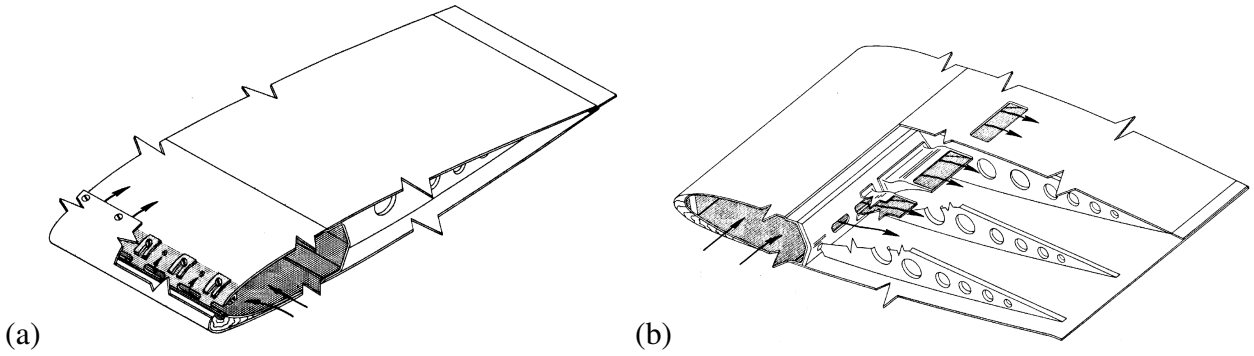

Figure 1.30: Early flow control system from the 1950s (a) Blowing slot near the airfoil leading edge (b) Blowing slots near the middle of the airfoil (from [76])

pressure "boundary layer control", noted that for blowing from slots, the maximum flight speed of a small helicopter could be significantly increased [49] (Figure 1.29). Since in this case a small reciprocating engine helicopter was used, the maximum flight speed of the helicopter was limited by the engine power, rather than the appearance of dynamic stall on the rotor, and the literature does not record whether the additional power of the air compressor would have been sufficient to achieve this increase if applied directly to the rotor. A similar configuration investigated on a rotor in the wind tunnel [76], see Fig. 1.30, could test the rotor up to stall, and a noted a significant increase in maximum advance ratio (from 0.3 to 0.46) before stall. This is equivalent to a 50% in maximum forward flight speed of the helicopter for a constant rotor rotation rate. As seen in Fig. 1.30, two nozzle configurations were tested. The blowing at the leading edge of the airfoil (Fig. 1.30a) was effective in increasing the maximum advance ratio, but the blowing at the mid-chord position (Fig. 1.30b) showed no improvement in the stall boundary. Both the flight experiments and the wind experiments also noted that with cyclic control of blowing (constant blowing only on the retreating side), that the same increase in flight speed or maximum advance ratio could be achieved with around half the compressed air required by constant blowing. These early experiments also demonstrated the similarity between the flow control on a pitching airfoil and in flight. The method was not further pursued, probably because advances in rotor design were able to increase the flight speed limits acceptably using passive methods without requiring active flow control. Modern helicopters operating at high altitude and thrust coefficient have renewed the interest in flow control by blowing, both as high frequency pulsed blowing and constant blowing.

Recent investigations into fluidic control devices (FCDs) on an airfoil have often been performed with synthetic jet actuators (SJAs) in mind. These jets rely on a small plenum chamber from which air is sucked in from the outside or ejected to the outside using a piston or diaphragm actuator, see

Fig. 1.31. A high-frequency train of air pulses is used to create a chain of vortex rings which act on the external flow This type of jet has zero mass flux (ZMF) when integrated over a cycle, and thus only electrical power (no air) needs to be provided, but the total power which can be added to the flow is much lower than for constant air jets. Synthetic jet actuators typically produce low subsonic jet velocities and work similarly to vortex generators in that resonant frequencies of the boundary layer are excited by the pulsation frequency. Investigators into flow control using blowing generally assume that the effect of pulsed blowing or ZMF blowing and suction is similar to that for constant blowing, but requiring less power and thus the constant blowing case is often used as a benchmark for the comparison of injector configurations [107]. Despite this assumption it is far from clear that pulsed blowing will perform in the same way as constant blowing for these jet configurations [26], although since investigations into pulsed blowing have a much larger number of variables which can be investigated, it is difficult to define the operating condition where a pulsed jet system will perform with maximum efficiency. Experiments by Traub et al. using SJAs [117] showed that a similar positive effect is achieved as with constant blowing, with an additional advantage attributed to the increased resistance of the boundary layer to separation due to the amplification of turbulent frequencies by the high frequency SJA injection. The same effect has also been noted for pulsed blowing from a high pressure source (not ZMF), by Greenblatt and Wygnanski [44]. As seen in Fig. 1.32, dynamic stall could be controlled by pulsed blowing from slots near the leading edge. Greenblatt and Wygnanski investigated a range of pulsing reduced frequencies, and found good control of dynamic stall in the range F^+=0.6-1.4. Using constant blowing at the same mass flux as the pulsed blowing resulted in a worsening of the dynamic stall behaviour compared to the case without blowing.

A number of flow control experiments have been performed using tangential blowing from slots in the airfoil surface. Investigations on airfoils with static stall for airfoils in incompressible flow [110] and on a generic flap [89] have shown pulsed blowing to be more effective than constant blowing. Experiments using synthetic jet actuators with zero mass flux [117] showed that the control of stall on a ramping airfoil could be achieved, with a saturation in effect around C_μ=0.01. Greenblatt and Wygnanski's experiments demonstrating dynamic stall control using pulsed blowing from a high pressure source [44] with $0.001 \leq C_\mu \leq 0.004$ noted that at these blowing rates pulsed blowing was more effective than constant blowing at the same C_μ. Both of these studies investigated dynamic stall with a small hysteresis and weak stall.

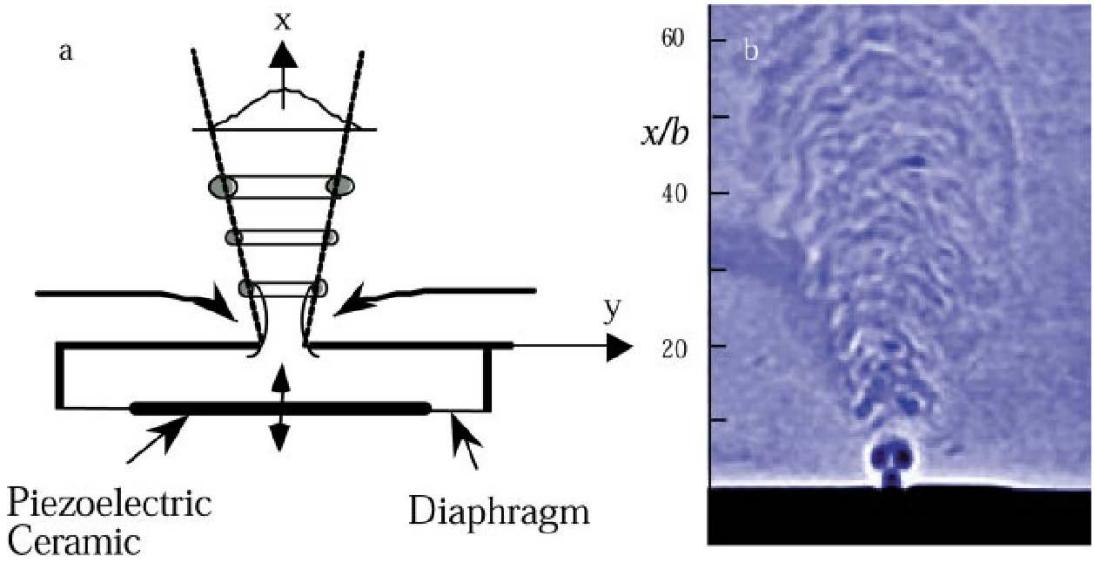

Figure 1.31: Left: Schematic diagram of a synthetic jet actuator Right: Schlieren image of a rectangular synthetic jet. (from [40])

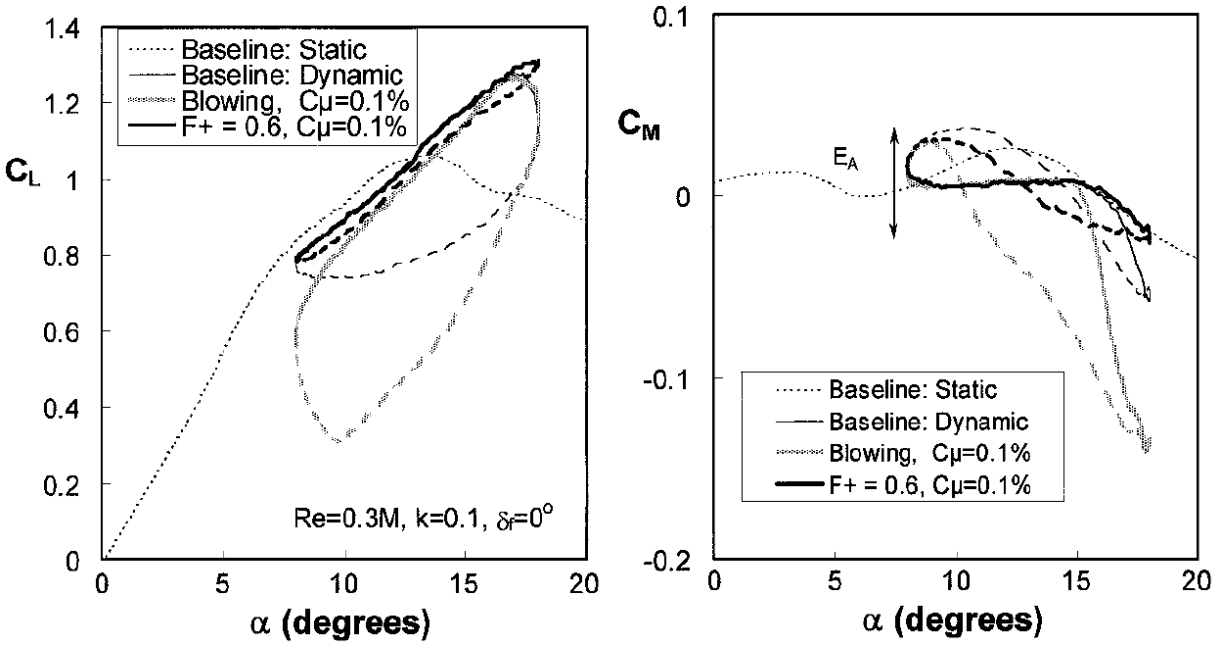

Figure 1.32: Results of dynamic stall control by high frequency pulsed and constant blowing, from [44]

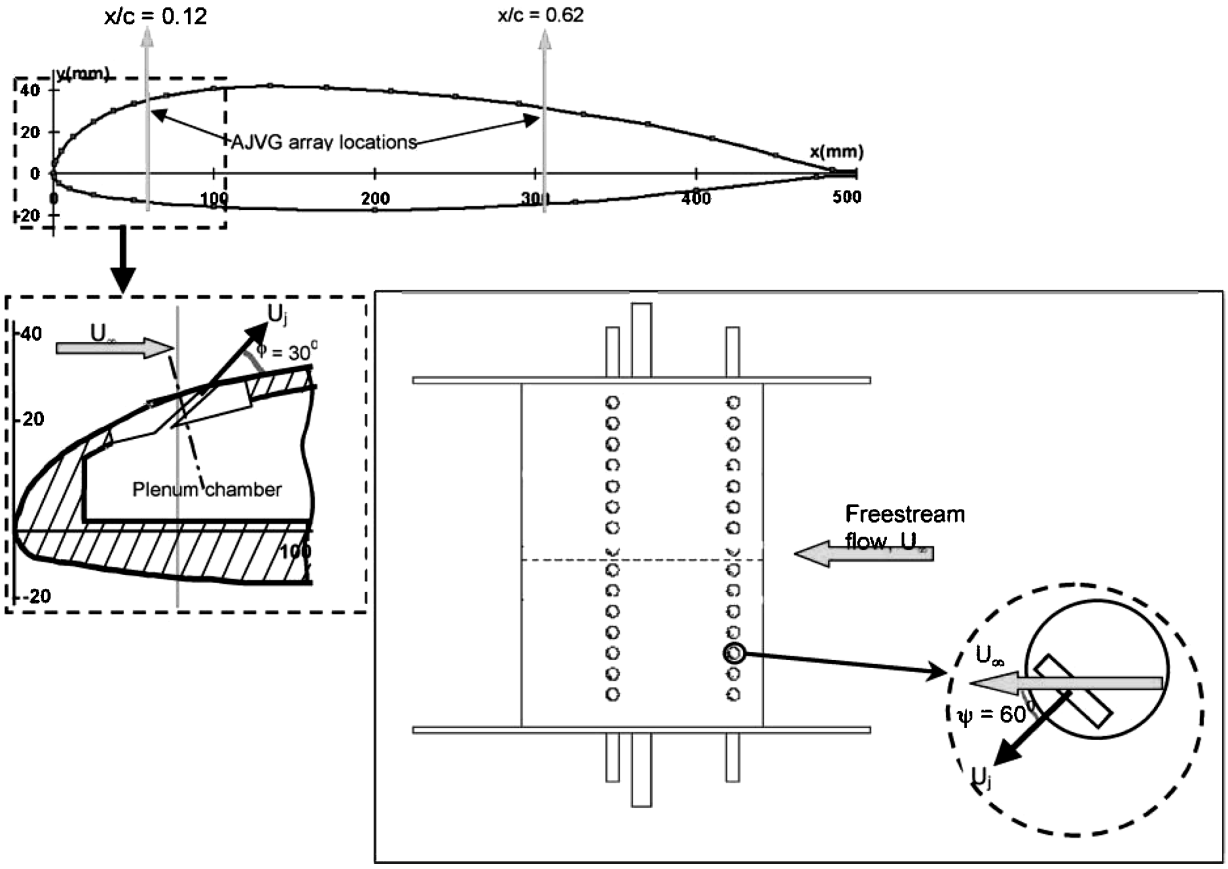

Figure 1.33: Air vortex generator geometries. (from [113])

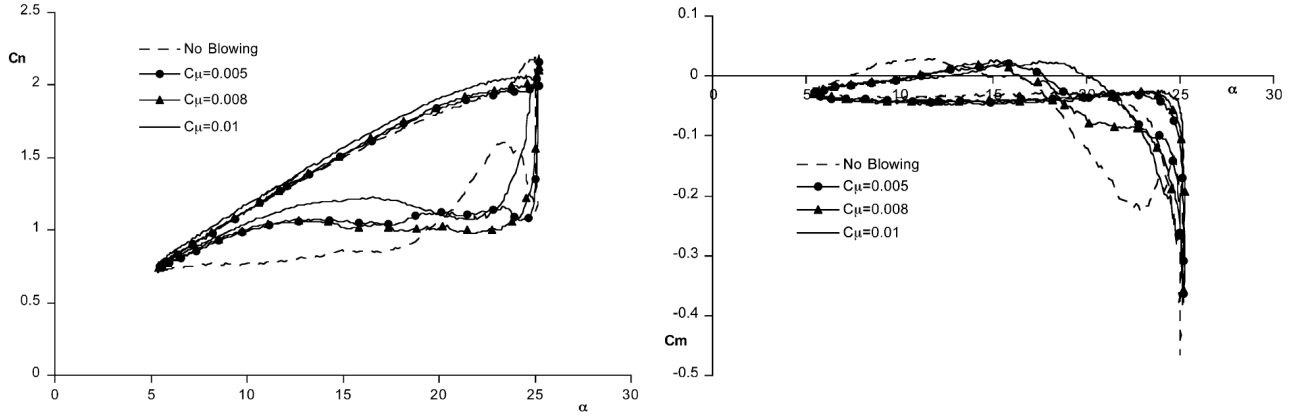

Figure 1.34: Results of dynamic stall control by high frequency pulsed blowing, from [113]

Singh et al. [113] used blowing from angled jets at M=0.13 and Re=1.1×10^6 on a pitching airfoil (Figure 1.33). For the jets located at x/c=0.12 and spaced at y/c=0.1 along the span with the jet exit pitched at ϕ=30° and skewed at ψ=60°, they found that for constant blowing at C_μ=0.008 there was good control of dynamic stall. As shown in Fig. 1.34, the pitching moment peak was significantly decreased, without significantly altering the lift hysteresis. An important result of tests such as this is to show that it is possible to change the lift and pitching moment time histories independently of each other, meaning that a separate optimisation of both values may be possible. As with other flow control results, the dynamic stall control by Singh et al. delayed the onset of stall by around two degrees in pitching angle of attack. Sensors which show this property are generally capable of suppressing stall completely for motions where the maximum angle of attack exceeds the stall angle by less than the amount which the actuators can delay the stall. Further experiments by the same group [112] found that for the control of static stall that pulsed blowing at reduced pulsing frequencies of F^+=0.7 and F^+=1.3, was as effective as constant blowing with around twice the average mass flux.

Weaver et al. [121] investigated the control of deep dynamic stall in water tunnel experiments on a VR-7 airfoil. Control was by blowing through a tangential slot located at x/c=0.25. Figure 1.35 shows the change in the lift and pitching moment curves for a dynamic stall case by constant blowing. The blowing rates are significantly higher than for many other experiments investigating dynamic stall control by pulsed blowing (a factor of 100 greater than Singh et al., for example), and the change in the lift curves is significant. For the case with maximum blowing, at C_μ=0.566, the maximum lift is increased by 40% over the case without blowing, and the stall is completely eliminated. Lower blowing rates also resulted in a significant reduction of the stall hysteresis, without completely eliminating it. As seen in the pitching moment curves in Fig. 1.35, the pitching moment peak is eliminated when stall is suppressed, but even when stall is not completely suppressed, the pitching moment peak was reduced by 50%. Weaver et al.'s results were seen as the most promising for the control of deep dynamic stall, and thus the blowing rates were scaled to compressible flow in the wind tunnel for the design of the flow control experiment described in Chapter 4.

Weaver et al. [121] investigated a few points with pulsed blowing for lower blowing rates, and compared the results to constant blowing, as seen in Fig. 1.36. They found that found that for their configuration and points investigated, pulsed blowing was better than steady blowing with $C_\mu \leq$0.01, but for $C_\mu \geq$0.02, as required for the control of deep dynamic stall, steady blowing started to become equal or better in effectiveness. In Fig. 1.36, Left, it can be seen that both the constant and pulsed blowing increase the lift near maximum lift, after the kink in the lift curve which indicates the onset of trailing edge stall, and both results reduce the hysteresis in lift. However the constant blowing produces around twice the difference to the case without blowing as pulsed blowing at the same mass flux. Similarly for the pitching moment in Fig. 1.36, Right, both pulsed and constant blowing reduce

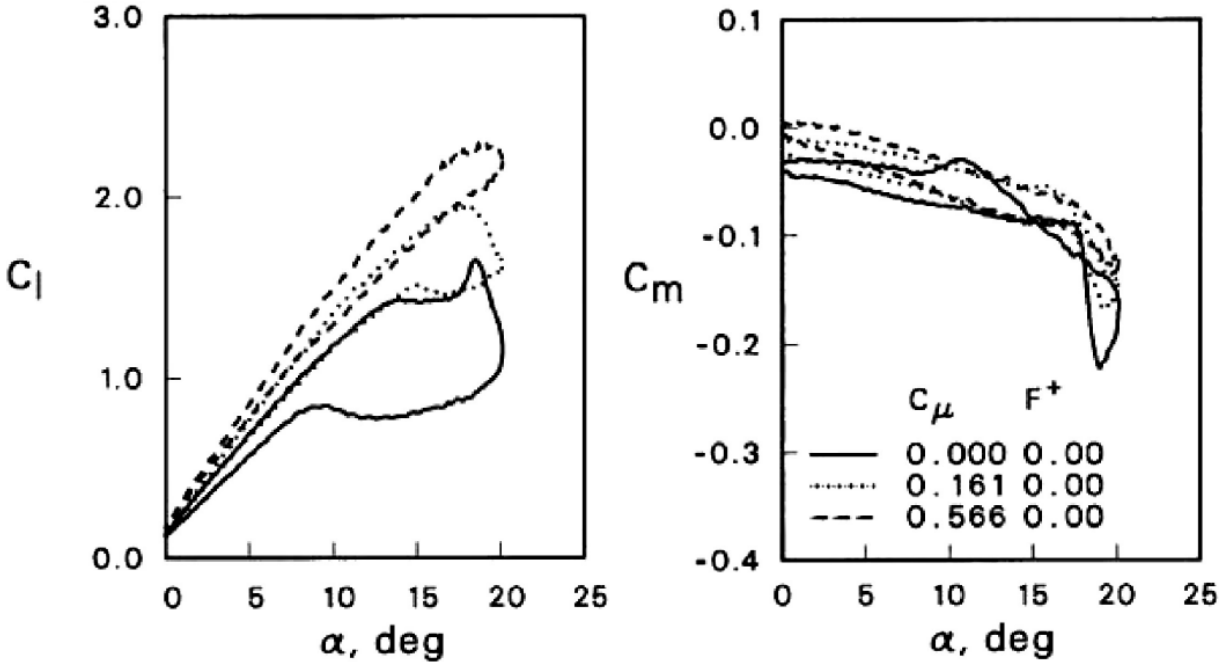

Figure 1.35: Results of dynamic stall control by constant blowing, from [121]

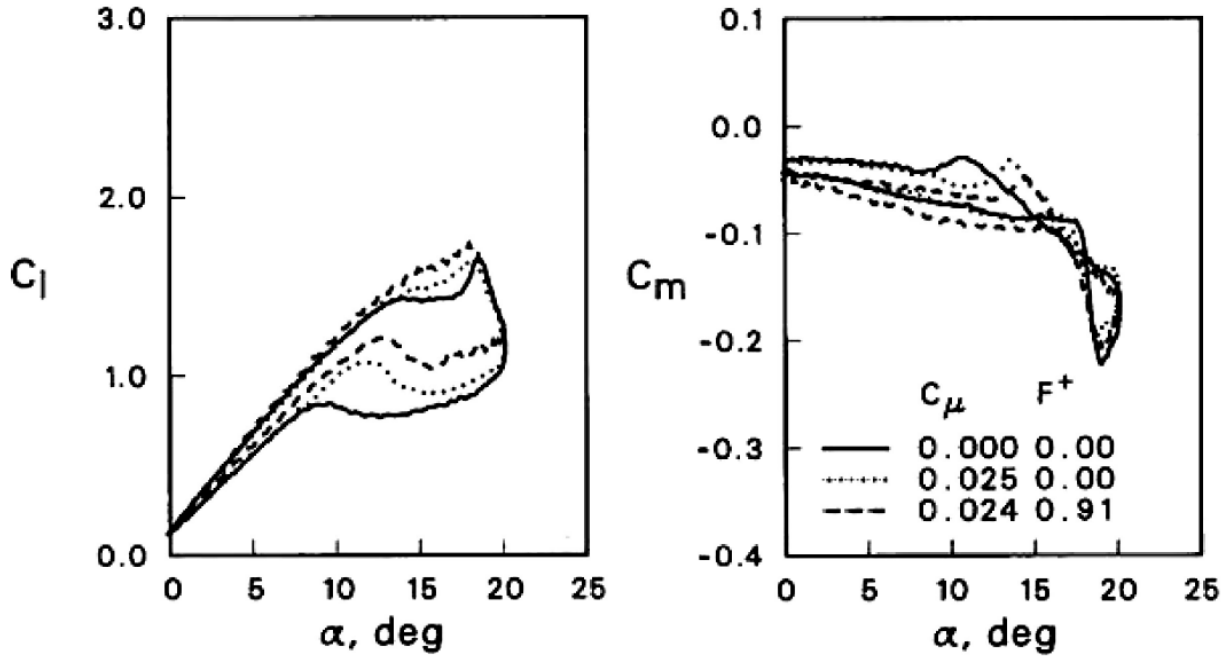

Figure 1.36: Results of dynamic stall control by constant and pulsed blowing, from [121]

the pitching moment peak, but the constant blowing has around twice the effect of pulsed blowing at the same mass flux. Weaver et al. varied the pulsed blowing frequency between F^+=0-2.7, with pulsed blowing at F^+=0.9 being the most effective. Thus for the experiments described in Chapter 4, valves were designed which would allow pulsed blowing at F^+=0.9. Weaver et al. also compared their results with other flow control configurations investigated in the same water tunnel facility, as shown in Figure 1.37.

Two recent experiments by the author [31, 32] (section 4.3) at M=0.3-0.5 showed control of deep dynamic stall for constant blowing normal to the airfoil chord, through round portholes at 10% chord,

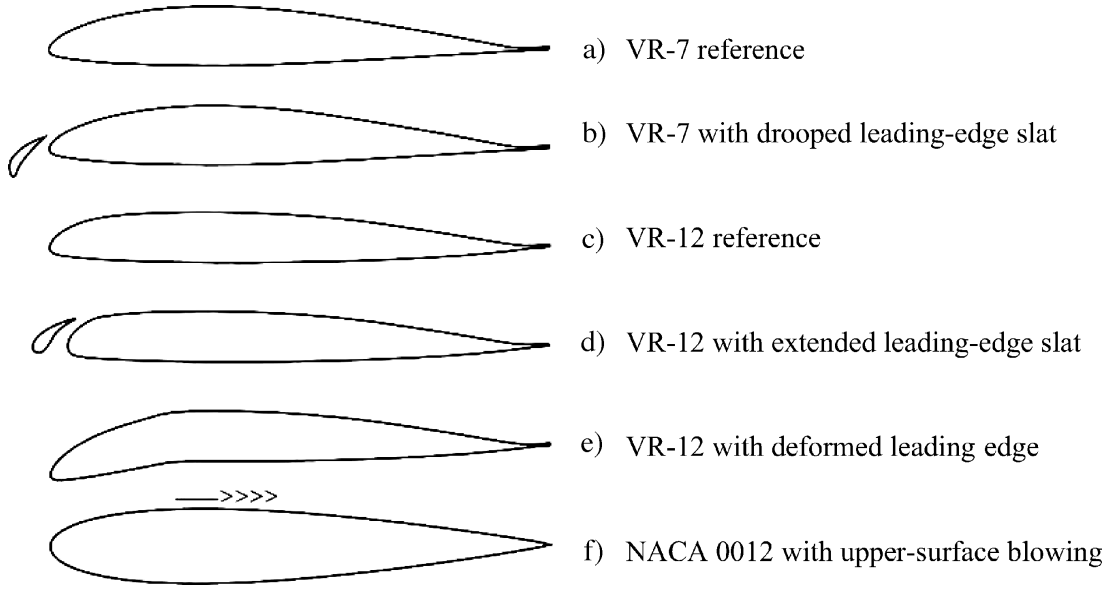

Figure 1.37: Airfoil configurations for the reduction of dynamic stall (from [121])

with diameter 1% chord. These jets pass through the boundary layer and allow attached flow to pass between the jets. Jet spacing along the airfoil breadth was varied from 6.7% chord to 20% chord. Stall could be delayed, and when stall occurred, the negative effects could be significantly reduced by blowing. These experiments were based on design computations using constant blowing [34], and the experimental results were at least qualitatively similar to the results of the design computations. Results by Packard et al. with constant blowing through similar jets on a laminar NACA 64_3-618 airfoil [91] showed good control of static laminar separation near the trailing edge of the thick airfoil, with maximum C_μ approximately 0.005.

1.5 Overview of topics in the cumulative habilitation thesis

This section provides a summary of the work presented in Chapters 2-4. The primary focus of this habilitation thesis is the control of dynamic stall by blowing, presented in Chapter 4. Chapter 2 introduces the wind tunnel, and discusses the testing rig for producing quasi-2D dynamic stall in the wind tunnel environment. Dynamic stall results are shown, and the effect of parameter variation on the dynamic forces is discussed in detail. In Chapter 3, the effect of the wind tunnel testing environment on the results is discussed in detail, as is the effect of rotation. The effect of the wall connection of the airfoil and the three-dimensional flow on the quasi-2D model is analysed in detail, showing the effects on the aerodynamic flowfield, and on the forces. Finally, in Chapter 4, the design and testing of a wind tunnel model to control dynamic stall by air jets is discussed in detail. A new numerical method for the design of actuators for dynamic stall control is demonstrated and verified, and the results are shown for a variety of parameter variation, including Mach number, Reynolds number, airfoil pitching amplitude and frequency, and jet pressure and pulsing rate.

In each chapter, numerical and experimental results are presented which illustrate the effects being investigated. These are supported by the text and illustrations from the papers used in this cumulative habilitation thesis, as noted in the text.

The wind tunnel and pitching motion rig

The DNW-TWG is a closed-test section wind tunnel with a closed cycle. The wind tunnel is powered by a 12 MW axial compressor, and the flow is cooled by a water-filled heat exchanger in the plenum. The flow downstream of the heat exchanger is straightened using a honeycomb system, and then the large vortices are reduced using a system of sieves. A 16:1 nozzle is used to accelerate the flow to the test section, and three exchangeable test sections are available. A perforated test section is used for three-dimensional models or transonic testing, and can be used from Mach 0.3 to 1.2, with suction of the flow through the walls by an additional 3 MW compressor. In this test section, the models can be mounted either using a rear sting or from the side-walls, depending on the configuration desired. A Laval test section is additionally available for supersonic testing between Mach 1.2 and 2.4, for sting-mounted models.

For two-dimensional airfoil testing, the adaptive-wall test section is used. Here the upper and lower walls of the wind tunnel are deformed to compensate for the blockage of the model and the bending of the streamlines. The result is that for two-dimensional airfoils at static angle of attack, the primary wind tunnel interference effect is the sidewall interference from the interaction between the airfoil and the wind tunnel boundary layer. Dynamic two-dimensional airfoil testing is achieved by using a hydraulic pitching motion rig which pitches the airfoil sinusoidally around its quarter-chord axis. A PID controller is used to force the pitching rig to follow a defined motion, which is generally sinusoidal, but can be set to arbitrary movements. For these tests the wind tunnel walls are adapted to the flow at the airfoil mean angle of attack, and remain unchanged during the dynamic testing.

The Mach number is set by a sonic throat downstream of the test section, and for cases with static aerodynamics can be set to better than 0.001 accuracy in the Mach number. The Reynolds number is set by varying the pressure in the wind tunnel by the application of vacuum down to P_0=0.3 bar, or pressure up to 1.4 bar. The working fluid is atmospheric air which is dried using a silica gel drying system.

Effect of the finite wing and rotation

A helicopter rotor differs from a two-dimensional airfoil both in its finite length and in its rotation, ignoring the interaction effects with preceding rotor blades which become important for some specific flight conditions. These effects were investigated numerically for a pitching three-dimensional finite wing to assess the effect on the forces produced by dynamic stall. The tip vortices caused by the finite wing cause a reduction in the lift on the finite wing centerline compared to the two-dimensional airfoil, and result in a reduction in the strength of the dynamic stall vortex produced. The shorter the finite wing, the stronger this effect. The three-dimensional wing also results in a weaker and less concentrated dynamic stall vortex, which causes less lift overshoot than in the two-dimensional case. When the same finite wing is rotated, the effect is to further reduce the strength of the vortices and the pitching moment peak over the nonrotating three-dimensional test case. The dynamic stall vortex weakens much faster than in the nonrotating case, and this results in a similar lift history to the nonrotating case, although the pitching moment is much less than in the nonrotating case. The varying pressure distribution over the length of the blade, caused by the varying Mach number under rotation causes a jet toward the blade tip in the boundary layer on the suction side of the rotor blade. On the suction side of the rotor blade, the higher Mach numbers nearer the rotor blade tip cause lower pressures, and this gradient causes an acceleration of the flow on the suction side towards the blade tip. On the pressure side of the rotor blade, the higher Mach numbers nearer the rotor blade tip cause higher pressures, and the flow is accelerated towards the blade root. Both the pressure gradient and the jet strength are much stronger on the suction side than on the pressure side.

Wind tunnel interference

The classical wind tunnel interference effects can be grouped into blockage, downwash and gradient effects. Gradient effects are due to a non-constant Mach number or pressure along the model of interest, and are manifested most strongly as a correction to the drag, for sting-mounted models without control surfaces, or as a change in the effectiveness of the control surfaces, when these are present. Equally, the blockage in the test section due to boundary layer growth on the wind tunnel walls can cause a gradient effect for other mounting systems. For airfoil testing at subsonic Mach numbers, the gradient effects can generally be neglected for adaptive-wall test sections, as used for the experiments here.

The blockage effect of a model is to raise the local Mach number, increasing lift at a given angle of attack. The effect is difficult to separate from other effects which cause a change in circulation, including sidewall interference and the downwash effect, but estimates of the magnitude can be easily gained by a one-dimensional analysis of the area change at the model. The downwash effect appears when the downwash produced by the wake of a model strikes the wind tunnel wall and is diverted upward. This causes a reduction in the lift which can be estimated by two-dimensional potential theory and is linear with the lift and model planform area. Both of these effects can be significantly reduced by using an adaptive-wall test section with the walls adapted to follow the freestream streamlines.

Although the gradient, blockage and downwash effects can be significantly reduced by adaptive wall test sections, this applies only to airfoils at static angle of attack. For dynamic tests the wind tunnel walls are adapted to the flow at the airfoil mean angle of attack, and do not compensate either the effects of higher or lower lift. Additionally, the dynamic blockage of the dynamic stall vortex cannot be compensated for. The exact amount of this interference effect is not well characterised, but tests with different wall contours (for example, adapted to other angles of attack), have shown that the force peaks are relatively unaffected by the selection of the wall contour, meaning that comparisons of different airfoils or flow control settings in the same wind tunnel will be valid. A dynamic correction

of the wind tunnel data is not undertaken.

The final effect, which cannot be well compensated by the adaptive wall test section, is the sidewall effect which is caused by the interaction between the airfoil and the wind tunnel wall. This causes a strongly three-dimensional flow on the airfoil near the wind tunnel walls, which causes a reduction in the effective angle of attack on the midline of the wind tunnel. Statically, a wind tunnel correction based on the measured lift can compensate the interference well, but for the unsteady pitching airfoil no correction method is currently available. The difference between the sidewall effect with and without a gap between the airfoil and the wall is investigated numerically with comparison to experiment in Chapter 3, and shown to be locally significant, but not detectable on the airfoil midline for an airfoil at static angle of attack.

Two dimensional dynamic stall

Quasi-two dimensional dynamic stall on an airfoil model in the wind tunnel is characterised by having a single set of values on the airfoil midline which can be evaluated. Further, phase-averaging the data simplifies the results, so that for each test point a single loop in lift (C_L) and pitching moment (C_M) against angle of attack (α) can be plotted, and together with an analysis of the phase-averaged pressure distributions, this allows a relatively simple understanding of the production of forces and moments. The drag (C_D) is generally not plotted, since for most cases it is inversely proportional to C_M. Three airfoils are compared in Chapter 2, with the EDI-M109 and OA209 airfoils exhibiting leading edge dynamic stall and the EDI-M112 airfoil exhibiting trailing edge stall at M=0.3 and 0.4 and both airfoils showing shock-induced dynamic stall at M=0.5. The slower stall produced by trailing edge stall produces lower pitching moment peaks and less lift hysteresis than comparable leading edge stall cases.

It could be noted in Chapter 4 by the comparison with experiments using forced transition by roughness elements on the surface that the effect of boundary layer transition on the separation for an OA209 airfoil was minimal. This can be explained by noting that the transition point of the suction surface moves forward with increasing angle of attack, reaching the leading edge of the airfoil significantly before the onset of dynamic stall. Dynamic stall is then initiated on parts of the suction side of the airfoil with fully turbulent flow, and is thus insensitive to the transition behaviour of the airfoil selected.

Increasing frequency and amplitude both result in the production of stronger dynamic stall vortices, as does increasing the maximum angle of attack reached during the pitching cycle. For the EDI-M109 airfoil, pitching at low frequency caused trailing edge stall, which changed to leading edge stall as the frequency was increased. Using a non-sinusoidal forcing motion resulted in a change in the dynamic stall only if the pitching rate at the moment of stall was different than for the sinusoidal pitching motion, which means that if the pitching rate at stall is known for a helicopter with elastic blades, then the effect should be well modelled by a stiff sinusoidally pitching airfoil. It was noted that the newer EDI-series airfoils have much better performance than the older OA209 airfoil.

Design of the wind tunnel model

A quasi-2D airfoil model for the investigation of dynamic stall control with jets was designed numerically, and the design process and results are shown in Chapter 4. Three-dimensional jet configurations including slots and skewed and inclined porthole jets were tested using a three-dimensional numerical domain of 20% chord width, with periodic boundary conditions. The numerical cost of performing three-dimensional unsteady numerical computations for a large number of configurations was prohibitive, so a new method using static computations was used to identify a small number of promising candidates which were then investigated using the more costly unsteady computations. It was shown that jet configurations which best increased the lift after stall in a static computation would also be best against dynamic stall. Further, the jet configurations divided into three groups, and were evaluated for their ability to reattach the flow by blowing along the airfoil, to anchor the separation position, to delay the separation and to slow the passage of the dynamic stall vortex over the surface of the airfoil. Additionally, the ability of the jets to break up the two-dimensional dynamic stall vortex into smaller three-dimensional structures was investigated. Each of these had been identified as an important effect to achieve by an analysis of the literature. Target blowing rates for the control of deep dynamic stall were scaled to compressible flow from low-speed experiments in the literature, as were frequencies for flow control by pulsed blowing.

In a final step, three jet configurations were evaluated using unsteady CFD against the reference airfoil without flow control for their ability to control dynamic stall using practical amounts of pressurised air. A 50 bar pressure source with limited flow rate was available for the experiment, and the potential configurations were evaluated against pressures and flow rates which were practically achievable. Each of the three jet configurations was found to provide a roughly equivalent amount of stall control, and the final configuration was chosen since it had the minimum change in the airfoil contour, meaning that the airfoil with the jets turned off could be used as a reference test case. This was important since any wind tunnel interference effects could thus be regarded as approximately equal in each pair of results with and without flow control to be investigated.

The wind tunnel airfoil model was comparable to the earlier EDI-M109 model, using a similar aluminium and carbon-fibre construction, and the structure was made to be as stiff as possible. The airfoil was instrumented with pressure sensors, accelerometers and temperature sensors. The wind tunnel model was built to include an air supply system with an internal pressure reducer from the high-pressure feed line, and air jet had its own individual valve. The valves were a special development which allowed fast switching at high pressure, in a small enough space to be installed in the wind tunnel model. Since the carbon-fibre shell of the airfoil model was glued shut, the valves needed to be very reliable, since they could not be repaired in the case of failure. By switching the valves in different groups the jet spacing could be investigated, and by turning the valves on and off rapidly, the effect of pulsing the jets at high frequency compared to constant blowing could be investigated.

Testing of the wind tunnel model

The testing of the wind tunnel model was done in two wind tunnel entries, and the flow control was tested over a range of parameters. The effect of Mach number and Reynolds number on both the dynamic stall and dynamic stall control were evaluated, as were pitching parameters including the mean angle of attack, amplitude and frequency. For cases where the maximum angle of the airfoil was only a few degrees above the dynamic stall angle, the stall could be completely suppressed by using an appropriate amount of constant blowing. For higher maximum angles, the pitching force could be significantly reduced, but the airfoil still stalled. In general, the stronger the pitching moment peak the stronger the (percentage) reduction in the pitching moment peak by using flow control, with

higher frequency and higher amplitude leading to more reduction in the pitching moment peak. When the airfoil stalled with flow control, residual pitching moment peaks remained which could not be further reduced by the application of blowing. It was shown that with increasing blowing pressure the pitching moment peak reduced, reached a minimum, and then increased again, leading to an optimum in the blowing pressure. In all cases without shocks in the flow the lift was relatively unaffected by the application of flow control, except that the hysteresis was reduced and the lift in the fully stalled flow was significantly increased. The stall was delayed by around 2°, and the time taken to stall was much longer than without flow control. This was partially due to the flow control causing a change in the stall behaviour of the airfoil from leading edge stall to trailing edge stall.

Although the dynamic stall behaviour was different, the flow control worked similarly well for cases with leading edge stall and for shock-induced stall, although for cases with shock-induced stall, blowing into the supersonic region of flow in the suction side resulted in a significant reduction in lift for attached flow before stall. Analyses of the aerodynamic damping showed that although the flow control reduced the positive aerodynamic damping, enough margin was left to be uncritical. Using an assumption of a perfect constant-temperature compressor, an analysis was made of the energy balance of the airfoil with and without blowing. It was found that using the jets always resulted in a higher total energy consumption on all parts of the pitching cycle, even though the drag of the airfoil was significantly reduced. A comparison between the numerical design and the experimental results showed that the CFD predicted a significantly more effective flow control for the amount of air used, but that the qualitative effect of constant blowing on the flow was captured.

Pulsed blowing

Pulsed blowing was investigated both at frequencies much higher than the pitching frequency, and at the pitching frequency. The valves could be pulsed at up to 500 Hz for high-frequency flow control. For high-frequency pulsed blowing some other authors had found that it was as effective as constant blowing with more than twice the mass flux, and others had found it to be less effective than constant blowing. Unfortunately, for the pulsing frequencies which could be achieved with the valves installed, the performance of the pulsed blowing on the wind tunnel model and test cases investigated was always worse than for constant blowing with the same mass flux. To achieve faster switching, the valves would have to be smaller, and mounted closer to the surface of the airfoil, since the establishment of the flow between the valve and the outer surface of the model took a significant time. This is a difficult technical challenge with the high pressures used, and the valves installed in the wind tunnel model were already unavailable commercially, and had to be developed specially for this wind tunnel model. An additional disadvantage of pulsed blowing is the additional vibration added to the model, with peak-to-peak vibrations of around 75% of the mean lift. The additional energy required by the valves was not otherwise analysed, but was around 2 kW for the one meter of airfoil tested, meaning that it was around 5% of the energy required to provide the compressed air.

Technically easier is pulsed blowing at the pitching frequency of the model. In this flow control case, the jets are turned on with constant blowing only at high angle of attack where separated flow is expected. Unfortunately at low pulsing frequencies the flow-through pressure reducer included in the wind tunnel model had a significant increase in pressure during the time when the valves were closed, which meant that a constant feed pressure could not be achieved. Experimental and numerical testing with pulsed blowing at the pitching frequency showed a clean change between the blowing and non-blowing states when the valves were switched, with minimal transients, indicating that this is a method by which the energy budget for flow control by blowing can easily be halved. This type of control of the blowing was already flown on a helicopter in the 1950s, although the analysis at that time was not capable of fully analysing the aerodynamics.

Three-dimensional dynamic stall on the two-dimensional model

An investigation of the three-dimensional effects of dynamic stall on the two-dimensional airfoil showed that significant differences to the nominally two-dimensional dynamic stall could be seen. A numerical analysis of the three-dimensional stall showed that the two-dimensional assumption in the integration of the experimental lift from a line of pressure transducers on the model centerline showed a significant discretisation error (up to 8%) for some cases using the jet blowing. An analysis of the pressure field on the surface of the airfoil using pressure sensitive paint (PSP) showed that this was primarily due to the positioning of a single pressure sensor near the jets. Further analysis of the PSP measurements showed that the flow fields of the air jets joined to form a wall which the dynamic stall vortex could not easily pass, resulting in a slowing of the vortex passage. The PSP measurements further showed that the three-dimensionality of the flow caused by the flow control jets was a maximum just before stall, and after stall a relatively two-dimensional flow field was produced.

Similarly to the effect of a finite wing, the dynamic stall vortex in the wind tunnel was shown to develop an increasingly bowed form as it moved downstream, with the dynamic stall vortex near the wind tunnel walls remaining anchored to the leading edge of the airfoil at the join between the airfoil and the wind tunnel wall. The three dimensional shape was visualised using PSP and verified by an array of pressure transducers on the surface of the wind tunnel model. The three-dimensional shape of the stall was seen where a dynamic stall vortex was formed, but where shock-induced stall was seen, only the separation under the shock foot was seen to have a slight three-dimensional shape, and otherwise the flow was uniform over the central portion of the airfoil.

Conclusions

The investigations of dynamic stall in this habilitation thesis show how the flight envelope of a helicopter can be extended to higher flight speeds, greater take-off weights, better maneuverability and higher service ceiling. In addition, the new understanding of dynamic stall will assist the development of more efficient passive and dynamic methods for the alleviation of dynamic stall.

Chapter 2

Pitching airfoil experiments

The pitching airfoil experiments described in this document all use a similar set-up and are all performed in the adaptive-wall test section of the DNW-TWG wind tunnel in Göttingen. This section describes the basic setup of the experiments and wind tunnel, as well as some example results for airfoils without dynamic stall control.

2.1 Description of the experimental arrangement

The experimental arrangement consists of the wind tunnel, model support and airfoil model. The instrumentation, data acquisition and data analysis are described for the general test case.

2.1.1 DNW-TWG with adaptive-wall test section

The German-Dutch Wind Tunnel Association's Transonic Wind Tunnel Göttingen (DNW-TWG) with the 1 m x 1 m adaptive wall test section is a Göttingen-type closed circuit wind tunnel which can produce flow with $0.3 \leq M \leq 1.0$ and $30\,\text{kPa} \leq P_0 \leq 140\,\text{kPa}$, with a turbulence level of 0.07% at M=0.5 and 0.05% at M=0.3 (Figure 2.1). The adaptive test section has flexible top and bottom walls which can be driven to a shape computed to minimise the wall interference velocity. The flow angularity is set by the error in wall adaptation and is $\leq 0.01^\circ$. For dynamically pitching experiments, the adaptive test section walls are statically adapted at the model mean angle of attack.

When the adaptive test section in the TWG is empty, the top and bottom walls need to diverge in order to keep the Mach number constant along the test-section and compensate for the boundary layer growth on all four side-walls. Since the boundary layer also grows on the static side-walls, the center plane of the tunnel has a flow divergence, characterised by half the physical divergence of the top wall. The top wall divergence to account for the turbulent boundary layer of the empty test section in the TWG is 2.8 mm/m or a divergence of 0.080° at 0.5m from the centerline [13].

The DNW-TWG has an automatic feedback controller for Mach number (M), total pressure (P_0) and total temperature (T_0), so that these are kept constant over the test period. The wind tunnel can be operated constantly over periods of 12 hours or more, if required, but model access is over a plenum which is normally at the freestream pressure (P_∞), so stopping and venting the tunnel is necessary for any manual model adjustments.

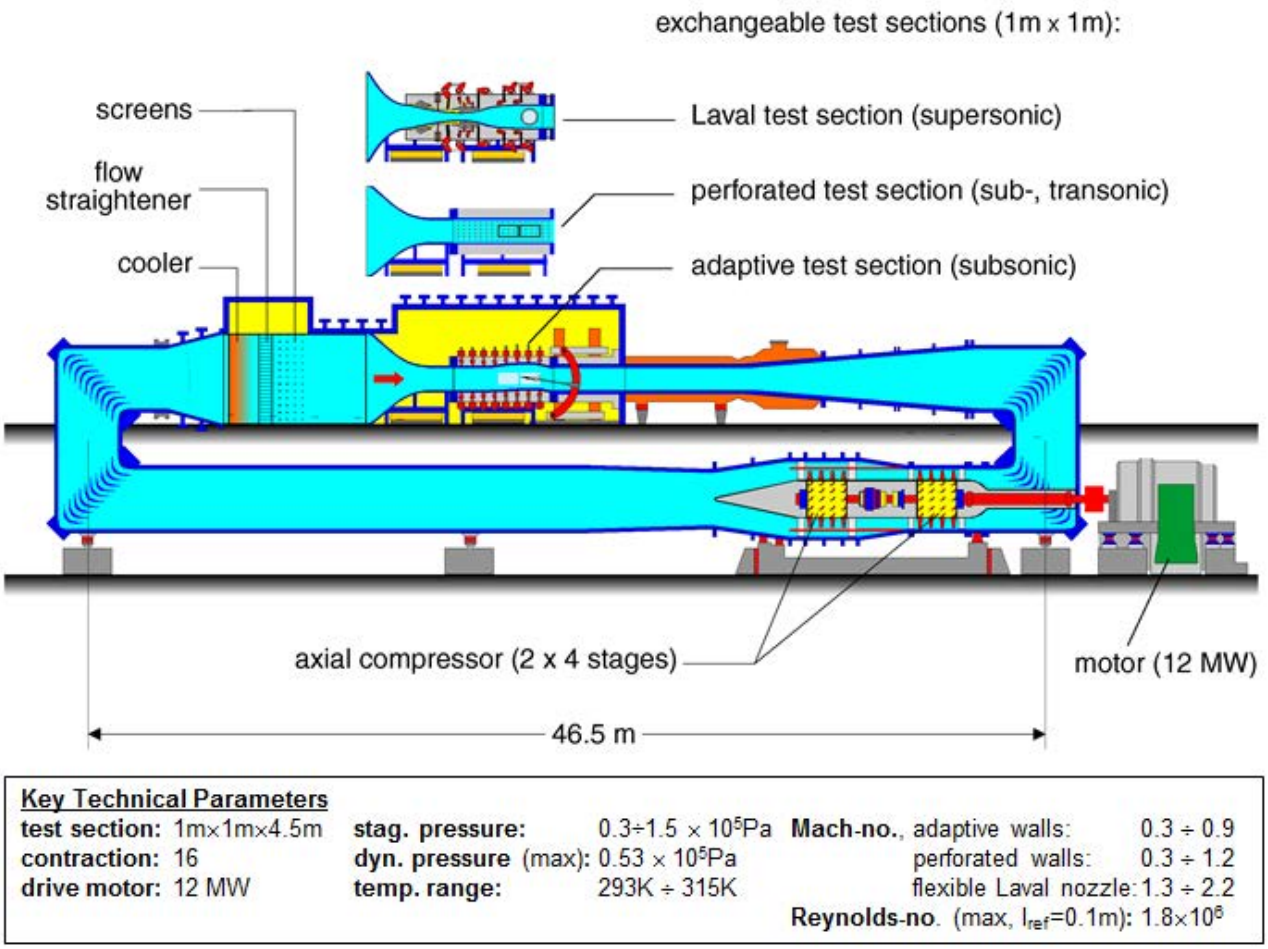

Figure 2.1: Transonic Wind tunnel Göttingen (TWG). Source: DNW

2.1.2 Pitching motion test stand

The pitching motion test stand (NVS) is an addition to the DNW-TWG, operated by the Institute of Aeroelasticity in Göttingen. As seen in Figure 2.2, the NVS is a U-shaped structure which wraps around the adaptive-wall test section. The model is driven by two hydraulic motors, one on each side of the tunnel. The drives are essentially identical, and Figure 2.3 shows the drive on the east side of the tunnel, where flow is from left to right in this picture. Each hydraulic motor is switched by a fast-acting solenoid in a control loop where the angle of attack for the motor is monitored by a potentiometer. The drive shaft is decoupled for small misalignments of the shaft and motor by a bellows. A safety clamp is available to limit the maximum and minimum angles of attack of the model, and this can be adjusted to completely clamp the shaft while the model is being worked on. The aerodynamic loads are borne by a bearing around the drive shaft and the lift, drag and pitching moment on the model are measured by a force balance. The force balance is to ensure that the model

Figure 2.2: The pitching motion device, dismounted from the DNW-TWG.

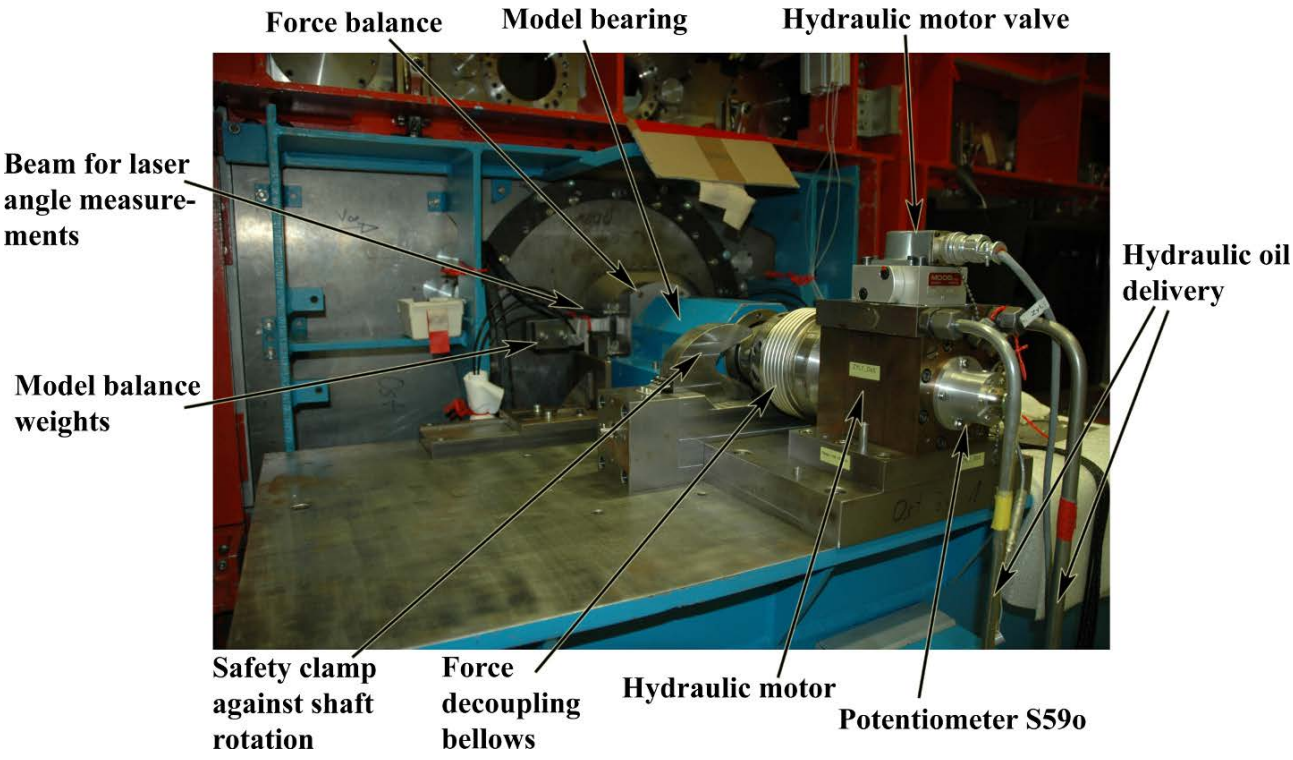

Figure 2.3: The eastern drive shaft and hydraulic motor.

does not exceed the design loads, and its measurements include the parts of the model affected by the wind tunnel wall boundary layer, thus the integrated forces from the pressure sensors on the model midline are preferred for the measurement of lift and pitching moment.

The angle of attack of the model is simultaneously measured by sensors in the hydraulic motors, which are used for the PID controller, and by laser distance meters mounted outside the test section. Four laser distance meters are used, two on each side of the wind tunnel, and on each side one upstream and one downstream of the model axis. The distance is measured to a straight beam which pitches with the airfoil. The laser distance meter measurements are calibrated with an inclinometer and the four measurements of angle of attack are averaged to remove noise and torsion effects.

2.1.3 Wind tunnel airfoil model

The wind tunnel airfoils are carbon fiber models (Fig. 2.4), with chord length c=0.300 m and breadth b=0.997 m (aspect ratio 3.3). The models are constructed of two carbon-fiber half-shells, one for the upper side and one for the lower side, around an internal spar system, which depends on the airfoil loading requirements. The instrumentation is installed inside the hollow space of the model, and then the shells are glued together and the aerodynamic surface is finished. The attachment to the pitching motion test stand is over metal "feet", which can be bolted to the drive shafts.

When the model is mounted in the wind tunnel (Figure 2.5), a 1.5 mm gap remains between the model and sidewall, as also seen in Figure 2.6, and this is not further sealed. The effects of this 1.5 mm gap are important, as described further in Chapter 3. Investigations in section 3.1 have showed that the region of uniform flow in the middle of the model has a width of 0.75 m, or 1.25 chords on either side of the centerline. Due to the pressure difference between the plenum chamber and the test section, the gaps between the drive shafts and the test section wall are sealed with thin steel plates (Figure 2.6, Left).

Loads are computed by CFD for expected steady and unsteady flow conditions and applied to the model over an FEM solver in the design stage. The design target is that the airfoil sections will deform less than 0.1 mm in the worst case, although a heave of the airfoil is allowed, and sometimes the test matrix is expanded to include some test points with higher deformation. Maximum vertical loads are usually of the order of 7000 N, and maximum heave movements of around 2 mm are unavoidable

Figure 2.4: OA209-FCD model

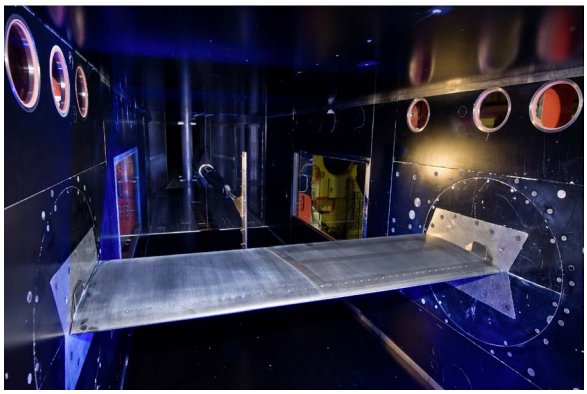

Figure 2.5: The OA209-FCD model installed in the adaptive-wall test section of the DNW-TWG.

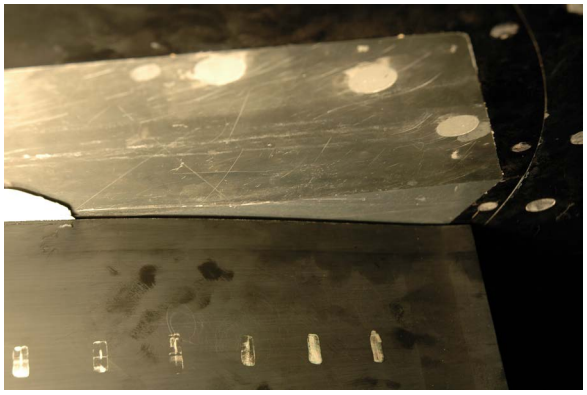

Figure 2.6: Left: Drive shaft sealing, Right: Gap between the model and the wind tunnel side wall.

under these loads. Before installation, the models are statically balanced around the drive shaft using offset weights (See Fig. 2.3), and the test conditions are limited by the maximum normal force safe to apply to the model (computed by the FEM analysis), and the maximum torsional force of the drive system (approx. 600 Nm)

The airfoils are instrumented with pressure sensors (Kulite type XCQ-093), from which the dynamic lift, drag and pitching moment can be integrated, and accelerometers to monitor potential vibration, flutter and resonance conditions which could exceed the designed tolerances. Additionally, the airfoils are mounted on a 3-component balance (Lift, drag and pitching moment) which is mainly used for model monitoring. The balance shows a systematic error of around 20% in comparison to the integrated pressures on the centerline, due to the measurement of the parts of the airfoil which are inside the wind tunnel boundary layers.

Behind the model in Figure 2.5 is a wake rake equipped with static pressure probes. It is positioned two model chords downstream of the model trailing edge and consists of a row of total pressure probes and a number of static pressure sensors. This allows the drag coefficient to be computed from the model wake for static angles of attack. The wake rake does not deliver time-resolved data and so is not used for points where the angle of attack was dynamically varied. The wake rake (Figure 2.7) is used to measure the drag of the model by a measurement of the total pressure loss in the model wake. In contrast to the drag measurement by the pressure sensor integration, the wake rake measurement includes the viscous drag, and is thus essential for performance measurements on airfoils at low angle of attack. Both the measured Pitot profile and the integral drag measurement are available to the experimenter. The wake rake can be driven in the vertical direction, but not in the horizontal direction, and thus the wake can only be measured on the centerline of the model.

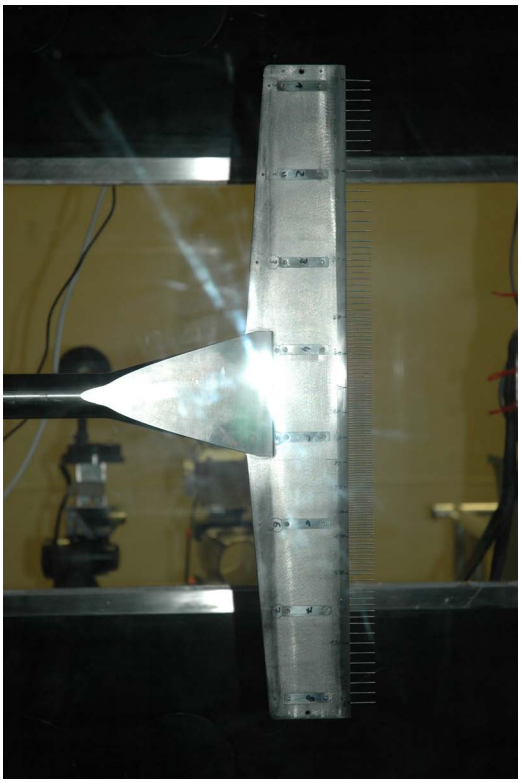

Figure 2.7: The wake rake.

The wake profile is stored, and the drag is computed automatically according to:

$$C_{D_{rake}} = \int_0^L \frac{2}{L} \left(\frac{P}{P_\infty}\right)^{\frac{1}{\gamma}} \left(\frac{P_0}{P_{0_\infty}}\right)^{\frac{\gamma-1}{\gamma}} \sqrt{\frac{1-\left(\frac{P}{P_0}\right)^{\frac{\gamma-1}{\gamma}}}{1-\left(\frac{P_\infty}{P_{0_\infty}}\right)^{\frac{\gamma-1}{\gamma}}}} \left[1-\sqrt{\frac{1-\left(\frac{P_\infty}{P_0}\right)^{\frac{\gamma-1}{\gamma}}}{1-\left(\frac{P_\infty}{P_{0_\infty}}\right)^{\frac{\gamma-1}{\gamma}}}}\right] dz \qquad (2.1)$$

In addition, the pressure on the centerline of the walls is measured by a steady measurement system for the computation of the wall contours, and by an additional unsteady pressure measurement system. For airfoil measurements, the pressures on the side-wall of the test section are typically measured in three sections on the midline and above and below the airfoil on the one side-wall. All of these data and the wall positions are available to the experimenter.

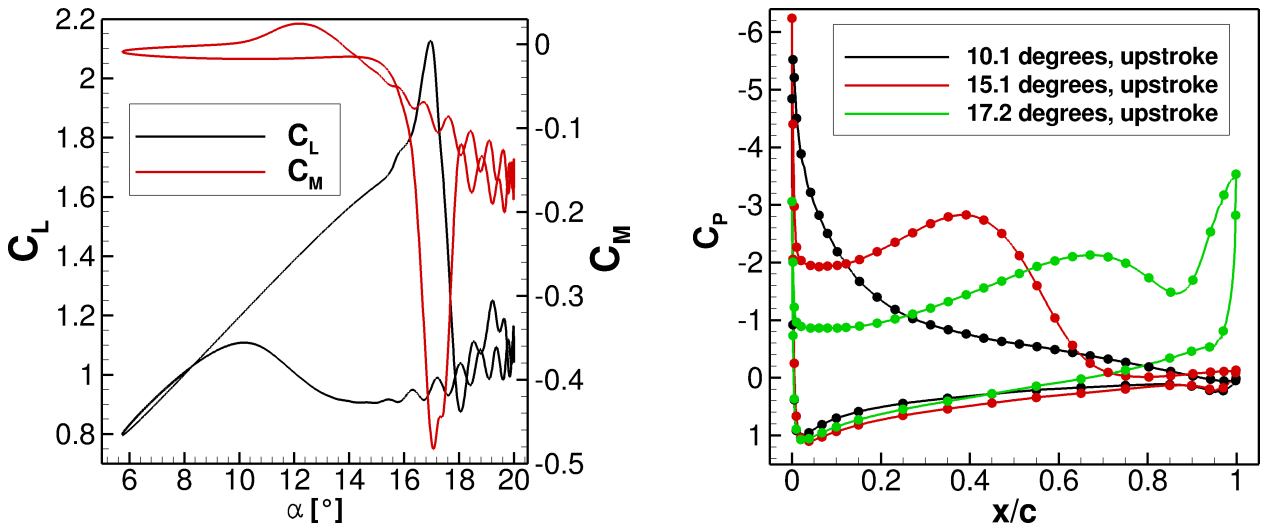

Figure 2.8: Left: Typical lift and pitching moment from a 2D numerical computation of dynamic stall on a rotor airfoil. Right: Example pressure distributions during a pitching cycle

2.1.4 Pressure sensor positioning [1]

At dynamic stall conditions on rotor blade airfoils, separated flow creates a dynamic stall vortex, which causes a lift peak as it forms, and then a rapid drop in lift and a negative spike in pitching moment as it swims off from the airfoil, with a typical dynamic numerical result in Fig. 2.8, Left. In wind tunnel experiments where dynamic stall is produced, a much wider variety of pressure distributions are produced than for static attached flow at the same Mach number, as shown in Fig. 2.8, Right, particularly since the vortex shedding seen during the dynamic stall process produces large pressure gradients around the mid and trailing part of the airfoil. A ring of pressure sensors are positioned around the model midline and integrated to find the dynamic lift, drag and pitching moment of the airfoil, and the limited number of discrete sensor positions mean that the computation of these forces will always be subject to a discretisation error. The pressure sensor positions must then be optimised to have a low discretisation error for a wide range of pressure distributions.

Time-accurate and static computations with high spatial resolution using the DLR-TAU solver in RANS and URANS modes are used to develop an optimised distribution of the pressure sensors for a new airfoil model. Static polars between Mach 0.3 and 0.8 are used, as well as dynamic pitching motion at the SIMCOS DS2 test condition (M=0.31, Re=1.16e6, α=12.87$\pm$7.13°, (ω^*=0.101)), so that the pressure sensor positions are optimised for a large number of pressure distributions. The accuracy in lift, drag and pitching moment is evaluated for each test point for different distributions of the pressure sensors, and a layout of the pressure sensors is found which reduces the error in lift, drag and pitching moment below 1% full scale.

The pressure distributions from CFD solutions for static polars and for dynamic stall are required as an input. The lift, drag and pitching moment are integrated from the C_P distributions, and these are used as reference values. Finally, for each distribution of the pressure sensors, the data is reduced to only the sensor positions and re-integrated using the same algorithms. The difference between the two solutions is then the absolute error.

Figure 2.9 shows the results of absolute error for lift and pitching moment at constant angle of attack, for static polars at Mach 0.3, 0.4, 0.5, 0.6, 0.7 and 0.8. As expected, the absolute error in both lift and pitching moment increases over each polar (although the relative error remains relatively constant), and then falls as the next polar begins. As can be seen, a significant reduction in the absolute

[1] Text and illustrations in this section are taken from [29]: A.D. Gardner, K. Richter, "Optimised pressure sensor positioning on a rotor blade airfoil model for dynamic stall experiments", STAB Mitteilung, 2012.

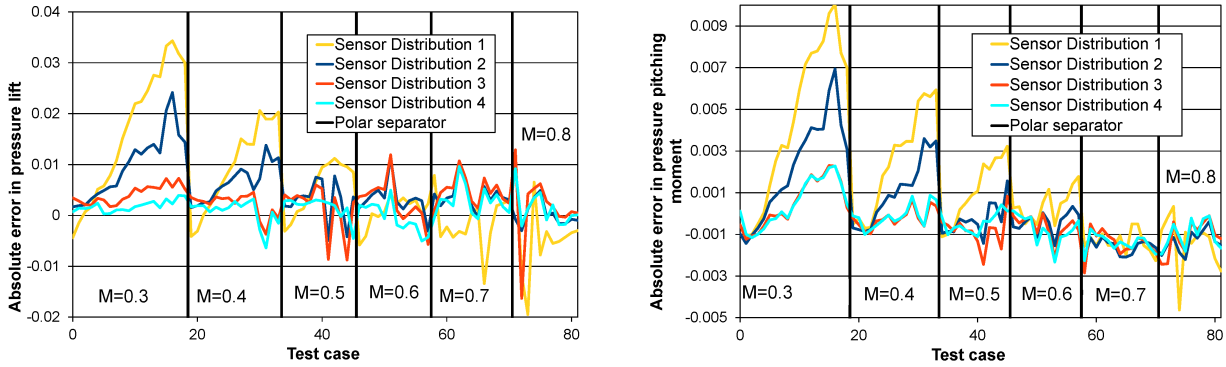

Figure 2.9: Absolute errors due to the sensor discretisation for static polars Left: Lift, Right: Pitching moment

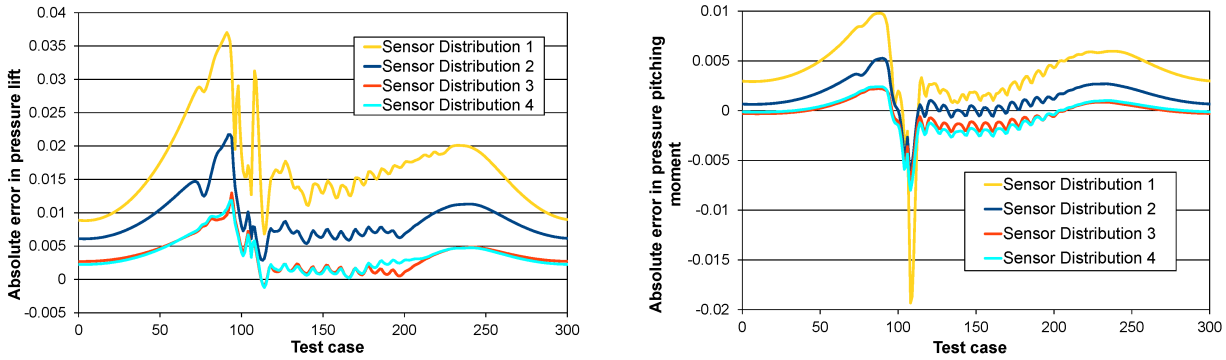

Figure 2.10: Absolute errors due to the sensor discretisation for dynamic pitching at M=0.31, Re=1.16e6, α=12.87$\pm$7.13°, (ω^*=0.101) Left: Lift, Right: Pitching moment

error in lift and pitching motion is possible by the optimisation of the sensor positions and increasing the number of sensors. Sensor distribution 1 has 44 sensors, sensor distribution 2 has 48 sensors, and sensor distributions 3 and 4 both have 50 sensors. It should be emphasised that by historical standards, 44 dynamic sensors in a single section is a large number, but for the distribution tested, a systematic error of up to 3% was noted in the lift. The systematic optimisation reduced the maximum error to under 1%, with most test cases having significantly less error. For the dynamic stall test case (Figure 2.10), the improvement is even more marked, and particularly the systematic error in the pitching moment around dynamic stall could be significantly reduced.

2.1.5 Data analysis

Data is acquired using a Dewetron digital data recorder, and all channels are acquired with the same time-scale. The data recorder is timed so that the sampling rate is fixed to the airfoil pitching rate, and 1024 samples are acquired per period (i.e. 6144 Hz for pitching at 6 Hz). To allow the convergence of averaging, 160 periods of data are acquired, for a total measurement time which varies with the airfoil pitching rate (27 seconds for 6 Hz pitching). After the data has been acquired, it is archived together with all of the wind tunnel data including wall shape and flow conditions.

Each of the data points is typically phase-averaged for a mean and standard deviation of C_P, C_L, C_D and C_M. The mean is used for comparison with CFD and between different measurement points, and the standard deviation gives a measure of the cycle-to-cycle variation. Cycle-to-cycle variations come from structural vibrations and turbulence or separated flow. Thus for each angle of attack on the upstroke and each on the downstroke a pressure distribution and set of forces is available.

The repeatability of nominally identical points measured on different days can be used as a substitute for error. For simple models with attached flow the repeatability of $\overline{C_L}$ and C_{L_p} is better than 1%, and the repeatability of $\overline{C_D}$, $\overline{C_M}$, C_{D_p} and C_{M_p} is within 3% for nominally identical test points. For flow control with strongly 3D flow, the repeatability is worse, and the systematic discretisation errors increase.

The systematic errors due to the wind tunnel blockage and sidewall effect can be corrected for steady tests. In this case, the angle of attack is corrected and C_L and C_D are only slightly corrected due to the change in angle of attack (so that the lift/drag ratio remains essentially unchanged). For unsteady pitching, no reliable correction method for the wind tunnel effects is known, and the data is mainly analysed in an uncorrected form. Due to the setting of the adaptive walls at mean angle of attack the dynamic correction is mainly due to 3D sidewall effects, and can be analysed by computations of the 3D pitching airfoil in the wind tunnel, although due to the computational cost this is not usually undertaken.

2.2 Dynamic stall results[2]

Investigation of dynamic stall on different airfoils yields a large number of new results, particularly as the quality of data improves. Improvements in airfoil design mean that the drag is reduced, as the lift and drag divergence Mach number are increased. Investigating dynamic stall provides insights about the best methods of designing new airfoils, and about options for the control of dynamic stall

This section includes results taken in the DNW-TWG on the airfoils EDI-M109, a modern laminar airfoil with chord to thickness ratio of 9%, EDI-M112 an airfoil of the same family with a thickness ratio of 12%, and the OA209, an older helicopter airfoil with a chord to thickness ratio of 9%. Each of these airfoils performs differently under dynamic stall and the differences are illustrative of the decisions which occur in an airfoil design program.

The design of helicopter airfoils has changed in recent years to rely more strongly on numerical prediction of both the dynamic and static properties of potential airfoil designs. Due to problems with the accuracy of prediction models for the dynamic properties of airfoils, and in particular for dynamic stall, experimental investigations are still required to assess the dynamic performance of airfoils. As part of the German Luftfahrtforschungsprogramm (LuFo IV), the German Aerospace Center, University of Stuttgart and Eurocopter Deutschland had a cooperation (INROS) to design and evaluate new helicopter airfoils with good static characteristics and acceptable dynamic stall characteristics (see also [61]). Two new airfoils were designed for a helicopter main rotor with maximum thickness d_a/c=9% and d_a/c=12%, designated EDI-M109 and EDI-M112 respectively. The use of unsteady criteria for the design is described by Klein et al. [59]. This section investigates selected experimental results illustrating the dynamic performance of the new airfoils.

2.2.1 Experimental arrangement

Carbon fiber models with a chord length c=0.300 m and a breadth b=0.997 m were produced for the 1 m x 1 m adaptive wall test section of the DNW-TWG. The adaptive test section has flexible top and bottom walls which can be adapted to minimise the interference velocities at the wall at the mean angle of attack of the model. The models are mounted horizontally in the test section, as seen in Fig. 2.11, and are driven with pitch-oscillations from shafts through the side-walls attached at the quarter-chord point. Hydraulic motors drive the model from both sides and are located outside the test section. The model could be driven in a $\Delta\alpha$=20° range without opening the tunnel, and mean angular velocities $\overline{\alpha'} \leq$200°/sec could be used with sinusoidal movement. The models were each fitted with a line of 48 Kulite unsteady pressure sensors (type XCQ-093), at an angle of 10° to the oncoming flow, near the centerline. The sensors were situated so as to guarantee a maximum discretisation error of 1% in lift, pressure-drag and pitching moment computed from the pressure taps during static measurements and dynamic stall. The discretisation error was estimated in the design

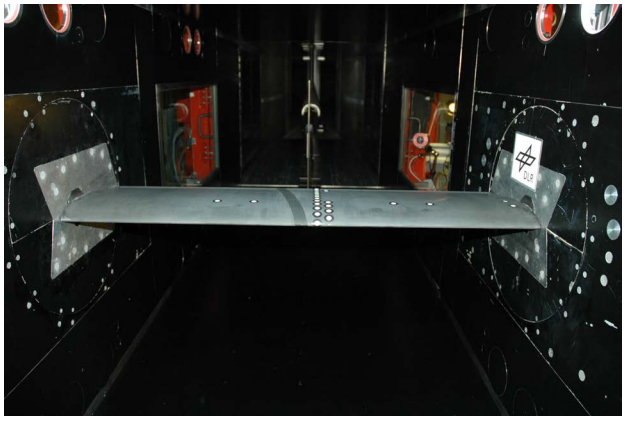

Figure 2.11: The EDI-M112 airfoil model installed in the test section of the DNW-TWG wind tunnel.

[2]Text and illustrations in this section are taken from [30]: Gardner, A.D., Richter, K., Mai, H., Altmikus, A.R.M., Klein, A. and Rohardt, C.-H., "Experimental investigation of dynamic stall performance for the EDI-M109 and EDI-M112 airfoils", *Journal of the American Helicopter Society*, Volume 58, Number 1, 2013. DOI:10.4050/JAHS.58.012005

phase by comparing discretised and non-discretised data for a given pressure sensor distribution using around 2000 computed dynamic and static pressure distributions for each airfoil. The angle of attack was measured using four high-frequency laser range finders on beams attached to each end of the model. A phase-locked data acquisition system, sampled each sensor with 1024 points per period for 160 periods.

The dynamic test points were produced for two classes of points, both with sinusoidal pitching motion about a mean angle: $\alpha = \overline{\alpha} + \alpha_{\pm}\sin(2\pi ft)$ at $M \in$[0.3, 0.4, 0.5] and with Reynolds numbers $4\times10^6 \leq Re/M \leq 7\times10^6$. Points were taken with large amplitudes $4^\circ \leq \alpha_{\pm} \leq 10^\circ$ and low frequency 3.3 Hz$\leq f \leq$6.6 Hz, to generate dynamic stall matching the main rotor rotation rate. A listing of the dynamic stall points used in this section is in Table 2.1. In addition, points with low amplitude $0.5^\circ \leq \alpha_{\pm} \leq 2^\circ$ and high frequency 13 Hz$\leq f \leq$45 Hz were tested to produce data for the damping criterion [69] for dynamic stall strength.

The experimental data for the EDI-M109, EDI-M112 and OA209 is presented with angle of attack uncorrected for wind tunnel effects, geometry changes in the model compared to the nominal airfoil or other effects. It should be noted that the experimental OA209 geometry used was built in the design shape (with rotation and trailing edge from the optimisation process) rather than the industrial shape (with shape modified by the manufacturing constraints). The EDI-M109 and EDI-M112 models were operated at up to M=0.8 and Re=5.8$\times10^6$, such that under the maximum load case the airfoil has a maximum contour deformation of 0.15 mm.

2.2.2 Data averaging

Variables were phase averaged over 160 cycles of 1024 points to get a mean and standard deviation for each point on the cycle. The standard deviation in α, $\sigma\alpha \leq 0.05^\circ$, and so is not plotted. Additionally, the mean lift $\overline{C_L}$, mean drag $\overline{C_D}$ and mean pitching moment $\overline{C_M}$ over a cycle were taken for each dynamic point by averaging the data over all cycles. The peak lift C_{L_p}, peak drag C_{D_p} and peak pitching moment C_{M_p} were found by analysing the phase-averaged data and finding the maximum value for lift and drag or the minimum value for pitching moment. The repeatability of $\overline{C_L}$ and C_{L_p} was better than 1%, and the repeatability of $\overline{C_D}$, $\overline{C_M}$, C_{D_p} and C_{M_p} was within 3% for test points which were nominally identical. Figure 2.12 illustrates the differences between the instantaneous and phase-averaged data. Over a large number of periods, the stochastic vortex shedding after stall is well averaged, and the standard deviation on the phase averaged data gives an indication of the cycle-to-cycle variation of the flow at that angle of attack. The standard deviation of the phase-averaged data is shown for every 16th point on all figures.

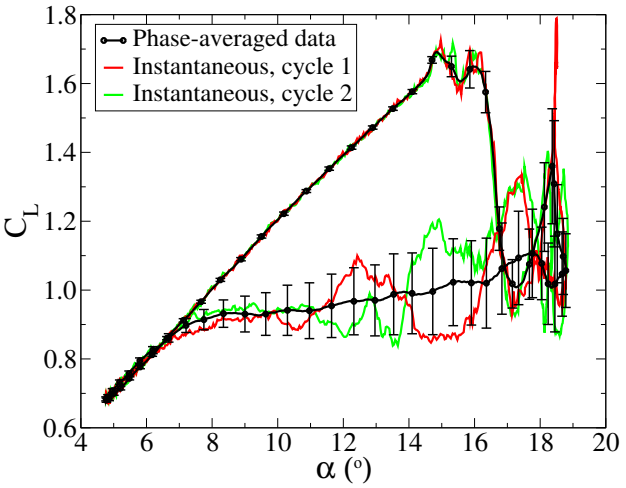

Figure 2.12: Comparison between instantaneous and phase-averaged data for the EDI-M109 airfoil at M=0.3, Re=1.8$\times10^6$, f=6.6 Hz, α=12$\pm$7°.

The damping coefficient D gives an indication of whether a negative damping will be too large to be counteracted by the structural damping and is computed from the theoretical and measured values of the aerodynamic damping [69]: $D = [-\oint C_M\, d\alpha(\alpha_{\pm})^2\pi^3 cf]/[2v_{\infty}]$, where D=1 for small oscillations with attached flow. This analysis was performed for each dynamic point measured, using the uniform INROS analysis code shared by ECD, ONERA, University of Stuttgart and DLR. The

Table 2.1: Dynamic airfoil data.

$\overline{\alpha}$ [°]	$\alpha_{\pm}$ [°]	C_{L_p} [-]	$\overline{C_L}$ [-]	C_{M_p} [-]	f [Hz]	$\overline{\alpha'}$ [°/s]	ω^* [-]
EDI-M109 at M=0.3, Re=1.2$\times$10^6							
13	7	1.66	1.07	-0.27	5.6	157	0.10
EDI-M109 at M=0.3, Re=1.8$\times$10^6							
10	4	1.50	1.12	-0.12	6.6	106	0.12
10	5	1.57	1.05	-0.22	6.6	132	0.12
10	6	1.65	0.99	-0.25	6.6	158	0.12
10	7	1.68	0.95	-0.28	6.6	185	0.12
11	7	1.59	0.99	-0.21	3.3	92	0.06
11	7	1.64	0.97	-0.26	5.0	140	0.09
11	7	1.69	0.99	-0.29	6.6	185	0.12
12	4	1.59	1.15	-0.23	6.6	106	0.12
12	7	1.69	1.05	-0.30	6.6	185	0.12
EDI-M109 at M=0.3, Re=1.8$\times$10^6 - Dual							
12	7	1.70	1.06	-0.31	6.6	185	0.12
EDI-M109 at M=0.4, Re=2.4$\times$10^6							
10	4	1.47	1.13	-0.12	6.6	106	0.09
10	5	1.55	1.08	-0.15	6.6	132	0.09
10	6	1.57	1.02	-0.18	6.6	158	0.09
10	7	1.59	0.97	-0.22	6.6	185	0.09
EDI-M109 at M=0.5, Re=3.0$\times$10^6							
10	4	1.35	1.13	-0.08	6.6	106	0.07
10	5	1.38	1.09	-0.08	6.6	132	0.07
10	6	1.40	1.05	-0.10	6.6	158	0.07
10	7	1.42	1.00	-0.12	6.6	185	0.07
EDI-M112 at M=0.3, Re=1.2$\times$10^6							
13	7	1.69	1.10	-0.18	5.6	157	0.10
EDI-M112 at M=0.3, Re=1.8$\times$10^6							
8	8	1.69	0.87	-0.13	6.6	211	0.12
10	4	1.55	1.18	-0.03	6.6	106	0.12
10	5	1.60	1.10	-0.09	6.6	132	0.12
10	6	1.65	1.05	-0.13	6.6	158	0.12
10	7	1.71	1.01	-0.18	6.6	185	0.12
11	7	1.45	0.92	-0.17	3.3	92	0.06
11	7	1.54	0.94	-0.19	5.0	140	0.09
11	7	1.62	0.96	-0.21	6.6	185	0.12
12	4	1.62	1.21	-0.14	6.6	106	0.12
12	7	1.78	1.09	-0.23	6.6	185	0.12
EDI-M112 at M=0.3, Re=1.8$\times$10^6 - Dual							
12	7	1.87	1.14	-0.29	6.6	185	0.12
EDI-M112 at M=0.4, Re=2.4$\times$10^6							
10	7	1.59	0.89	-0.19	6.6	185	0.12

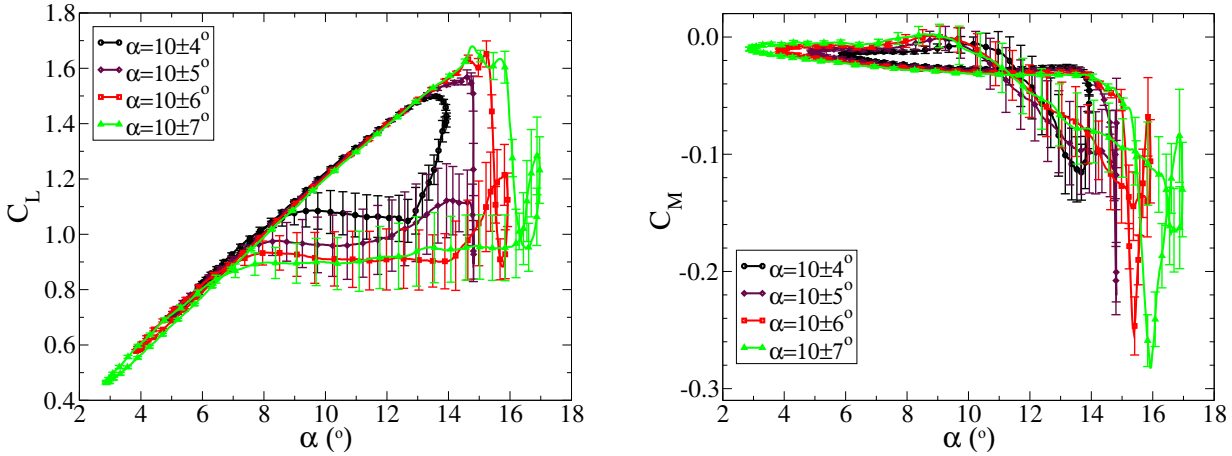

Figure 2.13: Comparison of lift (Left) and pitching moment coefficient (Right) for the EDI-M109 airfoil with various amplitudes at M=0.3, Re=1.8×10^6, f=6.6 Hz, α=10±4-7°.

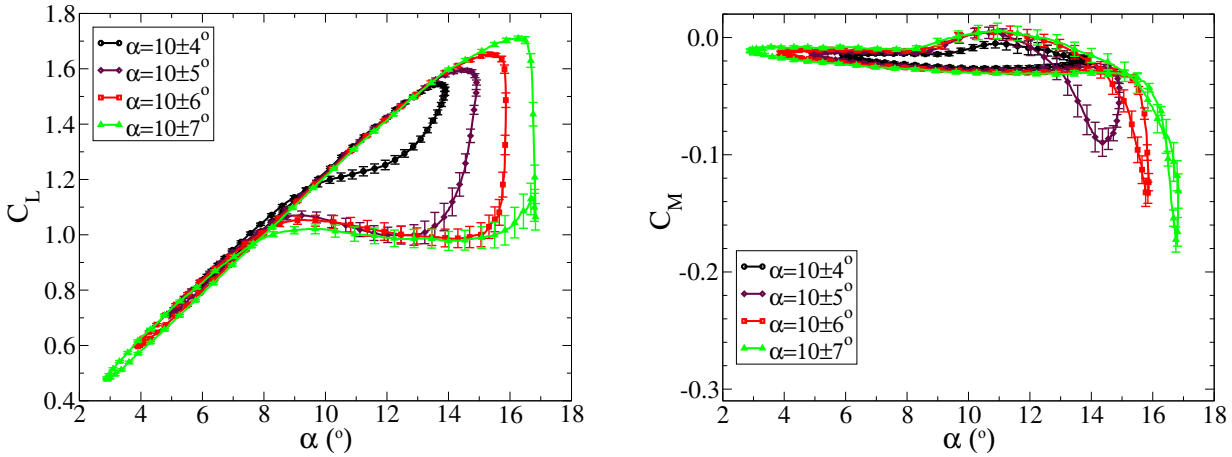

Figure 2.14: Comparison of lift (Left) and pitching moment coefficient (Right) for the EDI-M112 airfoil with various amplitudes at M=0.3, Re=1.8×10^6, f=6.6 Hz, α=10±4-7°.

damping was additionally computed for the separated modes 1/rev to 6/rev.

2.2.3 Variation of amplitude

The primary effect of increasing the amplitude is to increase the severity of the dynamic stall. Figures 2.13 and 2.14 illustrate the effect of varying the oscillation amplitude for the EDI-M109 and EDI-M112 airfoils respectively. In each case the oscillation frequency was f=6.6 Hz, but of necessity these will have different mean angular velocities, as shown in Table 2.1.

Figure 2.13 shows the EDI-M109 at a mean angle of $\overline{\alpha}$=10° at M=0.3. As the amplitude increases from $\alpha_{\pm}$=4° to $\alpha_{\pm}$=7°, the peak lift increases from C_{L_p}=1.50 to C_{L_p}=1.68, but the mean lift over one cycle decreases from $\overline{C_L}$=1.12 to $\overline{C_L}$=0.95, as shown in Table 2.1. This is typical of dynamic stall, and there is a corresponding increase in the mean drag over one cycle as the amplitude increases. Similarly, the pitching moment peak increases as the dynamic stall is strengthened at increasing amplitudes from C_{M_p}=-0.12 to C_{M_p}-0.29.

From static polars, where an infrared camera was used to measure the heat flux on both airfoils, it was seen that a step in the pressure distribution and an increased cycle-to-cycle variation in the pressure is associated with transition over a laminar boundary layer separation. The transition point on the top of the airfoil moves upstream with increasing angle of attack as shown in Fig. 2.15. The approximate angle at which the transition reaches the leading edge can thus be estimated from a

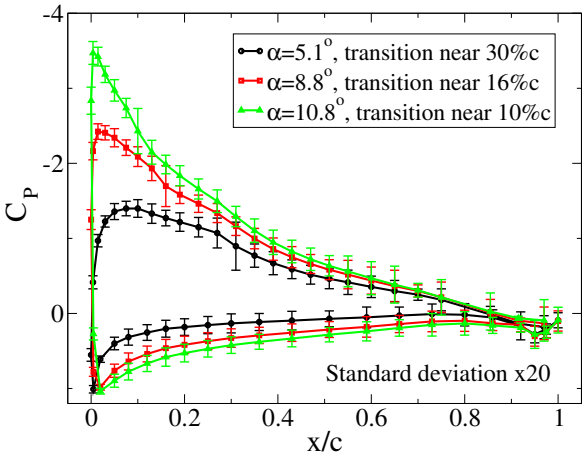

Figure 2.15: Time sequence of pressure distributions for the EDI-M112 airfoil at M=0.3, Re=1.8×10^6, f=6.6 Hz, α=10±6°, showing the movement of the transition position.

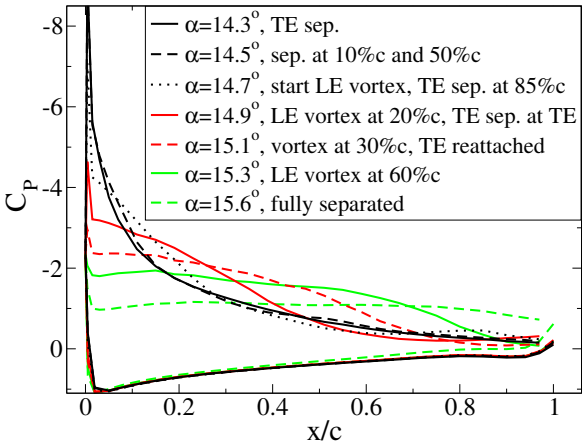

Figure 2.16: Time sequence of pressure distributions for the EDI-M109 airfoil at M=0.3, Re=1.8×10^6, f=6.6 Hz, α=10±7°, showing leading edge separation.

time-series of pressure distributions.

For the EDI-M109 at a mean angle of $\overline{\alpha}$=10° at M=0.3, the boundary layer transition on the top of the airfoil moves upstream on the upstroke reaching the leading edge at around α=10°. There is a reduction in slope of the lift curve at this point, which appears to be associated with the halting of the transition point movement. The EDI-M109 sees a significant increase in the cycle-to-cycle variation in the pressure signals near the trailing edge above α=13°, and by α=13.5° this has developed into a trailing edge stall.

As seen in Fig. 2.16, for the case α=10±7°, by α=14.3° the trailing edge stall is clearly visible and the pressure coefficient on the trailing edge is less than zero. At α=14.5°, the flow separates at 10% and 50% chord, and by α=14.7°, the leading edge vortex has started to move downstream. From this point, the aerodynamics is much more like a leading edge stall, since the leading edge stall vortex travels downstream, pushing the trailing edge separation off the end of the airfoil. The two peaks in the lift curve for α=10±7° in Fig. 2.13 at α=14.7° and α=15.8° are associated with the formation of the stall vortex at the leading edge, and with the passage of the stall vortex over the trailing edge. As the stall vortex moves toward the trailing edge, the pitching moment decreases toward a negative peak and at the point where the vortex crosses the trailing edge, the minimum pitching moment is reached. After stall a highly unsteady flow is observed, with reattachment at lower α for higher amplitudes. The pressure distributions (not shown) indicate that for the EDI-M109 at M=0.3, the reattachment starts at the trailing edge and moves upstream, with the suction peak being the last place to reattach.

Figure 2.14 shows the EDI-M112 at a mean angle of $\overline{\alpha}$=10° at M=0.3. As amplitude increases from $\alpha_{\pm}$=4° to $\alpha_{\pm}$=7°, the peak lift increases from C_{L_p}=1.55 to C_{L_p}=1.71 and the mean lift over one cycle decreases from $\overline{C_L}$=1.18 to $\overline{C_L}$=1.01 in the same way as for the EDI-M109, as seen in Table 2.1. Also similarly, the mean drag over one cycle increases as the amplitude increases, and the pitching moment peak increases from C_{M_p}=-0.04 to C_{M_p}=-0.18. The dynamic stall peaks for the pitching moment are significantly less than for the EDI-M109 at these flow and motion conditions, which is expected, since the 9% airfoil is designed for a higher Mach number than the 12% airfoil. On the upstroke, the boundary layer transition reaches the leading edge at around α=13°, and at the same angle the pressure signals near the trailing edge start to increase in cycle-to-cycle variation, and the start of the region of unsteady signals moves upstream with increasing α.

As seen in Fig. 2.17, for the case α=10±7°, by α=14.9° there is a clear trailing edge separation, which moves slowly upstream on the airfoil with increasing α until the leading edge is reached. For amplitudes of $\alpha_{\pm}$=5° and above, the trailing edge separation is followed by unsteady separated flow. The cycle-to-cycle variation in the lift coefficient in the separated region is significantly less than for the EDI-M109. As for the EDI-M109, the higher amplitudes reattach at lower α, but the difference between different amplitudes is reduced. At $\alpha_{\pm}$=4° there is unsteady flow, which might be a precursor to separation, and a significant hysteresis in the lift, but a full separation of the flow does not occur. The pressure distributions (not shown) indicate that for the EDI-M112 at M=0.3, the reattachment starts at the leading edge and moves downstream, with the trailing edge being the last place to reattach.

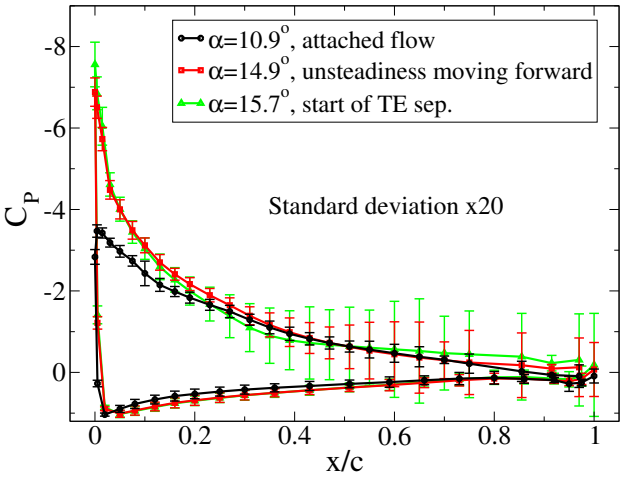

Figure 2.17: Time sequence of pressure distributions for the EDI-M112 airfoil at M=0.3, Re=1.8×10^6, f=6.6 Hz, α=10±7°, showing trailing edge separation.

For the EDI-M109 at M=0.4 at a mean angle of $\overline{\alpha}$=10°, shown in Fig. 2.18, the reduced frequency has reduced to ω^*=0.09 for the constant absolute frequency of f=6.6 Hz, as seen in Table 2.1. As the amplitude increases from $\alpha_{\pm}$=4° to $\alpha_{\pm}$=7°, the peak lift increases from C_{L_p}=1.47 to C_{L_p}=1.60. As for M=0.3, the mean lift over one cycle decreases from $\overline{C_L}$=1.13 to $\overline{C_L}$=0.97. Similarly to M=0.3, the pitching moment peak increases as the dynamic stall is strengthened at increasing amplitudes from C_{M_p}=-0.12 to C_{M_p}=-0.22. The boundary layer transition on the top of the airfoil reaches the leading edge at around α=9°, and the sudden change in the slope of the lift curves at α=12° is associated with the release of a leading edge stall vortex travelling downstream. The flow in the suction peak is supersonic, and although shock-induced stall is suspected, no strong shock is visible in the pressure distributions (not shown). For the EDI-M112 at this flow condition (not shown), the curves look very similar to Fig. 2.14 and in this case the pressure distributions have a strong shock at around 10% chord, followed by separated flow to the trailing edge, leading to trailing edge stall. At M=0.4 the EDI-M109 reattaches from the trailing edge, with the last attachment in the supersonic region, and

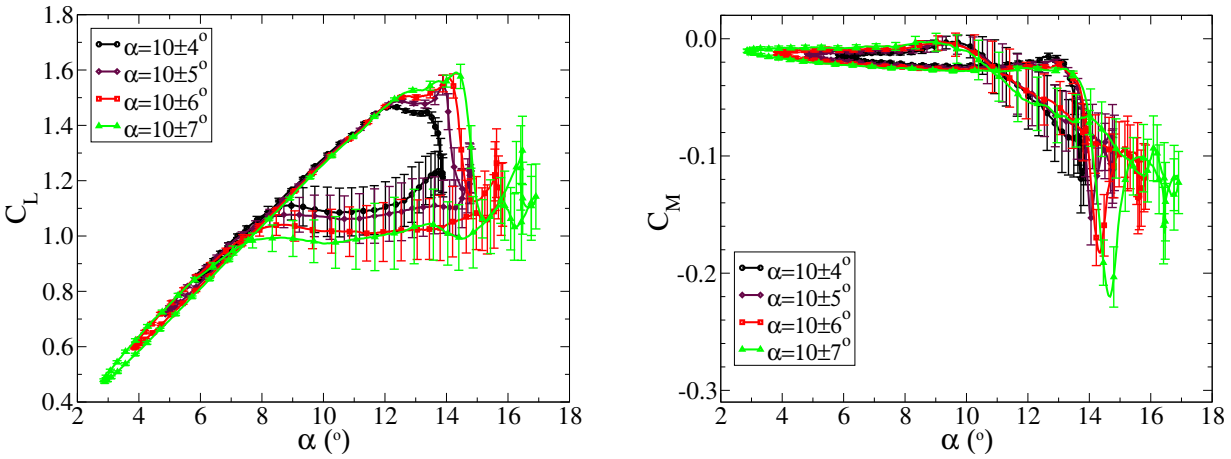

Figure 2.18: Comparison of lift (Left) and pitching moment coefficient (Right) for the EDI-M109 airfoil with various amplitudes at M=0.4, Re=2.4×10^6, f=6.6 Hz, α=10±4-7°.

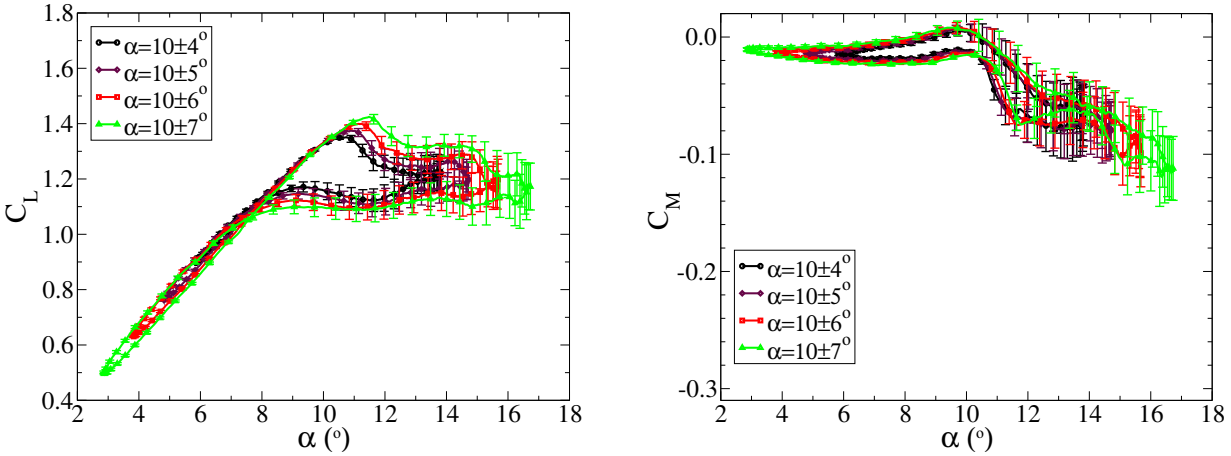

Figure 2.19: Comparison of lift (Left) and pitching moment coefficient (Right) for the EDI-M109 airfoil with various amplitudes at M=0.5, Re=3.0×10^6, f=6.6 Hz, α=10±4-7°.

the EDI-M112 has reattachment from the leading edge.

For M=0.5 the results change, and in Fig. 2.19 there is not the same loss of lift after separation as seen for M=0.3 and M=0.4. For M=0.3 a 16% reduction in mean lift was observed between the minimum and maximum amplitudes, but here the reduction is 11%. After stall no discrete peaks are formed, but the flow has a high cycle to cycle variation in the lift. There is still an increase in the peak lift from C_{L_p}=1.35 to C_{L_p}=1.42 as amplitude increases from $\alpha_{\pm}$=4° to $\alpha_{\pm}$=7°, a decrease in mean lift from $\overline{C_L}$=1.13 to $\overline{C_L}$=1.00, and an increase in the pitching moment peak from C_{M_p}=-0.08 to C_{M_p}=-0.12, as seen in Table 2.1. For the EDI-M109, the boundary layer transition nears the leading edge at around α=7° on the upstroke, probably remaining laminar until the shock, which appears at around the same angle of attack, strengthening up to α=10°, as shown in Fig. 2.20. The boundary layer separates after the shock, and this results in trailing edge separation at α=10-12° depending on the oscillation amplitude (at 11° in Fig. 2.20). After separation, a highly unsteady flow with supersonic attached flow near the leading edge and high lift remains, as seen in Fig. 2.20. Reattachment is from the trailing edge with the supersonic regions near the leading edge being the last to reattach. The EDI-M112 follows this scheme too, but the shock is significantly stronger.

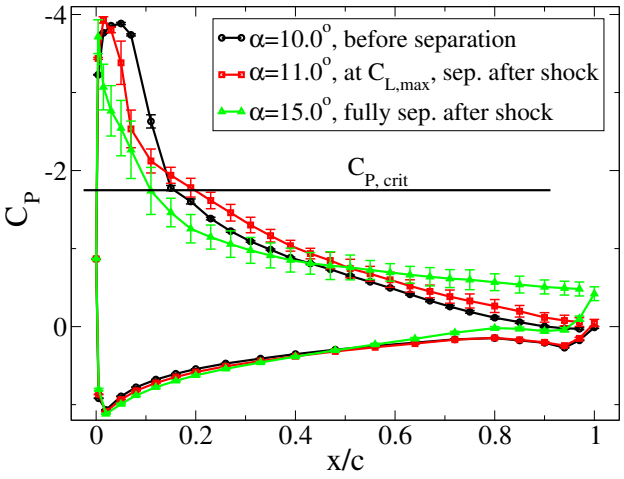

Figure 2.20: Time sequence of pressure distributions for the EDI-M109 airfoil at M=0.5, Re=3.0×10^6, f=6.6 Hz, α=10±7°, showing shock induced separation.

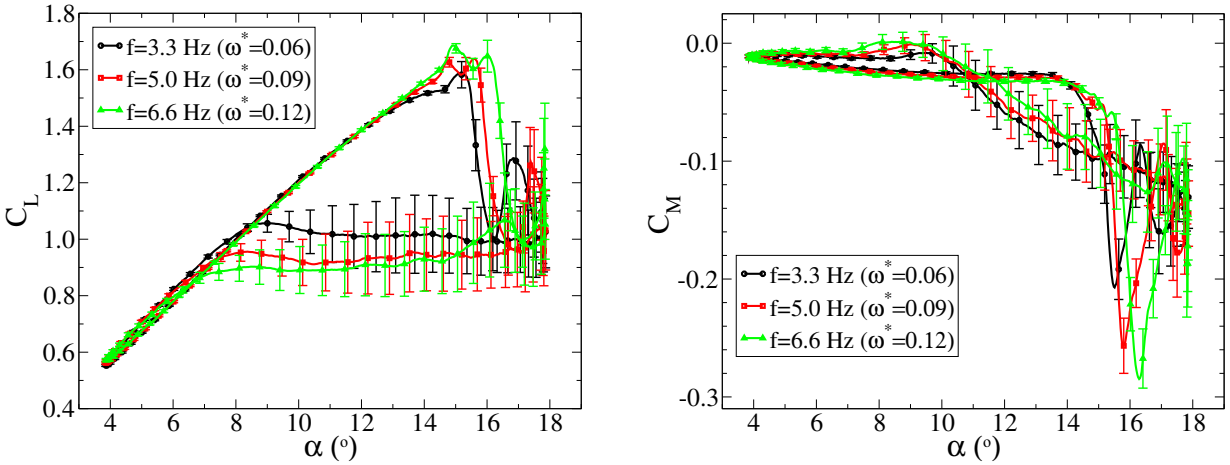

Figure 2.21: Comparison of lift (Left) and pitching moment coefficient (Right) for the EDI-M109 airfoil with various frequencies at M=0.3, Re=1.8×10^6, f ∈[3.3, 5.0, 6.6] Hz, α=11±7°.

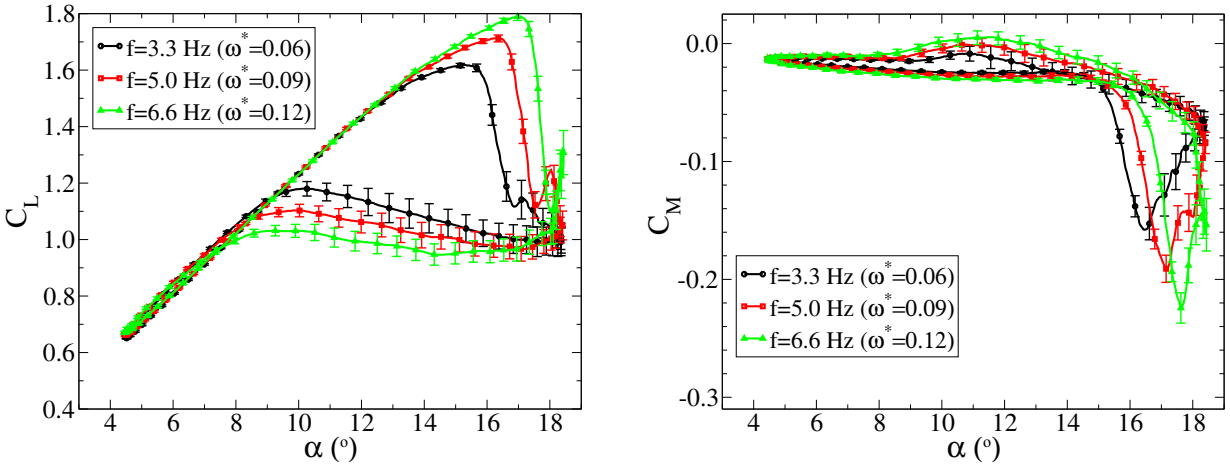

Figure 2.22: Comparison of lift (Left) and pitching moment coefficient (Right) for the EDI-M112 airfoil with various frequencies at M=0.3, Re=1.8×10^6, f ∈[3.3, 5.0, 6.6] Hz, α=11±7°.

2.2.4 Variation of frequency

The frequency was varied at constant amplitude, to separate the effects of varying mean angle of attack ($\overline{\alpha}$) by amplitude ($\alpha_\pm$) variation at constant frequency (f) and by frequency variation at constant amplitude. Figures 2.21 and 2.22 illustrate the effect of varying the oscillation frequency for the EDI-M109 and EDI-M112 airfoils respectively. For both airfoils it can be seen that the lower frequencies have a stronger curvature above α=11° in the lift vs α curve than for higher frequencies. The higher frequencies also have a higher peak in lift and a lower lift in the separated part of the cycle. The effect of the frequency is strongest on the height of the pitching moment peak. The higher reduced frequencies increase the pitching moment peak significantly. Moving from ω^*=0.06 to ω^*=0.09 increases the peak height by 24% for the EDI-M109 and 21% for the EDI-M112, and increasing the frequency from ω^*=0.09 to ω^*=0.12 increases the peak height by 11% for the EDI-M109 and 18% for the EDI-M112.

For the EDI-M112 the primary stall behaviour is unchanged with frequency, as shown in Fig. 2.22, with a trailing edge separation starting at around α=13° and propagating upstream. As seen in Fig. 2.23, although the highest frequency results in the highest angle of attack before separation, the time between the start and end of separation is lower for ω^*=0.12 (18 ms) than for ω^*=0.06 (25 ms). For higher frequencies the reattachment is delayed to lower angles and the cycle-to-cycle variation in the lift is reduced during the detached flow phase. The reattachment is always from leading to trailing

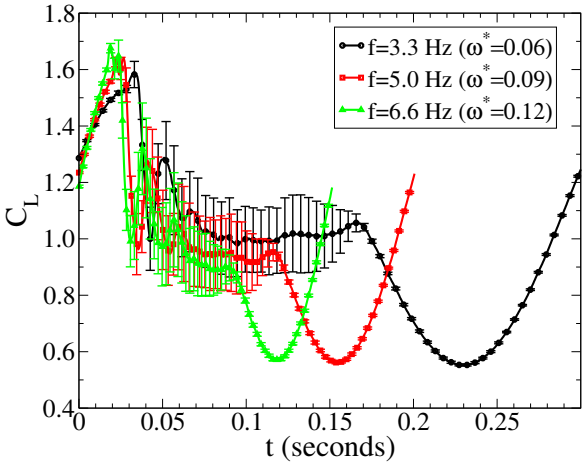

Figure 2.23: Lift coefficients plotted against time for the EDI-M112 airfoil with various frequencies at M=0.3, Re=1.8×10^6, f ∈[3.3, 5.0, 6.6] Hz, α=11±7°.

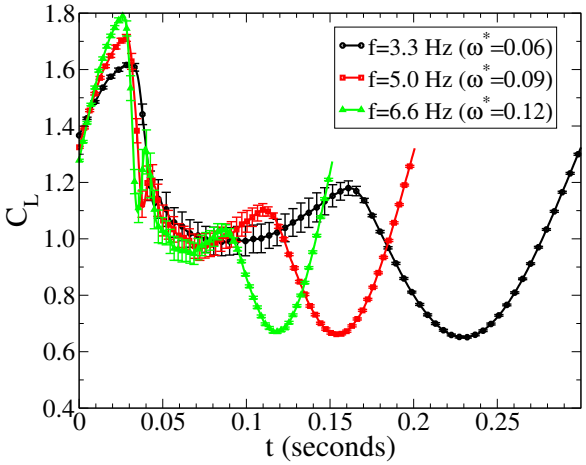

Figure 2.24: Lift coefficients plotted against time for the EDI-M109 airfoil with various frequencies at M=0.3, Re=1.8×10^6, f ∈[3.3, 5.0, 6.6] Hz, α=11±7°.

edge.

For the EDI-M109 a drastic change in the separation takes place, as shown in Fig. 2.21. Here at f=6.6 Hz leading edge stall is seen, similar to that in Fig. 2.13, but at f=3.3 Hz trailing edge stall occurs. The boundary layer at the trailing edge begins to become unstable at α=13° for all cases, separating soon after, and then the separated region propagates upstream. At f=6.6 Hz and f=5.0 Hz, a leading edge separation occurs before this can propagate to the leading edge, but for f=3.3 Hz, the time before separation is sufficient for the trailing edge separation to reach the leading edge and cause full separation of the airfoil.

Due to the lower frequency, the time between the start of trailing edge separation and loss of lift is more than doubled (from 10 ms to 21 ms) for f=3.3 Hz over f=6.6 Hz, as shown in Fig. 2.24. In all cases the reattachment is from trailing edge to leading edge with the suction peak being the last to reattach. The reattachment at f=3.3 Hz is at significantly higher α than the cases at higher frequency, and this angle decreases with increasing frequency.

The dynamic stall peak in the pitching moment increases with increasing amplitude, increasing mean angle of attack and with increasing frequency. If these values are combined as the normalised mean angular velocity: $\overline{\alpha'_{norm}} = \frac{\omega^*}{M} \times (\alpha_{max} - \alpha_{C_{L_{max}},static})$, where $\alpha_{C_{L_{max}},static}$ is the angle of attack at maximum lift for a static polar at these flow conditions, $\alpha_{max} = \overline{\alpha} + \alpha_{\pm}$, ω^* is the reduced pitching frequency and M is the Mach number then an approximately linear relationship to peak pitching moment C_{M_p} can be seen.

As seen in Fig. 2.25, in this case, the data at varying amplitudes $4° \leq \alpha_{\pm} \leq 8°$, mean angle of attack $8° \leq \overline{\alpha} \leq 12°$ and frequency $3.3\,\text{Hz} \leq f \leq 6.6\,\text{Hz}$ fall approximately onto a single line for each airfoil and Mach number for M=0.3-0.5. To test the idea in Fig. 2.25 that the strength of the dynamic stall peaks is a function of the maximum angle of attack, cases were compared with the same maximum angle of attack and a different mean angle of attack at a constant pitching frequency. For light dynamic stall, where the maximum angle of attack of the airfoil is approximately equal to the angle of attack at separation, this results in similar dynamic stall qualities, and the dynamic stall strength is nearly independent of the minimum angle of attack. As the maximum angle of attack increases, the similarity is reduced.

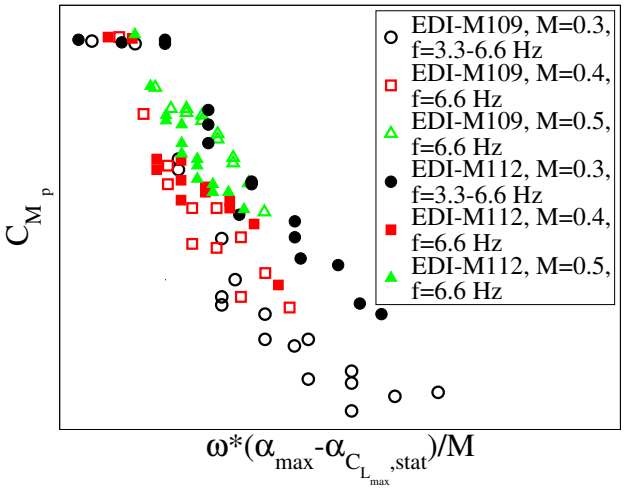

Figure 2.25: Relationship of C_{M_p} to normalised mean angular velocity at Re/M=6×10^6 for varying amplitude, mean angle of attack and frequency.

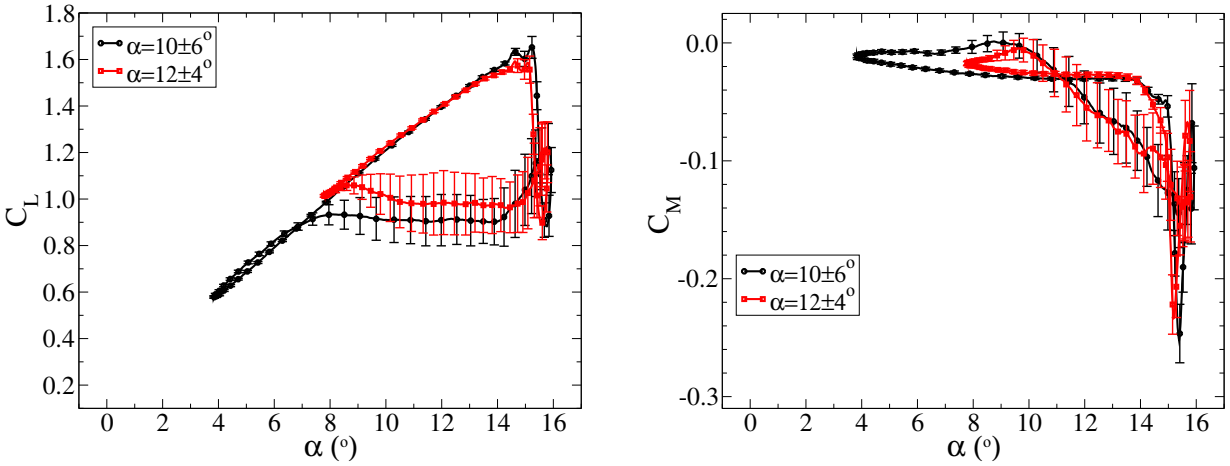

Figure 2.26: Comparison of lift (Left) and pitching moment coefficient (Right) for the EDI-M109 airfoil with constant maximum angle of attack at M=0.3, Re=1.8×10^6, f=6.6 Hz, α=10±6°, 12±4°.

At M=0.3 and Reynolds number Re=1.8×10^6, pitching with α=10°±6° and α=12°±4° give similar results, as shown in Fig. 2.26, with a difference in C_{M_p} of 8% between the two cases shown. For the EDI-M112, pitching with α=8°±8°, α=10°±6° and α=12°±4° also gives similar results, as shown in Fig. 2.27, with a difference in C_{M_p} of 1% between the three cases shown.

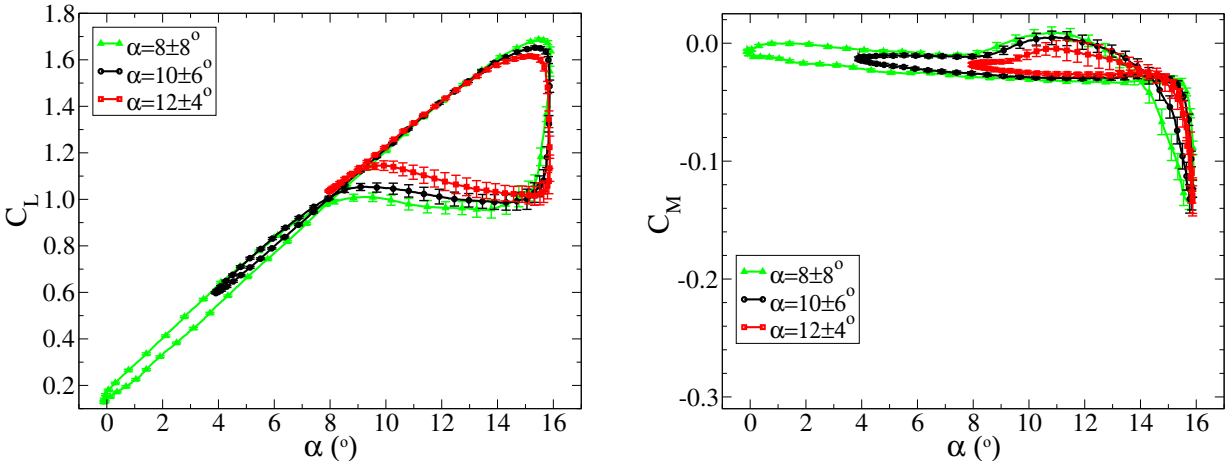

Figure 2.27: Comparison of lift (Left) and pitching moment coefficient (Right) for the EDI-M112 airfoil with constant maximum angle of attack at M=0.3, Re=1.8×10^6, f=6.6 Hz, α=8±8°, 10±6°, 12±4°.

2.2.5 Higher order pitching motion

The effect of higher order pitching motion on dynamic stall is interesting because the primary pitching motion of 1/rev for a helicopter blade is always overlaid with effects due to the elasticity of the blades. At conditions with dynamic stall the elasticity can have a significant effect on the local angle of attack of a section of blade. In order to partially simulate this, a dual-sine pitching motion: $\alpha = 12° + 7° \sin(2\pi ft) + 1° \sin(5 \times (2\pi ft + \frac{\pi}{2}))$, was generated and compared to a pure sinusoidal pitching motion: $\alpha = 12° + 7° \sin(2\pi ft)$. As seen in Fig. 2.28, these pitching motions share the same maximum and minimum angles of attack, but have different shapes with the dual-sine signal having a double peak at the maximum and minimum angles.

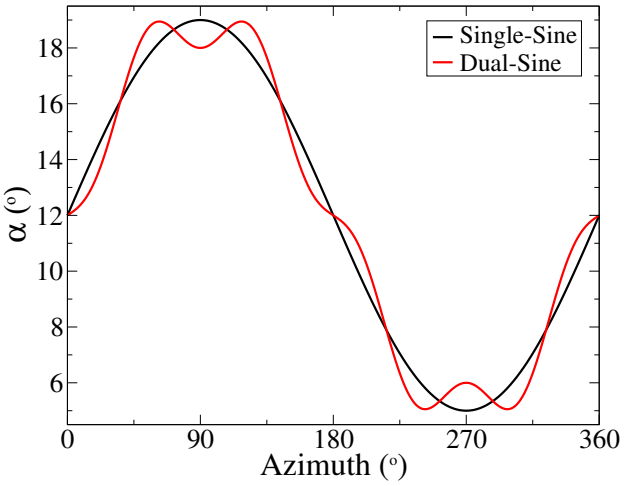

Figure 2.28: Comparison of the pitching motions between single-sine motion at 1/rev and a dual-sine mixture of 1/rev and 5/rev sine movements.

For the EDI-M109 the additional higher frequency motion adds more wiggles into the lift curve, as shown in Fig. 2.29, but qualitatively the result is the same. At α=12° on the upstroke, the 5/rev motion causes the upward movement to momentarily become much slower. This can be seen in Fig. 2.29 by the more closely clustered symbols for the dual-sine case, where the time between two symbols is equal for the dual-sine and reference cases. The separation for the dual-sine case is at higher angle of attack, due to the higher angular velocity around the separation angle. The time between the end of the linear lift increase and the loss of lift is the same in both cases, but the higher angular velocity of the dual-sine case moves this time to a higher angle. For this case, it appears that using a dual-sine motion does not have any significant effect on the dynamic stall behaviour of the airfoil, so long as the maximum and minimum angles of attack remain constant.

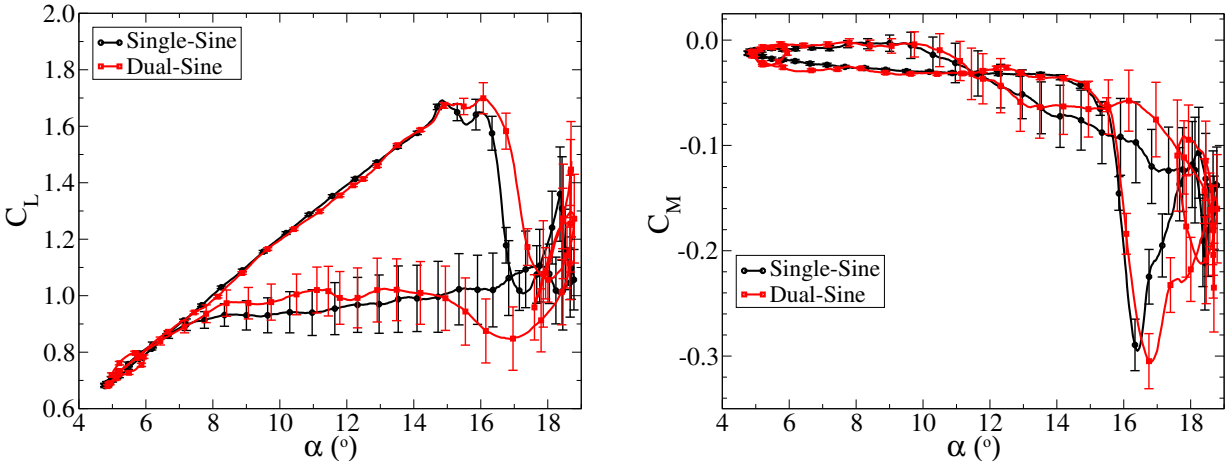

Figure 2.29: Comparison of lift (Left) and pitching moment coefficient (Right) for the EDI-M109 airfoil with single and dual-sine pitching motion at M=0.3, Re=1.8×10^6, f=6.6 Hz, α=12±7°.

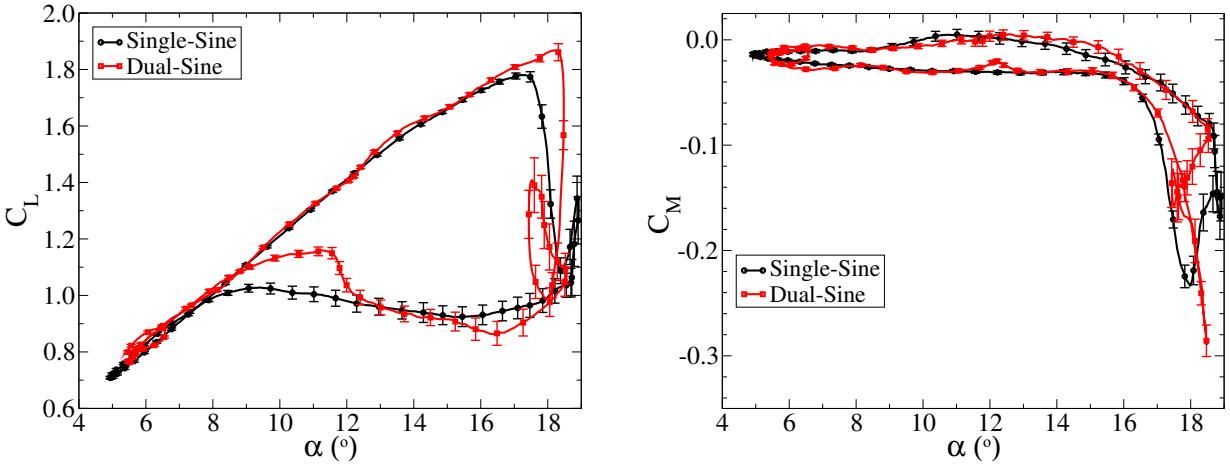

Figure 2.30: Comparison of lift (Left) and pitching moment coefficient (Right) for the EDI-M112 airfoil with single and dual-sine pitching motion at M=0.3, Re=1.8×10^6, f=6.6 Hz, α=12±7°.

For the EDI-M112 the dual-sine case has more wiggles added into the lift curve, as shown in Fig. 2.30, and in contrast with the results for the EDI-M109, the dual-sine case had a significantly higher pitching moment peak than for the simple sinusoidal pitching motion. The lift coefficients vary at α=12° on the upstroke, where the 5/rev motion causes the upward motion to momentarily become much slower. The increase in the lift and in the pitching moment for the dual-sine case has the same cause as seen for the EDI-M109. The two lift coefficients are nearly identical at α=15°, and from this point, the time to separation is the same, as shown in Fig. 2.31, although the angle is different due to the higher angular velocity around the separation angle. The effect on the pitching moment peak is large, with a 35% increase in the pitching moment peak for the dual sine

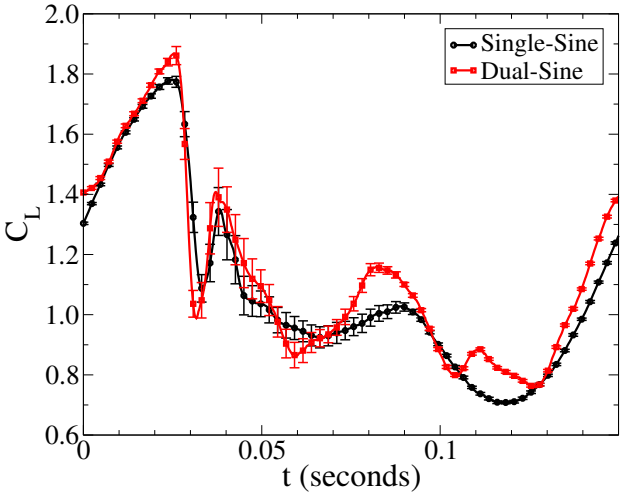

Figure 2.31: Lift coefficients plotted against time for the EDI-M112 airfoil with single and dual-sine pitching motion at M=0.3, Re=1.8×10^6, f=6.6 Hz, α=12±7°.

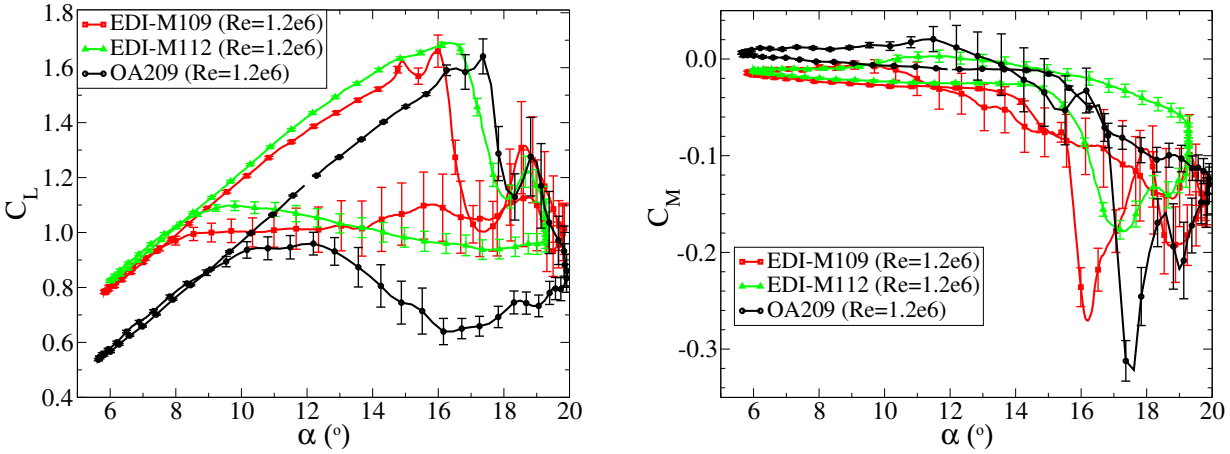

Figure 2.32: Comparison of lift (Left) and pitching moment coefficient (Right) for the EDI-M109, EDI-M112 and OA209 airfoils at M=0.31, Re=1.2×10^6, f=5.7 Hz, α=13±7°.

case over the simple sinusoidal motion.

2.2.6 Comparison of the airfoils

A comparison of the dynamic properties of the airfoils provides a different suggestion about how far along the rotor the transition from the EDI-M109 to the EDI-M112 should be made than if the purely static polar data is used. From a purely static perspective, the thicker 12% airfoil will be better at lower Mach numbers, but the thinner 9% airfoil will be better at higher Mach numbers. Figure 2.32 shows a comparison between the EDI-M109, EDI-M112 and the OA209 airfoil [23] measured at M=0.3 in the DNW-TWG [38]. The OA209 airfoil data was sampled at 128 points per period, in contrast to 1024 points per period for the EDI airfoils. The OA209 model was not measured at the high dynamic pressures used with the EDI airfoils, so the EDI airfoils were tested for one point which has been extensively investigated by the DLR as the DS2 test case [34, 103].

At M=0.3 the EDI-M109 has a significant improvement in mean lift and a reduction in the pitching moment peak, when compared to the OA209 at this test point, as shown in Fig. 2.32. The advantage of the EDI-M112 over the OA209 is larger at this test point, with the pitching moment peak halved, and the lift increased over the EDI-M109. The change when the boundary layer transition reaches the leading edge and the slope of the lift curve reduces is visible in a divergence of the lift curves of the EDI-M109 and EDI-M112 during the upstroke. At α=10° the lift of both the EDI-M109 and EDI-M112 airfoils has the same gradient and both airfoils have transition moving upstream on the top surface. At α=14° the lift of both airfoils has the same gradient and both airfoils have transition at the leading edge. Between these points, the transition on the EDI-M109 reaches the leading edge at around α=11° and for the EDI-M112 the transition reaches the leading edge at around α=12°. The increased cycle-to-cycle variation in the flow after stall (leading to increased vibration) is up to twice as large for the OA209 as for the EDI-M112, and 3.5 times as large for the EDI-M109 as for the EDI-M112.

At M=0.4 the advantage of the EDI-M112 over the EDI-M109 increases, as shown in Fig. 2.33, since the EDI-M112 has a soft trailing edge stall with a relatively small pitching moment peak, where the EDI-M109 has a leading edge stall with a pitching moment peak nearly as big as that found for the OA209, which unfortunately was only tested at a much lower Reynolds number. For this case the lift curves in the upstroke are parallel and the boundary layer transition reaches the leading edge for both cases at around α=11°.

In Table 2.2, the absolute value of $\frac{abs(X_{M112}-X_{M109})}{abs(X_{M112})}$ indicates how similar the airfoils are, and the sign indicates which airfoil has a better value for that comparison, with positive numbers indicating

Table 2.2: Comparison of the EDI-M109 and EDI-M112 for dynamic stall test cases at Re/M=6×10^6.

α	$\alpha_{\pm}$	f	Comparison $\pm\frac{abs(X_{M112}-X_{M109})}{abs(X_{M112})}$				
(°)	(°)	(Hz)	$\frac{\overline{C_L}}{\overline{C_D}}$	C_{L_p}	C_{D_p}	C_{M_p}	D
Comparison at M=0.3							
8	4	6.6	0.34	0.02	1.56	0.04	-0.11
8	5	6.6	0.40	0.03	1.64	0.04	-0.22
8	6	6.6	0.62	0.02	3.54	3.28	0.73
8	7	6.6	0.60	0.01	3.69	1.86	0.43
10	4	6.6	0.65	0.03	4.09	3.46	1.27
10	5	6.6	0.59	0.02	2.58	1.44	1.33
10	6	6.6	0.57	0.00	1.54	0.88	0.60
10	7	6.6	0.54	0.02	1.08	0.61	0.33
12	4	6.6	0.55	0.01	1.23	0.73	1.42
12	5	6.6	0.53	0.01	0.98	0.55	0.82
12	6	6.6	0.50	0.04	0.77	0.41	0.45
12	7	6.6	0.47	0.05	0.55	0.27	0.29
Comparison at M=0.4							
8	4	6.6	0.48	0.05	1.54	0.00	-0.30
8	5	6.6	0.64	0.07	3.29	2.28	0.64
8	6	6.6	0.53	0.09	0.92	0.16	-0.50
8	7	6.6	0.56	0.07	1.18	0.54	-0.25
10	4	6.6	0.52	0.09	0.47	-0.02	3.00
10	5	6.6	0.53	0.07	0.61	0.16	0.29
10	6	6.6	0.53	0.07	0.77	0.33	0.17
10	7	6.6	0.51	0.07	0.78	0.44	0.00
12	4	6.6	0.49	0.08	0.37	0.09	0.87
12	5	6.6	0.49	0.07	0.49	0.18	0.47
12	6	6.6	0.47	0.08	0.52	0.22	0.23
12	7	6.6	0.44	0.07	0.26	0.08	0.20
Comparison at M=0.5							
8	4	6.6	0.43	0.07	1.01	1.82	-0.64
8	5	6.6	0.42	0.07	0.57	0.28	-0.44
8	6	6.6	0.39	0.06	0.32	-0.10	-0.31
8	7	6.6	0.34	0.06	0.12	-0.22	0.00
10	4	6.6	0.40	0.08	0.28	-0.02	-0.41
10	5	6.6	0.36	0.07	0.13	-0.20	-0.13
10	6	6.6	0.31	0.07	0.10	-0.13	-0.09
10	7	6.6	0.26	0.07	0.04	-0.16	0.05
12	4	6.6	0.32	0.08	0.00	-0.20	-0.19
12	5	6.6	0.27	0.08	0.02	-0.15	-0.10
12	6	6.6	0.24	0.07	0.06	-0.05	0.03
12	7	6.6	0.22	0.07	0.07	0.01	0.10

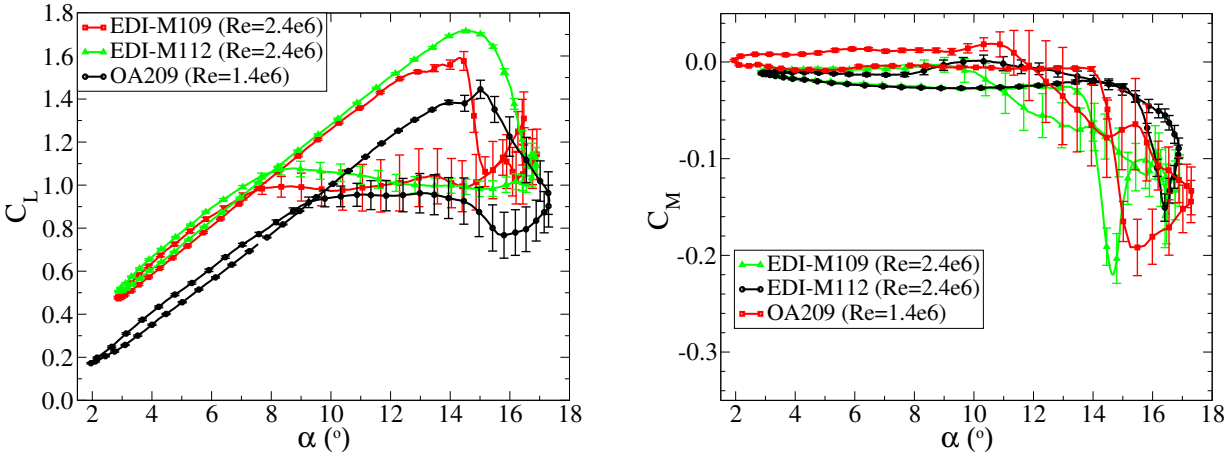

Figure 2.33: Comparison of lift (Left) and pitching moment coefficient (Right) for the EDI-M109 and EDI-M112 at Re=2.4×10^6 and the OA209 at M=0.4, Re=1.2×10^6 (OA209), with f=5.7 Hz, α=10±7°.

that the EDI-M112 was better. It can be seen that the EDI-M112 has a lower pitching moment peak than the EDI-M109 for dynamic stall conditions at M=0.3 and M=0.4 and has a significantly higher (34-64%) mean glide ratio (as computed by the pressure taps) over a pitching cycle. The peak in the pitching moment is smaller for the EDI-M112 than the EDI-M109 for M=0.3 and M=0.4 and the peaks in lift and drag coefficient are better (lift peak is increased, drag peak is reduced). The EDI-M112 always has positive aerodynamic damping, and the damping is mostly higher than for the EDI-M09. The EDI-M109 has slightly negative aerodynamic damping at M=0.3 and M=0.4 for the test cases α=10±4° and α=12±4°. The higher modes (2/rev-6/rev) had damping too small for significance, except when dual-sine motion was used, and an increase in the 5/rev damping was noted. At M=0.5 the decision is not so clear, as the performance ($\overline{C_L}/\overline{C_D}$) is still 22-43% better for the EDI-M112, but the dynamic stall peak (C_{M_p}) in the pitching moment is up to 22% stronger for the EDI-M112. Both airfoils have positive aerodynamic damping at M=0.5.

Based on this information, the pitching moment peak data suggests that the crossover point for the airfoil change between EDI-112 and EDI-M109 should be at between M=0.4 and M=0.5 on the retreating blade at maximum aircraft speed. The $\overline{C_L}/\overline{C_D}$ performance data suggests that the crossover should be at above M=0.5. Both of these indications may be different to the suggestion based on static airfoil polars.

2.2.7 Damping-criterion

It has been posited by Liiva [69] that there is a correlation between low aerodynamic damping for high-frequency, low amplitude oscillations and poor unsteady aerodynamic performance, and Klein et al. [59] suggest that these test cases indicate airfoils which will have a problem with higher order excitation of the blade. These low-amplitude cases would be particularly interesting for the airfoil design phase, because they potentially give a simple guideline to exclude a particular airfoil. A large number of these test cases were measured at $M \in$[0.3, 0.4, 0.5] and Re/M=6×10^6 and these are listed in Fig. 2.34. Liiva's original experiments used excitation at a frequency corresponding to 6/rev, which would be 39.6 Hz for the EDI-series airfoils. Liiva used oscillation angles of $\alpha_\pm$=2.5° and $\alpha_\pm$=5.0° around the dynamic stall angle and noted changes in the damping coefficient of the model at higher angles of attack. These cases require $\overline{\alpha'}$=400°/sec and $\overline{\alpha'}$=800°/sec respectively, but due to the limitations of the pitching test rig used in this investigation, test points with $\overline{\alpha'} \leq$200°/second were considered. The frequency of the pitching motion was varied 13 Hz$\leq f \leq$45 Hz, the amplitude varied 0.5° $\leq \alpha_\pm \leq$2° and the mean angle of attack varied 12° $\leq \overline{\alpha} \leq$20°.

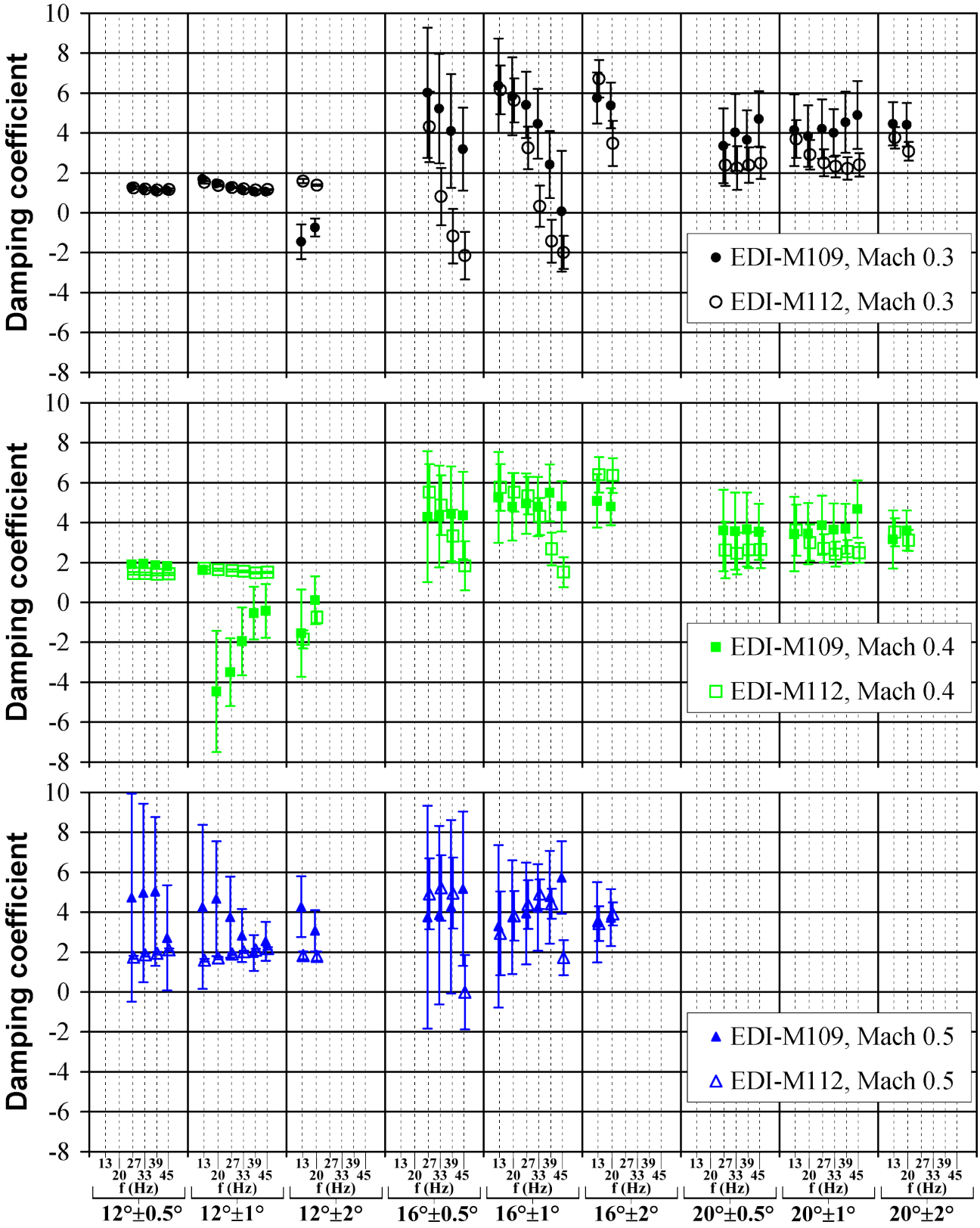

Figure 2.34: Overview of damping data at Re/M=6×10^6 for the analysis of the airfoil using the damping criterion.

A comparison of the aerodynamic damping for both new airfoils for all test cases is shown in Fig. 2.34. For M=0.3 at $\overline{\alpha}$=12°, the damping for both airfoils is positive and equal at $\alpha_{\pm}$=0.5° and $\alpha_{\pm}$=1.0°. At $\alpha_{\pm}$=2.0°, the damping for the EDI-M109 is suddenly negative, and clearly different than for the EDI-M112. At $\overline{\alpha}$=16°, the EDI-M112 generally has a slightly lower damping, and both airfoils show a strong tendency to lower damping at higher frequency. The cycle-to-cycle variation of the results is significantly increased compared to $\overline{\alpha}$=12°. At $\overline{\alpha}$=20°, the EDI-M112 again has a slightly lower damping than the EDI-M109, but the difference is small compared to the scatter of the data. No significant effect of amplitude or frequency on the damping is seen at $\overline{\alpha}$=20°. Since from the previous section the EDI-M112 has a lower pitching moment peak the EDI-M109 at M=0.3, then the only data which supports this conclusion is at α=12±2°. Otherwise, no strong correlation is seen to the dynamic stall data.

At M=0.4, the points at $\overline{\alpha}$=16° and $\overline{\alpha}$=20° mostly overlap in the damping, and there is no significant effect of amplitude or frequency on the damping. At $\overline{\alpha}$=12° the results of the two airfoils is only significantly different at α=12±1°, where the EDI-M109 shows negative damping with damping increasing with increasing frequency. Since the data at both α=12±0.5° and α=12±2° show exactly the opposite tendency, it is difficult to say that a general correlation can be found between lower damping for the EDI-M109 at this case and the higher pitching moment peaks for the EDI-M109 at M=0.4 seen in the previous section. At M=0.5, no data could be taken at the highest angle of attack due to excessive model loads. At $\overline{\alpha}$=16° the data overlaps within the scatter, and at $\overline{\alpha}$=12° the EDI-M112 has a slight trend to lower damping.

The hypothesis that low aerodynamic damping of an airfoil with low amplitude, high frequency pitching motion is an indicator of poor dynamic stall performance is not supported by the experimental data. In contrast, the results for the two airfoils mostly lie within the scatter of the results, or are even in the opposite direction to that expected. The difference may be low because both of these airfoils have good dynamic stall performance, and a comparison with an airfoil with poor dynamic stall performance may give other results. Additionally the higher amplitudes at 6/rev originally applied by Liiva may give different results. The damping-criterion, as applied here, is not sensitive enough to distinguish between similar airfoils of a single design family within a design process and select a better airfoil for dynamic performance.

2.2.8 Conclusion

A high-quality dynamic aerodynamic test of two new airfoils, the EDI-M109 and EDI-M112, was carried out in the DNW-TWG. The results are:

1. The amplitude and frequency of the pitching motion was varied, and the strength of dynamic stall increased with increasing amplitude and frequency.
2. The pitching moment peak size was found to have an approximately linear correlation to the normalised mean angular velocity $\overline{\alpha'_{norm}} = \frac{\omega^*}{M} \times (\alpha_{max} - \alpha_{C_{L_{max}},static})$. Test cases where the maximum angle of attack and oscillation frequency was preserved while varying amplitude had similar dynamic stall qualities.
3. A mixture of 1/rev and 5/rev pitching motion changed the angular velocity at the separation angle, resulting in EDI-M109 performance qualitatively similar to that for pure 1/rev pitching and quite different EDI-M112 performance.
4. The EDI-M112 has both better mean glide ratio and a smaller pitching moment peak than the EDI-M109 for dynamic stall conditions at M=0.3 and M=0.4. At M=0.5, the EDI-M112 still has a better mean glide ratio, but the pitching moment peak is higher than for the EDI-M109.
5. No positive correlation was found between the aerodynamic damping at high-frequency, low amplitude oscillations, and the severity of dynamic stall. The damping-criterion, as applied here, is not sensitive enough to distinguish between similar airfoils of a single design family within a design process and select a better airfoil for dynamic performance.

Chapter 3

3D effects on pitching airfoil experiments

The 3D effect on dynamic stall of a finite wing with one free end was extensively investigated by Lorber et al. [71, 72] using surface pressure transducers and hot-film anemometers. In [71], Lorber noted for an unswept wing that the "somewhat subjective" effect of the free end on the vortex positions was twofold: Firstly, the tip vortex reduced the local angle of attack at the wing tip, meaning that the initial separation took place at the wall and the separated region expanded outward toward the wing tip with increasing angle of attack. Secondly, the propagation rate of the dynamic stall vortex decreased toward the wing tip, as the stall vortex interacted with the tip vortex. Experiments by Piziali [92] also showed these effects with tufts.

Numerical investigations by Spentzos et al. [115] of a finite wing used a symmetry condition at the wind tunnel wall and also noted the faster propagation of the vortex with distance from the wing tip. Due to the symmetry condition, however, the path of the dynamic stall vortex was more normal to the onflow outside the direct effect of the tip vortex than noted in Lorber's experiments.

The 3D vortex dynamics have been verified by ONERA in [11] and [68] with an experimental and numerical investigation of an untwisted finite wing in dynamic stall. The finite wing was investigated using particle image velocimetry (PIV), tufts, laser Doppler velocimetry (LDV) and computational fluid dynamics (CFD) with the Spalart-Allmaras and k-ω turbulence models, see also [58].

For the nominally 2D airfoil, supported at both sides, there have been fewer investigations, since this arrangement is usually assumed to result in a reasonable approximation of 2D dynamic stall on the model centerline. As noted in the numerical investigation in section 3.2 [28], when both ends of a 3D airfoil in dynamic stall are free, then the initial stall is at the midline of the airfoil and the dynamic stall vortex will be curved, as also noted by Lorber [71]. In section 3.2 a significant difference to the 2D forces were seen for an aspect ratio of 8, which reduced to around the experimental uncertainly at an aspect ratio of 16. It was particularly noted that the peak lift and pitching moment are significantly reduced (by 19% and 23% respectively compared with 2D) for an aspect ratio of 8 due to the stall vortex curvature. Visbal et al.'s [119] experiments and computations for a low-aspect airfoil with two free ends at a very low Reynolds number of 10000 suggest that in this case the vortex rolls up as an arch vortex with clear tracks on the airfoil. However, it is not yet clear whether these results are relevant to dynamic stall at high Reynolds number.

Dynamic stall computations on the pitching EDI-M109 and EDI-M112 airfoils including the wind tunnel environment were performed by Klein et al. [60] to compare with experiments in the German-Dutch wind-tunnel association's transonic wind tunnel Göttingen (DNW-TWG). It was shown that the lift and pitching moment peak overshoot seen in 2D computations in comparison with experiment was reduced in 3D computations.

3.1 Effect of wall connection [1]

The accuracy of static wind tunnel data is improved by the application of wind-tunnel wall corrections, including classical circulation and blockage corrections [20]. When a multipart wind-tunnel correction for static testing is used (for example, correcting blockage, sidewall effects, and model deformation), assessing the relative correctness of the different parts is difficult. For constant cross-section wind tunnels, the primary interference is the increase in Mach number due to the blockage, which increases the uncorrected lift gradient [16, 111]. Adaptive-wall wind tunnels, which minimise the interference velocity at the top and bottom wall and compensate for the model blockage, have primarily sidewall interference, which causes a lift gradient reduction [41, 82, 103].

When a two-dimensional airfoil model is mounted between rigid wind tunnel sidewalls, a combination of a horseshoe vortex at the airfoil leading edge, thinning of the sidewall boundary layer, and a corner separation is expected. The effect of this sidewall interaction has been found to vary widely between wind tunnels [100], and with the increasing accuracy in the measurement of physical angle of attack, it is now possible to show that the sidewall interference has a considerable effect on the lift at the airfoil center section, and currently is the largest systematic error in measurement accuracy for many low Mach number test configurations in an adaptive wall test section. The corner separation effect is well known, for example for wing-body joins or airfoil-wall joins, and a separated region is formed at the intersection of the airfoil and wall, as in Figure 3.1.

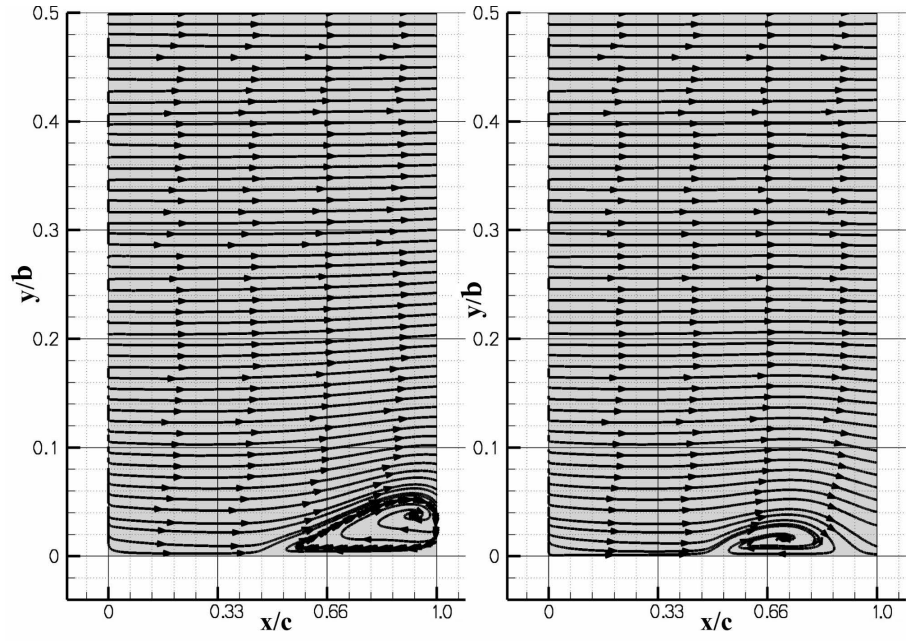

Figure 3.1: Corner separations for an NLR7301 airfoil in the DNW-TWG at α=0°. Flow is from left to right, and the wind tunnel wall is at y/b=0. Left: Suction side Right: Pressure side. [35]

A considerable improvement in static and dynamic testing accuracy is required to further improve computational fluid dynamics (CFD) models. This requires new approaches because many correction methods (for example, see Murthy [86]), do not achieve the accuracy required. Accuracy can be increased when multiple test campaigns of the same model are used in different wind tunnels [78], but this cannot be the standard approach. Analytical corrections for the sidewall effect in adaptive-wall test facilities can correct the lift slope for steady or unsteady measurements, but the experimental

[1] Text and illustrations in this section are taken from [27]: Gardner, A.D., Richter, K., "Effect of the model-sidewall connection for a static airfoil experiment", *Journal of Aircraft*, Vol. 50, No. 2, pp. 677-680, March-April 2013. DOI: 10.2514/1.C03201

Figure 3.2: EDI-M109 airfoil model in the TWG test section with the wake rake visible. Photograph from upstream of the model.

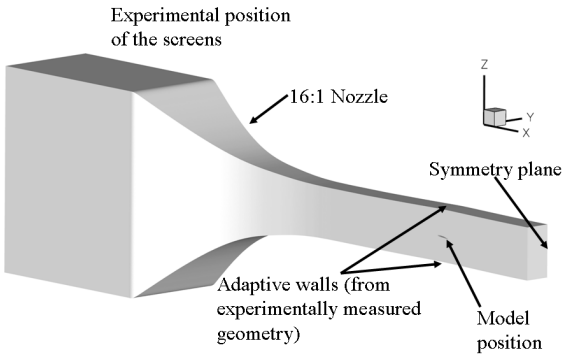

Figure 3.3: Computational domain of the TWG wind tunnel nozzle, test section and airfoil model.

pitching rate of the airfoil will be underestimated, causing a reduction in dynamic stall strength [19]. A number of recent results [61, 90] have shown significant improvement in the comparison between CFD modeling and experimental pressure distributions from the airfoil centerline, when the full three-dimensional wind-tunnel geometry is modeled rather than only a two-dimensional case enclosed by a far-field boundary condition, but this approach does not directly provide insights into how the wall interference can be reduced. For dynamic testing, the way forward appears to be to understand and reduce the wind-tunnel interference in the original measured data, reducing the reliance on corrections.

Experiments [30], described further in section 2.2, measured the effect of the corner separation on the helicopter rotor blade airfoil EDI-M109 with relative thickness 9% chord at static angle of attack using a row of static-pressure taps on the suction side of the airfoil surface at a constant 90% chord, in a line running normal to the wind-tunnel sidewall. These were connected with long tubes to a static-pressure measurement system.

Figure 3.2 shows the carbon-fiber model with a chord length c=0.3 m and a breadth b=0.997 m mounted in the 1 m x 1 m adaptive wall test section of the Transonic Wind Tunnel Göttingen (DNW-TWG). The adaptive test section has flexible top and bottom walls, which can be adapted to minimise the interference velocities at the wall at the mean angle of attack of the model. The model was mounted horizontally in the test section, and there are two mounting options available. In the first arrangement, investigated here using only CFD, the airfoil is longer than the width of the test section, and extends through the wind-tunnel wall. The gap between wall and model is sealed using wall inserts specially machined for each airfoil, and the angle of attack is changed by rotating a round insert in the sidewall (see Richter and Rosemann [104] for an example). In the second arrangement, investigated here using both experiments and CFD, the airfoil is shorter than the width of the test section, and is driven with round drive-shafts extending through the sidewalls, attached to the model at 25% c. A gap of 1.5 mm (0.5% c) remains between the model ends and the wind-tunnel walls, and this is not further sealed. This is a common mounting method for dynamic stall testing, also used by other groups [56, 77, 125]. The model was fitted with 48 Kulite unsteady pressure sensors (type XCQ-093) on the centerline, from which the pressure lift, pressure drag, and pitching moment were computed during static measurements and dynamic stall. The angle of attack was measured using four high-frequency laser range finders on beams attached to each end of the model.

The pressures measured were compared with Reynolds-averaged Navier-Stokes (RANS) computations of the test section and model. Figure 3.3 shows the computational domain, which starts in the settling chamber downstream of the screens to reduce large-scale turbulence. The flow is then

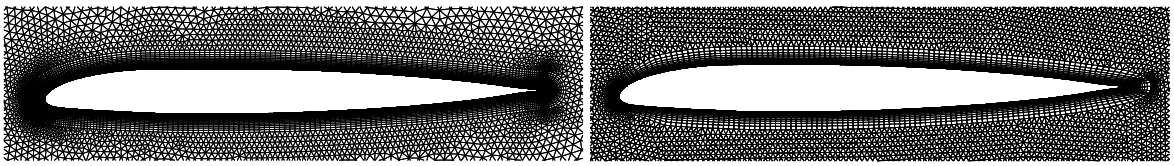

Figure 3.4: Comparison between the 2D grid (Left) and the 3D grid on the symmetry plane (Right), with grid mapped onto an OA209 airfoil.

accelerated by a 16:1 contraction area nozzle into the test section. The shape of the adaptive walls was the experimentally measured contour from the experiments, as was the angle of attack of the model. The domain is bounded by a symmetry plane on the midline of the wind tunnel. The domain was discretised using a hybrid grid with 28 prism layers with $y^+ \leq 1.0$ on the surfaces and tetrahedra in the field using the Centaur^{TM}unstructured grid generator. The surface of the airfoil was discretised with cells of approximately 1% chord, reducing to 0.07% chord at the leading and trailing edges. In each case, the grid had approximately 10 million points. To generate reference far-field computations, two-dimensional grids were generated with 28 prism layers and cells of 1% on the airfoil, reducing to 0.03% on the leading and trailing edges. A comparison between the two-dimensional and three-dimensional grids is shown in Fig 3.4. The domain was computed using the DLR-TAU unstructured solver [39] in RANS mode with all walls set to be fully turbulent using the Spalart-Allmaras turbulence model [114]. All computations were for Re/M=6×10^6.

The selection of the domain was verified by the comparison between experimental and numerical wall boundary-layer profiles. The thickness of the boundary layer on the test section wall was measured by a pitot probe at the model position at Mach 0.8, and the comparison with CFD shows that the shape of the boundary layer is adequately close to the experimental shape (Fig. 3.5), and that the velocity profile is significantly different from the flat-plate boundary layer profile, due to the acceleration by the nozzle.

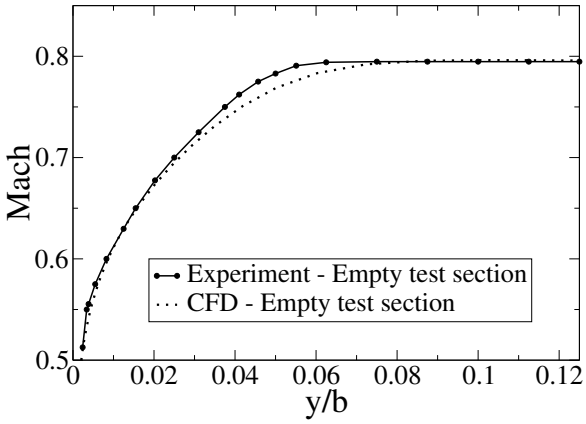

Figure 3.5: Comparison between experimental and numerical boundary layer profiles on the side-wall of the empty DNW-TWG adaptive test section at the model position. Comparison is at M=0.80, Re=13.6×10^6/m.

Two different geometries of the connection between the model and wall were computed, related to the two different airfoil mounting arrangements available in the DNW-TWG. First, the connection was modeled as a clean connection without gaps to match the experimental arrangement with the airfoil extending through the test section sidewalls. In this case, for M=0.3, Re=1.8×10^6 at constant α=7.06°, a corner separation is formed, which reduces the circulation on the airfoil centerline (Fig. 3.6a). In Fig. 3.6, the black points show the positions of the pressure sensors at 90% chord in the experiment and the flow in the corner between the airfoil and wind-tunnel wall is indicated by skin-friction streamlines. Second, the connection was modeled as a gap of 1.5 mm width, interrupted by the drive-shaft, similar to the experimental arrangement in which the airfoil is shorter than the test section width. In this case, for M=0.3, Re=1.8×10^6 at constant α=7.06°, the flow through the gap is significant and causes mass to move from the bottom to the top of the airfoil, reducing the separated region over that seen for the simple connection (Fig. 3.6b). Figure 3.7 shows a cut through the flow at constant x/c=0.90 for M=0.3, Re=1.8×10^6 at constant

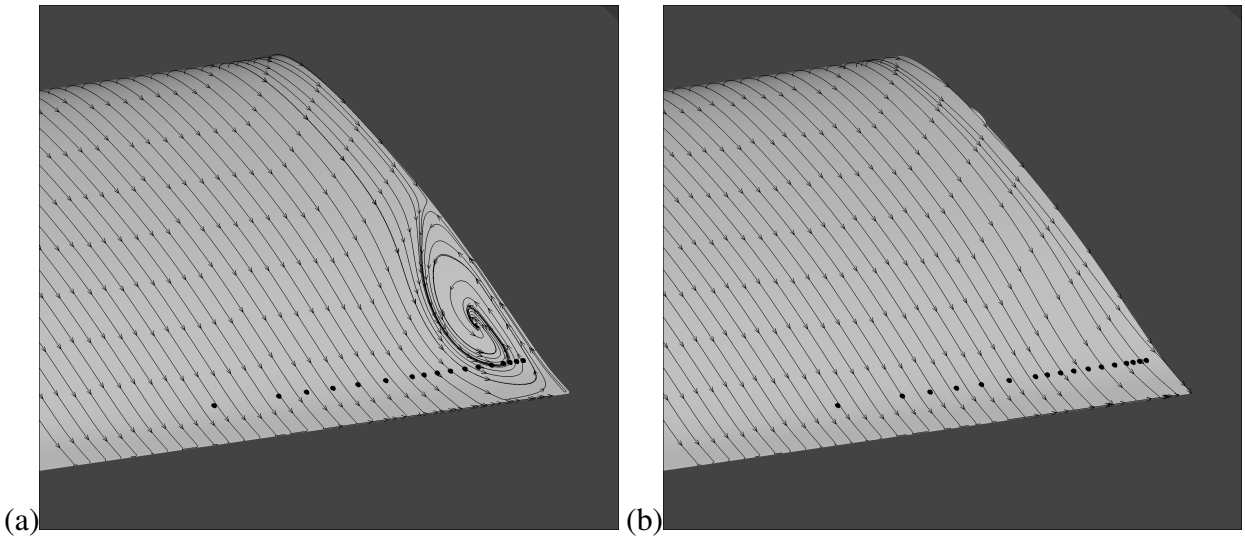

Figure 3.6: Skin-friction streamlines at M=0.3 showing: a) Separation for a gapless connection, and b) complex flow for a gap between the airfoil and wind-tunnel wall.

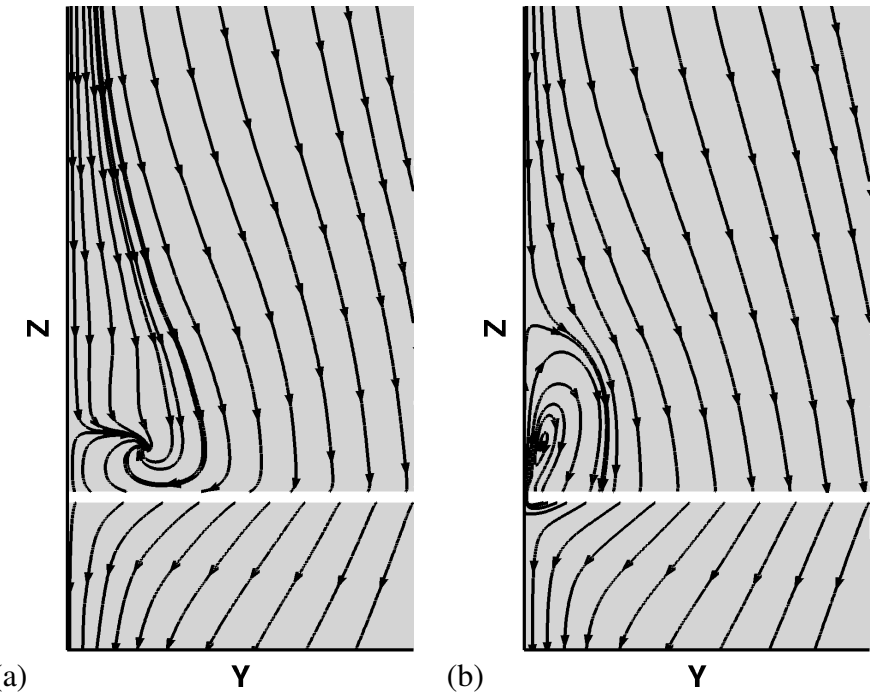

Figure 3.7: Flow streamlines in a y-z plane at M=0.3 showing: a) Separation for a gapless connection, and b) mass addition for a gap between the airfoil and wind-tunnel wall.

α=7.06°, showing how the mass addition due to the gap between model and wall gives a similar displacement to the separation for the gapless connection.

Figure 3.8a shows a comparison between experimental and CFD pressure coefficients at x/c=0.90 on the suction side of the airfoil, for a point in the linear part of the lift polar for M=0.3 and Re=1.8×10^6. For both the experiment and CFD, the physical, uncorrected angle of attack of α=7.06° is used. It can be clearly seen that the experiments (with a gap between model and wall) follow the numerical results for the gap between airfoil and wall, rather than the gapless connection. As seen in Fig. 3.8b, both of the three-dimensional CFD results match the C_P distribution on the model centerline well, except in the suction peak, despite the significant differences in the flow topology at the wall. The error in the uncorrected lift in the two-dimensional computation was 7.3% compared

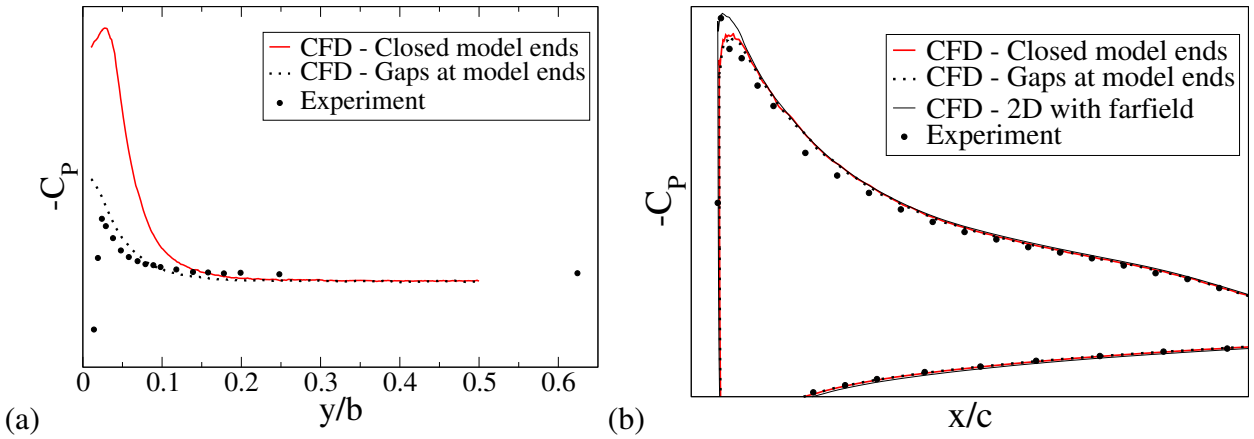

Figure 3.8: Comparison between experiment and CFD for M=0.3, Re=1.8×10^6 at constant α=7.06°: (a) Pressure distribution on the suction side at x/c=0.90, (b) Pressure distribution at the model centerline.

with the experiment, and this reduced to 2.8% and 2.3% error compared with the experiment for the three-dimensional computations with a gapless connection and with a gap between model and wall, respectively. The improved agreement in lift can be seen in the small movement of the pressure coefficient closer to the experimental values over the whole length of the airfoil, which has a significant integral effect in the lift compared with the two-dimensional computation. The two-dimensional computation reproduced the experimental suction peak better, and the three-dimensional computations would have shown a 0.4% increase in the error compared with the experiment if the suction peak were the same as the two-dimensional case. This is a small change compared with the difference between the two-dimensional and three-dimensional computations.

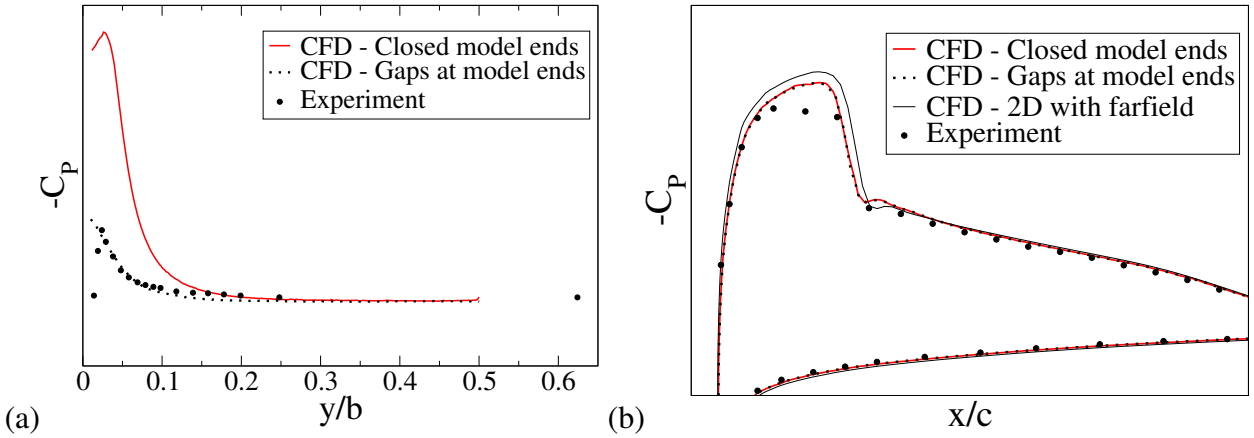

Figure 3.9: Comparison between experiment and CFD for M=0.6, Re=3.6×10^6 at constant α=4.65°: (a) Pressure distribution on the suction side at x/c=0.90, (b) Pressure distribution at the model centerline.

At M=0.6, Re=3.6×10^6 and α=4.65° the comparison of the static pressure coefficients at x/c=0.90 on the suction side of the airfoil for the geometry (Fig. 3.9a) again show that the CFD using the 1.5 mm gap between model and wall match the experimentally measured pressures (also with a gap), whereas the CFD results using the direct connection are quite different from the experimental data. A corner flow is produced similar to that seen in Fig. 3.6 for Mach 0.3. The error in uncorrected lift reduces from 10.4% for the two-dimensional computations to 4.5% and 4.1% error for the three-dimensional computations with a gapless connection and with a gap between model and wall, respectively. At

M=0.6, both methods of computing the wall connection also give similar pressures on the model centerline (Fig. 3.9b), although here the laminar flow before the shock in the experiment and the turbulent flow in the CFD lead to different minimum pressures in the supersonic flow region. The improvement in agreement of the pressure distribution for three-dimensional simulations over two-dimensional simulations is much more clearly visible at Mach 0.6 than at Mach 0.3, with a significant improvement in the pressure level for the supersonic region.

It has been shown that the gap between an airfoil and the wind-tunnel wall can have a significant effect on the three-dimensional near-wall flow topology for a static angle of attack, without being detectable at the midline of an airfoil model. Understanding the interaction between model and sidewall is necessary to improve the accuracy of wind-tunnel airfoil testing and reduce the sidewall interference. The measurements in this technical note show that care must be exercised, when comparing full three-dimensional modeling of the wind tunnel and model with experiments, not to draw the wrong conclusion from a good fit between computation and experiment. In this case, a good agreement can be gained by CFD modeling that produces the wrong flow topology, but the agreement will not necessarily remain good if the test conditions change.

3.2 Effect of finite wing length and rotation [2]

In a flying helicopter, the 2D aerodynamics of the rotor blade airfoil are supplemented by 3D effects due to the rotation, finite span of the blade and blade sweep. Additionally, effects of flying into the wake of a preceding blade may cause considerably more complex aerodynamics [95]. An example of 3D effects on the rotor can be made by comparing 2D computations with finite-span computations, and then rotating that same geometry.

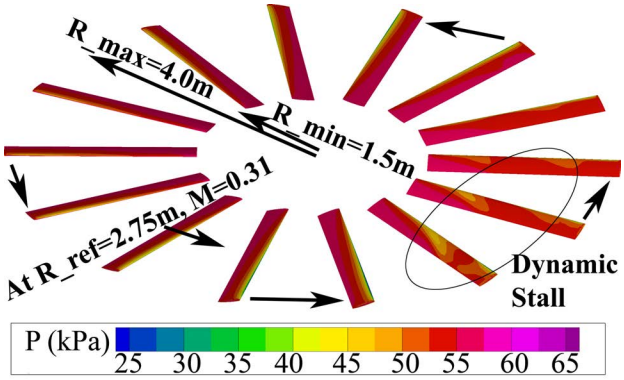

Figure 3.10: The rotating single blade rotor (SBR) test case. The blade is shown at steps of 26° with pressure contours. The blade is in dynamic stall in the lower right quadrant.

The data from finite-span non-rotating experiments is used as a predictive tool when corrected and used as input into a correctly calibrated comprehensive code (for example, [52]) where dynamic stall models estimate the dynamic stall performance of the airfoils. This method treats the relationship between 2D stall and 3D stall as a black box, and only the differences in blade loading are estimated. However it has been shown that for rotors in forward flight, a comprehensive code can be as good as a full 3D simulation [70]. However, comprehensive analysis can not be relied upon to produce accurate results when flight conditions with dynamic stall are considered. To improve future rotorcraft it is necessary to understand how 3D dynamic stall differs from 2D dynamic stall, so that the value of the existing 2D dynamic stall experimental data can be maximised. A full consideration of the dynamic stall problem on rotors must include 3D factors including time-varying effects of blade sweep and Mach number, or rotational effects including Mach number gradient and cross flow which significantly impact the performance of a rotor blade built from 2D airfoil sections.

It has been shown that 3D stall in a rotating system [14, 124] exhibits the development of far more complex structures than nominally 2D stall measured on finite-span models [84], and that for fully 3D rotor blade configurations, strong, localised surface jets appear, and the fine structure of the flow changes. A small 3D perturbation of the 2D test case, such as that from wind tunnel side-wall interference, can lead to significantly different dynamic stall results than expected from 2D computations [61]. Computations of a full helicopter configuration in dynamic stall have been demonstrated by several groups [96, 106], with fully grid-converged and time-step converged computations of the 3D flow. This approach yields quite acceptable prediction of the air-loads, but the results produced from dynamic stall in forward flight are complex to analyse. For a fully resolved URANS computation, the flow structures from each of the blade tips over multiple cycles, from blade-vortex interaction, from the blade roots and hub wake, from the separated area of reverse flow on the rotor as well as dynamic stall vortices, combine with the blade wakes to produce a complex 3D flow where the relation between cause and effect is extremely difficult to understand, and where the number of grid points make the postprocessing technically challenging. For this reason, only a few authors have adequately investigated the 3D aerodynamics in addition to the integral forces on the aircraft, for example, [94]. Simpler approaches predict that the appearance of a strong radial vortex along the blade delays the stall of the inboard sections [15]. Generally, the flow on the rotating blade will be angled toward the blade tip, when compared with the onflow, due both to the pressure gradient caused by the varying Mach number over the blade, and due to the centrifugal forces of the rotation. In order to separate

[2] Text and illustrations in this section are taken from [28]: Gardner, A.D., Richter, K., "Influence of rotation on dynamic stall", *Journal of the American Helicopter Society*, Volume 58, Number 3, 2013. DOI: 10.4050/JAHS.58.032001

different 3D effects, a numerical test case was designed in the long-term DLR-ONERA cooperation on the SImulation and COntrol of dynamic Stall (SIMCOS). This test case provides a unified geometry allowing individual quantification of each of the aerodynamic effects encountered when moving from 2D to 3D.

The SIMCOS Single Blade Rotor (SBR) test case uses an untwisted rotor blade of constant OA209 cross-section [23] and simple cut-off ends, as shown in Fig. 3.10. The OA209 is a tabbed helicopter airfoil developed in the 1960s by ONERA and Aerospatiale, and still flying on several helicopters. The minimum radius of the SBR is R_{min}=1.5 m, the maximum radius is R_{max}=4.0 m, and the chord length is c=0.3 m. A strong 1/rev pitching motion is used on the rotating blade to cause dynamic stall in hover, with the blade propagating into undisturbed flow at all times (with no downwash from previous blades/cycles). This configuration is compared with a forward translation of the blade using a constant velocity and the same strong pitching motion. In this way, the effect of rotation on the blade is investigated separately of other effects.

The blade movement is set such that at the reference plane, defined to be at the mid-point between root and tip of the blade at R_{ref}=2.75 m, the flow matches the SIMCOS DS2 test condition: M=0.31, Re=1.15e6, α=13°+7°sin(ωt), ω*=2πfc/v$_\infty$=0.1. For the DS2 test condition there is experimental data from the DNW-TWG [38, 73] and numerical investigations [34, 103]. Richter et al. [103] investigated the mesh densities and time step sizes necessary to get good CFD results for the OA209 airfoil, and test cases were identified where fully turbulent computations with a one-equation turbulence model gave good estimates of the airfoil performance when compared with experiment, including the test case used here.

3.2.1 Computational approach

Computations using the DLR-TAU code [39, 109] are presented for an untwisted rotor blade of constant OA209 cross-section. Unsteady Reynolds-averaged Navier-Stokes (URANS) computations were undertaken with DLR-TAU. The node-based finite-volume solver was used on a hybrid unstructured grid, generated using the Centaur^{TM}unstructured grid generator, consisting of four grid blocks communicating by the grid overset (chimera) method, as shown in Fig. 3.11. The solver used a central second order spatial discretisation scheme, and the chimera interpolation was also second order in space. First a 2D, unstructured grid was generated according to the guidelines of Richter et al. [103] for 2D grid convergence on this airfoil geometry and test condition. Each 2D plane is a hybrid grid of 130,000 points with 60 cells in the boundary layer and cell refinement to 1% chord in the separated wake region. Surface cells are 1% chord, reducing to 0.05% at the leading and trailing edges (See Table 3.1).

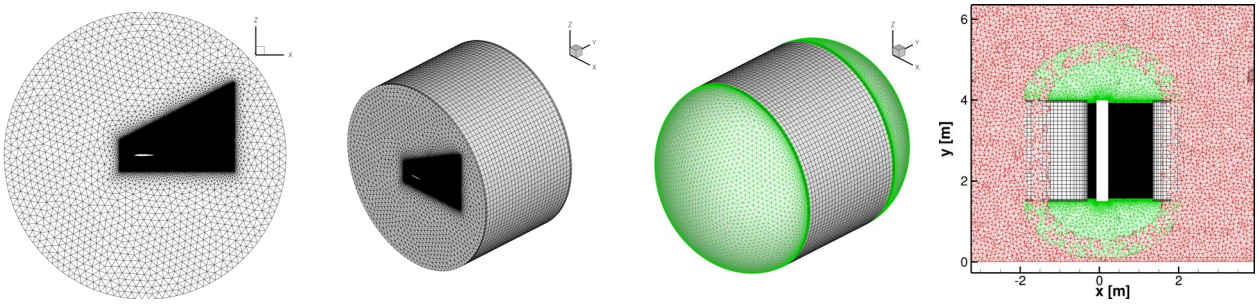

Figure 3.11: The grid along the Single Blade Rotor (SBR). From left to right: 2D grid; Stacked blade grid; Including blade tip grids; Embedded in background grid.

Table 3.1: Data for the 2D and 3D grids.

Option	Value
Rectangular boundary layer (BL) grid - 2D slices	
Structured layers in the BL	60
Cell stretching in the BL	1.1
y^+	$\leq$1.0
Surface grid - 2D slices	
Maximum cell size	1% chord
Leading edge cell size	0.05% chord
Trailing edge cell size	0.05% chord
Triangular grid - 2D slices	
Cell size in source near model	1% chord
Cell size at chimera interface	30% chord
Grid data for the 3D grids	
Grid nodes in one 2D plane	135000
2D stacks along blade	16 or 32
Stack spacing along blade L_S	80% c or 31% c
Nodes in blade grid	2.16 or 4.32 Million
Nodes in blade tip grids	360000
Nodes in background	460000
Total nodes	3.34 or 5.50 Million

Table 3.2: List of configurations.

Case	2D-CFD	Long blade	Short 80% c	Short 31% c
L_S	-	80% chord	80% chord	31% chord
R_{min}	-	0.5 m	1.5 m	1.5 m
R_{max}	-	5.5 m	4.0 m	4.0 m
R_{ref}	-	2.75 m	2.75 m	2.75 m
ω^*	0.1	0.1	0.1	0.1
$\overline{\alpha}$	13°	13°	13°	13°
$\alpha_{\pm}$	7°	7°	7°	7°

This 2D grid was then stacked along the blade at either a fine grid spacing of L_S=31% chord or a coarse grid spacing of L_S=80% chord. All configurations tested are listed in Table 3.2. The blade grid had an odd number of planes, so that a plane was at the midpoint of the blade (the reference plane at R_{ref}=2.75 m). Flow separation can only be computed at radial locations with a grid plane.

The grid was very fine in the flow direction and coarse in the radial direction. Due to the coarseness of the grid spacing in the blade radial direction, fine 3D structures were not modeled, and the computation behaved as a set of coupled 2D computations. This was a desired effect, since the complexity of a full-3D computation would have made the results much more difficult to analyse, and it was hoped that this grid configuration would simplify the process. The computation is grid-converged in the chord-direction, but not grid-converged in the radial direction, and the sensitivity to radial refinement is investigated for both the rotating and the non-rotating cases in the following sections.

The inner and outer tips of the resulting blade were meshed with tetrahedral grids, joined to the blade grid using the grid overset (chimera) method, as shown in Fig. 3.11. This combination of blade grids was then embedded in a hemispherical background grid, with a farfield condition set at all boundaries. In the rotating case, the hemispherical grid rotates with the blade around the rotation-axis, and the farfield boundary condition produces flow with velocity zero in the cabin frame, such that the blade always propagates into air without perturbations, as shown in Fig. 3.12. In the non-rotating case the farfield produces a M=0.31 onflow for the blade, and the blade again propagates into air without perturbations. The effective angle of attack of the blade at the mid-section is thus directly comparable in both the rotating and non-rotating cases, as the same grid and pitching motion are used, and the onflow at the midpoint is M=0.31 for both cases.

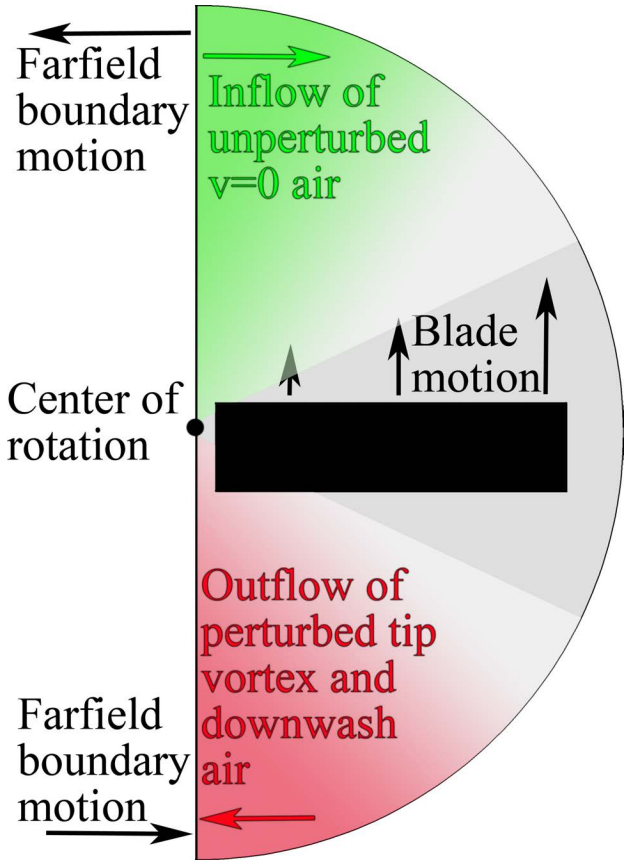

Figure 3.12: The computational domain of the Single Blade Rotor (SBR), showing how unperturbed flow is obtained for the rotating test cases.

The blade is pitched around the quarter-chord line, and this line also passed through the center of blade rotation at r=0 m. The plane of the hemispherical farfield grid is normal to the quarter-chord line, and placed at r=0 m. In addition to the normally spaced 2D stacks, there is a clustering of the 2D stacks at the blade ends at a stack spacing of L_S=16% chord, so that the tip effects will be isolated and the communication between the grid blocks will be correct.

All computations were fully turbulent, using the unmodified Spalart-Allmaras turbulence model [114], due to the good results obtained for this test case by previous investigators. A central scheme was used with the scalar dissipation method of Mavriplis [75]. A 2nd order Runge-Kutta time-stepping scheme was used, with no multigrid convergence acceleration and a CFL number of 1.8. Each cycle was computed with dual-time-stepping set to 1500 time-steps per pitching period, and 800 inner iterations were used to converge each time-step, following the guidelines of Richter et al. [103] for time-stepping convergence. Each computation was run for 2.5 pitching periods, and convergence between the cycles was noted after 1.5 pitching periods. Convergence of the computation was assumed when the lift and pitching moment for two consecutive cycles were within pre-defined tolerances, approximately equal to 1% of the value at the minimum angle of attack computed. Lift and pitching moment in this section are the pressure-parts of the forces only, and are computed in the 2D computation and at the midline of the 3D computations, by integration of the surface pressures. This simplifies the integration of extracted cuts and provides forces directly comparable to those measured in an experiment. The error in lift and pitching moment due to this simplification is significantly less than the convergence error.

3.2.2 Non-rotating test case

Cases without rotation were compared to investigate the effect of blade aspect ratio and radial grid density, as listed in Table 3.2. The short blade of 2.5 m length (aspect ratio 8.3) and grid spacing of L_S=31% chord was translated at M=0.31 without rotation into the oncoming flow. The sectional lift and pitching moment at the blade midline were compared with a 2D computation using the base 2D grid as in Fig. 3.11, with a 2D farfield boundary of 1000 chords radius added via a chimera interface, the same boundary radius as in the 3D test case. As seen in Fig. 3.13, the short blade with the grid density of L_S=31% chord has a decreased lift at the same angle of attack, and a reduced gradient on the lift curve in the attached flow. The lift peak for the finite-span blade is reduced by 19% compared to the 2D computation at the same conditions and the pitching moment peak is reduced by 23%.

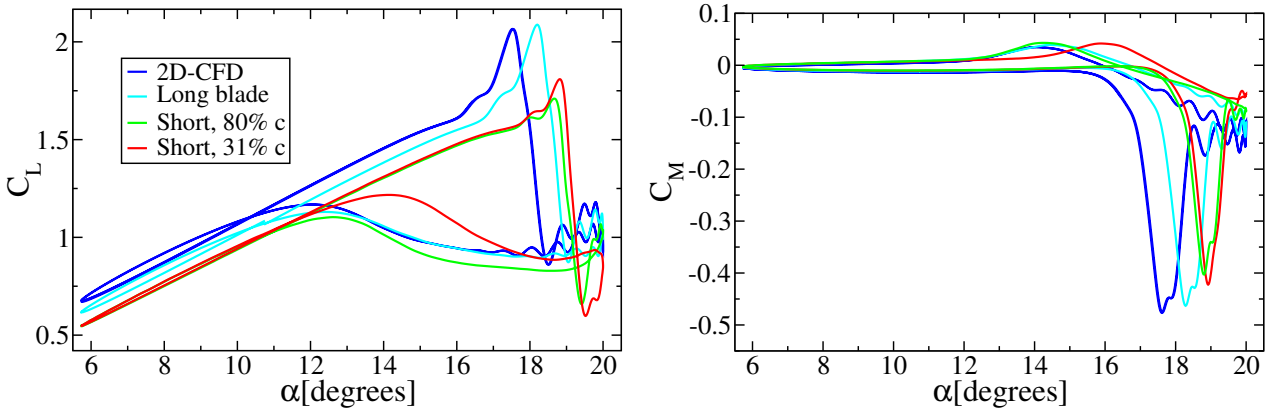

Figure 3.13: Comparison of lift (Left) and pitching moment coefficient (Right) between different blade lengths and spanwise grid densities for the non-rotating test case, including comparison to the 2D test case.

The radial grid spacing on the short blade was increased to a radial grid spacing of L_S=80% chord, to investigate the effect on grid density on the stall behaviour. The lift and pitching moment curves in Fig. 3.13 are essentially unchanged by the change in radial grid density except in the fully separated flow, showing that both radial spacings give a similar engineering approximation of the solution (although neither solution is grid-converged). The reduction in lift at the mid-span is due to the proximity of the blade ends, and as a comparison, a long blade (5.0 m, aspect ratio 16.7) with radial grid plane spacing of L_S=80% chord was also tested, matching the radial grid density of the coarser of the two shorter blades. Here the lift in the attached flow increases compared to the short blade, but remains less than the 2D computation and the slope of the lift in attached flow is also increased over the shorter blade. The pitching moment peak also lies between 2D and 3D test cases with the short blade, indicating that only the proximity of the blade ends, and not the grid density is responsible for the 3D effects observed. The spanwise location of initial separation in all three test cases is the model midline.

As noted by other authors [103], the overshoot in the lift at stall for the 2D computation with Spalart-Allmaras turbulence models is well known, but is not seen in finite-span experiments. The "lift overshoot" is the peak in lift, which starts for the 2D computation in Fig. 3.13 at α=16° and rises to C_L=2.07. Data from pitching airfoil experiments tends to have a significantly reduced peak and be approximately horizontal in this region. The overshoot was significantly reduced in the 3D case with an aspect ratio of 8.3, but was large for an aspect ratio of 16.7, indicating that the overshoot is numerically correct for the 2D case, but is reduced in 3D configurations with smaller aspect ratios. The change is probably due to the curvature of the dynamic stall vortex reducing the vortex

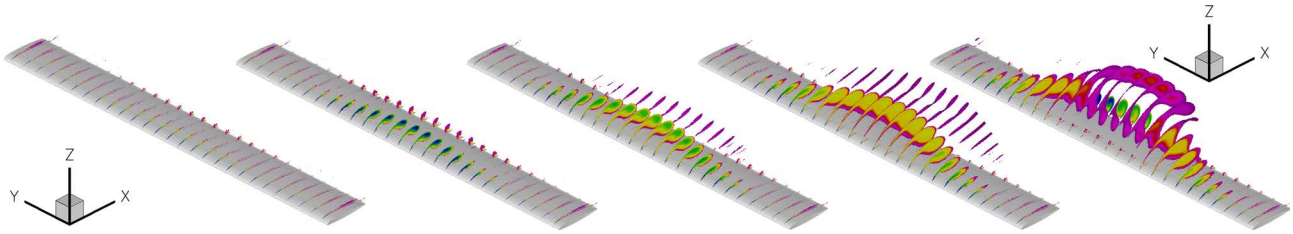

Figure 3.14: Separation on the non-rotating airfoil during the upstroke, as indicated by iso-contours of λ_2 vortex criterion [51]. From left to right: α=17.62°; α=18.25°; α=18.62°; α=18.95°; α=19.37°.

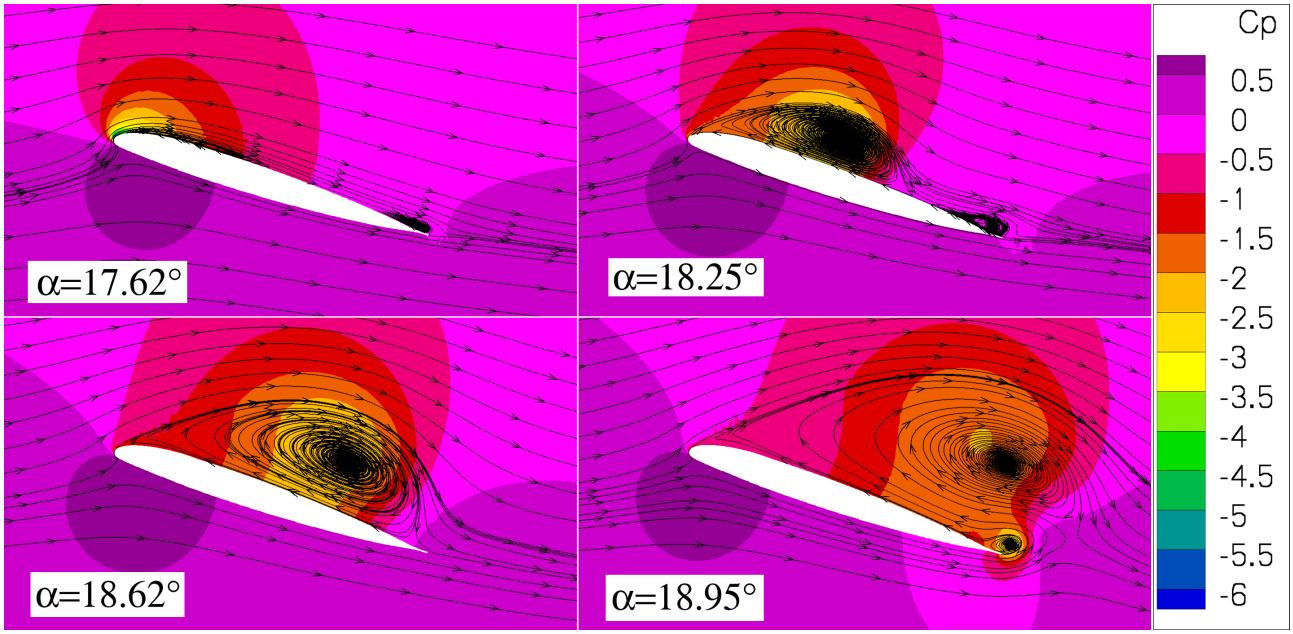

Figure 3.15: The separation process for the non-rotating configuration at the reference plane (R_{ref}=2.75 m) during the upstroke. Shown are contours of C_P and streamlines. Top left: α=17.62°; Top right: α=18.25°; Bottom left:α=18.62°; Bottom right: α=18.95°.

strength. The qualitative change in the form of the lift peak at stall with the switch to a 3D grid of the same streamwise point distribution is the same as seen between pitching airfoil experiments and 2D computations, and can help the further development of 2D turbulence models for dynamic stall computation.

Figure 3.14 illustrates the flow separation using contours of the λ_2 vortex criterion [51]. The contours are on the 2D planes along the blade and only the planes outside the chimera overlap are illustrated. In Fig. 3.14 the separation first appears at the midline of the non-rotating rotor blade at the trailing edge of the blade. This is followed by a leading edge separation at the midline, and the planes to the left and right of the midline separate in order after this. The planes in the middle are fully separated with vortices swimming off from the blade, while the separation nearer to the ends is just starting. Due to the different separation times of the leading edge, the main separation vortex is curved, at times at an angle greater than 45 degrees to the oncoming flow.

Figure 3.15 illustrates the separation process at the reference plane (R_{ref}=2.75 m), using C_P contours and volume streamlines. The separated flow starts with individual separations on the leading and trailing edges of the airfoil, which grow to meet near the middle of the airfoil. As the angle of attack increases, the leading edge vortex grows, finally suppressing the trailing edge vortex and covering the entire airfoil. The development of the primary dynamic stall vortex at this point ends as the dynamic stall vortex swims off from the airfoil, and a counter-rotating vortex begins to be formed from the

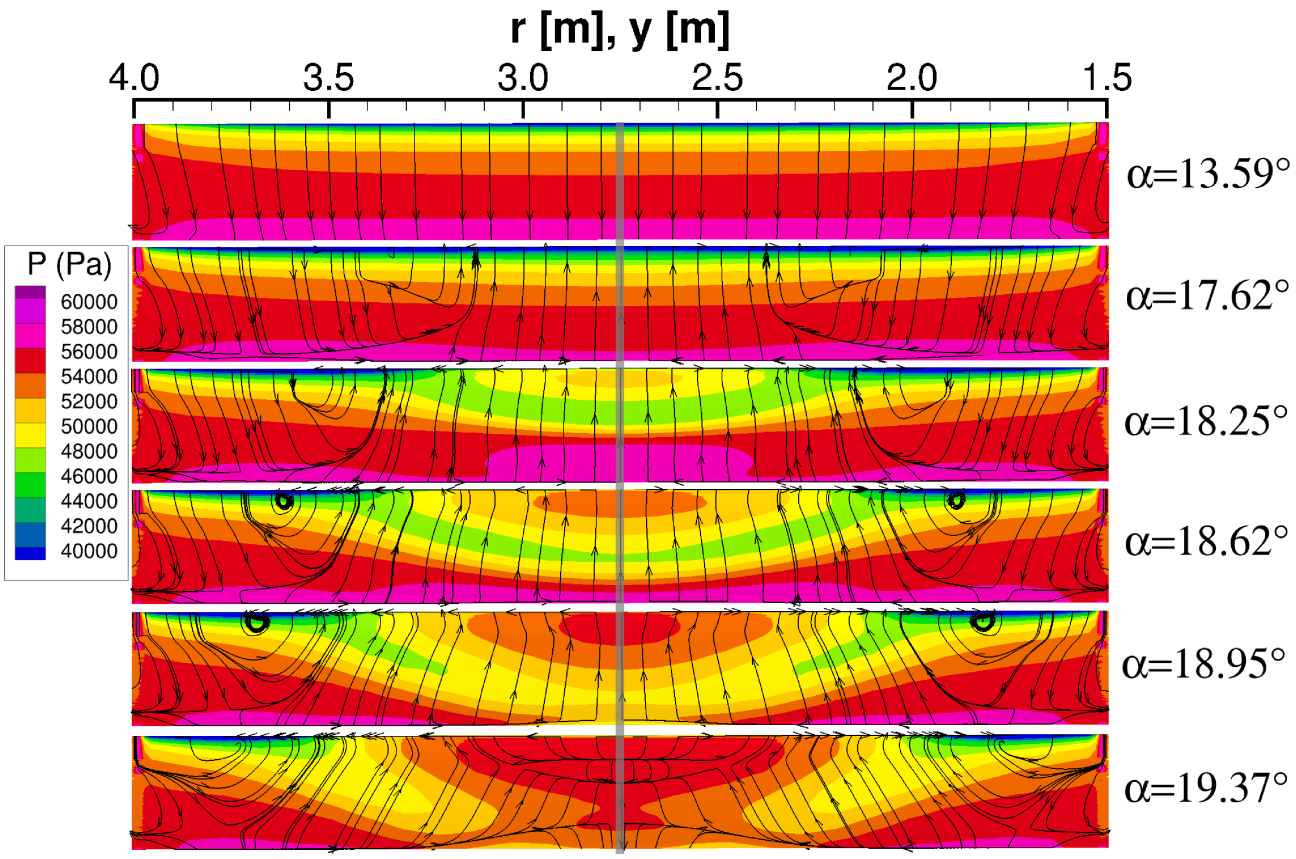

Figure 3.16: The separation process on the suction-side surface for the non-rotating configuration during the upstroke. Shown are contours of pressure and wall streamlines. The reference section (R_{ref}=2.75 m) is marked with the grey stripe. From top to bottom: α=13.59°; α=17.62°; α=18.25°; α=18.62°; α=18.95°; α=19.37°.

trailing edge of the airfoil. The generation of the stall vortices is qualitatively similar to the flow in the purely 2D computation (not shown), with a similar main stall vortex and counter-rotating vortex from the trailing edge. The purely 2D case separates at a lower angle of attack, and has a stronger main stall vortex than the 3D test case.

The flow on the suction side of the blade is illustrated with pressure contours and surface streamlines in Fig. 3.16, where the oncoming flow is from the top of the figure.

As seen at α=17.62°, the flow is separated and symmetric about a plane in the middle of the blade; towards the tip the flow is attached. At α=17.62°, in the center section of the blade, the flow is uniform and separated for a width of around two chord lengths. At increasing angles of attack, the region of separated flow widens, and the flow angle away from the centerline increases. The strong spanwise flow away from the blade midline in the 3D computation is probably the cause of the weaker stall vortex than in the 2D computation. The tip flow affects about one third of the blade on each side, meaning that a significantly 3D flow is generated.

Even in the attached flow in Fig. 3.16 at α=13.59°, the flow is significantly non-parallel and this is seen in the comparison of the spanwise surface pressure distributions at the quarter-chord position on the suction side in Fig. 3.17. Here the fine and coarse grids for the short blades always have the same pressure distribution. The non-rotating short blades have a much stronger pressure gradient towards the center than the non-rotating long blades, but the pressure at the centerline is the same for each grid density on the short blades, and for the long blade. As seen in Fig. 3.13, this pressure gradient affects the separation process, including reducing the height of the lift peak. However, the lift peak has a qualitatively similar shape, possibly because no net spanwise-flow is induced. The rotating blades, however, induce a strong spanwise flow toward the blade tip, as seen in the next section.

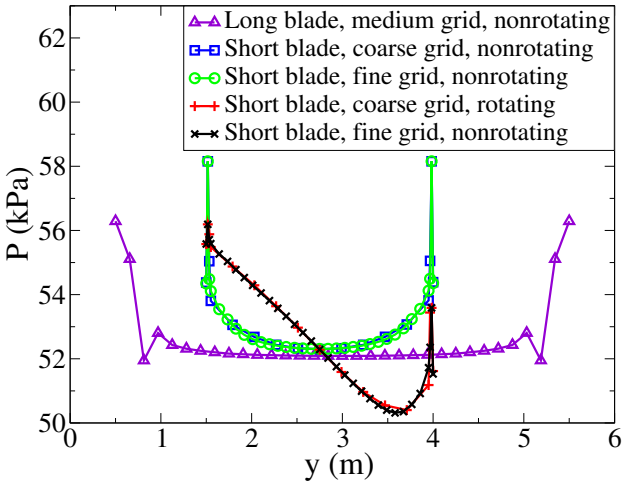

Figure 3.17: The local pressure distribution on the airfoil top at the 25% chord position, at α=13.59° just before stall for the different grids and rotating/non-rotating cases.

3.2.3 Rotating test case

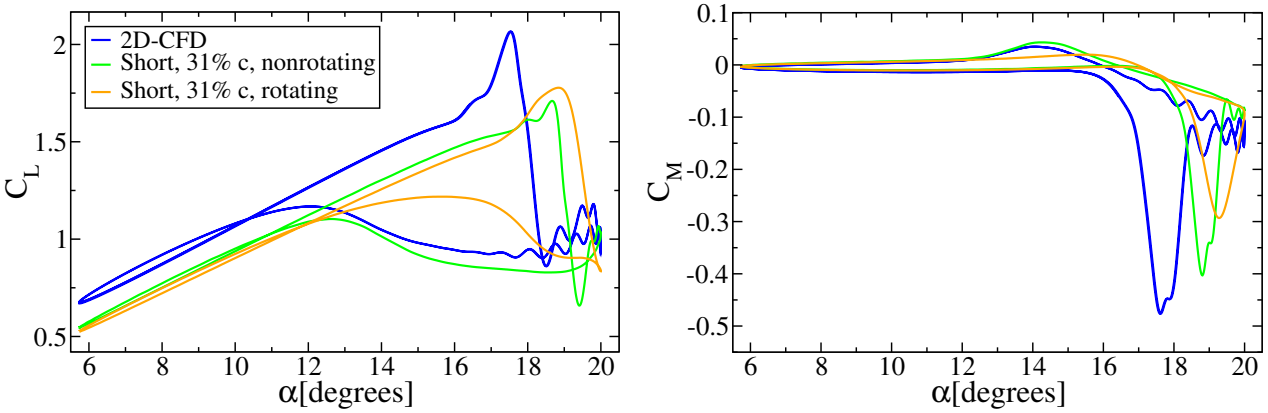

Figure 3.18: Comparison of lift (Left) and pitching moment coefficient (Right) between the rotating and non-rotating test cases for the SBR geometry.

Simulations of the short blade with grid spacing of L_S=31% chord were performed with rotation, and the results compared with the non-rotating case. In Fig. 3.18 it can be seen that the effect of rotation is to reduce the slope of the lift curve at the reference section, and to delay separation. The lift peak is increased, but the stall process takes longer, which is associated with a 25% reduction in the height of the pitching moment peak. The forces after stall and reattachment are changed significantly, with much earlier reattachment.

The difference in the flow separation process is illustrated in Fig. 3.19, and it can be seen that the separation starts further toward the blade tip than for the non-rotating case. The stall occurs first at r=3.32 m, and the stalled region expands inboard. The reference section at R_{ref}=2.75 m sees a delay of stall by about $\Delta\alpha$=1°, and a change in the flow on the airfoil at stall. In contrast to the non-rotating case, where the axis of the dynamic stall vortex is parallel to the blade at the midpoint, in the rotating

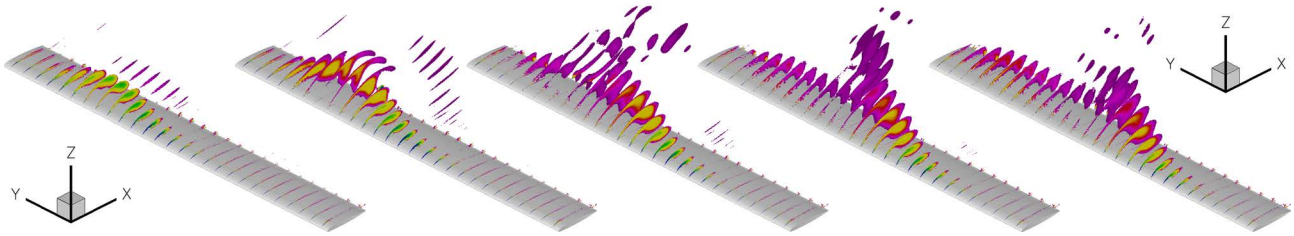

Figure 3.19: Separation on the rotating airfoil during the upstroke, as indicated by iso-contours of λ_2 vortex criterion [51]. Rotation is anticlockwise around a point to the right of the picture. From left to right: α=17.84°; α=18.44°; α=19.24°; α=19.59°; α=19.83°.

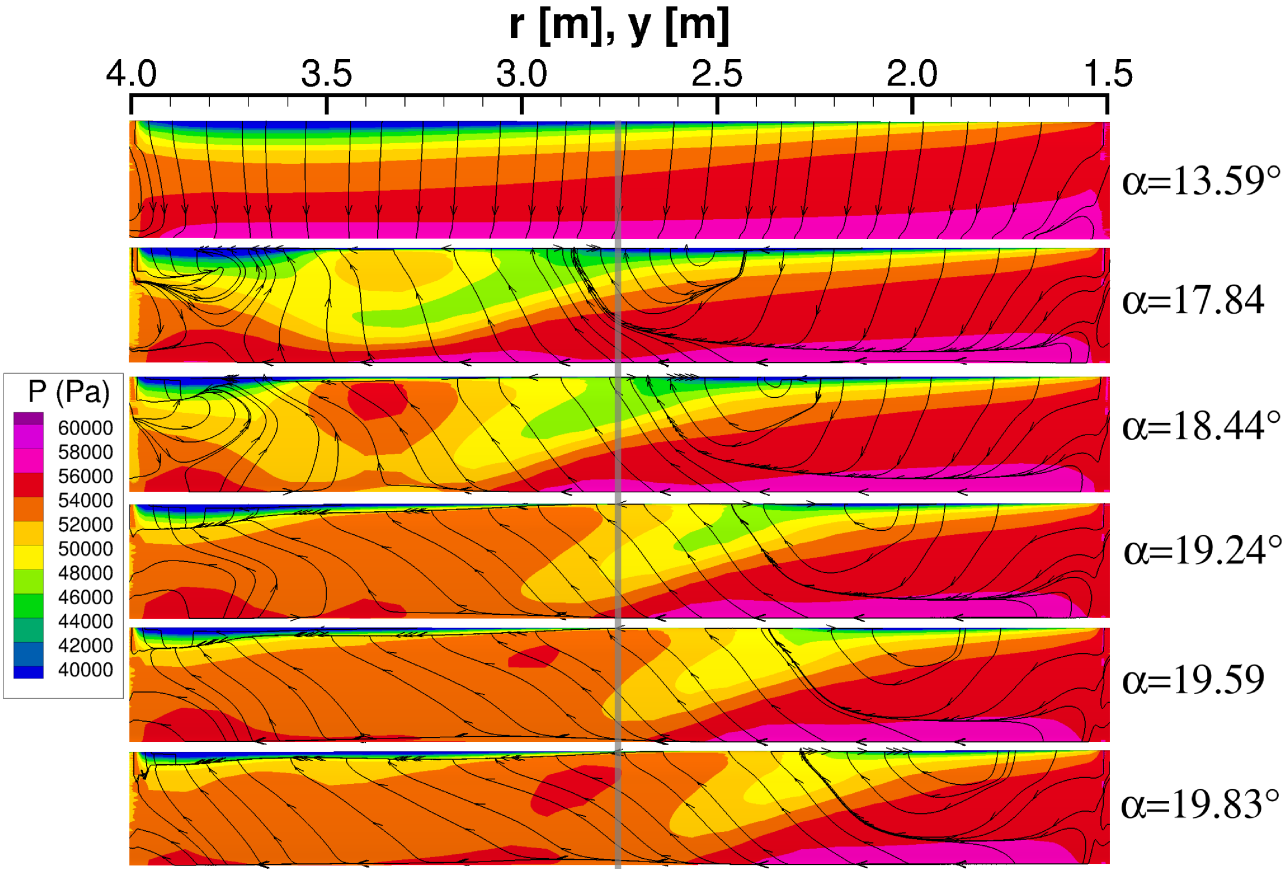

Figure 3.20: The separation process on the suction-side surface for the rotating configuration during the upstroke. Shown are contours of pressure and wall streamlines. Rotation is clockwise around r=0. The reference section (R_{ref}=2.75 m) is marked with the grey stripe. From top to bottom: α=13.59°; α=17.84°; α=18.44°; α=19.24°; α=19.59°; α=19.83°.

case the dynamic stall vortex is at an angle of 20-30° trailing the blade axis (depending on the section of vortex observed), leading to strong out-of-plane flow at the reference section.

The flow on the suction side of the blade is illustrated with pressure contours and surface streamlines in Fig. 3.20. Here it can be seen that at α=13.59°, where the flow is still fully attached, the flow has an angle in the direction of the blade tip. To evaluate the flow angle, flow velocities and pressures were extracted for α=13.59° along two spanwise lines outside the boundary layer on the suction and pressure sides near the quarter-chord line of the rotor blade. To simplify the extraction of the data, the lines were described by constant x/c=0.25 and z/c=±0.1. Data from these lines is in Fig. 3.21, and it can be seen that the flow is driven by a pressure gradient due to the varying Mach number, which is approximately linear with radial position, resulting in a net flow angle. The flow on the suction

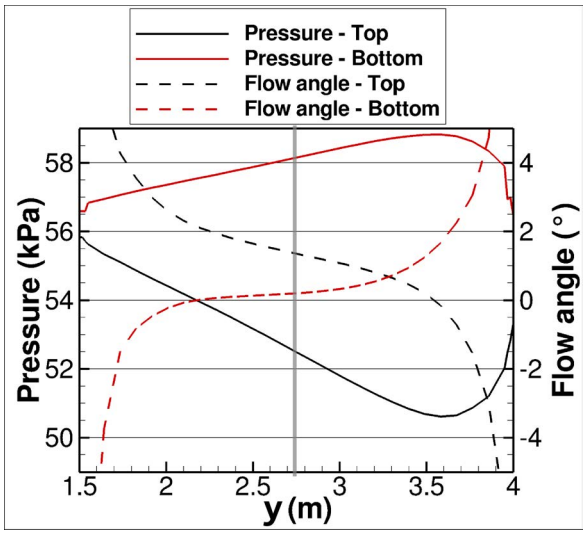

Figure 3.21: The flow angle and local pressure distribution along the lines x/c=0.25, z/c=±0.1, at α=13.59° just before stall for the rotating configuration. The reference section (R_{ref}=2.75 m) is marked with the grey stripe.

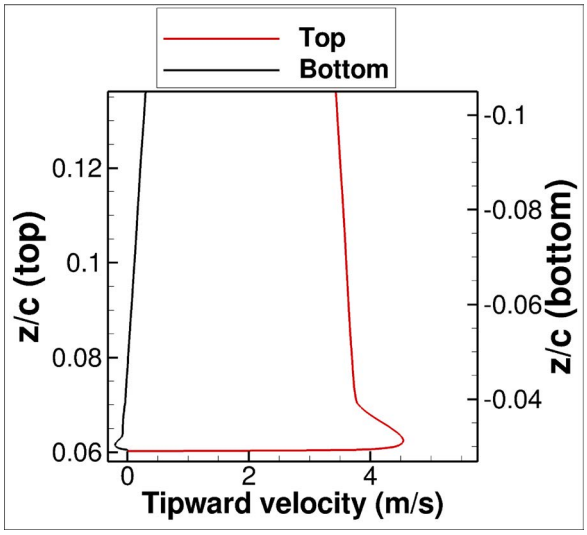

Figure 3.22: The tip-ward flow velocity along the line x/c=0.25, r=R_{ref}=2.75 m, at α=13.59° just before stall for the rotating configuration.

side of the airfoil is clearly driven by the decreasing pressure in the direction of the blade tip, and this results in positive flow angles (flow angles towards the tip), with a flow angle of 1.4° at the reference section at R_{ref}=2.75 m.

The situation on the pressure side of the airfoil is more difficult to explain, since the pressure gradient should result in a flow toward the root of the blade. Instead, the flow angle is slightly positive for most of the blade, with a flow angle of 0.2° at the reference section. The centrifugal force would tend to increase the angle, but even without this, the meeting of the flow from the suction side and the pressure side to form a shear layer at the trailing edge will cause an interaction between the flow angles of the two sides. The interaction will tend to cause the suction side flow to have less of an angle toward the tip, and the pressure side flow to have more of an angle toward the tip. The angle difference will also drive the formation of vortices with their axis in the flow direction which will form in the wake of the blade, as observed experimentally in [14]. This is probably the cause of the kink in the streamlines at around x/c=0.8 at α=13.59° in Fig. 3.20. The large flow angles near the ends in Fig. 3.21 appear to be caused by the tip vortices interacting with the surface flow.

It is not possible on the basis of these computations to definitively separate the centrifugal and shear-layer interaction effects, but an estimate of the relative strength of the centrifugal force can be made. The relative effects of the centrifugal and aerodynamic forces can be estimated by the Richardson number (Ri), defined as:

$$Ri = \frac{a h_{Ri}}{v_{Ri}^2}, \tag{3.1}$$

where $a = r\omega^2$ is the local acceleration, h_{Ri} is a reference length in the direction of the acceleration and v_{Ri} is the relevant aerodynamic reference velocity. For Ri <1.0 the aerodynamic forces are stronger and for Ri >1.0 the centrifugal forces are stronger. The centrifugal stresses in the rotor flow have an uneven effect on the flow. For the flow outside the boundary layer, reasonable estimates might be $v_{Ri} = r\omega$ (the local onflow velocity) and h_{Ri}=c, giving $Ri = c/r$, or Ri=0.11 at the reference section. This means that for the flow outside the boundary layer, the centrifugal forces can be regarded as a second order effect and disregarded for this analysis. For the flow in the boundary layer, h_{Ri} will be

the order of the boundary layer thickness or smaller, but the velocities in the boundary layer go to zero, meaning that the centrifugal force will dominate at the bottom of the boundary layer, switching at some point to flow dominated by aerodynamic forces at the top of the boundary layer. The flow velocity toward the rotor tip is shown on the top and bottom of the airfoil in Fig. 3.22 for a vertical cut through the flow at R_{ref}=2.75 m and x/c=0.25. The lines shown in Fig. 3.21 intersect these lines at z/c=0.03. Reference [14] noted fine structures caused by the proportionately higher centrifugal acceleration of the lower parts of the boundary layer compared to the higher parts, with the effect of boundary layer "jetting", and this can be seen in the velocity overshoot in the boundary layer, especially on the top of the airfoil. Due to the coarse grid in the spanwise direction, these gradients due to the centrifugal forces will not result in any fine structures in the CFD solution.

As seen in Fig. 3.20, at the point of initial separation at α=17.84°, a region of supersonic flow is present near the tip of the blade at around r=3.75 m. This is made visible on the surface by the shock-induced separation line seen in the surface streamlines. The supersonic flow is quite distinct from the location of initial separation at r=3.32 m, and the initial separation is shockless at Mach 0.36. The initial separation progresses both inboard and outboard with increasing angle of attack during the upstroke, until essentially the whole blade has separated flow. The parts of the blade with remaining attached flow are the inner end, which is affected by an inner tip vortex and the supersonic region upstream of the shock in the outer part of the blade. As the angle of attack increases, the supersonic region extends further toward the root, and the shock moves upstream on the airfoil. The end effects appear to be much more localised on the blade than for the non-rotating case (as seen in Fig. 3.16).

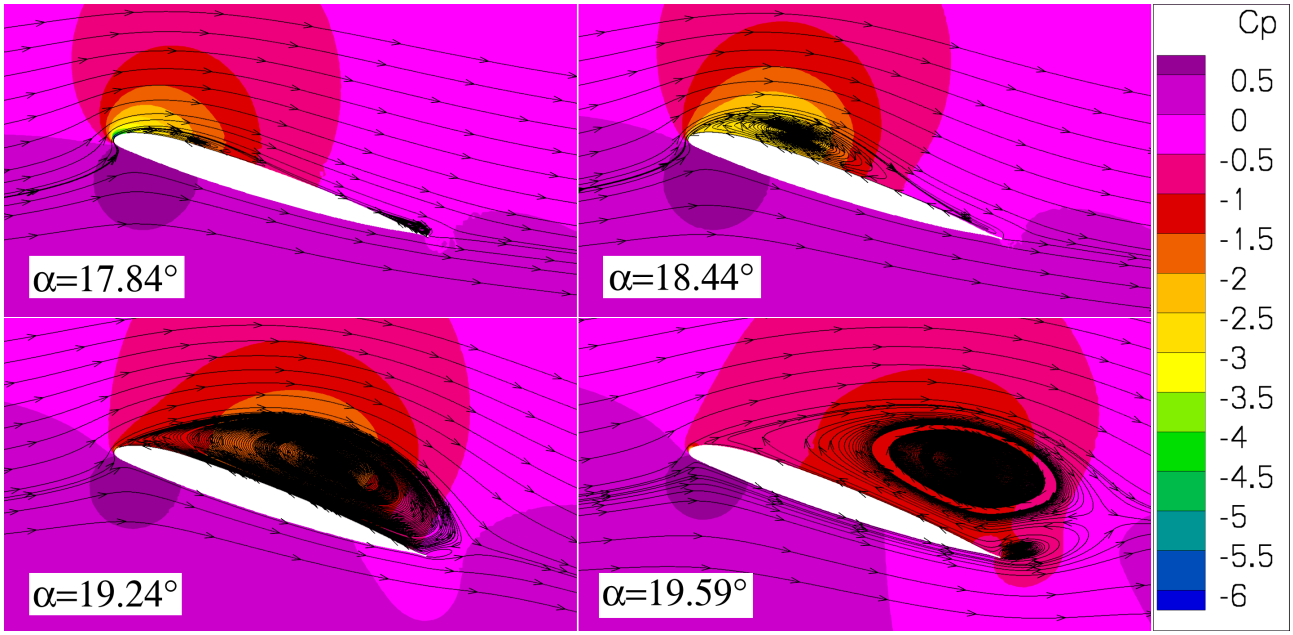

Figure 3.23: The separation process for the rotating configuration at the r=2.75 m plane on the rotor blade during the upstroke. Shown are contours of C_P and streamlines. Top left: α=17.84°; Top right: α=18.44°; Bottom left: α=19.24°; Bottom right: α=19.59°.

At the reference section, the topology of the separated flow is similar to that for the non-rotating case. As seen in Fig. 3.23, the separated regions on the leading and trailing edge appear not to touch for the rotating case (α=17.84°), but as seen in Fig. 3.20, the two separations do actually touch on the surface. As the leading edge separation grows (α=18.44°), the trailing edge separation is fully suppressed at a much earlier stage of the separation than for the non-rotating case. When the leading edge vortex covers the whole of the airfoil (α=19.24°), the height of the separated region is smaller than for the non-rotating case (see Fig. 3.15 at α=18.62°). This reduced height continues until after

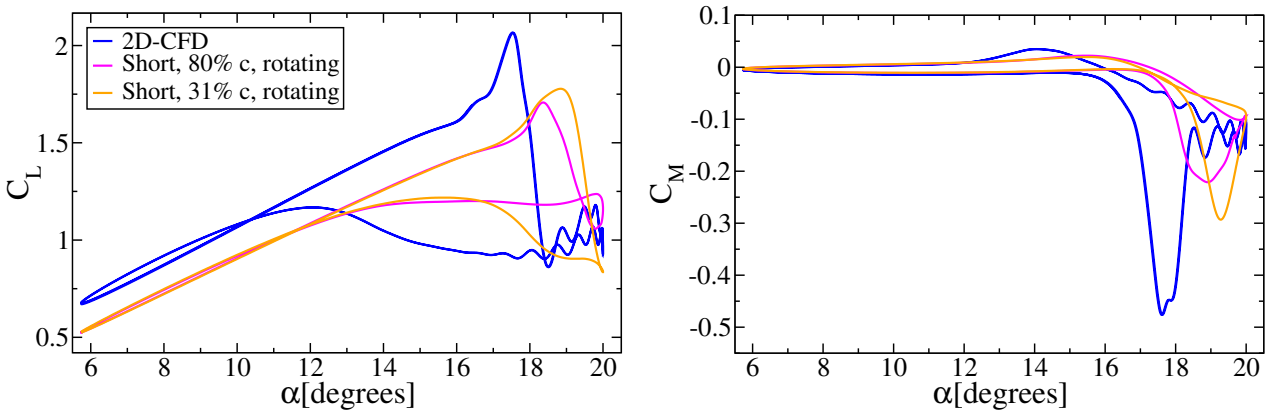

Figure 3.24: Comparison of lift (Left) and pitching moment coefficient (Right) between different grid densities for the rotating test case.

the dynamic stall vortex starts to swim off from the airfoil (α=19.59°), and the counter-rotating vortex from the trailing edge is also stronger than for the non-rotating case.

The separation behaviour is different for the case with the coarser grid with spacing L_S=80% chord, as seen Fig. 3.24. This is caused by a motion of the initial separation point by 50% chord towards the blade tip, since separation is computed only on the grid planes, which are now further apart. The propagation of the separation point inboard is also slower in the case with the coarser grid, leading to a greater vortex angle and a slower separation at the reference section. Thus for the rotating case, the grid density has an effect on the solution. Finer grids were not investigated in this test case due to limits of the computational power available, and since the resolution of 3D structures on the blade was not part of the approach selected for this investigation. This is an open topic for future work. The long blade was also tested for the rotating case, but in contrast to the shockless initial separation seen in the shorter blade, the dynamic stall on the longer blade was induced by a strong shock at the blade tip, and so the results are not directly comparable.

3.2.4 Discussion

The changes in the flow between the 2D computation and the 3D computation without rotation appear to be due to a combination of the effect of the finite blade affecting the circulation in the reference section and the 3D flow resulting from the varying separation time over the length of the blade. Figure 3.25 shows the pressure distributions at the midpoint of the blade at the point of maximum lift for the 2D and 3D non-rotating test cases. Despite the reduced lift in the 3D test case, the flow is qualitatively similar. The spatial distribution of the footprint of the vortex on the blade is similar between the two cases, and the main difference is that the strength of the vortex is reduced for the 3D case.

In both the 2D and 3D non-rotating test cases, the angle of attack for maximum pitching moment follows the angle of attack for maximum lift so closely that the pressure distribution is not significantly changed from that seen in Fig. 3.25. Thus these curves may also be taken to illustrate the point of maximum pitching moment. The maximum pitching moment occurs before the center of the dynamic stall vortex passes over the trailing edge of the airfoil. As the center approaches the trailing edge, where the moment arm is longest, the effect of the vortex on the pitching moment is weakened by the vertical movement of the vortex away from the surface and by the passage of some of the vortex footprint over the trailing edge. The movement of the vortex center away from the airfoil surface, is driven by the counter-rotating vortex, as seen in Fig. 3.15.

For the rotating case, the point of maximum lift and the point of maximum pitching moment are

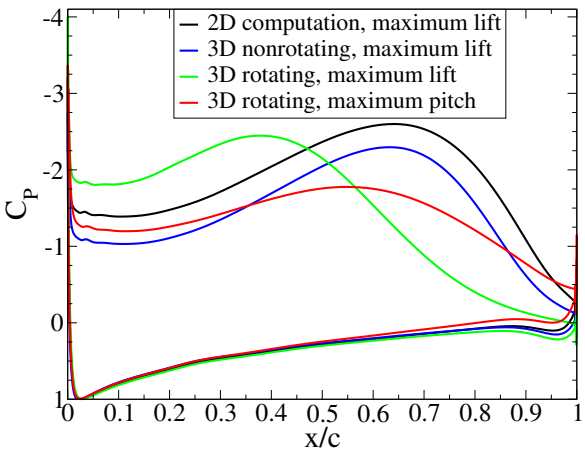

Figure 3.25: C_P distributions for maximum lift/maximum pitching moment at the reference section (R_{ref}=2.75 m) for: 2D test case at α=17.39°; Test cases with spacing L_S=31% chord: non-rotating test case at α=18.67° and rotating test case at α=18.84° and at α=19.28°.

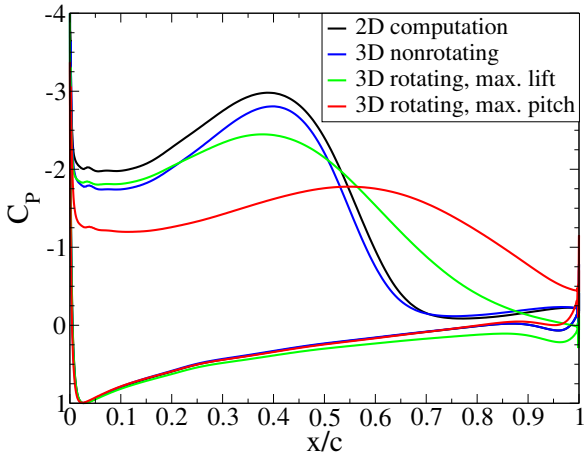

Figure 3.26: C_P distributions for a comparison of the young vortex strength and size at the reference section (R_{ref}=2.75 m) for: 2D test case at α=16.72°; Test cases with spacing L_S=31% chord: non-rotating test case at α=18.25° and rotating test case at α=18.84° and at α=19.28°.

more separated in time, such that they give different pressure distributions at the reference section, as seen in Fig. 3.25. At the point of maximum lift, the vortex is much further upstream than for either of the other test cases, and the minimum pressure due to the vortex lies between the other two test cases. It is to be expected, though, that the strength of the vortex reduces in all test cases as the vortex moves downstream. At the point of maximum pitching moment, the vortex position is similar to that seen for both the 2D and 3D non-rotating computations, but the strength of the vortex footprint on the airfoil is reduced for the 3D case. The vortex moves away from the airfoil earlier for the rotating case, due to a stronger counter-rotating vortex from the trailing edge than for the non-rotating case (Compare Figs. 3.15 and 3.23), and is reduced in strength in the rotating test case.

The pressure distributions are plotted for the young vortex in Fig. 3.26, such that for all cases the vortex core is at the position which gives maximum lift for the rotating test case. Here the difference in the vortex strength can be seen, and the 2D case has the strongest, and most localised vortex. The footprint of the vortex for the 3D non-rotating case is qualitatively similar to that seen for the 2D computation, but it is weaker. The footprint of the vortex for the rotating test case has a weaker peak than seen for the other two cases, and the footprint is much wider on the airfoil. The trailing edge of the airfoil has attached flow in the rotating test case, as seen from the trailing edge pressure coefficient in Fig. 3.26, whereas the 2D and 3D non-rotating test cases both have a trailing edge separation which has not yet been suppressed by the main stall vortex. The widening of the footprint in the 3D test case may be partially a simple effect of the angle of the vortex to the rotating blade, as seen in Fig. 3.20, but the reduction of the minimum C_P in the center of the vortex would not be explained by this simple effect. Instead the 3D separation in the rotating test case appears to have a related, but different mechanism to the simple boundary layer-driven process of the 2D or non-rotating cases, with the dynamic stall driven by the root-ward propagation of the dynamic stall vortex.

3.2.5 Conclusions

A new configuration consisting of an untwisted single rotor blade was computed to investigate the differences in dynamic stall behaviour due to the presence of rotation. The results show that the rotation causes the stall process to take longer at the reference section, with a less localised stall vortex footprint on the blade surface and a 25% reduction in the height of the pitching moment peak. For the rotating cases, the axis of the dynamic stall vortex is at an angle of 20-30° trailing the blade axis. In contrast, for the cases without rotation the dynamic stall vortex was parallel to the blade at the midsection, and then curved toward the leading edge at points nearer to the blade tips. The rotation of the blade caused radial flow for the attached flow during the upstroke, with a flow angle of 1.4° towards the blade tip on the suction side of the blade at the reference section, caused by the Mach-number driven pressure gradient. Despite a pressure gradient in the opposite direction, the flow on the pressure side at the reference section of the blade also had flow towards the blade tip, with a flow angle of 0.2°, and the cause of this could not be isolated between the centrifugal force and the entrainment due to the flow angle on the suction side of the blade.

The 3D grid computed without rotation had lower lift at the reference section than for a 2D computation, and the lift overshoot classically observed for Spalart-Allmaras turbulence models during 2D dynamic stall was significantly reduced for the 3D case with an aspect ratio of 8.3, but remained large for an aspect ratio of 16.7. The trailing edge separation is fully suppressed at a much earlier stage of the separation for the rotating case than for the non-rotating case. When the leading edge vortex covers the whole of the airfoil, the height of the separated region is smaller for the rotating case than for the non-rotating case. This reduced height continues until after the dynamic stall vortex starts to swim off from the airfoil, and the counter-rotating vortex from the trailing edge is also stronger for the rotating case than for the non-rotating case.

The 3D separation in rotation appears to have a related, but different mechanism to the process of the 2D or non-rotating cases, with the dynamic stall driven by the propagation of the dynamic stall vortex towards the blade root. The simplified test case proved to be a valuable aerodynamic analysis tool for investigating the complex separated flow seen in dynamic stall without over-complicating the solution.

3.3 3D flow on the model centerline [3]

A 2D model of the OA209 airfoil (Fig. 3.27) with chord length c=0.300 m and breadth b=0.997 m was produced for the 1 m x 1 m adaptive wall test section of the DNW-TWG wind tunnel. The model was constructed of two carbon-fiber half-shells, an aluminum spar and aluminum mounting feet, and was fitted with a line of 48 Kulite unsteady pressure transducers (type XCQ-093), at an angle of 10° to the oncoming flow, near the centerline. The standard aerodynamic coordinate system is used, with flow in the positive x-direction, airfoil breadth in the y-direction and the z-coordinate directed vertically upward. To investigate 3D flow effects, the wind tunnel model was also equipped with lines of pressure transducers at constant x/c=0.51 and x/c=0.80, starting at the centerline (y/c=0) and extending towards the wind tunnel side-wall (y/c=-1.67). The model was driven using drive shafts through the wind tunnel side-walls with a hydraulic pitching motion device, and the wind tunnel top and bottom walls were statically adapted to the mean angle of attack. As shown in Fig. 3.27, one side of the airfoil was coated with white pressure-sensitive paint (PSP) on the suction side and observed from a window in the sidewall (as indicated by the red arrow). The close-up of the coating in Fig. 3.28 also shows the flow control system, which could suppress dynamic stall by constant blowing through 42 porthole jets of 3 mm diameter positioned at x/c=0.10 with spacing y/c=0.067. Experiments with this flow control system are in chapter 4.

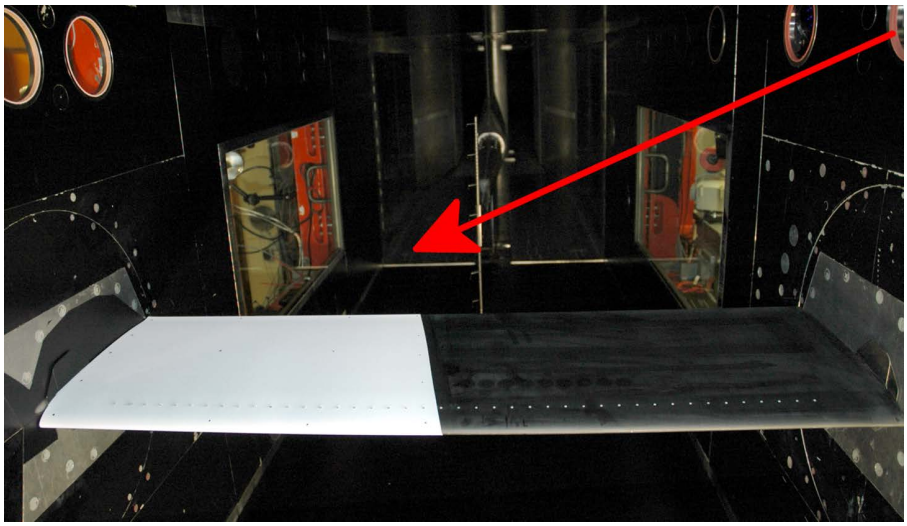

Figure 3.27: The OA209-FCD model installed in the DNW-TWG. The red arrow indicates the camera angle for PSP.

Figure 3.28: Closeup of the jets and edge of the PSP coating. The black markers are used to map the PSP result onto the 3D geometry of the model surface.

[3] Text and illustrations in this section are taken from [25]: Gardner, A. D., Klein, C., Sachs, W., Henne, U. , Mai, H., Richter, K., "Investigation of three-dimensional dynamic stall on an airfoil using fast response pressure sensitive paint", Experiments in Fluids, Volume 55, No. 9, 2014. DOI: 10.1007/s00348-014-1807-4

The data was recorded phase-locked at 1024 points per period for 160 periods and then phase averaged. On the diagrams in this section the points indicate the mean value and the scatter bars indicate the standard deviations. The instantaneous lift (C_L), drag (C_D) and pitching moment (C_M) are integrated from the line of pressure transducers near the centerline and also phase averaged. The pressure transducers were positioned so that for the set of possible pressure distributions computed with CFD (without blowing) the error in C_L, C_D and C_M is always less than 1% of the peak value.

3.3.1 High speed PSP measurements

High speed pressure sensitive paint is becoming increasingly applicable to helicopter applications, with several groups recently reporting encouraging results for a rotor in hover and forward flight [123], a high-speed rotating blade in hover [54], and for rotating blades and pitching airfoils [45]. The pressure-sensitive paint used in this experiment was developed by the DLR in cooperation with the Organic-Chemistry Institute of the University of Hohenheim, Germany. Several unsteady PSP formulations, containing sensor dye and binder, were evaluated in calibration tests [62]. It was found that PtTFPP-based PSP in combination with a styrene-based polymer is suitable for the unsteady pressure measurement. To enlarge the porosity of this polymer, TiO_2 powder was added. This paint was applied with a spray gun directly to the model surface without an additional screen layer underneath, in-situ in the wind tunnel. A total paint thickness of 10 ± 2 micrometer was achieved on the model. The temperature sensitivity of the paint was determined from the calibration curves to be approximately -800 Pa/°C.

A constant UV-LED illumination was used together with the intensity method to acquire luminosity images from a camera mounted above the model in the wind tunnel side-wall, as shown in Fig. 3.27. In this method the paint is simultaneously illuminated and observed by a camera. The paint emits light and the light intensity (brightness) is a function of pressure, illumination and observation angle. Images were taken for flow-off conditions to reference the illumination and observation angle data, and thus the intensity of the measurement images remains only a function of pressure. The measurement images were then mapped onto a 3D volume using marker tracking (the markers can be seen in Fig. 3.28) and calibration data applied to convert light intensity to pressure.

A CMOS camera, the Photron Fastcam SA1 was used for PSP data acquisition. This camera has a resolution of 1024 x 1024 pixels, with a pixel size of 20 μm, 12 bit dynamic range, 35% quantum efficiency and 5400 Hz maximum data acquisition rate at full pixel resolution. The camera was operated with a f=50 mm lens, corresponding to a pixel resolution of approx. 15 pixel/mm. To get sharp images for the whole model, the camera was equipped with a miniaturised Scheimpflug adapter fulfilling the setup requirements at the wind tunnel.

Both “in-situ” and “a-priori” calibrations were performed. At the same time as the airfoil was coated with PSP, several test samples were also coated with PSP. These test samples and the coated model were calibrated in the test section of the wind tunnel between 30 - 100 kPa at 25°C (in-situ). After the wind tunnel test was finished, an intensive a-priori calibration was performed with exactly the same hardware that was used in the wind tunnel test using the PSP test samples coated at the same time as the model. These a-priori calibrations were performed between 10 - 150 kPa for 10, 15, 20, 25, 30, 35, 40, 45 and 50°C. For both types of calibrations the same set-up (camera, lens, filter, LED, viewing angle, etc.) was used. For 25°C the in-situ calibration and the a-priori calibration have good agreement. For the final data reduction the values of the a-priori calibration were used, since the temperature information can also be taken into account in this way. This is the standard DLR evaluation strategy for PSP measurements.

The PSP data requires a zero-offset from an adjacent pressure transducer. When this is performed the PSP and pressure transducer signals follow each other well, as shown in Fig. 3.29, with some aliasing due to the differing sampling rates of the two data sets. The pressure transducers were sampled at 5878 Hz, with an anti-aliasing filter at 3 kHz. The PSP data was sampled at 367 Hz and the sampling was phase locked so that this was equivalent to 1024 and 64 points per pitching period, respectively. The measurements were phase-averaged, to provide the images in this section.

The model structure was unevenly heated by the wind tunnel flow and the pressure transducers, and as a result the surface temperature of the model varied by 2-5 K, depending on the test condition. An extreme example is shown in the infrared thermographic image in Fig. 3.30. The flow is around 30°C and is from left to right and the effect of the aluminum strut can be clearly seen in the dark (cold, 27°C) stripe on the model surface. Just downstream of the leading edge of the model, boundary layer transition with a local separation is observed as a dark line and the portholes for the flow control are visible downstream of this line. In the background the model is reflected in the metallic wind tunnel side-wall. The PSP follows the relative changes in pressure accurately, but the data has a temperature offset, which varies with position on the model. No pointwise temperature offset data was taken, so the data could not be directly adjusted. Using the unadjusted data would result in comparisons as seen in Fig. 3.31.

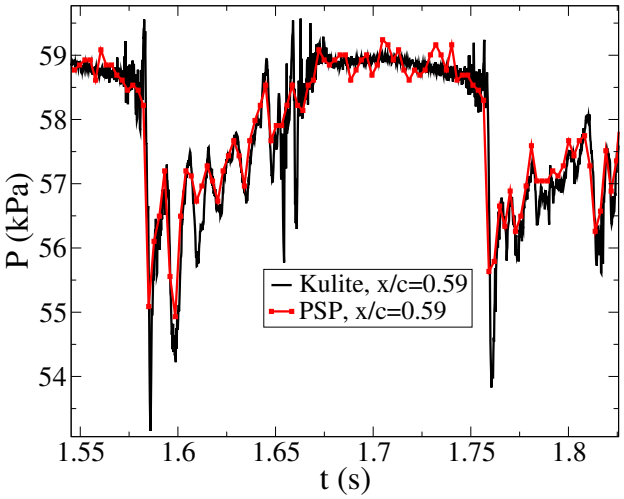

Figure 3.29: Model pressure comparison over time for a single pressure transducer and a PSP point at x/c=0.59 and M=0.3, Re=0.53×10^6, f=5.7 Hz (ω^*=0.11), α=13±7°.

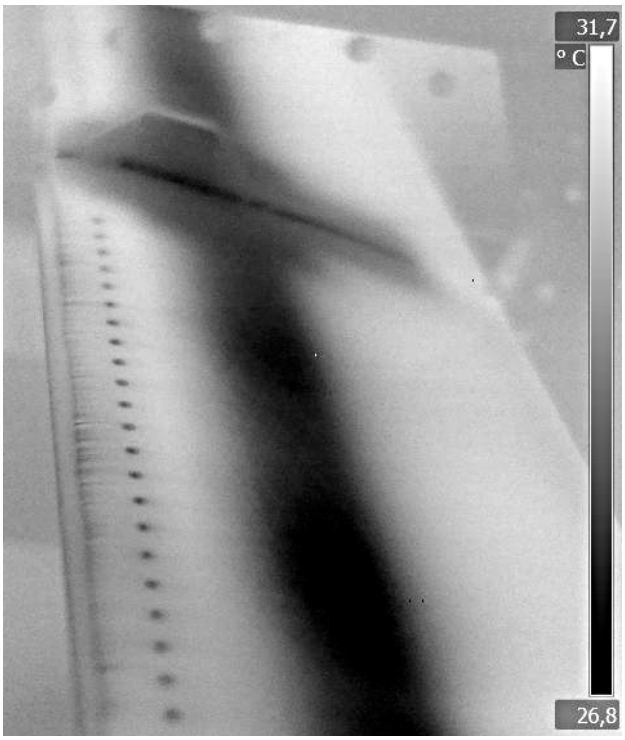

Figure 3.30: Model temperature with infrared thermography at M=0.3, Re=0.53×10^6, α=13°.

Despite the problems due to the temperature distribution, the pitching airfoil has the advantage of providing a large number of pressure distributions in a short time and so a compensation method based on computed pressures can be used. In this method, the local pressure C_P is modified by subtracting the pressure at that point at minimum angle of attack C_{P_0}. Phase-averaging the data then removes the worst of the measurement noise and a qualitative picture of the flow is achieved. The results of this method are seen in Fig. 3.32 for the data from the pressure transducers. The difference C_P-C_{P_0} is zero at the point of minimum angle of attack (Fig. 3.32a) and at high angle of attack C_P-C_{P_0} provides the position of the suction peak (Fig. 3.32b). When the airfoil stalls, the dynamic stall vortex is visible as a constant pressure with a sharp pressure rise at its downstream end. The position of the dynamic stall vortex is accurately shown in C_P-C_{P_0} around x/c=0.5 in Fig. 3.32c, and around x/c=0.8 in Fig. 3.32d, as seen in the comparison with the original C_P data.

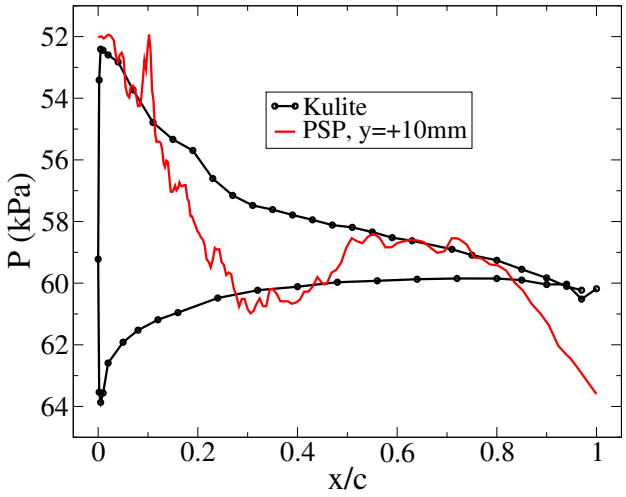

Figure 3.31: Direct, uncompensated pressure comparison between pressure transducers and PSP, noting effect of spar cooling at t=1.72 s in Fig. 3.29 at M=0.3, Re=0.53×10^6, f=5.7 Hz (ω^*=0.11), α=13±7°.

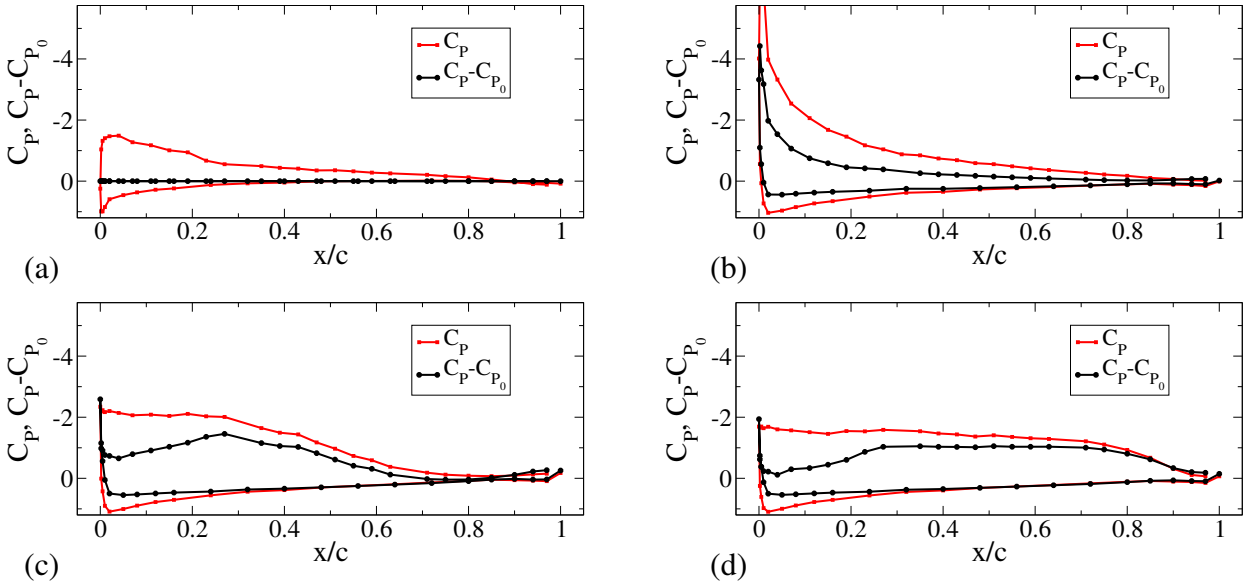

Figure 3.32: Comparison of C_P and C_P-C_{P_0} data at the pressure transducers on the upstroke for M=0.3, Re=0.53×10^6, f=5.7 Hz (ω^*=0.11), α=13±7°. (a) At minimum angle of attack (α=6°). (b) At high lift with attached flow (α=13.5°). (c) With stall vortex on the front half of the airfoil (α=15.5°). (d) With stall vortex on the back half of the airfoil (α=16.1°).

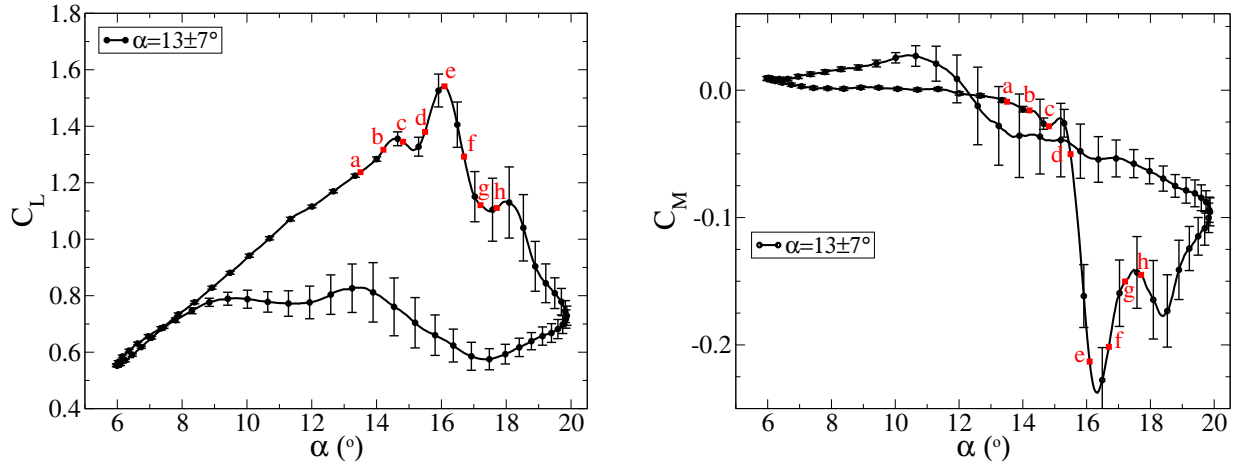

Figure 3.33: Force coefficients integrated from the pressure transducers at M=0.3, Re=0.53×10^6, f=5.7 Hz (ω^*=0.11), α=13±7°. Left: C_L Right C_M. Letters relate to the subfigures of Figs. 3.34 and 3.35.

3.3.2 Dynamic stall at Mach 0.3

The model was pitched at α=13±7° and frequency 5.7 Hz (ω^*=0.11) at M=0.3 and Re=0.53×10^6. Figure 3.33 shows the phase-averaged force coefficients integrated from the pressure transducers near the model midline. The plot of lift coefficient against angle of attack shows a roughly linear increase in lift on the upstroke with a kink at α=11° as the transition on the suction side reaches the leading edge. The lift then rises linearly (but with a lower gradient) until the airfoil stalls. The dynamic stall vortex formation causes a small peak in the lift around α=15°. The dynamic stall vortex then moves downstream, increasing in size and strength, causing a second peak in the lift around α=16°. A sharp reduction in lift follows, as the stall vortex is convected away from the airfoil. A large hysteresis follows, with flow reattachment around α=9° on the downstroke. The pitching moment shows a similar process, but a large negative pitching moment peak is caused by the dynamic stall vortex, with the peak shortly after maximum lift.

Figures 3.34 and 3.35 show typical results of the 3D flow with PSP and pressure transducer measurements. Both figures include 8 phase-averaged subfigures (a-h) taken during pitch-up, covering the time during dynamic stall. The time points are the same (i.e. Figs. 3.34a and 3.35a show the same flow, and so on), and the times are noted as the red letters in Fig. 3.33.

In Fig. 3.34 the flow is from left to right and the view is from over the suction side of the airfoil. The wind tunnel wall is at the top of the picture at y/c=1.67 and the model centerline at the bottom at y/c=0. Figure 3.34a shows the attached flow before stall and the end-effects of the wind tunnel wall (a tip vortex from the 1.5 mm gap between model and wall) can be seen as a triangle of increased pressure at the top right of the figure, as discussed further in section 3.1 [27]. The thickness of the wind tunnel wall boundary layer is roughly y/c=0.25. The stripes in C_P-C_{P_0} are a small measurement artifact due to the readout procedure of the CMOS sensor which are not visible in individual PSP images, but the stripes are amplified by the subtraction process to become visible. Since the pressure sensors indicate uniform flow in the mid-region of the model, a small region where C_P-C_{P_0} is still affected by the temperature can be identified, as seen in the triangle of lower C_P-C_{P_0} near the leading edge on the model midline.

As the model pitches up, the flow passes successively through the states in Figs. 3.34a-h. In Fig. 3.34a, the flow is attached and the suction peak is visible as a green stripe near the airfoil leading edge. As the angle of attack increases, the suction peak becomes stronger, and in Fig. 3.34b the airfoil stalls and this progresses in Fig. 3.34c. At stall, the suction peak reduces and a dynamic stall vortex is produced, and the footprint of the dynamic stall vortex is visible as a green suction

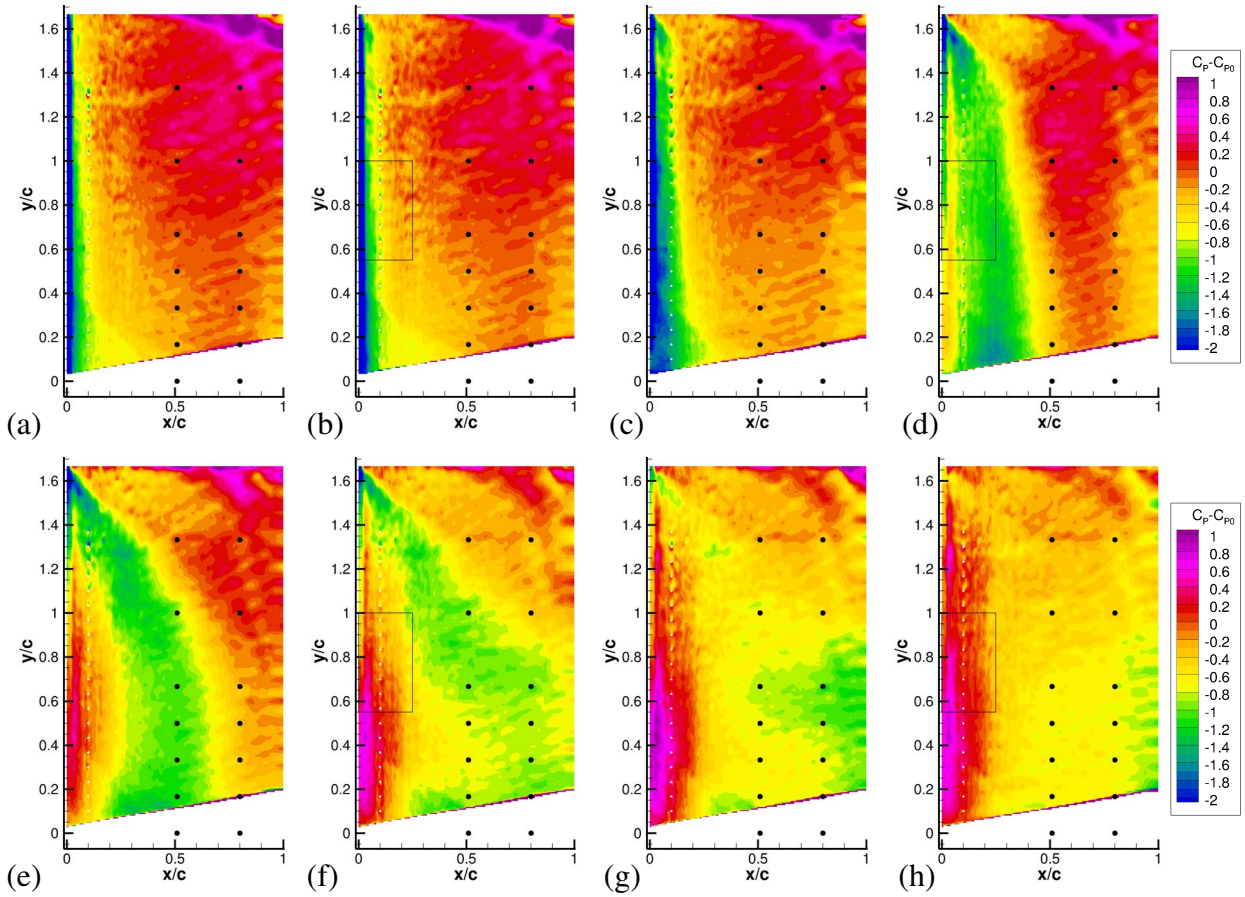

Figure 3.34: PSP pressure distributions (C_P-C_{P_0}) illustrating the 3D flow during stall for M=0.3, Re=0.53×10^6, f=5.7 Hz (ω^*=0.11), α=13±7°. (a) α=13.5° (b) α=14.2° (c) α=14.8° (d) α=15.5° (e) α=16.1° (f) α=16.7° (g) α=17.2° (h) α=17.7°. The black dots illustrate the symmetric reflection of the pressure transducer positions used in Fig. 3.35. The black rectangles indicate the regions for which the C_P distributions are shown in Fig. 4.68

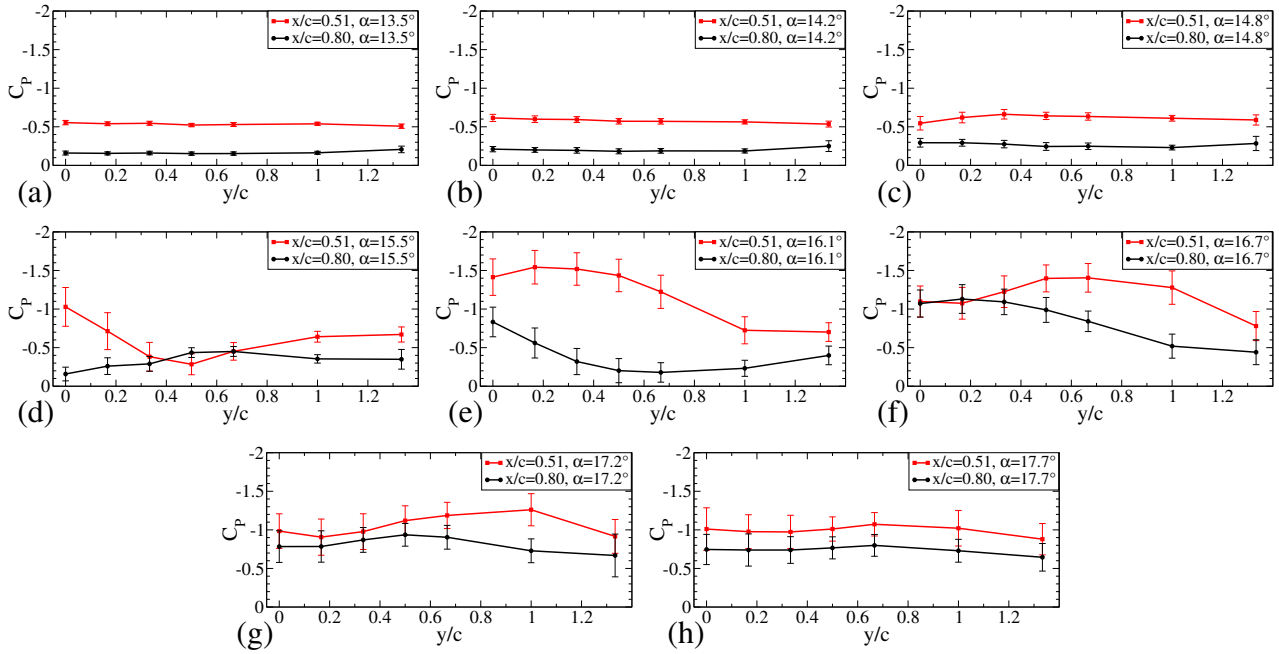

Figure 3.35: Pressure distributions (C_P) illustrating the 3D flow during stall for M=0.3, Re=0.53×10^6, f=5.7 Hz (ω^*=0.11), α=13±7°. (a) α=13.5° (b) α=14.2° (c) α=14.8° (d) α=15.5° (e) α=16.1° (f) α=16.7° (g) α=17.2° (h) α=17.7°

stripe. This means that the suction region starts in Fig. 3.34b near the leading edge and propagates downstream in Figs. 3.34c and 3.34d. In Figs. 3.34e and 3.34f the vortex moves downstream and becomes progressively more bowed in shape. It can be seen in the PSP images that although the vortex is initially normal to the oncoming flow, that it appears to be anchored to the airfoil leading edge at the wall and to turn during its passage over the airfoil, ending at an angle of around 30° to its original orientation as it passes over the trailing edge of the airfoil. The previous investigations of Lorber and Spentzos et al. [71, 115] with a free-end noted a slowing of the vortex rather than the anchoring at the leading edge of the wall connection noted here, but qualitatively the flows are similar. This is consistent with the findings in section 3.1, which showed that the small gap between airfoil and wall causes a wingtip vortex more similar to a free end than to a closed end.

As the vortex moves downstream the suction due to the vortex on the airfoil reduces, as can be seen in the comparison between Figs. 3.32c and 3.32d. Thus in Fig. 3.34e, which is taken at the same time as Fig. 3.32d, the vortex is no longer so strongly visible. For Figs. 3.34d and 3.32c the angle of attack is α=15.5° and for Figs. 3.34e and 3.32d the angle of attack is α=16.1°. Figures 3.34f-3.34h show the vortex passing over the airfoil trailing edge and the airfoil flow becoming fully separated.

The passage of the vortex is also illustrated by the spanwise pressure distributions in Fig. 3.35, where the pressure transducers are on the part of the model without PSP. Since the flow should be symmetric, the transducer positions are equivalent to the black dots in Fig. 3.34. Figures 3.35a-h are at the same times as Figs. 3.34a-h, and show the same flow. Figure 3.35a shows attached flow as Fig. 3.34a, and in Figs. 3.35b and 3.35c, the flow is separated as seen in Figs. 3.34b and 3.34c, but the dynamic stall vortex has not yet reached x/c=0.51.

The footprint of the dynamic stall vortex causes slightly higher pressures downstream of the core, due to the downwash directly hitting the airfoil, and lower pressures directly under the vortex and upstream of the vortex. Thus in Fig. 3.35d, at α=15.5°, the vortex is over (x/c, y/c)=(0.51, 0.0) and at (x/c, y/c)=(0.80, 0.0) the pressure has risen due to the vortex downwash. For x/c=0.51 the pressure rises with distance from the centerline and is at a maximum at (x/c, y/c)=(0.51, 0.50) due to the downwash.

The vortex passes further over x/c=0.51 and x/c=0.80 in Fig. 3.35e, but it is not until α=16.7° (Fig. 3.35f) that the vortex reaches the transducer at (x/c, y/c)=(0.51, 1.0). In Figs. 3.34d and 3.34e the green low pressure stripe of the vortex is stationary for y/c$>$1.2. Finally, in Fig. 3.35g at α=17.2°, the start of fully separated flow on the airfoil is reached.

Using the two points in Fig. 3.35f where the suction is at a maximum: (x/c, y/c)=(0.51, 0.50) and (0.80, 0.0), results in a vortex angle of β=30° to the original vortex orientation, which agrees well with the value from the PSP image at the same time (Fig. 3.34f). Numerical investigations such as those in section 3.2 and [28, 60] suggest that that vortex curvature is responsible for a reduction in both the lift and pitching moment force peaks, and that a similar angle would result in a 25% reduction in the pitching moment peak over the ideal 2D case, which is roughly the overestimation noted by Richter et al. [103] in the 2D computation of a similar 3D wind tunnel model with dynamic stall in the DNW-TWG, also at Mach 0.3.

Visbal et al. [119] observed that for a low Reynolds-number plunging wing that the ends of the vortex detached from the wing ends and retreated to the midline of the airfoil, forming a compact Ω vortex with attached flow nearer to the wing tips. Figure 4.33g shows that the attached flow does not appear and the flow is fully separated to the ends of the airfoil. No indication of the ends of the vortex detaching from the wing ends is seen, and thus the spot seen in Fig. 3.34g (in green) is not the impression of an Ω vortex. Apart from the initial trailing-edge separation observed by [119] which also does not appear here, the stall process is otherwise similar in both experiments.

Increasing the Reynolds number to Re=1.15$\times$10^6 results in a similar shape of the dynamic stall vortex to that seen at Re=0.53$\times$10^6, as seen in Fig. 3.36. The PSP frames during separation are slightly different in time to those in Fig. 3.34 and a similar structure of the dynamic stall vortex

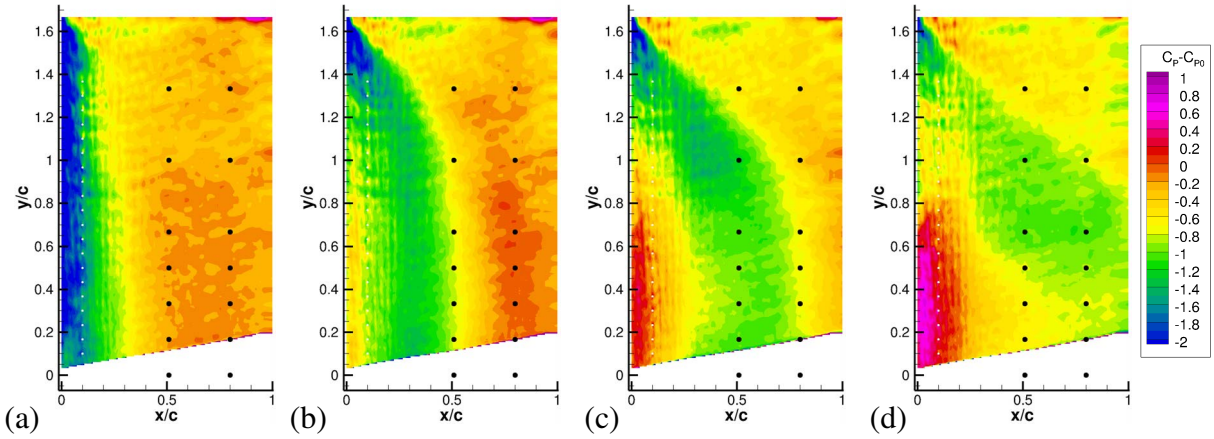

Figure 3.36: PSP pressure distributions (C_P-C_{P_0}) illustrating the 3D flow during stall at M=0.3, Re=1.15×10^6, f=5.7 Hz (ω^*=0.11), α=13±7°. (a) α=14.3° (b) α=14.9° (c) α=15.6° (d) α=16.1°. The black dots illustrate the symmetric reflection of the pressure transducer positions.

shape is produced. In Fig. 3.36b, the dynamic stall vortex is parallel to the airfoil leading edge in the middle of the airfoil, but nearer the wall it is slowed. As the vortex moves rearward on the airfoil in Figs. 3.36c and 3.36d, the region of airfoil for which the vortex is parallel to the airfoil leading edge reduces until the entire vortex is at an angle to the oncoming flow, producing the same effect as at Re=0.53×10^6. Thus the dynamic stall vortex curvature is independent of Reynolds number.

3.3.3 Dynamic stall at Mach 0.5

When the Mach number is increased to 0.5, the OA209 airfoil undergoes shock-induced dynamic stall. The suction peak which appeared at Mach 0.3 is replaced by a region of supersonic flow bounded by a shock at its downstream end. The flow separation appears first at the shock foot and extends downstream with increasing angle of attack also causing the retreat of the shock upstream. At Mach 0.5 no dynamic stall vortex is visible and instead the force coefficients for dynamic pitching are a hysteresis around the coefficients for the static polar. This process is described in detail in section 4.3.7.

Figure 3.37 shows results for M=0.5, Re=0.85×10^6, f=5.7 Hz (ω^*=0.06), α=11±7°. The lift overshoot is no longer as strong as seen at M=0.3 and the hysteresis in pitching moment after stall is reduced. The shock-induced stall is illustrated in the pressure distributions in Fig. 3.38. In Fig. 3.38a

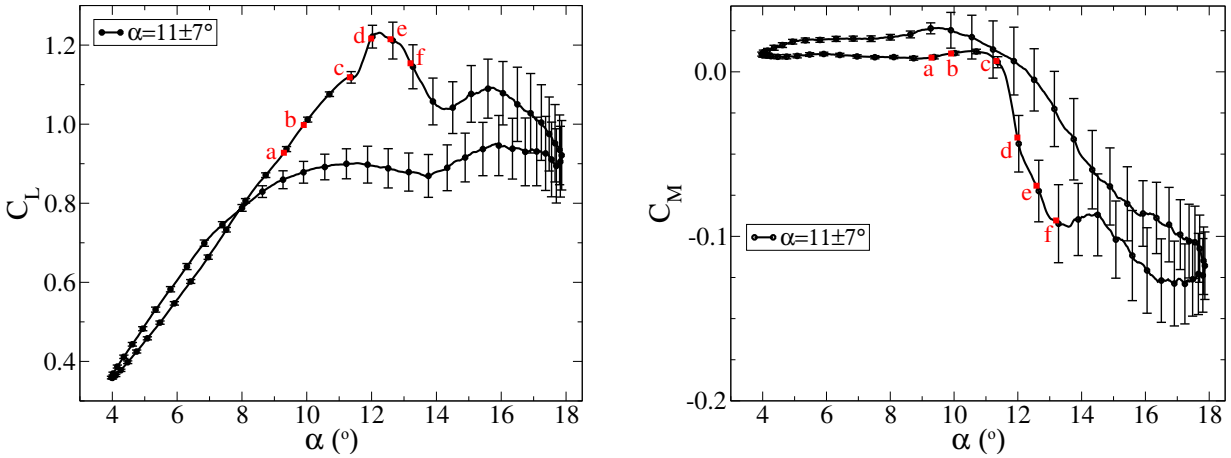

Figure 3.37: Force coefficients integrated from the pressure transducers at M=0.5, Re=0.85×10^6, f=5.7 Hz (ω^*=0.06), α=11±7°. Left: C_L Right C_M. Letters relate to the subfigures of Figs 3.38, 3.39 and 3.40.

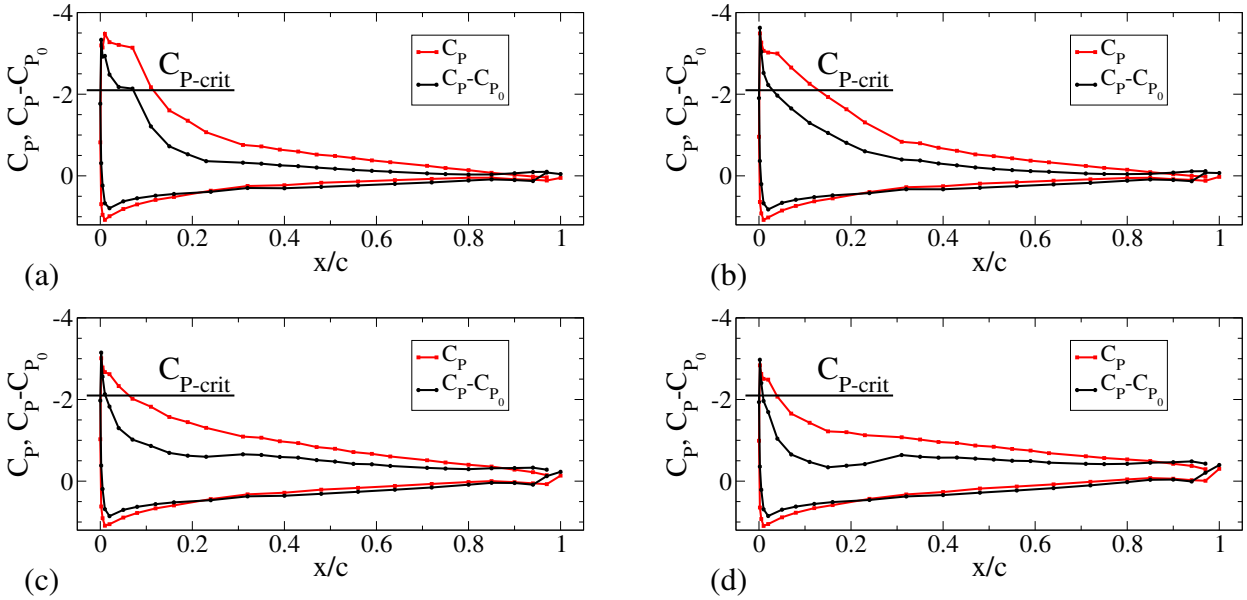

Figure 3.38: Comparison of C_P and C_P-C_{P_0} data at the pressure transducers on the upstroke at M=0.5, Re=0.85×10^6, f=5.7 Hz (ω^*=0.06), α=11±7°. (a) Before stall (α=9.3°). (b) Start of stall (α=9.9°). (c) Stall continuing (α=11.3°). (d) Fully stalled (α=12.0°).

at α=9.3°, the flow is attached and the initial separation is in Fig. 3.38b at α=9.9°. With advancing time (and increasing angle of attack) in Figs. 3.38c and 3.38d, the separated flow extends downstream and the shock moves upstream, reducing the size of the region with supersonic flow and C_L. The pressure difference to that at minimum angle of attack (C_P-C_{P_0}) does not capture the qualitative change in the flow as clearly at M=0.3, however both the retreat upstream of the shock and supersonic region, and the increase in surface pressure on the airfoil downstream of the shock due to the separation process are visible.

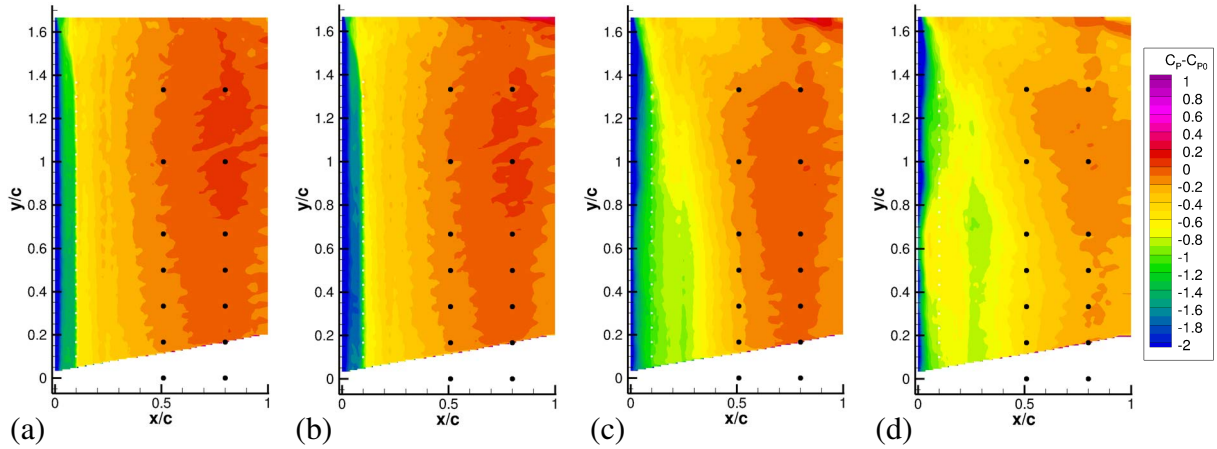

Figure 3.39: PSP pressure distributions (C_P-C_{P_0}) illustrating the 3D flow during stall at M=0.5, Re=0.85×10^6, f=5.7 Hz (ω^*=0.06), α=11±7°. (a) α=9.3° (b) α=9.9° (c) α=11.3° (d) α=12.0° The black dots illustrate the pressure transducer positions used in Fig. 3.40.

The PSP images of C_P-C_{P_0} in Fig. 3.39 show that no visible dynamic stall vortex forms on the airfoil. Figure 3.39a shows the attached flow before stall and the initial separation occurs shortly before Fig. 3.39b. The flow directly under the shock (at x/c=0.15) separates and the separated region spreads both upstream and downstream. The separated region is just barely visible in Fig. 3.39b at x/c=0.15 and y/c<0.3. By Fig. 3.39c, the flow on the model midline is separated to the trailing edge, the separated region is expanding in the y direction on the airfoil, and is separated for y/c<0.9. The

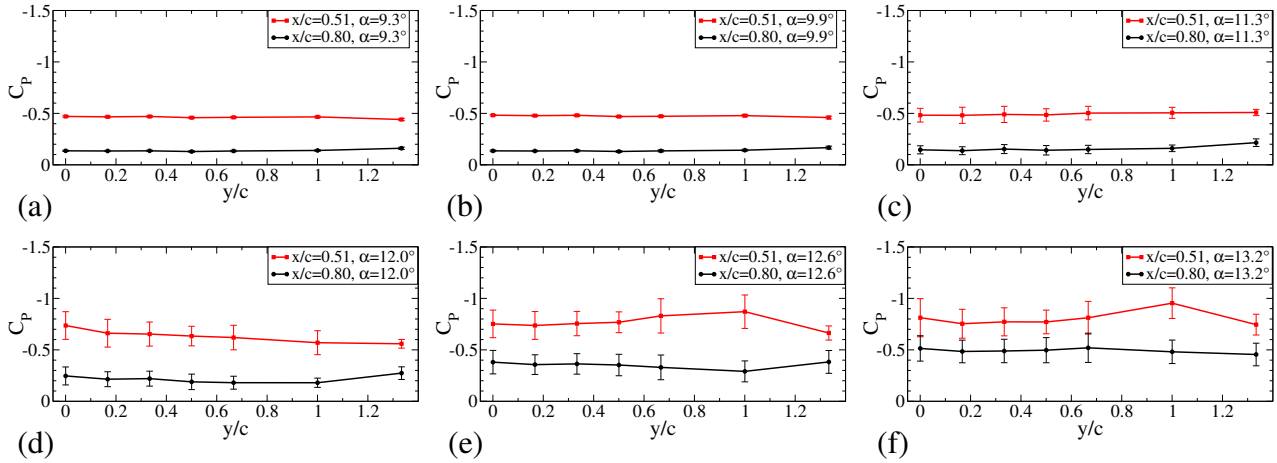

Figure 3.40: Pressure distributions (C_P) illustrating the 3D flow during stall at M=0.5, Re=0.85×10^6, f=5.7 Hz (ω^*=0.06), α=11±7°. (a) α=9.3° (b) α=9.9° (c) α=11.3° (d) α=12.0° (e) α=12.6° (f) α=13.2°

end-effect due to the model-wall connection is always visible as a triangle at the top right of the images and the shock system inside the wind tunnel boundary layer (the first y/c=0.25 from the wall) at the upstream side of the model, remains unchanged during stall.

A problem with the use of C_P-C_{P_0} can be identified for M=0.5 in Figs 3.38d and 3.39d, where C_P-C_{P_0} appears to indicate a second suction peak. A comparison with the measured C_P in Fig. 3.38d shows, however, that this is an artifact of the subtraction of data from the minimum angle of attack. Additionally, the shock causes a local temperature inhomogeneity which will increase the error in the PSP measurement near the shock.

The surface pressures as C_P-C_{P_0} give only a rough impression of the shock-induced stall process, however as seen in Fig. 3.40, the C_P distributions measured at the two x-stations x/c=0.51 and x/c=0.80 show a mild transition to fully separated flow between α=11.3° and α=12.0°. The stall is first seen as an increase in the cycle-to-cycle scatter of the data, illustrated by the enlarged scatter-bars in Fig. 3.40c, which leads to an increased suction at both x/c=0.51 and x/c=0.80 in Fig. 3.40d. The initial stall is weighted toward the midline of the airfoil, extending outward in Fig. 3.40e. The arrival of stall at x/c=0.51 and x/c=0.80 is delayed compared to the initial stall at the shock position. Two further time-points are included in Fig. 3.40 than in Fig. 3.39 and it can be seen that Fig. 3.40d already shows fully separated flow in the middle of the airfoil. The separated region spreads to y/c>1.3 in Fig. 3.40e and 3.40f so that the flow over the whole airfoil is stalled.

3.3.4 Conclusions

The dynamic stall of a nominally 2D airfoil was investigated using high-speed pressure sensitive paint (PSP) and pressure transducers, concentrating on the suction side of the airfoil. The 3D nature of the stall was illustrated, with a curved 3D vortex at M=0.3 and a 3D shock-induced stall at M=0.5. The main results were:

1. The dynamic stall vortex at M=0.3 was initially formed on the airfoil midline and propagated downstream. The propagation rate near the wind tunnel sidewalls was much less than that in the model centerline, leading to curvature of the stall vortex. Other investigations have indicated that vortex curvature is responsible for a reduction in both the lift and pitching moment force peaks.
2. The dynamic stall at M=0.3 and both Reynolds numbers Re=0.53$\times$10^6 and Re=1.15$\times$10^6 was qualitatively similar, both in the forces produced and in the PSP pressure distributions.
3. At M=0.5, a shock-induced stall formed a separation bubble under the shock at the model midline which expanded upstream, downstream and in the spanwise direction with increasing angle of attack and time. No dynamic stall vortex could be detected at M=0.5.
4. The PSP paint had a high temperature sensitivity of -800 Pa/°C and this lead to a temperature error in the C_P measurement which could not be directly corrected.
5. Using the difference C_P-C_{P_0} where C_{P_0} is the pressure distribution at the minimum angle of attack resulted in a qualitative illustration of the progress of stall and the dynamic stall vortex.

Chapter 4

Dynamic stall control by blowing

Air jets of dry compressed air can be used to reduce the effect of dynamic stall. The energy of the air jet is locally added to the flow to reduce flow separation, back-flow or vortices. Air jets share many characteristics with other flow control systems, including flaps, slats and vortex generators, and guidelines can be devised for the application of flow control devices for the reduction of dynamic stall.

Flow control investigations have two primary aims: Firstly, by introducing a precisely directed change into the system, more can be learned about the dynamic stall process and secondly, strategies to reduce the negative effects of dynamic stall, while preserving the positive effects can be tested.

Dynamic stall has the primary positive effect of significantly increasing the maximum lift before stall compared with static stall, so that an increased performance can be gained from a reduced wing area. There are a number of negative effects and the primary aims of a successful dynamic stall control method is to combat these deficiencies.

- A large hysteresis in the lift means that although the maximum lift is high, the mean lift over a pitching cycle is significantly reduced for attached flow, which means that the total lift over the rotor disk is reduced. A successful dynamic stall control method will reduce the lift hysteresis while preserving high maximum lift.

- The forces on the airfoil fluctuate rapidly, in lift, drag and pitching moment, and these result in high vibrations. A successful dynamic stall control method will reduce these gradients, either by slowing the aerodynamic processes or reducing the absolute height of the step changes.

- The absolute maximum value of the negative pitching moment peak is often 10-20 times that of the pitching moment for attached flow. This exceeds the structural constraints of the pitch links and causes damage. A successful dynamic stall control method will reduce the absolute value of the pitching moment peak.

- The low lift during the hysteresis means that there are particular azimuthal angles of a rotor in stall without sufficient lift which results, for example, in high speed pitch-up. A successful dynamic stall control method will increase the lift of a fully stalled airfoil and help increase the maneuverability of the helicopter..

This list of goals allows us to understand whether an implemented change will be useful for combating dynamic stall, but offers little insight into how the changes can be achieved. A number of general strategies for reducing the negative effects can be identified.

- Reducing the total amount of circulation convected away from the airfoil will result in both a smaller step-change in the lift, and in less vorticity available to be bound up into a dynamic stall vortex.

- Reducing the rate of circulation propagation away from the airfoil reduces the gradient of force change and thus the vibration. Practically, the only way to do this results in a larger, dynamic stall vortex which convects more slowly downstream which also results in reduced dynamic forces due to the higher pressure in the vortex core.

- Since the rotor blade is a 3D structure, a localised high force is not necessarily a problem if this is not repeated at the same time on many radial position of the blade. Thus making the dynamic stall vortex less parallel to the rotor blade or breaking up the 2D vortex into multiple 3D vortices is a method of reducing the peak forces on the blade while still retaining high peak forces on individual 2D airfoil sections.

- If the downstream propagation of the vortex can be slowed, then the gradients of the forces will be lower, resulting in reduced vibration. This can be achieved by splitting the 2D vortex into multiple smaller vortices or by introducing effective blockages into the path of the vortex.

- For fully stalled flow, if the bounding streamline above the airfoil can be moved closer to the airfoil surface, then the lift in fully separated flow will be increased. Additionally, reducing or reversing the back-flow along the airfoil suction side during fully separated flow will result in an increase in the lift. During the flow separation process, the vorticity of the boundary layer is entrained into the dynamic stall vortex by back-flow along the airfoil suction surface, so reducing or reversing the back-flow reduces the vorticity available to be bound up in a dynamic stall vortex.

- If the point of initial separation can be moved rearward from the airfoil leading edge to the elastic axis of the airfoil (x/c=0.25), then the initial positive excursion in pitching moment can be reduced, and the maximum size of the dynamic stall vortex can be reduced. This can be achieved by vortex generators, turbulators, or laminar airfoil designs with a delayed adverse pressure gradient. Care must be taken in these cases not to increase the airfoil drag at low angles of attack (vortex generators) or to cause a premature stall (laminar airfoils).

- Delaying the dynamic stall to higher lift coefficients will result in more lift and less time in stall for a given airfoil motion. Combining a stall delay with a slowing of the stall process will often result in a significant reduction of the peak forces.

With these strategies in mind, configurations can be identified which will improve the airfoil behaviour under dynamic stall. Currently an automated optimisation method for the design of dynamic airfoils is not possible in the same way as for static airfoils, but by understanding the aerodynamics potentially positive configurations can be identified and tested.

4.1 Design of constant blowing experiments using CFD [1]

The DLR projects SIMCOS (advanced SIMulation and COntrol of dynamic Stall) and STELAR (Stall and Transition on Elastic Rotor Blades) are part of a long-term German-French cooperation to investigate dynamic stall (DS) and improve numerical modelling with regards to dynamic stall. They were performed in parallel with the ONERA projects SIMCOS and EHIRHE. As part of these projects the effect of pulsed and constant blowing jets on dynamic stall was investigated both experimentally and numerically for an OA209 airfoil in the DNW-TWG wind tunnel.

The airfoil OA209 was chosen, because it is an openly available contour [23] which is in use on the outer section of a number of Eurocopter helicopters, and for which both the DLR and the ONERA have good databases of experimental results taken in the DNW-TWG and the ONERA-F2 [36, 47, 83] wind tunnels. It is an airfoil of thickness d_a/c=9%, which displays leading edge stall and a number of interesting and difficult dynamic stall behaviours. This family of airfoils has been extensively investigated at the DLR with results on laminar separation bubble bursting [38] and for leading edge vortex generators (LEVoGs) for dynamic stall control [12, 73]. A numerical study [103] investigated the mesh densities and time step sizes necessary to get good results for the clean OA209 airfoil, and test cases were identified where fully turbulent computations with a one-equation turbulence model gave good engineering estimates of the airfoil performance when compared with experiment. Additional studies on the OA209 including clean [83] and LEVoG [47] test cases were carried out, providing an examination of the dynamic stall process using time resolved particle image velocimetry (TR-PIV), dye injection and surface pressure measurements to investigate the onset of dynamic stall at low Mach and Reynolds numbers.

In the current study, a new wind tunnel model was designed which was to include injector holes or slots as Fluidic Control Devices (FCDs). Fluidic Control Devices have the advantage that, when turned off, the original airfoil contour and performance are available. Constant blowing or pulsed blowing at up to 500/cycle at total pressures of up to 50 bar can be realised experimentally using valves [88] in the model installed behind each injection point. An air supply positioned outside the tunnel and provided the blowing air through a plenum chamber/air-pipe. A constant compressed air supply of up to 50 bar is available at the TWG, and the injected air can be removed by a suction pump (to preserve constant mass flow in the circuit) at a rate of up to 10 kg/s. The actual wind tunnel experiment is considerably more complex than the CFD model, but it was unknown at the start of this investigation what could be practically implemented in time for the experiment. Modelling the high-frequency effects of an actuated jet on the boundary layer by URANS methods is difficult and computationally expensive (although some qualitatively good results exist in the literature [101]), and it was initially unclear how the high-frequency pulsed blowing would work experimentally, so the decision was made to investigate designs for constant blowing. The constant blowing case should define a lower limit of actuator effectiveness and an upper limit of air use. This chapter describes injection with supercritical jet conditions, where the gas expands to supersonic conditions after injection.

Computations using the DLR-TAU code are presented for a 3D slice of the dynamically pitching OA209 airfoil. Different types of air jets were investigated and evaluated for their ability to reduce the negative effects of dynamic stall, while preserving the positive effects. The values of pitching moment peak height and peak drag height were minimised, as was the mean drag. The mean lift and the instantaneous lift at high angles of attack were maximised and high values were used as an indicator of reduced lift hysteresis.

[1] Text and illustrations in this section are taken from [34]: Gardner, A.D., Richter, K., Rosemann, H., "Numerical investigation of air jets for dynamic stall control on the OA209 airfoil", *CEAS Aeronautical Journal*, Volume 1, Issue 1, Page 69-82, 2011. DOI 10.1007/s13272-011-0002-z and [24] Gardner, A.D. "Numerical investigation of air jets for dynamic stall control on the OA209 airfoil", DLR internal report: DLR-IB 224-2009 A 32, DLR Institute of Aerodynamics and Flow Technology, Göttingen, Germany, 2009.

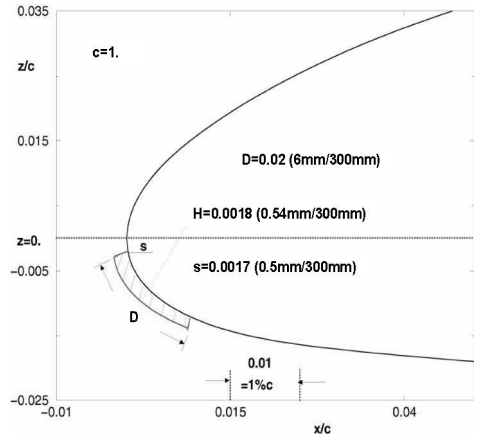

Figure 4.1: Experimental arrangement for the LEVoG experiments ([73]).

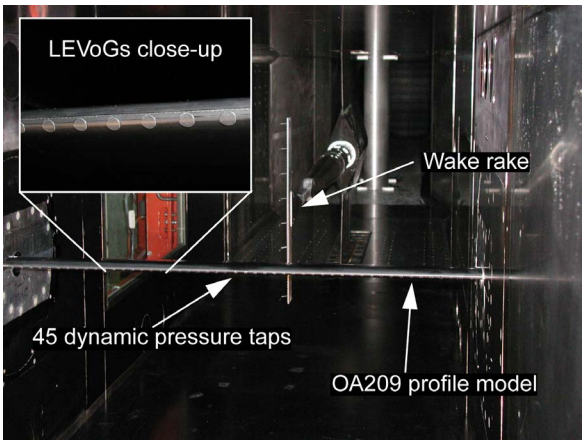

Figure 4.2: Photograph of the LEVoGs installed on a wind tunnel model ([73]).

4.1.1 The LEVoG experiments of Mai et al.

The Leading Edge Vortex Generator (LEVoG) experiments of Mai et al. [73] are an important reference point for this numerical investigation. They are the most recent investigations of the OA209 in the TWG and include measurements on both the clean and modified airfoil at the test condition DS2. Most particularly, the pneumatic flow control mechanisms implemented on the OA209 must be at least as good as the LEVoGs, since active flow control systems are capable of better flow control than passive systems. Figure 4.1 shows the general experimental arrangement when LEVoGs were attached to the airfoil.

The streamwise position, height, diameter and spacing of the LEVoGs was varied within the experiment, and the configuration -45°, spacing 20 mm, height 0.54 mm, diameter 6mm is the optimal configuration. The position around the nose was varied, and is referenced here by an angle, where 0° describes the position of the LEVoGs when the center of the LEVoG is at the center of the nose (The stagnation point at α=0°). A LEVoG position of -45° has the LEVoG attached to the lower side of the airfoil, with the center at approximately -45° when referenced to the center of curvature of the nose. Figure 4.2 shows the LEVoGs mounted on the model in the wind tunnel with the optimal configuration.

Static polar results in Figure 4.3 show that the separation angle for the OA209 was around 14°, and this was not significantly altered by the LEVoGs. The lift after separation was marginally improved and drag on the airfoil at lower lift coefficients was acceptable. For the dynamic case (Figure 4.4) the improvement in the pitching moment and drag coefficient during dynamic stall is significant and the reattachment process is changed. PIV images taken during this experiment show a dynamic stall vortex which is reduced in size. Finally, Figure 4.5 shows the thermographic images of the airfoil top surface taken at a static angle of attack of 19° with tracks behind the LEVoGs which join into larger structures on the surface.

Further experiments by Heine et al. [47] indicate that the effect of the LEVoGs is to move the position of the separation rearward, with the separation point first occurring away from the leading edge and then moving forward. In this way both the drag is reduced and the moment arm of the separation is reduced. The LEVoGs add vortices in the flow direction that work to break up the main dynamic stall vortex into smaller structures helping to further reduce the size of the separation peak. The reattachment is helped by the additional energising of the boundary layer, and so occurs sooner than with the standard OA209.

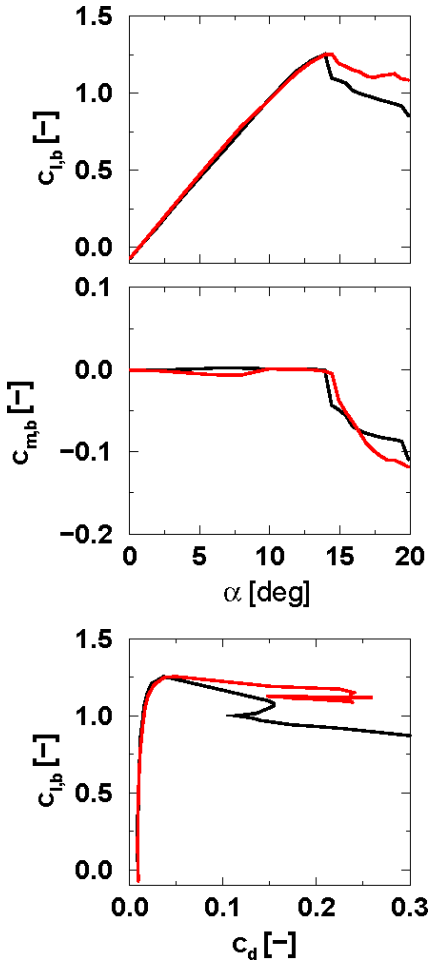

Figure 4.3: Results for static polars at the DS2 test conditions. Black is clean and red is for the LEVoGs ([73]).

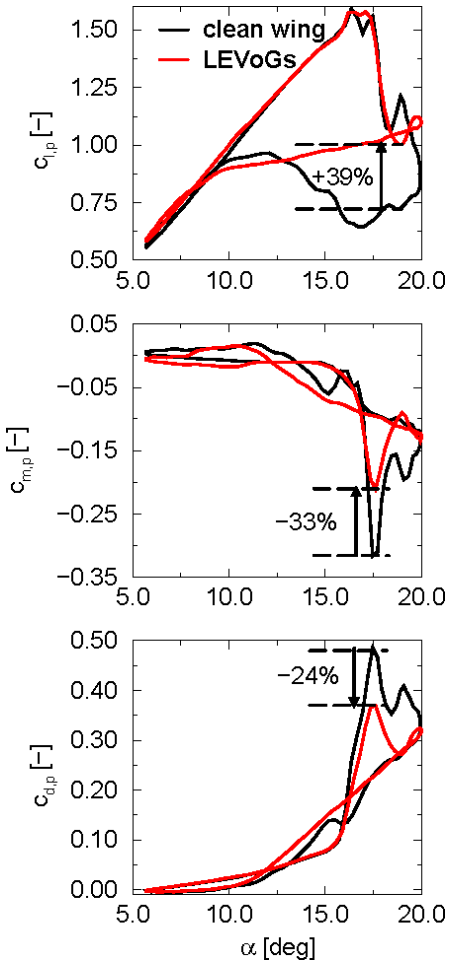

Figure 4.4: Results for dynamic stall at the DS2 test conditions. Black is clean and red is for the LEVoGs ([73]).

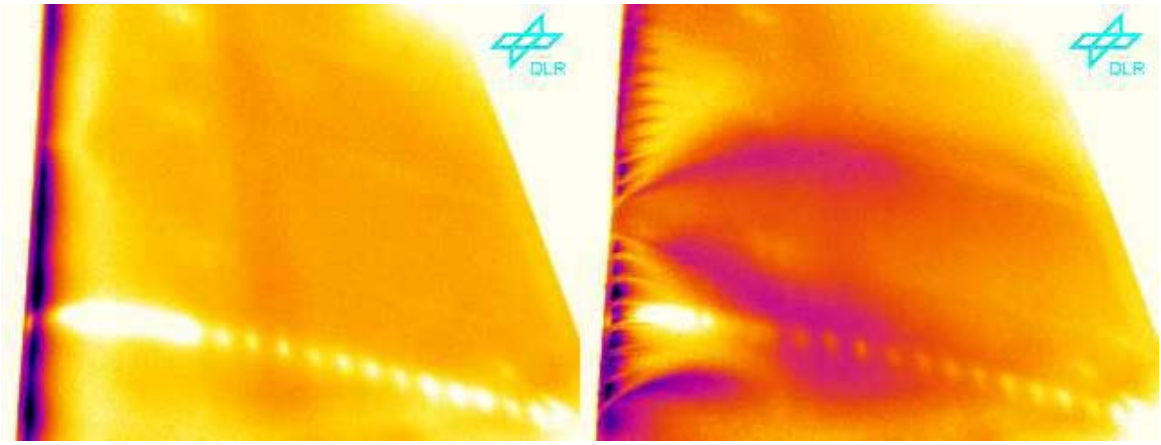

Figure 4.5: Thermography on the airfoil top at a static angle of attack of 19°. Left is clean and right is with LEVoGs ([73]).

4.1.2 Definitions

The following definitions are used to characterise flow control and dynamic stall:
Reduced frequency: $\omega^* = \frac{2\pi fc}{v_\infty}$, with f the oscillation frequency (Hz), c the chord and v_∞ the freestream velocity.
Jet momentum ratio: $C_\mu = \frac{2}{bc}\frac{\dot{m}_j v_j}{\rho_\infty v_\infty^2}$, with $\dot{m}_j$ the mass flux out of the jets, v_j the jet speed at the jet exit (set to be a constant value, M=1.0) and b the span width of the rotor blade. C_μ is well-defined for the incompressible case ($C_\mu = \frac{A}{c}\frac{v_j}{v_\infty}$), ($A$ is the jet area), but its extention to compressible flow depends on the jet conditions used as a reference. The extension above is simplest, but differs from some definitions used in the literature.

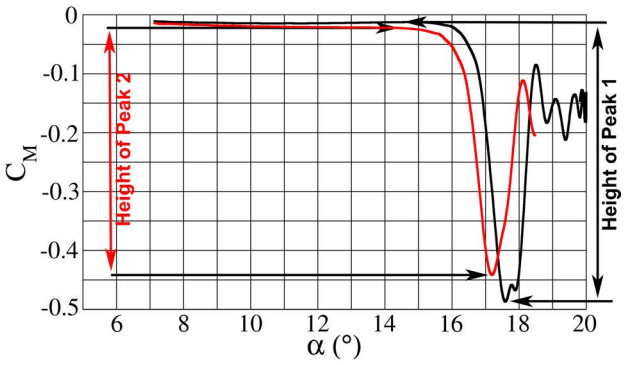

Figure 4.6: Measurement of the peak height for two sets of data.

Jet mass ratio: $C_q = \frac{\dot{m}_j}{\rho_\infty v_\infty cb}$
Drag and pitching moment peak heights: C_{M_p} and C_{D_p} are the difference between the value at the peak and "flat" value a short time beforehand (Fig. 4.6).
Mean values of lift and drag: $\overline{C_L}$ and $\overline{C_D}$ are averaged over one pitching cycle.
Mass flux: $\dot{m}_j$ is an output of the TAU solver for the jet boundaries. It is averaged over one pitching cycle and normalised to one meter of blade span width.

4.1.3 Computational approach

Computations using the DLR-TAU code are presented for a 3D slice of the dynamically pitching OA209 airfoil at the DS2 test condition: M=0.31, Re=1.16e6, α=12.87$\pm$7.13°, ω^*=0.101. Reynolds-averaged Navier-Stokes (RANS) and Unsteady RANS (URANS) computations were undertaken with the DLR-TAU solver [39, 109]. The node-based finite-volume solver was used on a hybrid unstructured grid consisting of prismatic layers close to the viscous surfaces and a tetrahedral field, generated using the Centaur^{TM}[1] unstructured grid generator. All computations were fully turbulent, using the Spalart-Allmaras turbulence model [114] with the Edwards modification (SAE) [17], due to its excellent speed and stability, and the good results obtained for this test case by previous investigators. A central scheme was used with the scalar dissipation method of Mavriplis [75]. A lower upper symmetric Gauss-Seidel (LUSGS) implicit flux solver was used, with no multigrid convergence acceleration and a CFL number of 2.

The RANS computations were run for 10000 iterations, for a total of around 60-80 CPUh, although true convergence was not reached due to the separated flow at the conditions computed. The coefficients were instead averaged over the last 2000 iterations to obtain the values quoted in this section. This averaging is not truly physically correct due to the RANS scheme and the dual time-stepping method meaning that each iteration is not truly comparable to a slice of physical time, but the approximation is sufficient for the engineering estimate of relative performance required.

The URANS computations used 1600 time steps per period with 400 inner iterations per timestep. Significantly more inner iterations were required for convergence with jet injection than had been previously observed for clean cases. A minimum of 3 pitching cycles needed to be computed for convergence, with each cycle costing 3400-4400 CPUh. Convergence of the computation was assumed when differences between the lift, pitching moment and drag between the second and third cycles were within pre-defined tolerances, approximately equal to 1% of the value at the minimum angle of attack computed.

The grid was generated according to the guidelines of Richter et al. [103] for grid convergence on this geometry and test condition, with grid cells of 1% chord on the top and bottom of the airfoil and finer cells of 0.15% on the leading and trailing edges and around the jets (See Table 4.1). A 3D slice of the airfoil with a width of 20% chord (60 mm) was used. This slice was bounded by periodic side-walls (Fig. 4.7) which allow a net spanwise flow for jet configurations with all jets skewed in one direction. The domain was selected to capture the qualitative effects required to make a good decision about which jet to choose, with a small number of node points (under 2 million) so that the geometry could be computed with acceptable cost by the URANS solver.

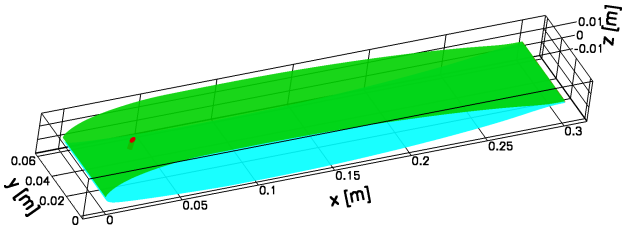

Figure 4.7: Airfoil gridded area.

It is expected that this domain is insufficiently wide to see 3D effects for the main dynamic stall vortex, but the 3D effects in the first 20-40% of the airfoil will be preserved, as needed for the jets. This type of computational domain has also been used by a number of other investigators, amongst them Prince et al. [97], who got quite good results when compared with experiment for passive air-jet vortex generators in incompressible flow. In order for the effect of the jet boundary layer to be captured, the jets were modelled as short tubes sunk into the surface with a length of twice the jet diameter (or slot width), with a boundary setting the total temperature (T_0=300 K), pressure and density (P_0/ρ_0=90909) at the bottom end (Fig. 4.8). The constant temperature is a concession to the verifying wind tunnel experiment which will use high-pressure gas supply with a plenum inside a large aluminium block at room temperature. The static conditions at the jet exit will depend on the inviscid cross-sectional area of the injector at the sonic point, which is a function of the boundary layer thickness and the interaction between the jet and the external flow. In cases where a tangential slot of width 0.5 mm was to be used, the surface of the airfoil was changed, shifting the surface inward by 0.75 mm (to include the 0.25 mm wall outside the slot), and blending in all the changes back to the original contour within a length of 7% chord (Fig. 4.9). The same method was used for all tangential slot configurations shown in this section. The cells around the injectors were constrained to 0.08% chord, and the walls of the injectors were modelled as fully turbulent, with a prismatic sublayer equivalent to that on the model surface (Fig. 4.8).

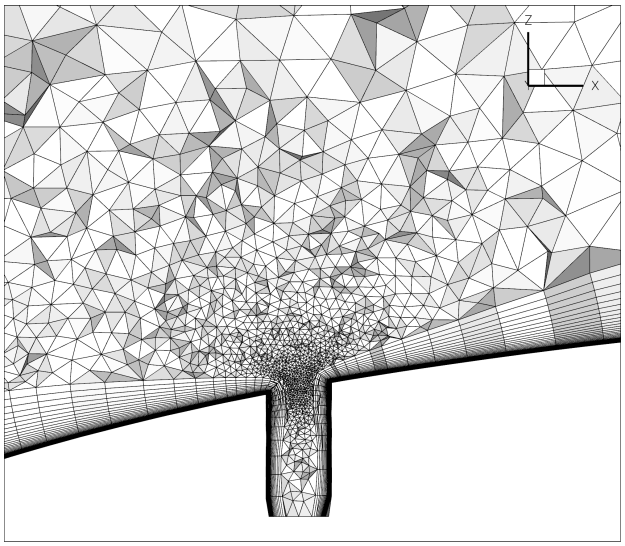

Figure 4.8: Cut through the grid at the injector position in the middle of the grid for TC12.

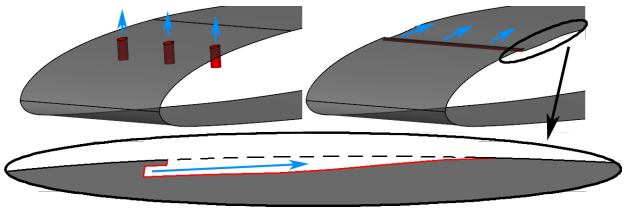

Figure 4.9: Comparison of airfoil modifications for portholes (left) and for tangential injection (right and bottom).

Table 4.1: Grid data for the 3D grids.

Option	Value
Whole grid	
Grid nodes	1.2-1.7 Million
Prismatic grid	
Layers	44
Stretching	1.15
y^+	$\leq$1.0
Surface grid	
Maximum cell size	1% chord
Nose cell size	0.16% chord
Trailing edge cell size	0.16% chord
Injector cell size	0.08% chord
Tetrahedral grid	
Cell size in source near model	1% chord
Cell size at farfield	10% chord

Figure 4.10 shows the comparison between different farfield boundary distances. Finally 17 chords was selected as providing a good balance between the number of cells in the farfield and preserving the qualitative behaviour of the experiment and the 2D CFD. The closer farfield approached the model to 2 c on the upwind side, while leaving 5 c on the wake side.

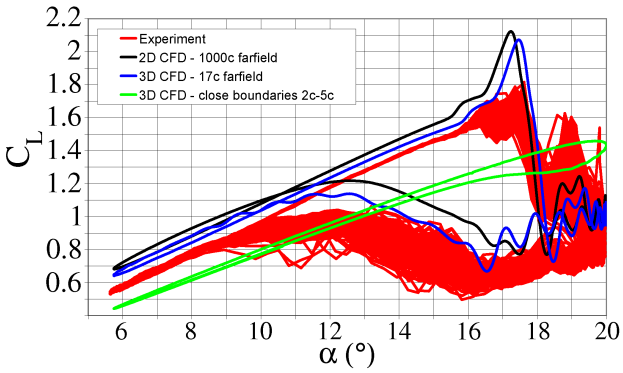

Figure 4.10: Comparison between the results for DS2 for different farfield boundary distances, compared with experiment. Finally 17 chords was selected as providing a good balance between the number of cells in the farfield and preserving the qualitative behaviour of the experiment and the 2D CFD.

The forces on the airfoil are the sum of the forces for all nodes on the surface. For the non-slip boundaries, the pressure and viscous forces are computed from the pressure and skin friction. The non-slip boundaries are the airfoil top, airfoil bottom, airfoil trailing edge and the internal surfaces of the injection holes including points belonging to both the injection holes and the injection inflow surfaces. For the injection inflow surfaces the forces are computed from the mass flux and velocity across the inflow plane. Thus the lift, drag and pitching moment should be equal to the true forces seen in an experiment on this configuration excepting the force in the y-direction due to the gas delivery by a pipe in the blade spanwise direction.

4.1.4 Deep dynamic stall on the OA209

The SIMCOS DS2 test case (M=0.31, Re=1.16e6, α=12.87$\pm$7.13°, ω^*=0.101) shows all the typical behaviour of deep dynamic stall at low Mach numbers. At low angles of attack, on the upstroke, the flow is attached and is qualitatively similar to the statically attached flow (Fig. 4.11, left). At stall, a large dynamic stall vortex appears, which is associated with a peak in the lift and pitching moment coefficients (Fig. 4.11, middle). The vortex attachment point is at the nose and the large main vortex stretches to the leading edge while a counter-rotating vortex is formed from the trailing edge. After

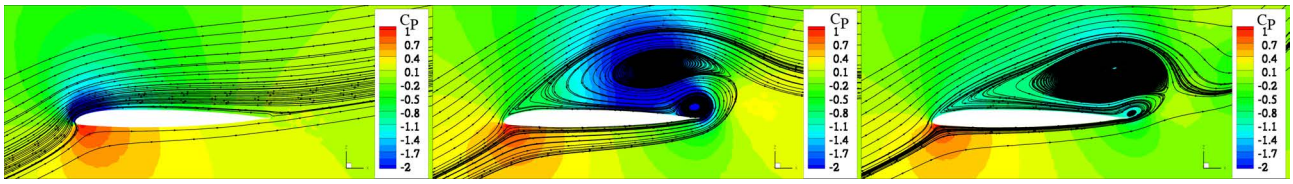

Figure 4.11: Comparison of flow topologies on the periodic plane before (left), at (middle) and after (right) dynamic stall for the "Clean" OA209 airfoil. The three cases correspond to α=15.6°, 17.9° and 19.5° respectively for an instantaneous solution at the periodic plane.

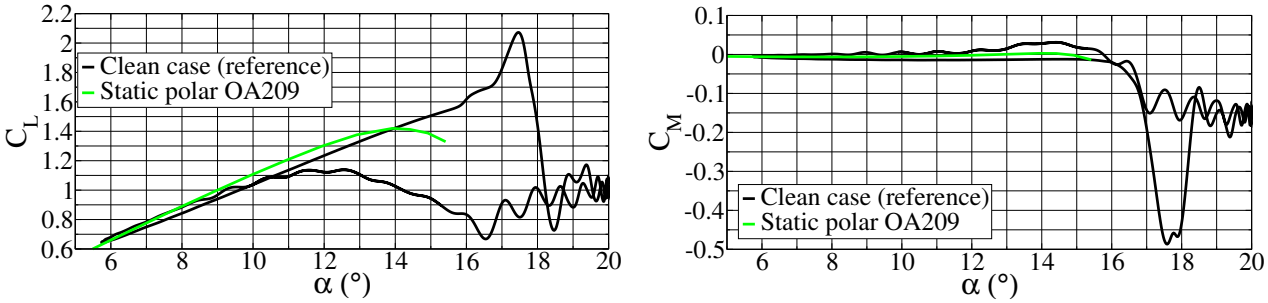

Figure 4.12: URANS results of the coefficients over one pitching cycle α=12.87±7.13°, ω^*=0.101 for: (left) Lift coefficient, (right) Pitching moment coefficient. Shown is the result for the "Clean" OA209 airfoil compared with a static polar computed with RANS on a 2D grid with a farfield boundary.

stall (Fig. 4.11, right) the dynamic stall vortex moves downstream, and the pressure minimum in the center of the dynamic stall vortex wanders over the trailing edge of the airfoil, sustaining the negative peak in the pitching moment while the lift rapidly reduces. Additionally, the attachment point of the dynamic stall vortex (the separation point of the flow on the top of the airfoil) moves forward. The movement of the attachment point can be observed by the movement of the forward streamline of the dynamic stall vortex between Figures 4.11 (middle) and (right) but is difficult to see in these pictures. The negative peak in the pitching moment is the main undesirable effect of dynamic stall, and is the maximum load for the pitch links on a helicopter blade. The reduction in size and strength of the dynamic stall vortex is a central target of dynamic stall control strategies. In addition, better anchoring the attachment point of the dynamic stall vortex can reduce the height of the peak in the pitching moment by reducing and stabilising the size of the dynamic stall vortex.

Fig. 4.12 shows the lift and pitching moment coefficients over a cycle for the OA209 airfoil at the DS2 test condition. The upstroke has attached flow, before a peak in the lift coefficient associated with the formation of the main dynamic stall vortex occurs (Fig. 4.12, left). A peak in the pitching moment coefficient is formed together with the lift peak (Fig. 4.12, right), and is sustained longer than the lift as the dynamic stall vortex moves downstream. After stall there is unsteady, separated flow, which continues up to the maximum angle of attack and to around α=16° on the downstroke. This unsteady flow is caused by the shedding of smaller vortices from both the leading and trailing edges of the airfoil. After around α=16° on the downstroke the flow stabilises, and the flow reattaches, so that the bottom part of the downstroke again has flow qualitatively similar to the fully attached flow on a statically inclined airfoil.

The dynamic stall control strategies followed in this section will concentrate on using blowing with air jets to keep the flow attached, reduce the strength of the dynamic stall vortex, and to anchor the separation of the flow and the attachment point of the dynamic stall vortex. Each type of air jet used one or more of these types of flow control and, in the following sections, the air jets are grouped by the main type of flow control which they display. The strategies are:

1. Dynamic stall vortex reduction. The strength of the dynamic stall vortex was reduced by blowing with a component in the airfoil spanwise direction to turn the dynamic stall vortex from a single vortex with only a y-component to its axis into one or more vortices with a vortex axis having components in the x, y, and z directions.
2. Coanda effect tangential blowing. Flow attachment was improved using air jets in the flow direction to push the separation point backward using the Coanda effect.
3. Limiting the separation by vertical blowing. The dynamic stall vortex was stabilised by using blowing normal to the airfoil chord line to provide an anchor point for the separation and limit its upstream travel.

4.1.5 The vertical slot and LEVoGs

A vertical slot of width 0.5 mm at 10% of chord (Figure 4.13) was actuated using pressures of 1.0 bar (C_q=0.0032) and 0.6 bar (C_q=0.0008). This configuration was chosen because it is an essentially 2D configuration which should show any problems in the 3D grid. The major problem with this configuration should be immediately visible from Figure 4.13; namely that although the flow in the volume where the dynamic stall vortex forms is affected, the slot forces a complete boundary layer separation in order to do it. The lack of flow through the jet plane from the front of the airfoil causes a lack of mass flux behind the injector leading to a large stall vortex which is bounded on the upwind end by the injector. In this way the dynamic stall vortex is nearly completely replaced by a classic static separation, which is not much of an improvement.

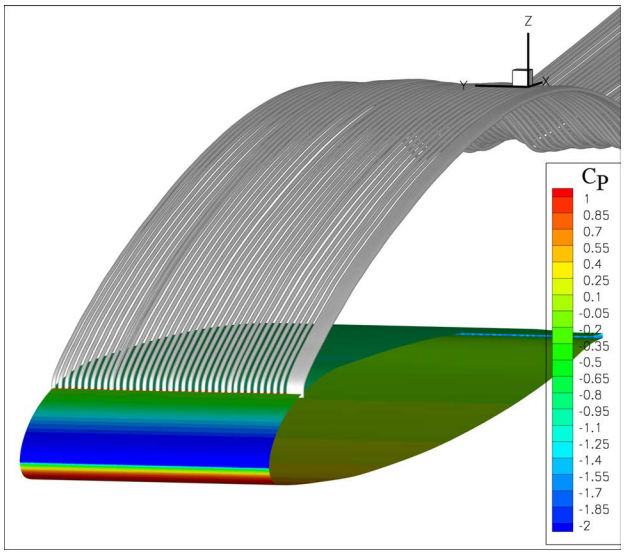

Figure 4.13: Jet streamlines (URANS) for the 0.5 mm width vertical slot situated at 10% chord, at 1.0 bar total pressure (C_q=0.0032), α=13° ↑. (Figure 14 from [24])

An investigation of the LEVoG configuration was done at a static angle of attack of 17.5°, which is well above the static separation point of α=13.5°. Computations were done using the RANS solver on a geometry with 17 LEVoGs at a position of -45° below the model centerline. Figure 4.14 shows similar bubble structures to those inferred from the thermographic infrared images taken during the experiments (Figure 4.5), as well as "track" structures in the wake of the LEVoGs, similar to those seen on thermographic images. The operating principle of the static LEVoGs is not yet completely clear, but it is clear that they create a strongly 3D structure, and that this is advantageous in reducing dynamic stall.

Initial investigations showed that using URANS computations directly as the sole tool for the numerical investigation of these air jets was too costly in both computing power and time. In contrast, RANS results above the static stall angle were found to be a relatively cheap method of identifying effective flow control devices. Thus, potential flow control devices were first investigated with RANS before a reduced number of devices were investigated using URANS with full pitching motion.

It was found that the control of mass flow in low pressure jets was too unreliable, and instead supercritical configurations should be investigated. This meant that the impulse of the jet was significant and had to be taken into consideration. Finally, it was found that the jets should pierce the boundary

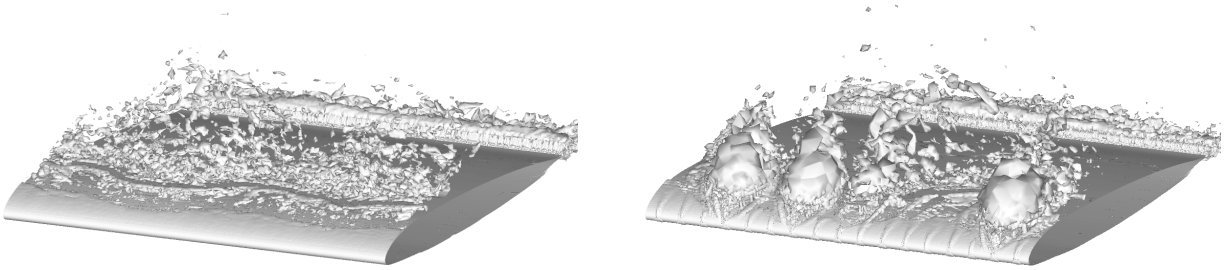

Figure 4.14: The computations on a static wing at α=17.5° showing contours of λ_2 at 1e-6. Left:Clean. Right: LEVoGs in the -45 degree position. (Figure 19 from [24])

layer without separating it, meaning that all configurations having slot injectors normal to the surface were removed from consideration because of the large separated regions which they caused.

4.1.6 RANS results at α=17.5°

Using RANS computations, 12 configurations (Fig. 4.15) were investigated at M=0.31, Re=1.16e6 for a steady angle of attack of α=17.5°, well above the static stall angle of α=14° (Fig. 4.12). This approach provided a qualitative estimate which jets would give a performance improvement over the clean case comparatively cheaply compared to URANS computations. The improvement in lift and drag compared with the reference airfoil identified interesting configurations, with only the three most interesting configurations extensively investigated using URANS on an airfoil with pitching motion. Each configuration was investigated for two air mass flow rates: a maximum flow rate of 0.22 kg/s per meter of blade and a flow of half that (0.11 kg/s/m), resulting in supercritical injection with pressure ratios across the jet of between 2 and 20. This approach simplified the local modelling of the jet since no feedback into the jet was expected and the main effect was of a macroscopic jet. The test cases are enumerated in Table 4.2 and Fig. 4.15. An example for each grouping can be seen in Fig. 4.16.

The test cases for the dynamic stall vortex reduction use jets which were inclined at 45° down-

Table 4.2: Test cases.

Case	Jet Type (d)	Position	Space	Incline/Skew
Reference case				
TC01	Clean OA209, width=60 mm, chord=300 mm			
Dynamic stall vortex reduction				
TC05	Hole (6 mm)	10% top	60 mm	45°/45°
TC06	Hole (3 mm)	10% top	60 mm	45°/45°
TC10	Hole (3 mm)	10% top	20 mm	45°/45°
TC16	Hole (2 mm)	10% top	60 mm	45°/45°
TC18	Hole (1 mm)	10% top	60 mm	45°/45°
Coanda effect blowing				
TC04	Slot (0.5 mm)	10% top	–	Tangent
TC13	Slot (0.5 mm)	10+75%t.	–	Tangent
TC14	Slot (0.5 mm)	75% top	–	Tangent
TC15	Slot (0.5 mm)	75% bot.	–	Tangent
Dynamic stall vortex limitation				
TC07	Hole (3 mm)	10% top	60 mm	Vertical
TC12	Hole (3 mm)	10% top	20 mm	Vertical

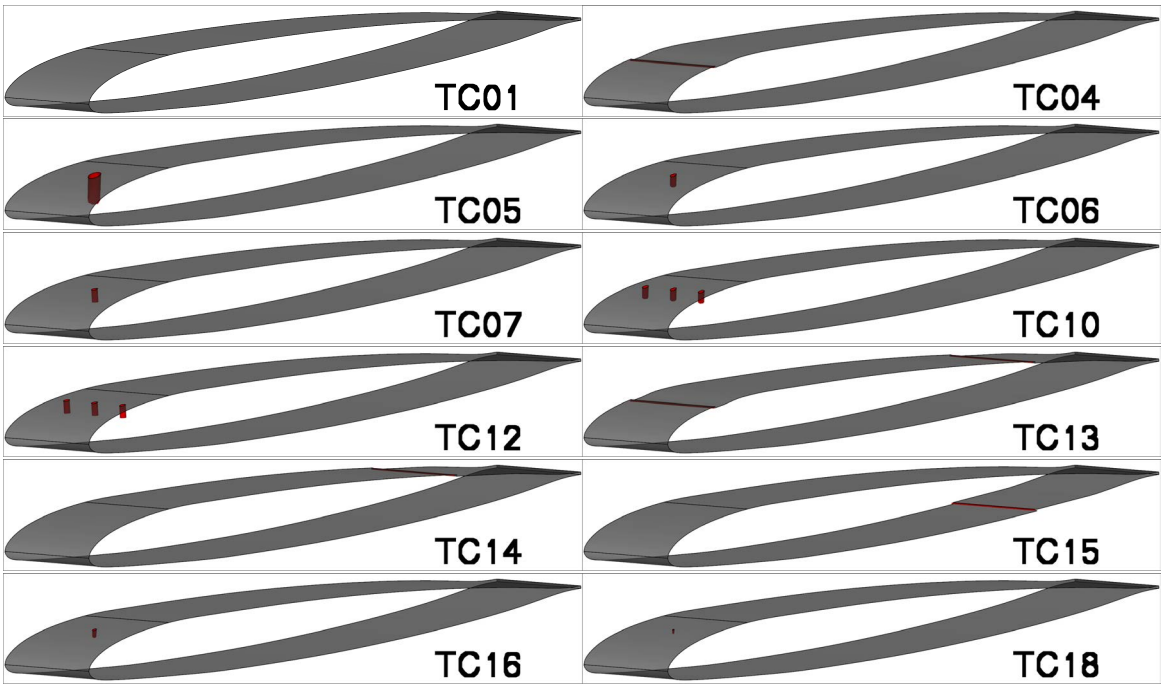

Figure 4.15: Test matrix of RANS computations.

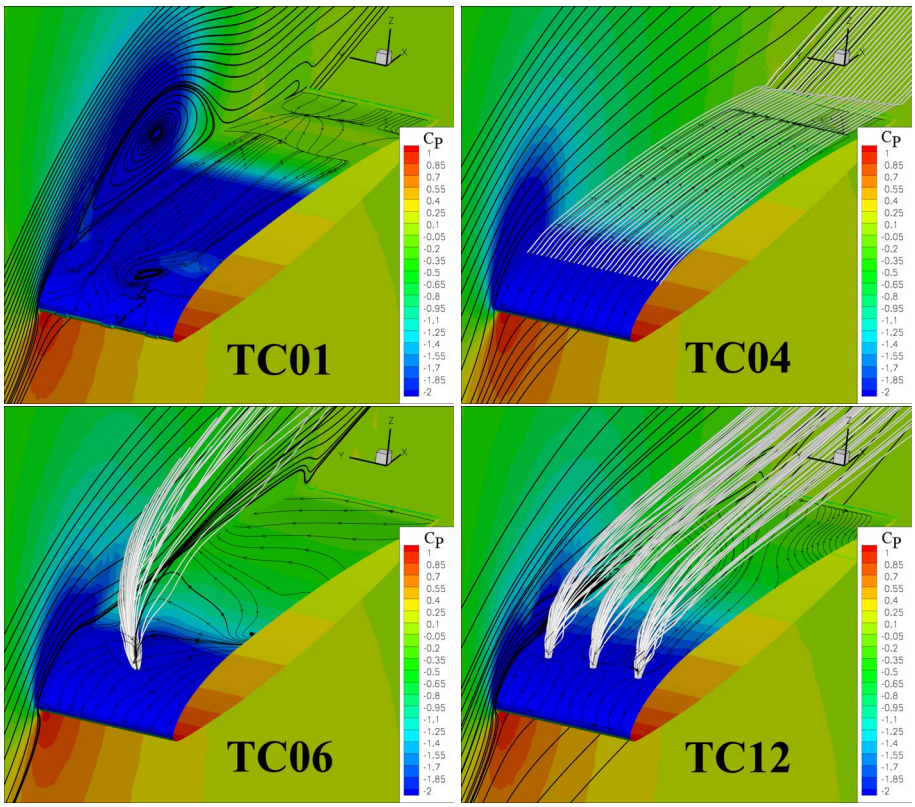

Figure 4.16: Test matrix for URANS computations with an example of each jet type group, showing flow state at α=16.35° on the upstroke for the maximum mass flow rate tested. (Top, left) Clean case with unsuppressed dynamic stall vortex (TC01); (Top, right) tangential slot 0.5 mm (TC04); (Bottom, left) 3 mm jet at 60 mm spacing inclined/skewed at 45°/45° (TC06); (Bottom, right) Vertical 3 mm jet at 20 mm spacing (TC12). Jets were at 10% chord.

stream, and skewed at 45° across the flow with a jet spacing of 60 mm (for example TC06 in Fig. 4.16) or 20 mm. The inclination is relative to the model chord and 45° was chosen to be approximately half way between the vertical jet and the tangential jet angles. In the RANS results, three effects of the jets are observed: firstly a vortex is generated at the root of the jet, which propagates along the top side of the OA209, secondly a sideways momentum is given to the flow so that the dynamic stall vortex is not purely 2D, and finally the angling of the jets downstream reduces the drag, by adding some of the jet thrust in the forward direction, and turning the flow further toward the surface due to the Coanda effect. The vortex along the wall will help the flow to remain attached longer, and it is hoped that the break-up of the 2D vortex will reduce the height of the dynamic stall peaks in lift, drag and momentum as the dynamic stall vortex separates. It is postulated that a similar 3D effect due to model end conditions (section 3.2 [35]), which causes a reduction in lift for experiments at moderate angles of attack, causes the overestimation of the size of the lift and pitching moment peaks at the moment that the dynamic stall vortex separates when compared with experiment [103].

The jet diameter and spacing were varied at constant mass flow for the dynamic stall vortex reduction. With reducing hole diameter and constant mass flow through the jets, smaller jets have higher Mach number, stagnation pressure and injected energy (Table 4.3). The overall effect of reducing the spacing to 20 mm is a reduction in lift and an increase in drag over the single jet case, since the flow is not turned as much toward the airfoil, and no vortices are created along the top surface of the airfoil. In fact the total effect of reducing the spacing to 20 mm (TC10) is to join the jet flows into a single blockage. As seen in Table 4.3, at C_μ=0.06 all of the 60 mm jet spacing configurations increased lift by 50-80%, and decreased drag by around 35%. The TC06 was selected for URANS testing due to practical considerations of the feeder pressure and geometry.

The test cases for the Coanda effect blowing use slots tangential to the airfoil surface to increase lift by turning the external flow back toward the airfoil (for example TC04 in Fig. 4.16). This is done by using the Coanda effect on the flow near the separation streamline, and by providing blowing in the streamwise direction along the wall so that the reverse flow, which would form near the airfoil for separated flow, is not permitted. Slot blowing at the 10% chord position caused fully attached flow on the rear 90% of the airfoil, and only a small separation of the front 10% of the airfoil. As seen in Table 4.3, for the TC04 at C_μ=0.06 the lift is increased by 70% and the drag is reduced by 60%, due in part to the direction of the jet rearward, and also to the almost complete absence of separated regions.

Two basic problems remain with the tangential slot jets. Firstly due to the large exit area of the slots the jet pressures used are low, leaving little room to operate at lower pressure to reduce power use, and the possibility of reducing the slot width is limited since the slot is already only 0.5 mm wide. Additionally the alteration of the airfoil contour at the point where the highest Mach number flow is found on the advancing blade is likely to be a serious problem unless the slot itself is a deployable object. The TC04 was nevertheless selected for URANS testing because of its good performance.

The test cases for the dynamic stall vortex limitation use vertical jets at 10% chord to limit the upstream travel of the dynamic stall vortex (similarly to the back-flow flap [3, 80]), and convert it to a static separation, with accompanying suppression of dynamic separation effects (for example TC12 in Fig. 4.16). The idea is to create a separation limiting effect similar to that possible for a vertical slot, but without forcing the boundary layer to separate fully.

This idea did not work fully for a jet spacing of 60 mm. However with a jet spacing of 20 mm (TC12) the size of the separation is limited by the front edge of the separation anchoring at the jet, and a modest improvement in lift, drag and pitching moment were achieved at C_μ=0.06, with around 30% improvement in lift and 30% reduction in drag over the reference case, as can be seen in Table 4.3. Confirming the selection of TC12 for further URANS study were the results at half pressure (C_μ=0.03), where the flow was fully turned and only a small separation was seen behind the jets. It is postulated that the additional ventilation provided to the back half of the airfoil between

Table 4.3: Results of the RANS investigations.

Case Name	P_j (bar)	$\dot{m}_j$ (kg/s/m)	C_L/Ref	C_D/Ref	C_{M_p}/Ref
Reference case					
TC01	0	0	1.00	1.00	1.00
DS vortex reduction (C_q=0.01, C_μ=0.06)					
TC05	3.04	-0.22	1.52	0.64	0.28
TC06	11.11	-0.22	1.72	0.66	0.27
TC10	3.35	-0.22	1.24	0.99	1.20
TC16	41.68	-0.22	1.72	0.62	0.23
TC18	278.9	-0.22	1.79	0.63	0.22
DS vortex reduction (C_q=0.005, C_μ=0.03)					
TC05	1.52	-0.12	1.02	0.93	0.90
TC06	5.55	-0.11	1.01	0.94	0.89
TC10	1.67	-0.11	0.94	0.88	0.81
TC16	20.84	-0.12	1.14	0.85	0.72
TC18	120.2	-0.11	0.97	0.96	1.01
Coanda effect blowing (C_q=0.01, C_μ=0.06)					
TC04	2.07	-0.22	1.70	0.39	-0.01
TC13	1.04	-0.22	1.01	0.64	0.54
TC14	1.99	-0.22	1.08	0.92	1.14
TC15	1.99	-0.22	1.09	0.90	1.14
Coanda effect blowing (C_q=0.005, C_μ=0.03)					
TC04	1.03	-0.11	0.86	0.74	0.56
TC13	0.52	0.01	1.05	0.87	0.79
TC14	1.00	-0.11	0.97	0.95	0.94
TC15	1.00	-0.11	1.03	0.95	0.95
DS vortex limitation (C_q=0.01, C_μ=0.06)					
TC07	24.40	-0.22	0.94	0.80	0.94
TC12	6.70	-0.22	1.31	0.73	0.59
DS vortex limitation (C_q=0.005, C_μ=0.03)					
TC07	12.20	-0.12	0.92	0.97	0.99
TC12	3.35	-0.12	1.23	0.59	0.10

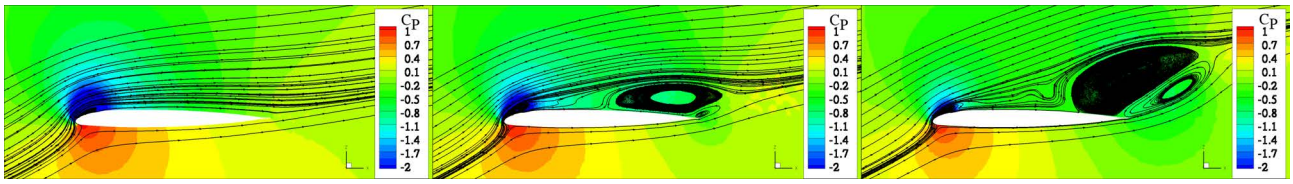

Figure 4.17: Comparison of flow topologies on the periodic plane before (left), at (middle) and after (right) dynamic stall for the "TC04" (tangential slot blowing) OA209 airfoil. The three cases correspond to α=16.4°, 17.5° and 18.5° respectively for an instantaneous solution at the periodic plane (between the jets).

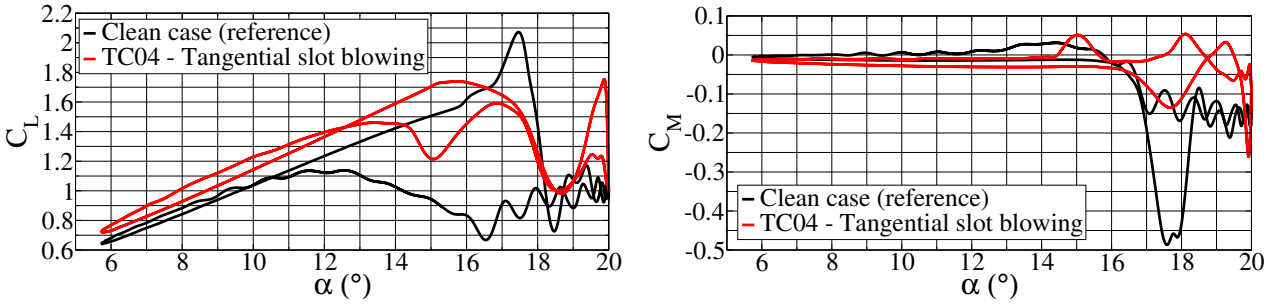

Figure 4.18: URANS results of the coefficients over one pitching cycle α=12.87±7.13°, ω^*=0.101 for: (left) Lift coefficient, (right) Pitching moment coefficient. Shown is the result for the "TC04" (tangential slot blowing) plotted against the "Clean" OA209 airfoil.

the jets causes the large difference to the vertical slot case investigated initially. For the half-pressure case, the improvement in lift over the reference case was only 20%, but the drag was only 60% of that for the reference case, and improvement of 10% over the case with full pressure.

The RANS computations indicated a reduction in drag and an increase in lift for configurations with air jets which allowed the configurations using each of the three control strategies to be identified. As an example of the Coanda effect blowing, the tangential slow configuration TC04 was selected. As an example of the dynamic stall vortex reduction, the inclined/skewed jet configuration TC06 was selected. As an example of the dynamic stall vortex limitation and anchoring the vertical jet configuration TC12 was selected. These configurations were then investigated using URANS computations with pitching motion.

4.1.7 URANS results with α=12.87±7.13° at C_μ=0.06

The test cases TC01, TC04, TC06 and TC12 were investigated with URANS computations on a dynamically pitching OA209 airfoil. The test cases are shown in Fig. 4.16 and have one example of each flow control method, together with the reference case. The images in Fig. 4.16 are all taken at α=16.35° on the upstroke, and large differences in the flow topology due to the flow control mechanisms are visible. The flow in the reference case has just developed the main dynamic stall vortex, where the cases with air blowing have all suppressed it to some degree. For the TC04, which used blowing from a slot parallel to the airfoil surface, the flow is fully attached except for a small, flat separation near the trailing edge. For the TC06, which used jets inclined in the flow direction and skewed to the left, the separation has been greatly reduced, and no real vortex is currently visible. A strong sideward component to the flow on the surface has been created due to the jet skew. For the TC12, which used vertical jets, the flow is separated both before and after the jets, but the size of both is reduced. A strong anchoring of the separation on the back of the airfoil at the position of the jets is visible, as is the termination of the separated region on the front of the airfoil by the jets.

Table 4.4: Results of the URANS investigations.

Case Name	P_j (bar)	$\dot{m}_j$(kg/s/m)	$\overline{C_L}$/Ref	$\overline{C_D}$/Ref	C_{M_p}/Ref	C_{D_p}/Ref
Reference case						
TC01	0	0	1.00	1.00	1.00	1.00
DS vortex reduction (C_q=0.01, C_μ=0.06)						
TC06	11.11	-0.22	1.07	0.56	0.74	0.68
DS vortex reduction (C_q=0.005, C_μ=0.03)						
TC06	5.55	-0.11	1.03	0.73	0.76	0.79
Coanda effect blowing (C_q=0.01, C_μ=0.06)						
TC04	2.07	-0.22	1.18	0.31	0.62	0.62
Coanda effect blowing (C_q=0.005, C_μ=0.03)						
TC04	1.03	-0.11	1.07	0.68	0.83	0.80
DS vortex limitation (C_q=0.01, C_μ=0.06)						
TC12	6.70	-0.22	0.99	0.58	0.15	0.22
DS vortex limitation (C_q=0.005, C_μ=0.03)						
TC12	3.35	-0.12	1.02	0.61	0.29	0.31

Coanda effect blowing:

The effect of the 0.5 mm slot used for the Coanda effect blowing test case (TC04) is to shift the separation vortex rearward and cause earlier reattachment (Fig. 4.17). The high Mach number of the air exiting the slot causes a small separation in front of the slot during the upstroke (Fig. 4.17, left), which expands as the angle of attack increases, but is qualitatively similar, even after stall. After stall, the blowing prevents the formation of the dynamic stall vortex until halfway back on the airfoil (Fig. 4.17, middle). This vortex is smaller, weaker and positioned further back than for the clean case, meaning that the lift and pitching peaks are reduced. As the dynamic stall vortex becomes very large and moves over the trailing edge of the airfoil (Fig. 4.17, right) the blowing of the jet still enforces attached flow along the majority of the airfoil.

The stall for the TC04 occurs at approximately the same angle as for the reference airfoil, and there is no large lift peak since no large dynamic stall vortex forms (Fig. 4.18, left). An increase in lift of up to 15% was seen during the attached flow part of the upstroke due to the jet being pointed directly aft of the airfoil, decreasing at lower angles of attack, and a net thrust (negative drag) was produced at low angles of attack due to the jet being pointed directly backward. While the improvements in mean lift (18%) and mean drag (69%) are impressive (Table 4.4) they come at the cost of a significant modification to the airfoil contour for the injection slot and the creation of a second dynamic stall vortex. The pitching moment peak from the first dynamic stall vortex is reduced by 38% (Fig. 4.18, right) and the shape of both the lift and pitching moment peaks is rounded when compared to the reference case. The rounding of the lift peak is due to the slow growth of a separation on the front part of the airfoil, which is prevented by the jet from spreading backwards as is the case for the clean airfoil. In addition, the growth of the main dynamic stall vortex limited to the back half of the airfoil. The vortex later swims off, but without giving a large dynamic stall peak. Due to the airfoil modification, the TC04 is not preferred to the porthole configurations TC06 or TC12.

Dynamic stall vortex reduction:

The effect of the inclined and skewed jets (TC06) is to reduce the size of the dynamic stall vortex and to stabilise its position at the jets. Fig. 4.19 (left) shows the flow on the periodic plane, just after the end of the attached flow section of the upstroke. Here the sidewards flow of the air jets

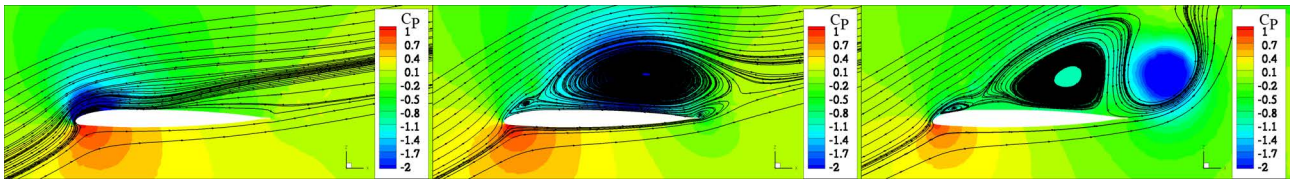

Figure 4.19: Comparison of flow topologies on the periodic plane before (left), at (middle) and after (right) dynamic stall for the "TC06" (inclined/skewed blowing) OA209 airfoil. The three cases correspond to α=16.4°, 19.2° and 19.7° respectively for an instantaneous solution at the periodic plane (between the jets).

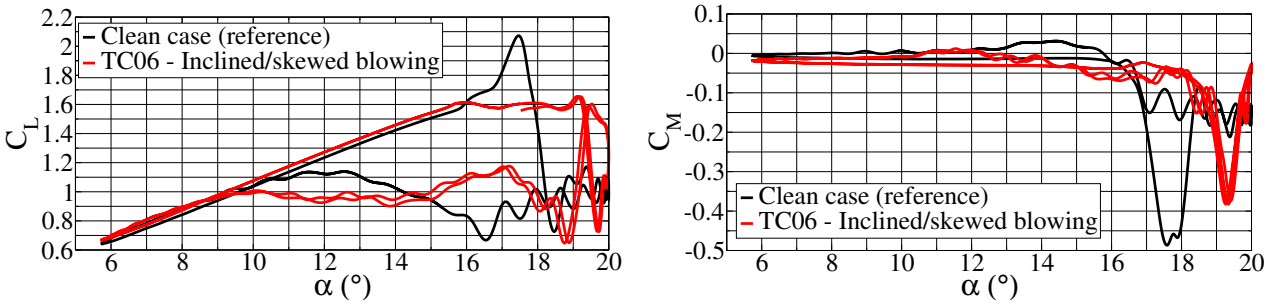

Figure 4.20: URANS results of the coefficients over one pitching cycle α=12.87±7.13°, ω^*=0.101 for: (left) Lift coefficient, (right) Pitching moment coefficient. Shown is the result for the "TC06" (inclined/skewed blowing) plotted against the "Clean" OA209 airfoil.

causes a stable deviation of the streamlines upward away from the trailing edge of the airfoil which does not immediately separate. Instead this state persists for around $\Delta\alpha$=3° until finally a dynamic stall vortex starts to form, at a delay of about $\Delta\alpha$=2° from the reference case (Fig. 4.19, middle). Finally the dynamic stall vortex moves downstream (Fig. 4.19, right), with a considerably reduced strength, but the counter-rotating vortex formed at the trailing edge is much stronger. As a result of the strengthening of the counter-rotating vortex, a second dynamic stall vortex is produced, which is as strong as the original vortex.

With TC06 a constant lift up to just over α=19° (Fig. 4.20, left) is produced, and the lift peak seen in the reference case does not appear. After separation and on the downstroke a second vortex is released from the surface creating a second peak not present in the clean case. The two peaks in the pitching moment are equally large (Fig. 4.20, right) and are reduced by 26% over the clean case. The first peak in pitching moment is moved around 2° higher in angle, consistent with movement seen in the drop in lift coefficient. Likewise the peak in drag (Table 4.4) is reduced by 32%, with a similar movement in the peak position. After this the flow in the reference and TC06 test cases is rather similar, although the reattachment for the TC06 is marginally later. For the test case DS2 investigated here, dynamic stall could not be avoided, but indications are that for light dynamic stall the separation may be delayed sufficiently to avoid dynamic stall entirely. As seen in Table 4.4, the improvements in the mean lift and drag for TC06 were 7% and 44% respectively.

Due to the narrowness of the computational domain (20% chord), the splitting of the main dynamic stall vortex into smaller vortices with x, y and z components to the axis was not captured. It is expected that these vortices would have a width of around 1 chord and so a computational domain of at least 2-3 chords would be needed to capture this behaviour, for a computational cost around 10 times that of these investigations. Additionally, due to the computational domain size a quasi-two-dimensionality is enforced at the trailing edge which will tend to strengthen both the dynamic stall vortex and the counter-rotating vortex from the trailing edge, so it remains to be seen whether a full 3D investigation can better estimate the respective strengths of these two vortices. This effect would

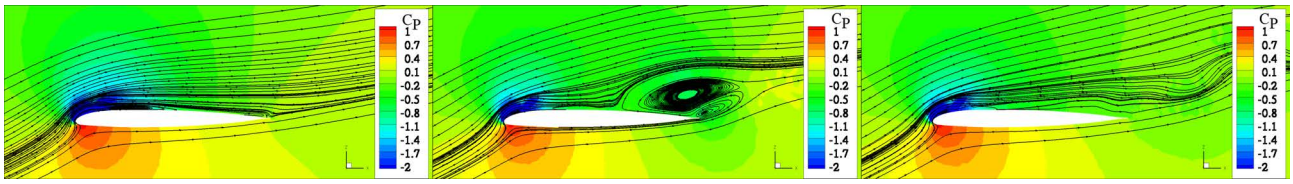

Figure 4.21: Comparison of flow topologies on the periodic plane before (left), at (middle) and after (right) dynamic stall for the "TC12" (vertical blowing) OA209 airfoil. The three cases correspond to α=16.4°, 17.5° and 18.5° respectively for an instantaneous solution at the periodic plane (between the jets).

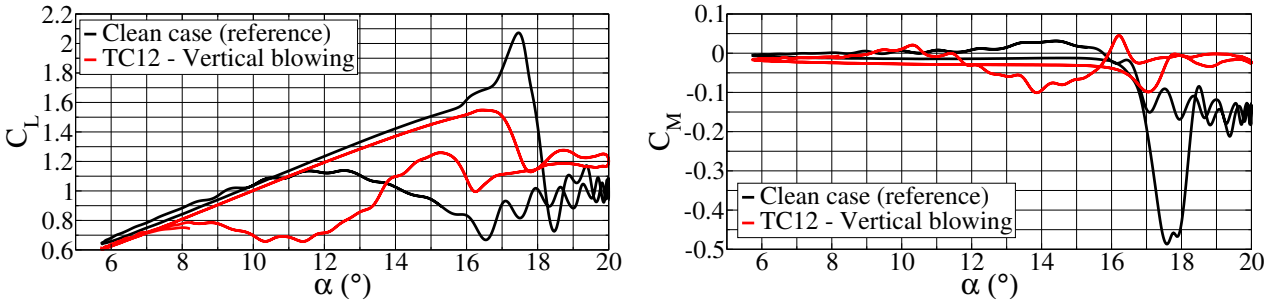

Figure 4.22: URANS results of the coefficients over one pitching cycle α=12.87±7.13°, ω^*=0.101 for: (left) Lift coefficient, (right) Pitching moment coefficient. Shown is the result for the "TC12" (vertical blowing) plotted against the "Clean" OA209 airfoil.

be expected to further reduce the strength of the dynamic stall vortex.

Dynamic stall vortex limitation:

The effect of the vertical jets for dynamic stall vortex limitation (TC12) is to cause the formation of a static separation bubble behind the injection position, which is stable in size and anchored in position by the jets. This separation is limited in height and does not block the flow. A separation is also formed in front of the jets, but this is stable and not connected to any other separation region. As seen in Fig. 4.21 (left), the vertical blowing is detrimental during the parts of the cycle with attached flow, since it forces the flow before and after the jets to separate, as well as reducing the lift due to the direct jet acceleration downward on the airfoil. In a practical implementation with constant blowing the jets would only be turned on during the parts of the cycle needing stabilisation, so this is not necessarily a problem. Switching the flow on and off once each per cycle was investigated numerically, and it could be shown that at the start and end of jet actuation the solution moved neatly between the solution for the jets and the solution for the clean OA209 airfoil in under $\Delta\alpha$=0.5° of movement.

At stall (Fig. 4.21, middle), a dynamic stall vortex similar to that seen for TC04 is formed near the rear of the airfoil. In addition a long, flat separation lying close to the airfoil surface stretches between the jets and the upstream side of the dynamic stall vortex. After stall (Fig. 4.21, right) the flat separations around the injectors stretch to the trailing edge and this causes the flow to be less unstable than for the reference case, even though separation is present. A similar arrangement using a vertical slot produces an unstable separated region, and the stabilising effect for TC12 is the ventilation of the separated region from the front between the individual jets.

As seen in Fig. 4.22 (left) the separation of the flow occurs at about the same angle of attack as for the reference airfoil (α=16°), but the stabilisation of the separation results in a much more stable coefficient history after separation. The lift near the maximum angle is improved by 20% between α=19°-20°. The flow reattaches around $\Delta\alpha$=3° later than for the reference case, meaning that the mean lift was reduced 1% from the reference case (Table 4.4), although when only the top half of the

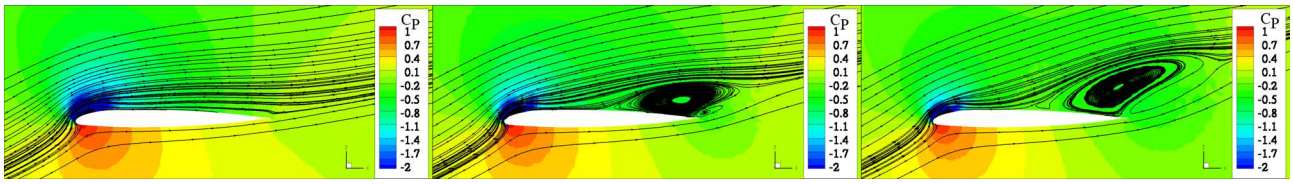

Figure 4.23: Comparison of flow topologies on the periodic plane before (left), at (middle) and after (right) dynamic stall for the "TC12" (vertical blowing) OA209 airfoil at half pressure. α=16.4°, 17.5° and 18.5° respectively for an instantaneous solution at the periodic plane (between the jets).

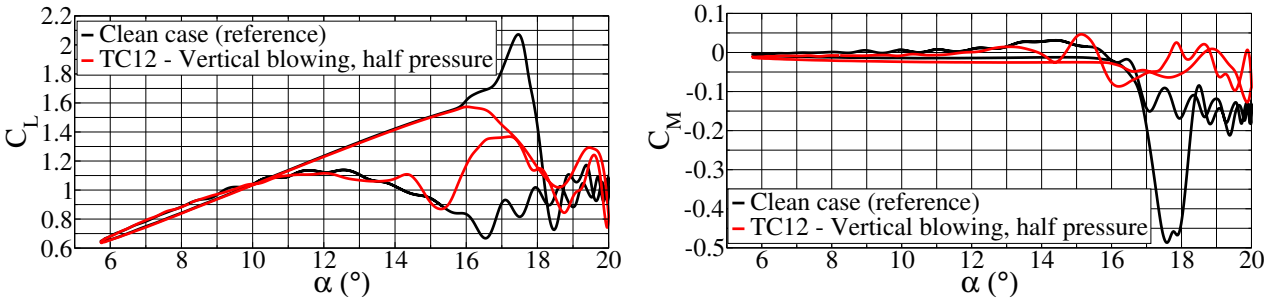

Figure 4.24: URANS results of the coefficients over one pitching cycle α=12.87±7.13°, ω^*=0.101 for: (left) Lift coefficient, (right) Pitching moment coefficient. Shown is the result for the "TC12" (vertical blowing) with half-pressure blowing plotted against the "Clean" OA209 airfoil.

cycle is considered, a modest 5% gain over the reference case is seen. The late reattachment can be solved by turning the jets off at the appropriate moment.

The improvement in the pitching moment coefficient (Fig. 4.22, right) is by far the best for any configuration investigated, and no second dynamic stall peak is formed. As reported in Table 4.4, a reduction in the pitching moment peak of 85% was found and the mean drag coefficient is improved by 42%.

4.1.8 URANS results with α=12.87±7.13° at C_μ=0.03

To investigate whether the improvements noted in mean lift, mean drag, pitching moment peak and drag peak were linear with the amount of air used for blowing, each of the test cases TC04, TC06 and TC12 were also tested with half-pressure blowing (C_μ=0.03). For TC04 (tangential slot blowing) and TC06 (inclined/skewed blowing), the effect of the pressure reduction was to create a qualitatively similar change to that for the full pressure case, but with the improvements in mean lift, mean drag, pitching moment peak and drag peak over the reference case approximately halved (Table 4.4). This means that the improvements will react linearly. For TC04, the pressure was reduced to around 1 bar, which was the limit for supersonic blowing in this case, which sets the lower limit for this linear relationship. For TC06 a further factor of 5.5 reduction in pressure would be possible before the pressure is at 1 bar and the blowing is no longer supersonic.

For the vertical blowing (TC12), halving the blowing pressure had less effect than expected by a linear dependency. As seen in Table 4.4, the mean lift and drag were marginally improved, mostly due to the reduction of the negative effects of the vertical blowing, since the jet effect downward and the size of the separation around the jets in the attached flow are both reduced (Fig. 4.23, left). As the dynamic stall vortex forms (Fig. 4.23, middle), the size is approximately the same as for the full-pressure case, but the separations around the jet are flatter and closer to the body. The dynamic stall vortex remains attached to the airfoil longer than for the full-pressure case (Fig. 4.23, right).

The improvement in the behaviour during the attached flow can be seen in the history of the lift

Table 4.5: Estimate of the power balance for the injector configurations for the top half of the cycle from α=15.1° on the upstroke to α=10.6° on the downstroke.

Case	W_j (kW/m)	$\overline{W_D}^{15.1\rightarrow 10.6^\circ}$ (kW/m)	Net power (kW/m)	Difference (kW/m)
Ref	0.0	29.7	29.7	0.0
TCO4, C_μ=0.06	21.0	13.7	34.7	5.0
TCO4, C_μ=0.03	4.8	21.6	26.4	-3.3
TCO6, C_μ=0.06	48.2	20.5	68.7	39.0
TCO6, C_μ=0.03	19.4	23.6	43.0	13.3
TC12, C_μ=0.06	40.4	16.0	56.4	26.7
TC12, C_μ=0.03	16.4	17.2	33.6	3.9

coefficient (Fig. 4.24, left) where the lift is now approximately the same as for the reference case. In addition the reduced pressure allows earlier reattachment of the flow during the downstroke. The reduction to the pitching moment peak was still 71% over the reference case, rather than 42% as might be linearly expected (Table 4.4) and it can be seen that the pitching moment history is qualitatively similar to that for the full-pressure blowing (Fig. 4.24, right).

4.1.9 Estimate of the power required for actuation

Estimating the power required for a realistic implementation of the actuation is difficult since no pulsed actuator for exactly these test cases has yet been built. An order of magnitude estimate of the power balance for the sections of blade undergoing dynamic stall can be made if it assumed that the power for the actuators is similar to the power required by a constant-temperature compressor for supply of a particular pressure and mass flux: $W_j = ln\left(\frac{P_j}{P_\infty}\right)\frac{RT_\infty \dot{m}}{2b}$, where it is assumed that the gas is being compressed from the local flight static pressure and temperature P_∞=57228 Pa and T_∞=258 K to the injector pressure P_j. This gas is air with heat capacity C=1004 J/K/kg and is supplied over a blade length of b meters. The engine power required to offset the drag is: $W_D = \frac{1}{2}C_D A_{Ref}\rho_\infty v_\infty^3$, which can be expressed in kW per meter of blade. Table 4.5 shows the power balance with these assumptions. The half pressure blowing case for the TC04 and the half pressure case for TC12 have net powers close to the original clean wing. The actuation power, pump efficiency and duct pressure losses are not included in this computation. The assumptions here use only the top part of the cycle, since for a helicopter the advancing blade will be at high transonic Mach numbers, which are not simulated in the wind tunnel.

4.1.10 Conclusion

The numerical investigation of air jets for dynamic stall control has been described for the SIMCOS DS2 test case (M=0.31, Re=1.16e6, α=12.87±7.13°, ω^*=0.101). The dynamic stall control strategies concentrated on using blowing with air jets to keep the flow attached, reduce the strength of the dynamic stall vortex, and to anchor the separation of the flow and the attachment point of the dynamic stall vortex. Steady RANS computations were first used to narrow a wide field of candidates to one candidate for each flow control strategy.

Computations using URANS on the pitching airfoil showed that each of the three candidates investigated increased the mean lift and reduced the mean drag over a pitching cycle, while reducing the peaks in pitching moment and drag caused during the production of the dynamic stall vortex. Each configuration was investigated for two blowing pressures to investigate the linearity of the flow control

effect. From the results of the URANS computations, a configuration using vertical 3 mm portholes at 10% chord and 20 mm spacing (TC12) is the preferred configuration, with a configuration using a 3 mm inclined porthole at 60 mm spacing (TC06) as a second choice and a tangential slot (TC04) as the third choice. For the best configuration (TC12), improvements in the pitching moment peak of 85% and in the drag peak of 78% were observed, together with a 42% reduction in the mean drag over the unsteady pitching cycle. Based on these results a wind tunnel model for the DNW-TWG was constructed to investigate pulsed blowing on the vertical jet configuration.

The vertical jets have the interesting property of stabilising the separation point at the point of injection, with a small separation in front of the jets which stabilises the large vortex behind the jets by a constant flow between the jets. This avoids the unsteadiness in attachment position and size of the large vortex which would otherwise appear, such that the flow after separation is less unsteady than without flow control.

An open question from this investigation is the effect of a 3D computation with sufficient domain width to see full 3D development of the stall vortex, since the domain width here was so narrow as to enforce mainly 2D behaviour at higher stall angles.

4.2 Design of pulsed blowing experiments using CFD [2]

Experiments using synthetic jet actuators (SJAs) or pulsed blowing [44, 117] assume that a similar flow control can be achieved as with constant blowing, but using significantly less power, although the results do not show this unambiguously. The investigation in section 4.1 identified configurations of constant blowing jets, which reduced the effects of dynamic stall. RANS computations at a constant angle of attack above stall and URANS computations with pitching motion were compared, showing that jet configurations which increased lift and reduced drag in the RANS computations also reduced dynamic stall in the URANS computations with pitching motion. Estimates of required power were also made in section 4.1. This section investigates pulsed jet configurations on an airfoil at a static angle of attack above stall, with the assumption from section 4.1 that increased lift and reduced drag indicates a configuration which reduces dynamic stall on a pitching airfoil. This approach results in a large computational saving over computations with pitching motion, since the computations converge on the time scale of the jet pulse (0.0017 seconds), rather than on the scale of the pitching motion (0.17 seconds).

4.2.1 Grid and solver

Computations using the DLR-TAU solver are presented for a 3D slice of a dynamically pitching OA209 airfoil at M=0.31, Re=1.16e6, α=12.87$\pm$7.13°, ω^*=0.101 by the same method as in section 4.1. Reynolds-averaged Navier-Stokes (RANS) and Unsteady RANS (URANS) computations were undertaken with the DLR-TAU release 2009.1.0 [109]. The node-based finite-volume solver was used on an unstructured grid generated according to the guidelines of Richter et al. [103] using the Centaur^{TM}[1] unstructured grid generator. All computations were fully turbulent, using the Spalart-Allmaras turbulence model [114] with the Edwards modification (SAE), due to its excellent speed and stability, and since results match the experimentally observed dynamic stall behaviour at this test condition. The grid domain was a 3D slice of a 300 mm-chord airfoil with a width of 20% chord (60 mm), bounded by periodic side-walls (Figure 4.25), with a total of 1.5 or 1.2 million grid nodes, for the cases with and without actuators respectively.

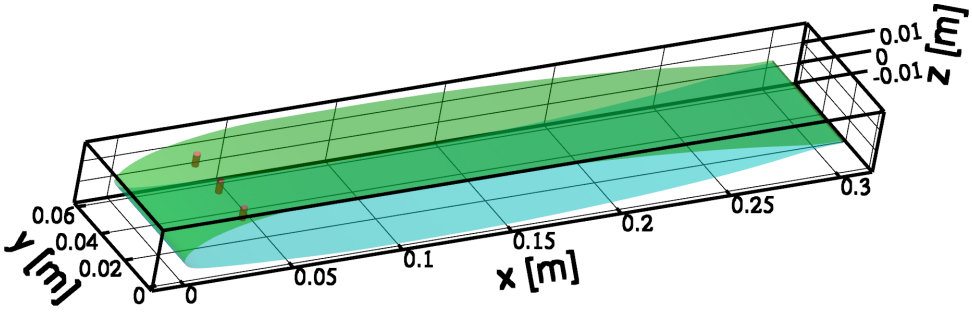

Figure 4.25: Airfoil gridded area for the TC12 geometry.

The RANS computations used 10000 time-steps (70 CPUh), but true convergence was not reached due to the highly separated flow conditions computed. Coefficients were averaged over 2000 time-steps to obtain the values quoted in this section. The URANS computations with a pitching airfoil for the constant-blowing or clean test cases used 1600 time-steps per period with 400 inner iterations per time-step. Significantly more inner iterations were required for the cases with constant jet blowing

[2]Text and illustrations in this section are taken from [26]: Gardner, A.D., Knopp, T., Richter, K., Rosemann, H. "Numerical investigation of pulsed air jets for dynamic stall control on the OA209 airfoil", In: *Notes on Numerical Fluid Mechanics and Multidisciplinary Design: New Results in Numerical and Experimental Fluid Mechanics VIII*, Springer Verlag, 2013. ISBN 978-3-642-35679-7, pp. 287-295, DOI: 10.1007/978-3-642-35680-3_35

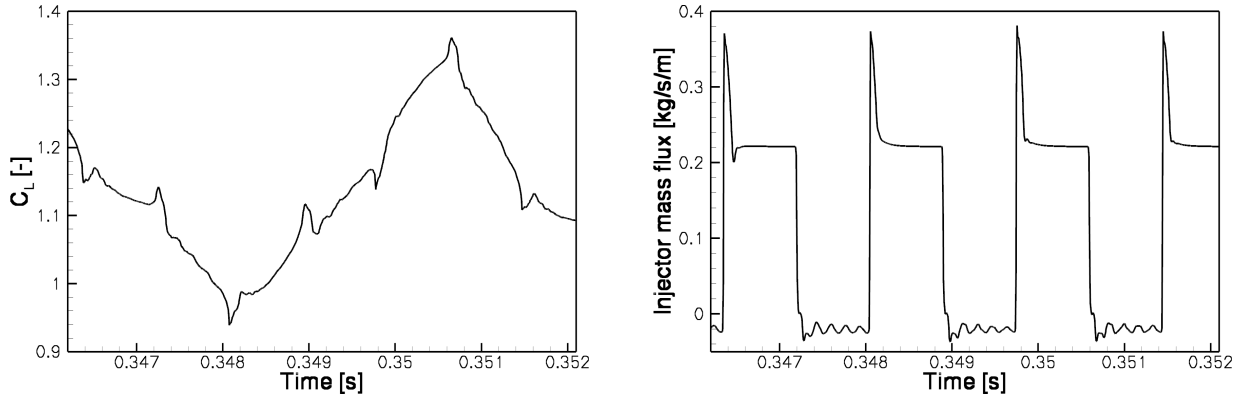

Figure 4.26: URANS computations at constant angle of attack α=20°. Showing the one lift cycle Left = Lift, Right = Mass flux.

than previously observed for clean cases. A minimum of 3 pitching cycles were computed for convergence, where convergence was assumed if the force coefficients for the second and third cycles were always within 1% of the coefficient value at minimum α. Each cycle cost 4000 CPUh.

For URANS simulations of constant blowing at a static angle of attack, the time-stepping was 1.7e-5 seconds, but for pulsed blowing the computations were not stable, with both stability and convergence first achieved for a time-step of 2e-6 seconds. This converted to 800 time-steps per pulse or 85000 time-steps per period for computations with pitching motion at DS2, with an increase in computational time by about a factor of 5 over constant blowing.

The forces on the airfoil are the sum of the pressure and viscous forces for all nodes on the surface (including the airfoil top, airfoil bottom, airfoil trailing edge and the internal surfaces of the injection holes), and the forces on the injection inflow surfaces computed from the mass flux and velocity across the inflow plane. The lift, drag and pitching moment are equal to the true forces seen in an experiment on this configuration excepting the unmodelled forces in the gas delivery tubing.

4.2.2 The "pulsed injection" actuator boundary condition

As part of SIMCOS and the LUFO IV project Aeronext, the DLR-TAU code was extended with a new boundary condition for flow control [63]. The "pulsed injection" boundary condition, used with a time-stepping method (URANS), allows time-variant combinations of blowing and suction either by constant mass flow, constant pressure, or constant total conditions. This boundary condition was used for the numerical prediction of flow control by jets in SIMCOS and Aeronext [34, 116].

The boundary conditions of the free jet can be set as incompressible or compressible, and the supersonic exit-plane of a Laval nozzle can be simulated setting the expansion ratio and total conditions. The eddy viscosity and the turbulent length scale are set using the method in chapter 5 of [93] to agree with available experimental data. The eddy viscosity ν_t is $\nu_t(x,t) = 0.11\sqrt{k_\nu}d = 0.11\sqrt{\frac{3}{2}}\mathrm{Tu}\,U_{\max}\frac{d}{2}$ with turbulent kinetic energy k_ν, turbulence intensity Tu, inflow diameter d, and maximum inflow velocity $U_{\max}$. The pulse duty cycle can be set between zero and one, and the code stability during switching of the square-wave signal is improved by smoothing the function to remove the singularities in the second derivative. In the mode used here, the total conditions are set by the user and the mass flux varies during the computation. This means that the flow cannot be turned off so we used an "off" cycle with a light suction of about 10% less than the local pressure, as seen in the mass flow rates across the boundary (Figure 4.26, Right). In all test cases shown, pulses at 589 Hz (100 pulses/pitching cycle for DS2) at duty cycle 50% were used.

Numerical tests have shown that the exact value of the mass flow of the free jet is necessary to correctly compute the aerodynamic coefficients. Thus the boundary condition cannot be set on the

Table 4.6: Results for constant angle of attack comparing RANS and URANS computations.

Case Name	P_j (bar)	$\dot{m}_j$(kg /s/m)	Duty Cycle	$\overline{C_L}$	$\overline{C_D}$	$\overline{C_L}$ /REF	$\overline{C_D}$ /REF
RANS, α=20.0°							
Clean	-	-	0.0	0.84	0.302	1.0	1.0
Half Pressure	3.35	0.125	1.0	1.07	0.251	1.27	0.83
Full Pressure	6.7	0.195	1.0	1.15	0.205	1.37	0.68
URANS, α=20.0°							
Clean	-	-	0.0	0.99	0.363	1.0	1.0
Half Pressure	3.35	0.125	1.0	1.06	0.223	1.07	0.61
Full Pressure	6.7	0.222	1.0	1.19	0.188	1.20	0.52
Pulsed 50%	6.7	0.103	0.5	1.19	0.423	1.20	1.17

Table 4.7: Results of the URANS investigations with pitching airfoil motion.

Case Name	P_j (bar)	$\dot{m}_j$(kg /s/m)	Duty Cycle	$\overline{C_L}$ /REF	$\overline{C_D}$ /REF	C_{M_p} /REF	C_{D_p} /REF
Clean	-	-	0.0	1.00	1.00	1.00	1.00
Half Pressure	3.35	0.125	1.0	1.02	0.61	0.29	0.31
Full Pressure	6.7	0.222	1.0	0.99	0.58	0.15	0.22
Pulsed 50%	6.7	0.103	0.5	NA	NA	0.96	0.92

surface of the airfoil since this would ignore the interaction between the jet and airfoil boundary layers. Instead the pipe leading to the injection porthole must be considered along with the boundary layers of the jet, and thus the actuation boundary is recessed in "pots" of two hole diameters depth under the surface of the airfoil (Figure 4.25).

4.2.3 Results

Using RANS computations, the TC12 configuration from section 4.1, consisting of vertical jets of 3 mm diameter (1% chord) at 10% chord and a spacing along the blade of 6.7% chord was investigated. This configuration has previously been shown to decrease dynamic stall when constant blowing is used. The flow was M=0.31, Re=1.16e6 for a steady angle of attack of α=20°, well above the static stall angle of α=14°. This approach allowed an engineering estimate of the performance improvement for a given injector over the clean case with comparatively little computing power when compared to pitching URANS computations, but with an unavoidable increase in the uncertainty associated with the results. The improvement in lift and drag compared with the reference airfoil was used as an indicator for the ability to control dynamic stall. The configuration was investigated for two total pressures (6.7 and 3.35 bar), giving air mass flow rates of around 0.2 kg/s per meter of blade and 0.1 kg/s/m. This supercritical injection had pressure ratios over the injector between 6 and 12. As a reference, the flow-off case without portholes was modelled.

For constant blowing, this jet configuration limits the upstream travel of the dynamic stall vortex (similarly to the back-flow flap [80]), and converts it to a static separation, with accompanying suppression of dynamic separation effects, but without forcing the boundary layer to separate fully. The separation on the airfoil is anchored in position by the jets and is limited in height avoiding blocking the flow. The separated region in front of the jets is stable. It was hoped that pulsed blowing would provide the same results, but with considerably less air use.

The results of the RANS computations with constant blowing are shown in Table 4.6, and an improvement over the reference case (half pressure/full pressure) in lift (27%/37%) and drag (17%/32%)

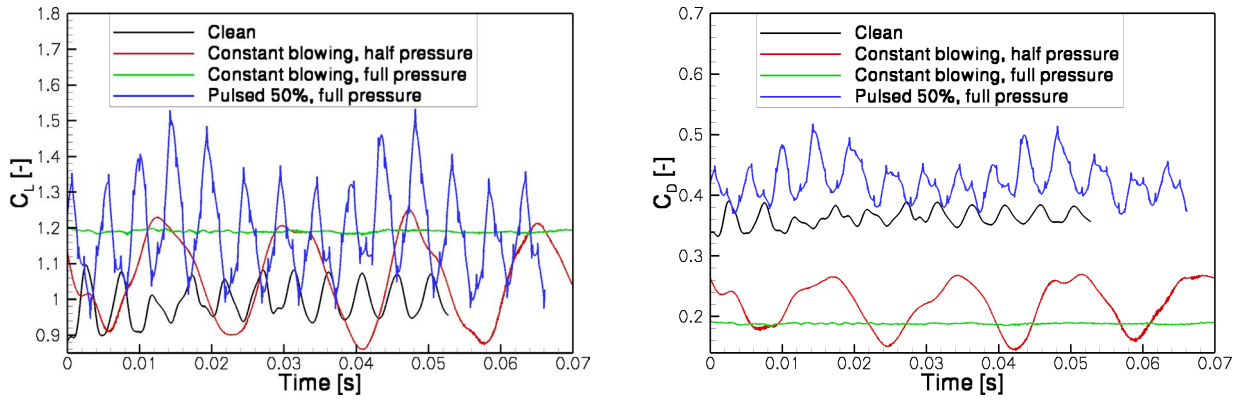

Figure 4.27: URANS computations at constant angle of attack α=20°. Showing the averaging windows for: Left = Lift, Right = Drag

was seen. For the URANS computations with constant blowing (Also Table 4.6), the absolute values of the lift and drag mean values remain similar for the jet blowing cases, but the mean lift and drag of the reference case are higher than for the RANS computations, meaning that the blowing cases now have a 7%/20% increase in lift and a 39%/48% decrease in drag over the reference case. The difference is because for unsteady flow the RANS computations do not average to the theoretically correct solution. The URANS computations with pulsed blowing created an increase in lift equal to that for the full pressure blowing (which required double the air mass flux), but more drag than the reference case.

Figure 4.27 shows the URANS results for lift and drag at constant angle of attack. The constant blowing at full pressure stabilises the flow, by providing a stable anchor for the separated flow on the top of the airfoil. For the half pressure blowing a new high-frequency unsteady behaviour is created as the jets cause a second smaller vortex to form on the front of the airfoil. The URANS results for pulsed blowing increase the lift similarly to full pressure blowing (20%), but the drag is 17% worse than for the reference case. As seen in Figure 4.26, the oscillation of the flow for pulsed blowing is unrelated to the pulsation frequency (although some peak locking to the pulsation edges occurs), and is caused by the small vortex in front of the jets. The overshoot in jet mass flux as the flow is established swiftly reduces to constant flow. This overshoot causes part of the increase in drag over the constant blowing case, with the remainder caused by the vortex splitting and rejoining as the jet is switched.

Figure 4.28 shows the flow conditions around the jets during jet starting and stopping. Before the start of the blowing, a vortex is over the jet. As the jet flow starts, a barrel-shock is pushed out, and the vortex is split at the jet. As the flow establishes, the jet narrows, until a parallel jet of the type seen for constant blowing is formed, and the two vortices behind the injector slowly merge. Finally static vortices are present; one in front and one behind the injector. As the flow is turned off, the vortex which was in front of the injector starts to extend downstream until at the start of the next cycle it is sitting directly over the injector.

Results for the jets at the SIMCOS DS2 test condition are shown in Figure 4.29 (M=0.31, Re=1.16e6, α=12.87$\pm$7.13°, ω^*=0.101). With constant blowing, a stable vortex is anchored behind the injection position. This stabilises the flow, even though separation is present. As seen in Figure 4.29, the injection of gas vertically reduces the lift in the attached flow due to the direct jet acceleration downward on the airfoil. The separation of the flow occurs at about the same angle of attack as for the reference airfoil (α=16°), but the stabilisation of the separation results in a much more stable coefficient history after separation, but the reattachment is significantly delayed. The mean lift was reduced 1% from the reference case (Table 4.6) and at α=20°, a 20% increase in the instantaneous lift is visible, the same as predicted by the URANS computations at α=20°. A reduction in the pitching moment peak

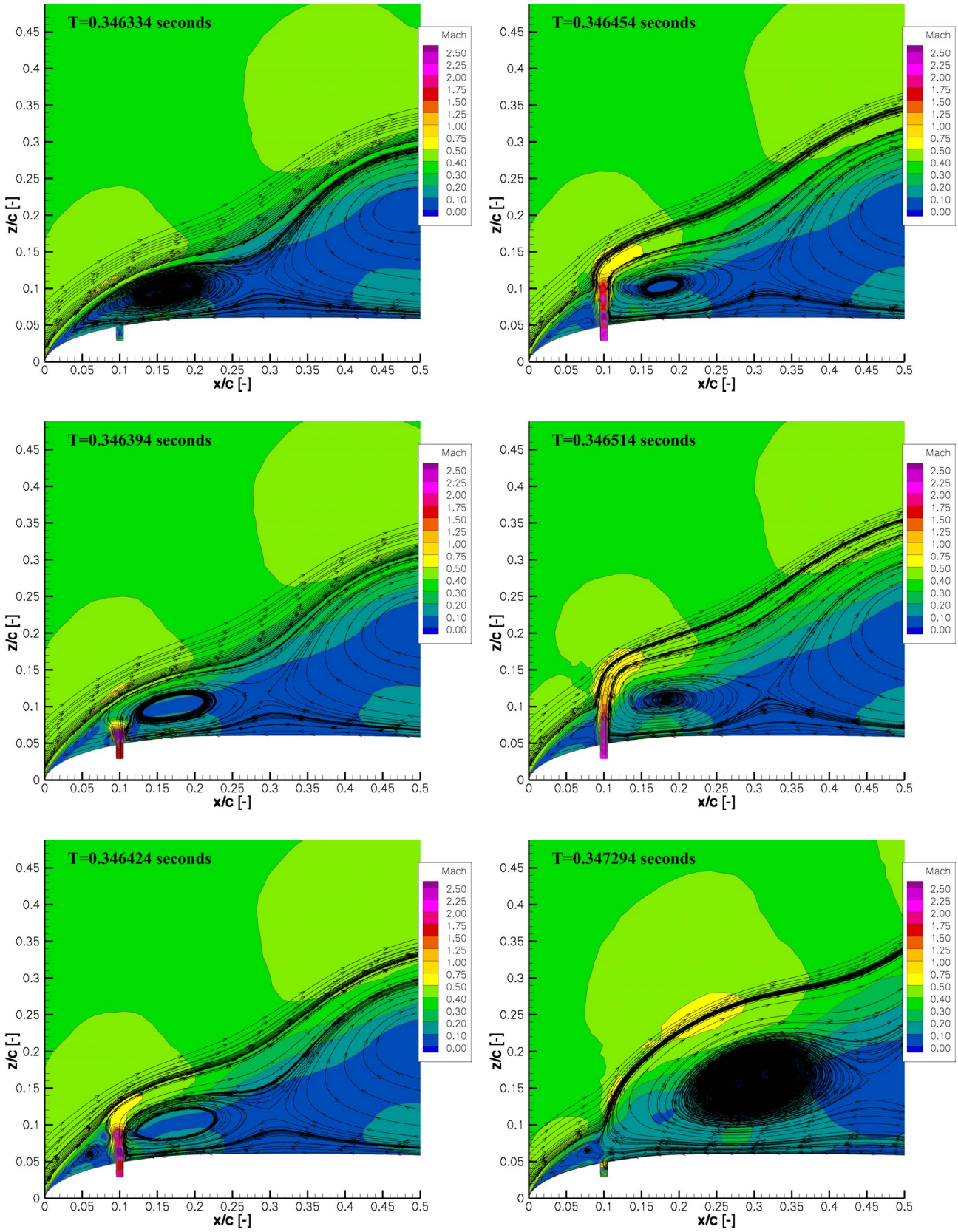

Figure 4.28: One pulse cycle: Left, Top to bottom: Before jet start, Initial shock, Barrel shock. Right top to bottom: Narrowing of jet, Fully developed jet, After jet is turned off.

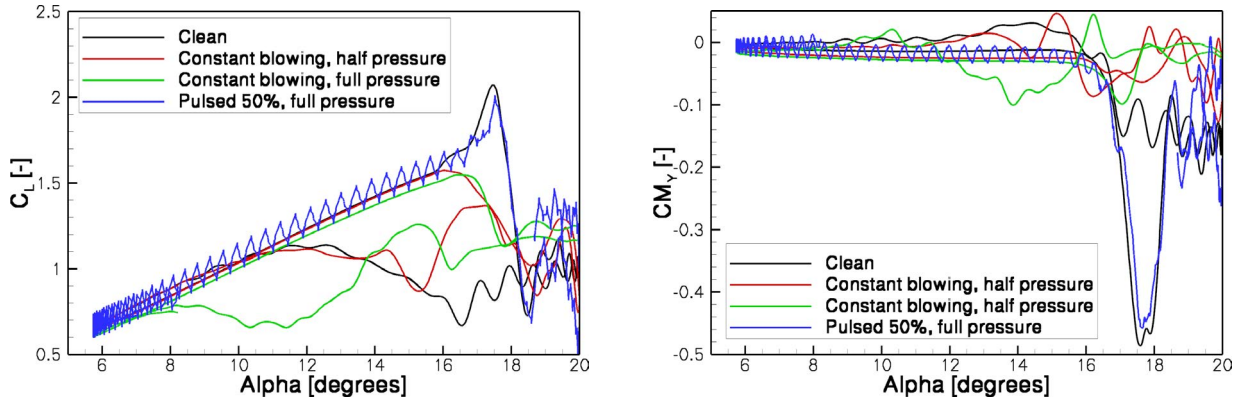

Figure 4.29: URANS computations for pitching at DS2. Comparison of different blowing methods: Left = Lift, Right = Pitching moment

of 85% was found and the mean drag coefficient improved by 42%.

For the half-pressure case (Figure 4.29), the performance is nearly as good as for the full-pressure case, with a considerable reduction in the pitching moment and drag peaks (71% and 69% respectively). Interestingly, the mean lift is slightly improved (2% higher than the reference case), due both to an improvement in the lift during the attached phase with the reduced jet effect, and to an earlier flow reattachment.

Computing pulsed flow together with pitching motion is especially challenging, requiring a large investment in computing time and requires the computations to be very stable. Although the results for the pulsed blowing at constant angle of attack were promising, stability problems limited the investigation with pitching motion and computations could not be continued beyond α=19° on the downstroke (Figure 4.29). A reduction in the pitching moment peak of 4% (Table 4.6) was seen for pulsed blowing over the reference case, and both the half pressure and the full pressure test cases with constant blowing were better at controlling dynamic stall. It appears that for the pulsed blowing, the main dynamic stall vortex is not stabilised, and a higher duty cycle than 50% will be necessary. Investigations into improving the numerical stability when pulsed blowing is used are continuing.

4.2.4 Conclusion

Test cases with constant blowing, which show increased lift and reduced drag for a RANS or URANS test case at a constant angle of attack above the static stall angle, also show improved dynamic stall behaviour. For the case that pulsed blowing at 589 Hz was used, an increase in both lift and drag was observed over the reference case, in contrast to the constant blowing case where an improvement in both lift and drag was observed. The modelling of pulsed jets for a pitching airfoil suffered from problems of computational stability. The dynamic stall vortex was not stabilised, and the lift, drag and pitching moment were similar to the reference case.

4.3 Results with constant blowing [3]

After the end of the numerical design described in sections 4.1 and 4.2 an airfoil model was built. A carbon fiber model (Fig. 4.30) with chord length c=0.300 m and breadth b=0.997 m (Aspect ratio 3.3) was produced for the 1 m x 1 m adaptive wall test section of the DNW-TWG in a similar configuration to that used for other dynamic stall investigations [38]. From investigations on similar models in section 3.1, the region of uniform flow in the middle of the model is around 0.75 m, or 1.25 chords either side of the centerline. The model was constructed of two carbon-fiber half-shells, an aluminum spar and aluminum mounting feet (Fig. 4.31(a)). Dry compressed air was supplied to jets at a maximum total pressure of 10 bar, and maximum flow rate of $\dot{m}_m$=0.25 kg/s for a breadth of model which is acted upon by the actuation jets L_{act}=0.84 m. Cavities in the spar distributed the air to 42 portholes of 3 mm (x/c=0.01) diameter positioned at x/c=0.10, with even distribution of the air assured by the choked flow at the jets. Pressure and acceleration instrumentation were mounted on the inside of the carbon-fiber shells, and the pressure system was integrated into the aluminum spar and controlled by cylindrical valves screwed into the spar.

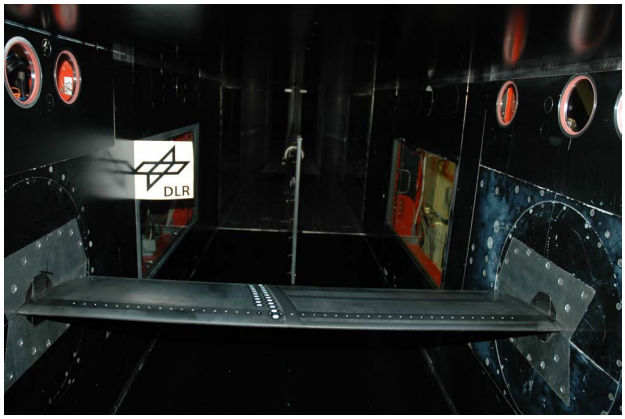

Figure 4.30: The OA209-FCD model installed in the DNW-TWG.

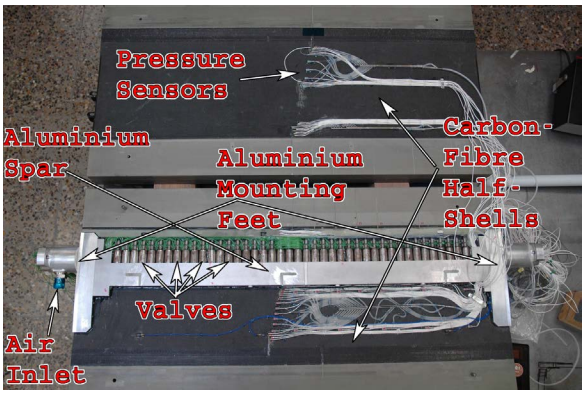

(a) Photograph inside model before closing

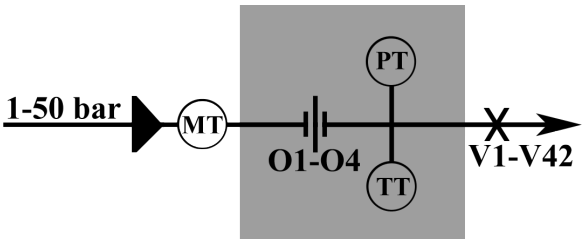

(b) Schematic of the pneumatic system

Figure 4.31: Pressure system and instrumentation inside the OA209-FCD model.

Figure 4.31(b) shows a schematic of the pressure system. Dry compressed air is supplied at between 1 bar and 50 bar. A Systec DF12 mass flux measurement system, based on differential pressure over a calibrated strut, temperature and pressure measurement (MT), is located outside the test section. Inside the aluminum spar of the model, the pressure is reduced by flow through four orifices (O1-O4), and the pressure (PT) and temperature (TT) of the system is measured. Finally, air with pressure between 1 and 10 bar is supplied to valves V1-V42, screwed into the spar. The valves were

[3] Text and illustrations in this section are taken from [32]: Gardner, A.D., Richter K., Mai, H., Neuhaus, D., "Experimental investigation of air jets for the control of compressible dynamic stall", *Journal of the American Helicopter Society*, Volume 58, Number 4, 2013. DOI: 10.4050/JAHS.58.042001 and [31] Gardner, A. D., Richter, K., Mai, H., Neuhaus, D., "Experimental investigation of air jets to control shock-induced dynamic stall", *Journal of the American Helicopter Society*, Volume 59, Number 2, 2014. DOI: 10.4050/JAHS.59.022003

developed by the DLR [87, 88] and can be individually switched on and off, and pulsed at frequencies of up to 500 Hz, although in this section the pulsed blowing is not used, and the blowing is always constant.

Figure 4.32 shows the fast switching valve. A single 8 mm diameter magnetizable valve ball (1) is the closure element of the valve, and its only moving part. Only the pressure difference between valve inlet and valve outlet keeps the ball in the valve seat (2). To open the valve the magnetic coil (3) generates a magnetic field, which is guided by magnetizable material in the housing of the valve. The magnetic field generates a force on the ball which rolls the ball off the valve seat. The force acts mainly perpendicular to the valve axis. When the magnetic field is switched off, the flow carries the ball back on the valve seat and the valve closes.

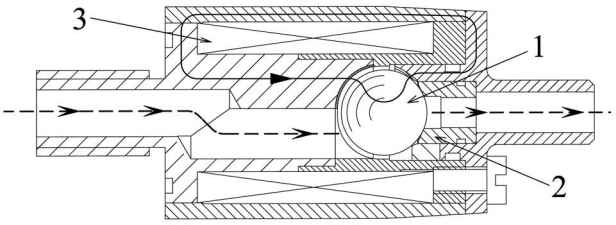

Figure 4.32: Closed fast switching valve. The solid line shows the magnetic flux, and the dashed line the gas path through the valve.

The air is ejected from the airfoil surface using portholes of 3 mm diameter at x/c=0.10, flush with the airfoil surface. The jets resulting from these portholes are directed normal to the airfoil chord line on the suction side of the airfoil, with a spacing of s/c=0.067 (20 mm).

The model was mounted horizontally in the adaptive-wall test section of the DNW-TWG wind tunnel and driven with pitch-oscillations from drive shafts through the side-walls attached at the quarter-chord position. The adaptive test section has flexible top and bottom walls which were statically adapted at the mean angle of attack of the model to minimise the interference velocities at the wall. Hydraulic motors, located outside the test section, drove the model from both sides. The model was moved with a strong pitching motion at amplitudes 4-7° and frequencies 2-5.7 Hz at M=0.3-0.5. A phase-locked data acquisition system, sampled each sensor with 1024 points per period for 160 periods. The model was equipped with a line of 49 Kulite unsteady pressure sensors (type XCQ-093), near the centerline. The line of sensors is at an angle of 10° to the oncoming flow so that no sensor will be in the turbulent wake of its predecessor. The sensors were situated to have a maximum discretization error (due to only having a finite number of sensors) of approximately 1% in lift, pressure-drag and pitching moment computed from the pressure taps during static measurements and dynamic stall without blowing.

Drag was measured for static points without blowing using a wake rake. The angle of attack was measured using laser triangulators at the ends of the model. An array of control accelerometers, angle meters and force balances ensured that maximal structural loads on the model were not exceeded during the experiments.

4.3.1 Numerical method

Computations using the DLR-TAU code are presented for a 3D slice of breadth 20% chord of the dynamically pitching OA209 airfoil using periodic boundaries, using the method described in section 4.1. The domain was selected to capture qualitative effects with a small number of node points (under 2 million) so that the geometry could be computed with acceptable cost by the URANS solver. It is expected that this domain is insufficiently wide to see 3D effects for the main dynamic stall vortex, but the 3D effects in the first 20-40% of the airfoil will be preserved. In order for the effect of the jet boundary layer to be captured, the jets were modeled as short tubes sunk into the surface with a length of 6 mm, with a boundary setting the total conditions at the bottom end. Unsteady Reynolds-averaged Navier-Stokes (URANS) computations were undertaken with the DLR-TAU code [39]. The

node-based finite-volume solver was used on a hybrid unstructured grid consisting of prismatic layers close to the viscous surfaces and a tetrahedral field, generated using the Centaur^{TM} unstructured grid generator. The grid and time-step settings used were according to the guidelines of Richter et al. [103] for convergence on this geometry and test condition. The computations were fully turbulent using the Spalart-Allmaras turbulence model, with 1600 time steps per period with 400 inner iterations per time-step. This time-step is on the order of the Strouhal frequency for vortex shedding around a 3 mm diameter cylinder at these conditions.

4.3.2 Data analysis

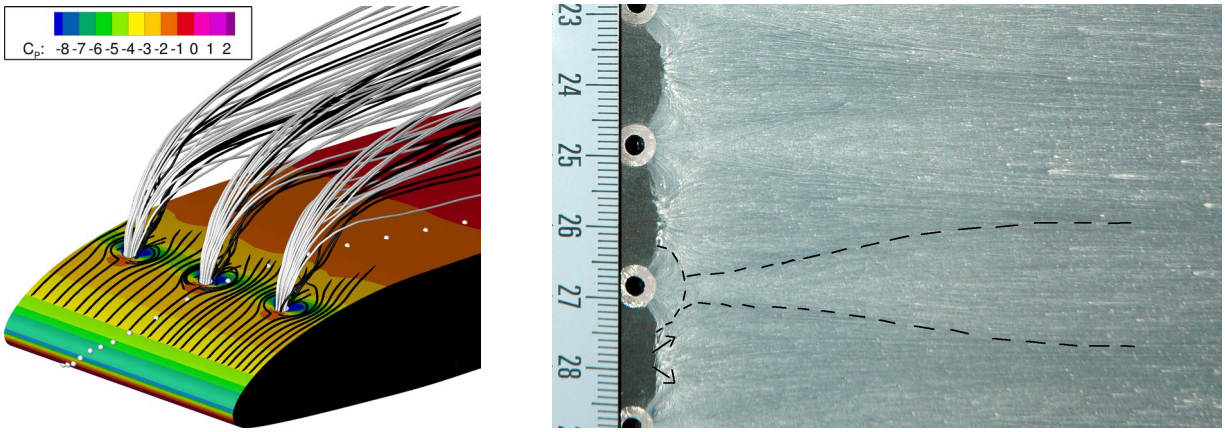

(a) CFD result at α=14.4° ↑ (b) Experimental oil flow picture

Figure 4.33: The complex flow around the jets for M=0.3, Re=1.15×10^6, α=13°, P_j=10 bar. Flow is from left to right and the white spheres are pressure sensor locations.

The experimental C_L, C_D and C_M are integrated from pressure transducers on the model surface. These were positioned using 2D computations assuming uniform flow across the y-coordinate (breadth) of the airfoil model without blowing. Figure 4.33(a) shows a CFD result for pitching at α=13±7° with M=0.30, Re=1.15×10^6, at α=14.4° on the upstroke. The surface C_P is indicated with colored contours, showing that a second suction peak appears at the position of the jets, which is not uniform over the y-coordinate. Volume streamlines illustrate the flow, with the white streamlines being material from the jets, and dark lines material from the freestream. The acceleration of material from the freestream out of the separated region behind the jets leads to a local decrease in C_P in the region directly behind each jet, and the flow blockage between the jets causes a local decrease in C_P between the jets. The re-expansion of the flow from between the jets is seen in oil-flow pictures at constant angle of attack (Fig. 4.33(b)).

In Fig. 4.33(a) the experimental pressure sensor positions are noted with white spheres. It is desirable to know whether the integration of the pressure signals will result in a reliable estimate of the integral force over the surface. Figure 4.34 compares the pressure distribution at this condition extracted from the locations of the pressure sensors in the CFD, with the pressure distribution obtained by averaging slices of the CFD solution at constant x/c across the breadth of the computational domain. The method of averaging slices yields a pressure distribution which can be integrated to yield the true forces for the 3D flow at α=14.4°, on the upstroke (Fig. 4.34). For this point, the discretization error (DE) in C_L was +8%, and the inclusion of the sensor at x/c=0.11 better reproduced the qualitative shape of the pressure distribution, indicating that this sensor should be used. At the same point, C_M was increased by 0.02 due to the DE. The DE is a function of the flow topology and angle of attack, and Fig. 4.35 shows results from 3D CFD with DLR-TAU, showing the difference between the forces as computed from the full surface and the sensor positions. The DE reduces when the gradients in the C_P distribution are low, thus the DE reduces sharply at stall, when the suction peak between the jets disappears. The difference between the DE as estimated from the 2D and the 3D computations is due to the differences in the pressure distributions on the surface. The results in Fig. 4.35 show that the DE is highest for cases where blowing with every jet or every second jet are used, causing an overestimation of the lift and the negative peak of the pitching moment to be underestimated. In contrast, when only every third jet is turned on, the jet near the sensor in Fig. 4.33(a) is turned off, resulting in a slight underestimation of the lift and overestimation of the negative peak of the pitching moment.

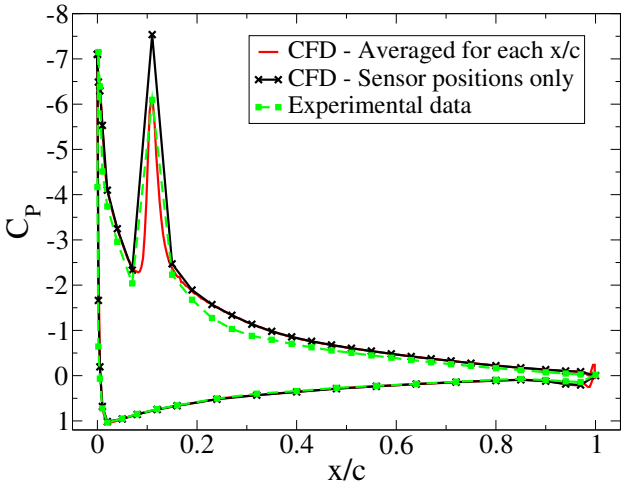

Figure 4.34: Comparison of CFD data for different discretizations, with experiment.

The forces on the model, calculated from the pressure sensors, need to be corrected for the mo-

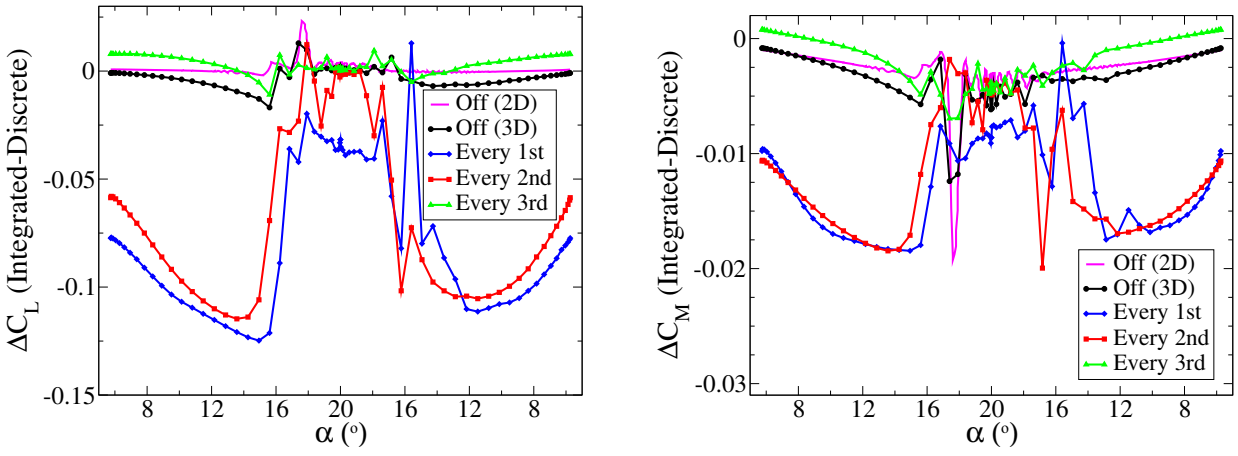

(a) Error in lift

(b) Error in pitching moment

Figure 4.35: Discretization error from 3D CFD computations with DLR-TAU. Error is plotted as difference between the full force and the force as computed from the experimental sensor positions.

mentum force F due to the air jets, computed from the impulse by:

$$F = \dot{m}v = \dot{m}_m / L_{act} \sqrt{\frac{2\gamma R T_0}{\gamma + 1}}. \tag{4.1}$$

The jet is assumed sonic at the surface of the model, and T_0, the total temperature, is assumed to be equal to the measured temperature of the aluminum spar in the model. Further, $\dot{m}_m$ is the mass flux as measured by the DF12 mass flux sensor, L_{act}=0.84 m is the breadth of model which is acted upon by the actuation jets, and γ=1.4 and R=287 J/kg/K are the gas constants for dry compressed air. The corrected values of C_L, C_D and C_M are computed from their uncorrected values, assuming that the jet force is directed normal to the model chord in a downward direction, at x/c=0.10. The values of F are in Table 4.8 for each point, as are approximate values for the changes to the lift (ΔC_L) and drag (ΔC_M). The qualitative results were not changed by these offsets.

Table 4.8: Dynamic airfoil data.

C_{L_p} [-]	$\overline{C_L}$ [-]	C_{M_p} [-]	P_j [bar]	$\dot{m}_m$ [kg/s]	F [N]	ΔC_L [-]	ΔC_M [-]	W_j [kW]	$\overline{W_D}$ [kW]	W_{D_p} [kW]
M=0.3, Re=1.15$\times 10^6$, f=5.7 Hz (ω^*=0.11), α=13$\pm$7°										
1.56	0.88	-0.232	0.0	0.000	0.0	0.00	0.000	0.0	12.2	41.9
1.64	0.94	-0.331	3.1	0.078	31.0	-0.03	-0.004	13.0	12.1	47.6
1.47	0.96	-0.179	5.9	0.150	58.8	-0.05	-0.008	35.5	10.2	38.1
1.42	0.94	-0.077	9.7	0.252	99.6	-0.09	-0.013	73.7	8.7	23.8
M=0.3, Re=1.15$\times 10^6$, f=5.7 Hz (ω^*=0.11), α=13$\pm$7°, with tape										
1.50	0.92	-0.178	0.0	0.000	0.0	0.00	0.000	0.0	12.2	32.5
M=0.3, Re=1.15$\times 10^6$, f=5.7 Hz (ω^*=0.11), α=13$\pm$4°										
1.40	1.03	-0.191	0.0	0.000	0.0	0.00	0.000	0.0	10.1	34.5
1.41	1.13	-0.031	9.7	0.234	92.8	-0.08	-0.012	67.6	5.5	12.1
M=0.3, Re=575000, f=5.7 Hz (ω^*=0.11), α=13$\pm$4°										
1.41	0.81	-0.241	0.0	0.000	0.0	0.00	0.000	0.0	6.5	19.9
1.35	0.94	-0.085	4.9	0.110	43.5	-0.08	-0.012	31.6	4.7	13.4
1.29	0.90	-0.096	7.9	0.184	72.6	-0.11	-0.016	58.9	5.5	15.3
1.09	0.78	-0.047	9.9	0.233	91.8	-0.15	-0.022	81.0	4.5	9.4
M=0.3, Re=575000, f=5.7 Hz (ω^*=0.11), α=13$\pm$4°, only every 2nd jet on										
1.50	1.05	-0.042	9.9	0.120	47.6	-0.09	-0.013	43.0	4.7	12.6
M=0.3, Re=575000, f=5.7 Hz (ω^*=0.11), α=13$\pm$4°, only every 3rd jet on										
1.45	0.97	-0.056	9.9	0.089	35.3	-0.06	-0.010	32.0	5.3	15.2
M=0.4, Re=1.5$\times 10^6$, f=5.7 Hz (ω^*=0.08), α=12$\pm$7°										
1.38	0.86	-0.187	0.0	0.000	0.0	0.00	0.000	0.0	27.0	80.8
1.30	0.90	-0.199	6.0	0.139	55.0	-0.03	-0.004	33.3	23.0	90.3
1.25	0.86	-0.082	9.9	0.235	92.8	-0.05	-0.007	68.2	19.1	59.4

Variables were phase averaged over 160 cycles of 1024 points to get a mean and standard deviation (plotted as scatter-bars) for each point on the cycle. The experimental data is presented with angle of attack uncorrected for wind tunnel effects, geometry changes in the model compared to the nominal airfoil or other effects. The standard deviation in α was less than 0.05°, and so is not plotted. The mean lift ($\overline{C_L}$) was taken for each dynamic point by averaging the data over all cycles. The pitching moment peak (C_{M_P}) is taken as the difference between the value of the phase-averaged coefficient, at the peak and "flat" value a short time beforehand, as in section 4.1, to compensate for the general shift in the pitching moment values which occurs with blowing. This data is shown in Table 4.8.

The repeatability of $\overline{C_L}$ and C_{L_p} was better than 3% for test points which were nominally identical. The repeatability of C_{M_P} was within 12%. The standard deviation of the phase-averaged data is shown for every 16th point on all figures. The Systec DF12 mass flux measurement system is calibrated to better than 1% accuracy at the conditions tested. The mass flux (in kg/s) is only approximately linear with P_j (in bar), but a regression through the measured points allows a rough estimate: $\dot{m} = 0.023P_j$ for cases where all valves were on, $\dot{m} = 0.012P_j$ for cases where every second valve was on, and $\dot{m} = 0.008P_j$ for cases where every third valve was on.

The flow control with constant blowing scales with the mass flux ratio:

$$C_q = \frac{\dot{m}_m}{\rho_\infty v_\infty c L_{act}}, \tag{4.2}$$

or the momentum ratio:

$$C_\mu = \frac{2}{cL_{act}} \frac{\dot{m}_m v_j}{\rho_\infty v_\infty^2}, \tag{4.3}$$

between the jets and the freestream, as defined for compressible flow [34]. Here, $\dot{m}_m$ is the mass flux and v_j the jet velocity, set as M=1.0.

Estimating the power required to provide the compressed air is difficult, however an order of magnitude estimate can be made assuming a perfect constant-temperature compressor for supply of a particular pressure and mass flux:

$$W_j = ln\left(\frac{P_\infty}{P_j}\right) \frac{RT_\infty \dot{m}_m}{L_{act}}, \tag{4.4}$$

expressed as kW per meter of blade, where it is assumed that the gas is being compressed from the local static pressure (P_∞) and temperature (T_∞) to the jet total pressure. Example values of W_j are in Table 4.8. The engine power required to offset the drag is:

$$W_D = \frac{1}{2} C_D A_{Ref} \rho_\infty v_\infty^3, \tag{4.5}$$

in kW per meter of blade, and the total power is defined as:

$$W_T = W_D + W_j. \tag{4.6}$$

4.3.3 Results at static angle of attack

Static polars were taken for a range of conditions, with the model stationary at each point, and the walls of the adaptive test section adapted to the model flow. Figure 4.36 shows drag polars taken at M=0.3. Since the portholes of 3 mm diameter potentially cause early boundary layer transition, the transition behavior was investigated by comparing with drag measurements where the holes are covered by a silicon-backed Teflon tape of thickness 62 μm. This tape was thinner than the 90-120 μm required to cause boundary layer transition at these conditions, using Eq. (7) from [118]. For static points without blowing, the complete drag was measured using a wake rake. In Fig. 4.36 the model has a lower drag when the holes are covered with tape. A laminar dip is present in the experimental data, both with and without tape, indicating that the laminarity of the boundary layer is only quantitatively (by a maximum of eight drag counts) and not qualitatively affected by the addition of the portholes.

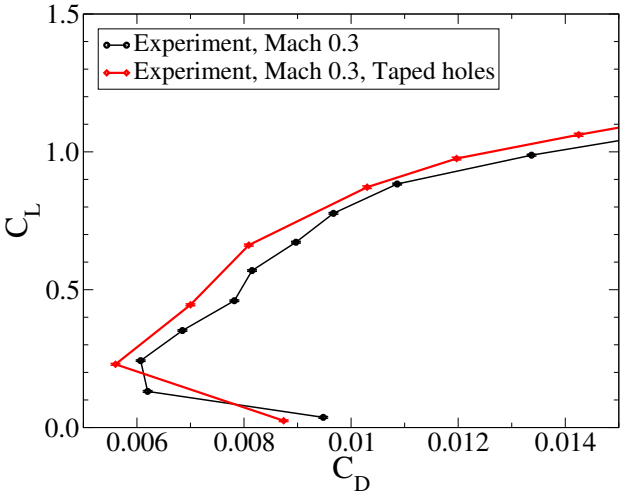

Figure 4.36: Experimental comparison of OA209 static drag polars without blowing for M=0.3, Re=1.15×10^6.

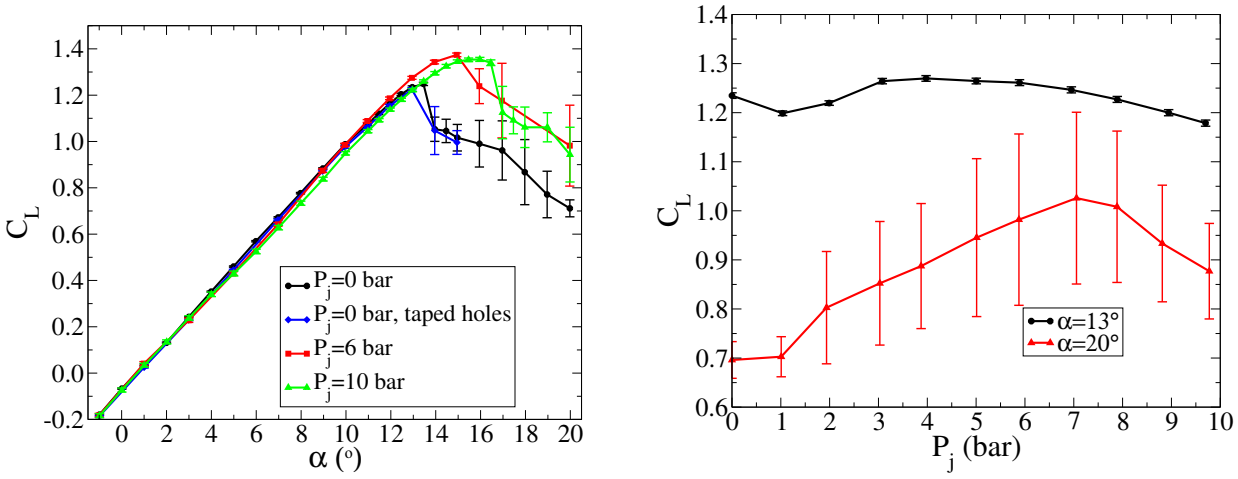

(a) Lift vs α

(b) Lift vs P_j at constant α

Figure 4.37: Experimental polars with and without constant blowing at M=0.3, Re=1.15×10^6.

Lift polars were measured at M=0.3 with and without constant blowing through all portholes (Fig. 4.37(a)). In the case without blowing, C_L increases monotonically up to C_{L_P}=1.25 at α=13.5° with a low scatter. The flow then separates and C_L decreases monotonically with increased unsteadiness compared with the attached flow, up to the maximum angle measured at α=20°. The polar with tape over the holes is identical to that without tape in the linear range. The polar with tape appears to stall earlier (at α=12.7°), but this polar was measured with fewer points, so a point is missing compared with the case without tape. Since the existing points agree well with each other, we conclude that the portholes did not affect C_{L_P} within the measurement accuracy. Points without tape, and using P_j=0 bar are used as the reference cases in this section.

When constant blowing was used, C_{L_P} increased by 10% to C_{L_P}=1.37 for P_j=6 bar (C_μ=0.069, C_q=0.010) and C_{L_P}=1.35 for 10 bar (C_μ=0.12, C_q=0.017). In addition, C_L at α=20° increased by approximately 40% compared to C_L for the case without blowing, due to the blowing controlling the static stall. In comparison, CFD during the design phase predicted a 37% increase using RANS in section 4.1 and a 48% increase using URANS in section 4.2, for blowing at P_j=6.7 bar.

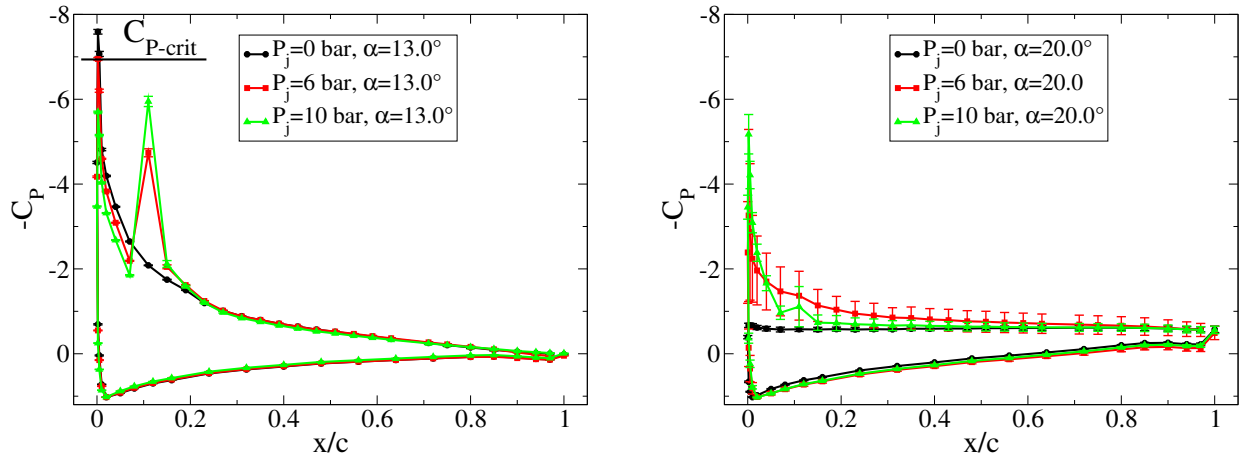

(a) α=13° before stall (b) α=20° after stall

Figure 4.38: Experimental C_P for constant blowing at M=0.3, Re=1.15×10^6.

If the angle of attack is now held constant, and the jet pressure is increased in steps, a pressure polar is obtained (Fig. 4.37(b)). For this flow condition, at P_j=10 bar, C_μ=0.12 and C_q=0.017, and these scale linearly with pressure. At α=20° and at low pressures, increasing the blowing pressure results in an increase in C_L, until at P_j=7 bar an increase in C_L of 48% is observed compared to the case with no blowing. After this, C_L reduces, or remains approximately constant with increasing pressure. Similarly, for α=13° with attached flow, a maximum improvement of 3.2% in C_L is seen at P_j=4 bar, decreasing thereafter. For the attached flow (Fig. 4.38(a)), increasing the pressure causes the suction peak at the jet position to become stronger and the suction peak near the leading edge to weaken, leading to an optimum effect at P_j=4 bar. For the separated flow (Fig. 4.38(b)), increasing the blowing pressure increases the suction peak near the leading edge, but at higher pressures this causes a stronger separation behind the jets which decreases the lift, leading to an optimum effect at P_j=7 bar.

4.3.4 Dynamic stall control at Mach 0.3

Figure 4.39 shows data for the pitching dynamic stall airfoil without blowing for the condition M=0.3, Re=1.15×10^6, f=5.7 Hz (ω^*=0.11), α=13±7°. The OA209 airfoil shows leading edge stall with a strong dynamic stall vortex, followed by unsteady separated flow. Additionally, Fig. 4.39 shows the variation in the forces due to the installation of tape over the blowing holes. The same silicon-backed Teflon tape of thickness 62 μm was used as in the cases with static angle of attack. Figure 4.39 shows that the case with taped holes has earlier separation, by around $\Delta\alpha$=-0.5° compared with the reference case, but C_{M_P} is relatively unchanged. The valve leakage when closed was measured at ≤0.04 atmosphere-liters per hour at P_j=2 bar for the worst valve, and is relevant for cases when pressure is applied but not all valves are open. To observe the effects of leakage, a pressure of 2 bar was applied when all valves were closed. The result, as shown in Fig. 4.39, is that the difference observed remained within the scatter.

The flow control effect with constant blowing is illustrated in Fig. 4.40 for P_j=3 bar (C_μ=0.035, C_q=0.005), P_j=6 bar (C_μ=0.069, C_q=0.010) and P_j=10 bar (C_μ=0.12, C_q=0.017), compared with the

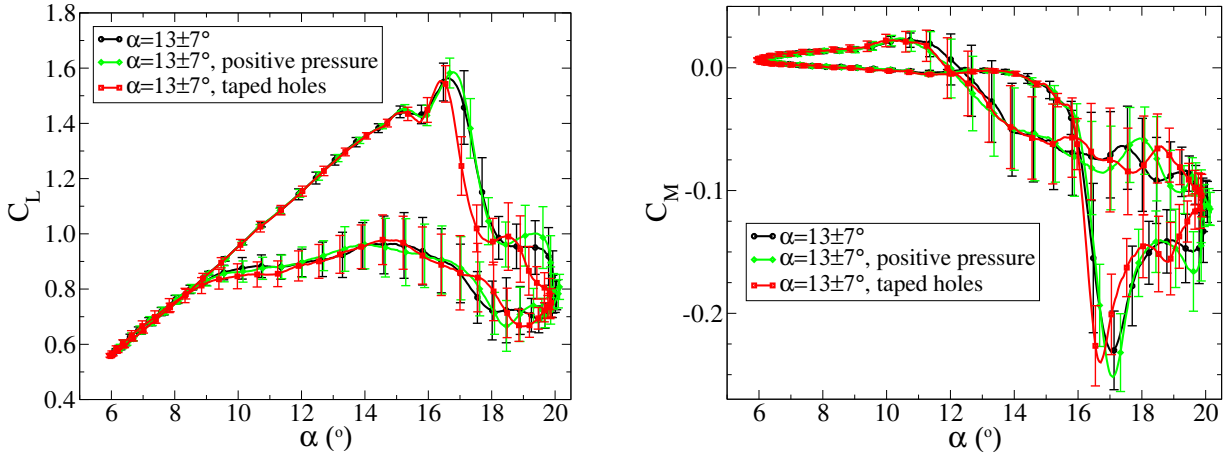

(a) C_L vs α (b) C_M vs α

Figure 4.39: Experimental comparison of airfoil data without blowing, with effects of tape and valve leakage.

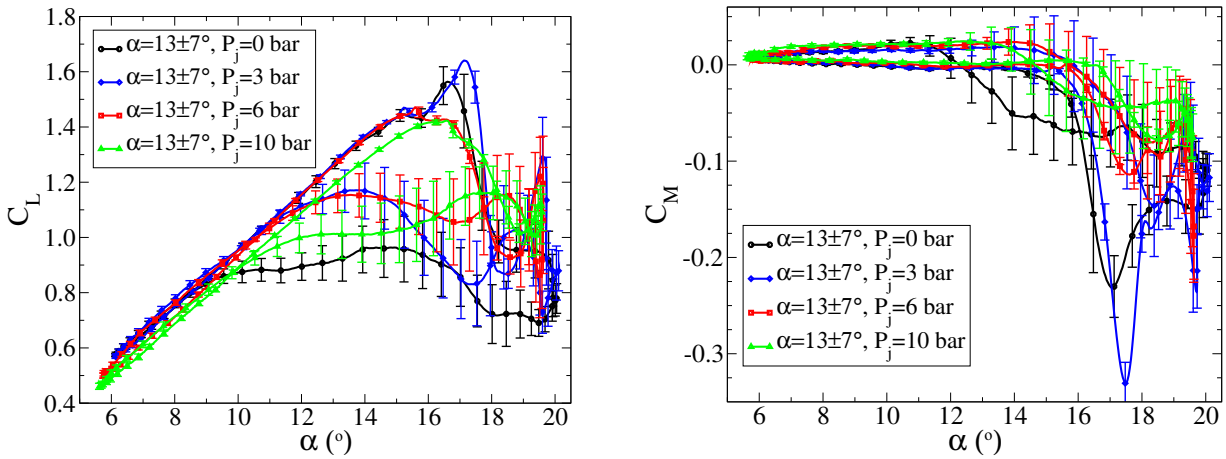

(a) C_L vs α (b) C_M vs α

Figure 4.40: Experimental comparison with and without constant blowing at M=0.3, Re=1.15×10^6, f=5.7 Hz (ω^*=0.11), α=13±7°.

reference case with no blowing. Data is for M=0.3, Re=1.15×10^6, f=5.7 Hz (ω^*=0.11), α=13±7°. Blowing at P_j=3 bar causes worse dynamic stall than no blowing, with an increase in C_{M_P} of 43% compared with the reference case. The jets strengthen the two leading edge stall vortices, causing the large pitching moment peaks. In contrast, $\overline{C_L}$ increased by 7.2%.

If the blowing is increased to P_j=6 bar (C_μ=0.069, C_q=0.010), an improvement in the dynamic stall behavior is observed, with C_{M_P} reduced by 51%. However at this condition the secondary stall peak is stronger than the initial peak, and this second peak is only 23% reduced from the reference case. An analysis of the time-resolved C_P distributions indicates that the initial stall is a trailing edge stall, which is then followed by a stronger leading edge stall causing the large second stall peak. At P_j=10 bar (C_μ=0.12, C_q=0.017), both the primary and secondary stall peak are about the same size, and C_{M_P} is reduced by 67% over the reference case. Analysis of the time-resolved C_P distributions indicates that for P_j=10 bar a pure trailing edge stall occurs, with the flow in front of the jets not stalling at all.

The effect of the dynamic stall control by the jets at P_j=10 bar in Fig. 4.40 is to slow down the

dynamic stall process, so that although it starts at α=16°, as for the case without blowing, C_{M_P} is reached at α=18.5° rather than at α=17° for the reference case. This slowed separation has the effect, as noted in the design study in section 4.1, of producing a significantly weaker dynamic stall vortex and thus causing lower pitching moments. The slowing of the stall is also seen at P_j=6 bar, but less strongly.

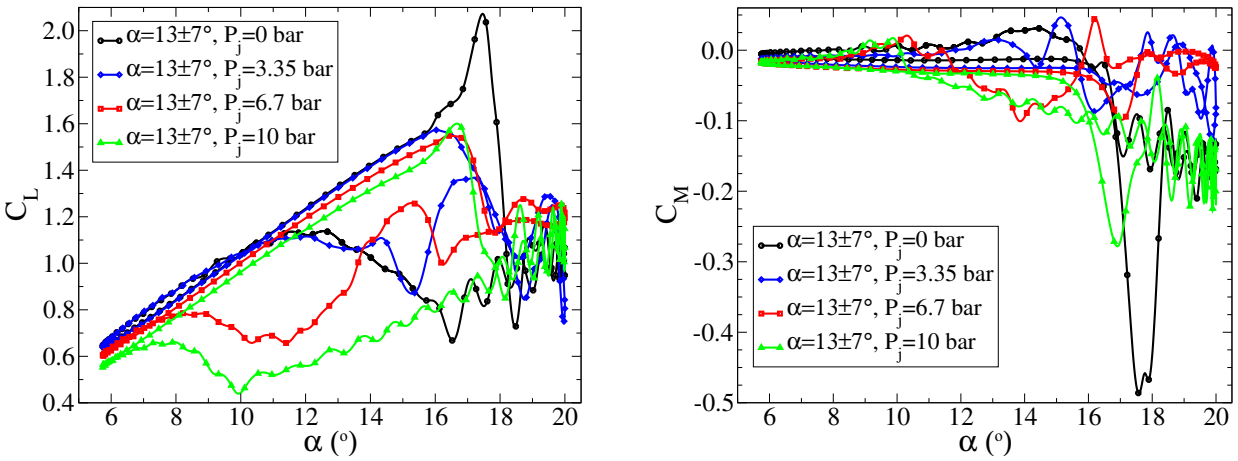

(a) C_L vs α (b) C_M vs α

Figure 4.41: URANS computed forces at M=0.3, Re=1.15×10^6, f=5.7 Hz (ω^*=0.11), α=13±7°, for constant blowing.

As a comparison, a similar pressure variation was computed using URANS (Fig. 4.41), with the coarse grid and settings from the design study in section 4.1. A dynamic stall control effect is achieved, which is qualitatively similar to that seen in the experiment. The CFD with P_j=6.7 bar has the same mass flux as the experiments with P_j=10 bar. A much stronger dynamic stall control effect is seen, with an 86% reduction in C_{M_P} at P_j=6.7 bar, which is significantly more than seen in the experiments. Further, the flow control at P_j=3.35 bar is significant, whereas in the experiment at similar pressures a net negative effect is seen. Instead of the increased slowing of the stall with increasing blowing seen in the experiments, the stall is faster with increasing blowing in the computations. Although the general dynamic stall control effect is predicted by the coarse CFD, the prediction requires more investigation of the grid and turbulence model than the settings which were primarily chosen in the experiment design phase to yield good engineering approximations at acceptable computational cost.

Despite the downward force from the jet at x/c=0.10, which causes a negative pitching moment, and contrary to the CFD, C_M for the experiment during the attached flow remains relatively constant. Figure 4.42(a) shows that the positive C_M caused by the additional suction peak formed between the jets offsets the downward force from the blowing. The critical pressure is exceeded, but the flow appears not to behave like the shock-induced separations seen at higher Mach numbers. After stall, at peak pitching moment (Fig. 4.42(b)), the C_M of the cases with blowing is increased by the preservation of a suction plateau in front of the jets, and by increasing C_P on the surface behind the jets, probably due to reduced strength of the dynamic stall vortex. The suction plateau is also the reason for the significantly increased lift after stall when constant blowing is used (Fig. 4.40). $\overline{C_L}$ increases by 7% for P_j=10 bar compared to the reference case without blowing.

A large number of devices to control dynamic stall have been tested over the years. One of these is leading edge vortex generators (LEVoGs) [38, 73]. As a comparison, LEVoGs were attached to the model and tested without blowing (Fig. 4.43). The LEVoGs reduced C_{M_P} by 24% and increased $\overline{C_L}$ by 4%.

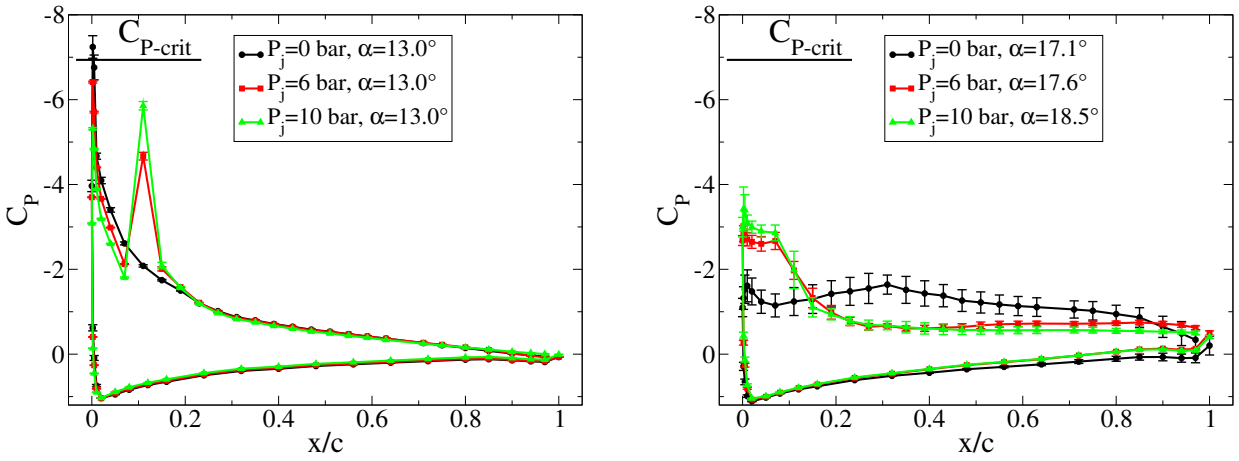

(a) α=13° before stall (b) At peak pitching moment in the first stall peak

Figure 4.42: Experimental C_P for constant blowing at M=0.3, Re=1.15×10^6, f=5.7 Hz (ω^*=0.11), α=13±7°.

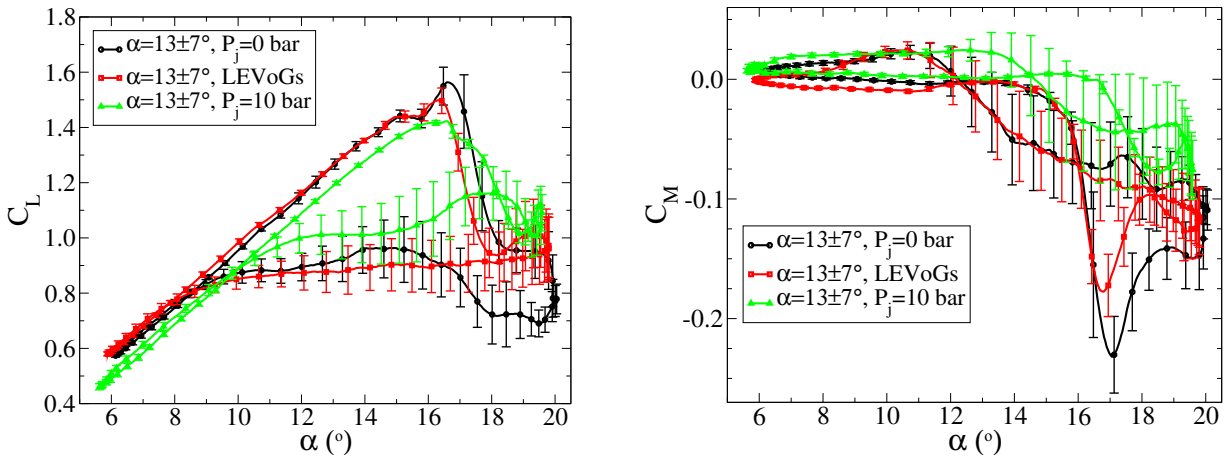

(a) C_L vs α (b) C_M vs α

Figure 4.43: Experimental forces at M=0.3, Re=1.15×10^6, f=5.7 Hz (ω^*=0.11), α=13±7°, for constant blowing and flow control by LEVoGs.

For α=13±4°, the stall is no longer so deep, and the pitching motion reaches the maximum angle of attack shortly after stall. In this case, the effect of the jets with blowing at P_j=10 bar to delay and slow stall means that the airfoil never fully stalls. In Fig. 4.44, C_{M_P} is reduced by 84%, with an increase of $\overline{C_L}$ by 9% and a increase in C_{L_P} by 1%. Experiments with light stall indicate that the dynamic stall control efficiencies found for deep dynamic stall represent a lower boundary of efficiency.

4.3.5 Investigation of optimum pressure and jet spacing

In contrast to the stall control for the static test cases, where a saturation of the positive effect was seen at P_j=7 bar, no saturation of the dynamic stall control effect was noted at M=0.3 and Re=1.15×10^6. At Re=1.15×10^6 the maximum pressure of the pneumatic system was reached at 10 bar, so to further increase C_μ and C_q, the Reynolds number was reduced to Re=575000. At this Reynolds number, the blowing coefficients at P_j=5 bar (C_μ=0.12, C_q=0.019) are roughly equivalent to those at

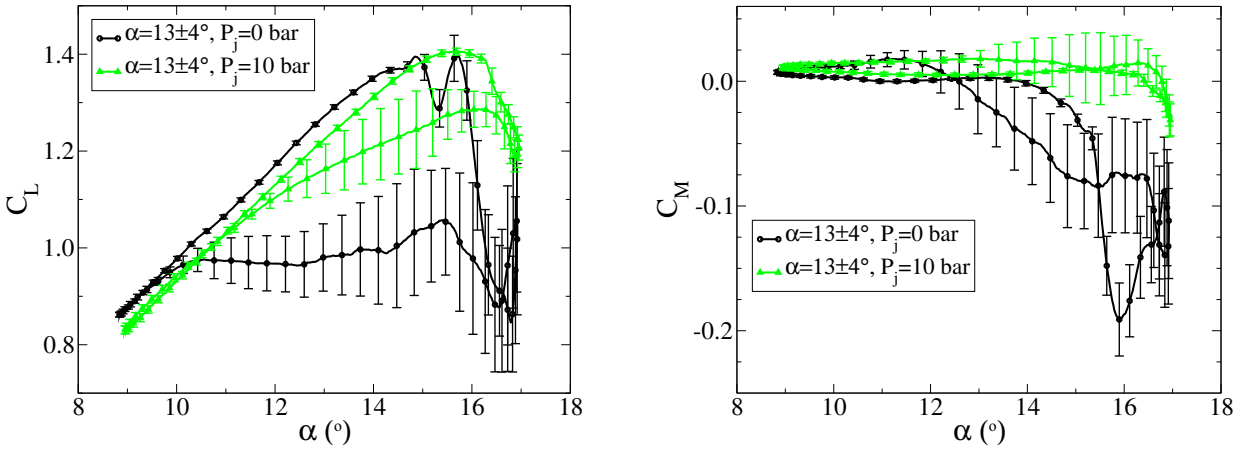

(a) C_L vs α (b) C_M vs α

Figure 4.44: Experimental comparison of forces for light stall at M=0.3, Re=1.15×10^6, f=5.7 Hz (ω^*=0.11), α=13±4°, with and without constant blowing at P_j=10 bar.

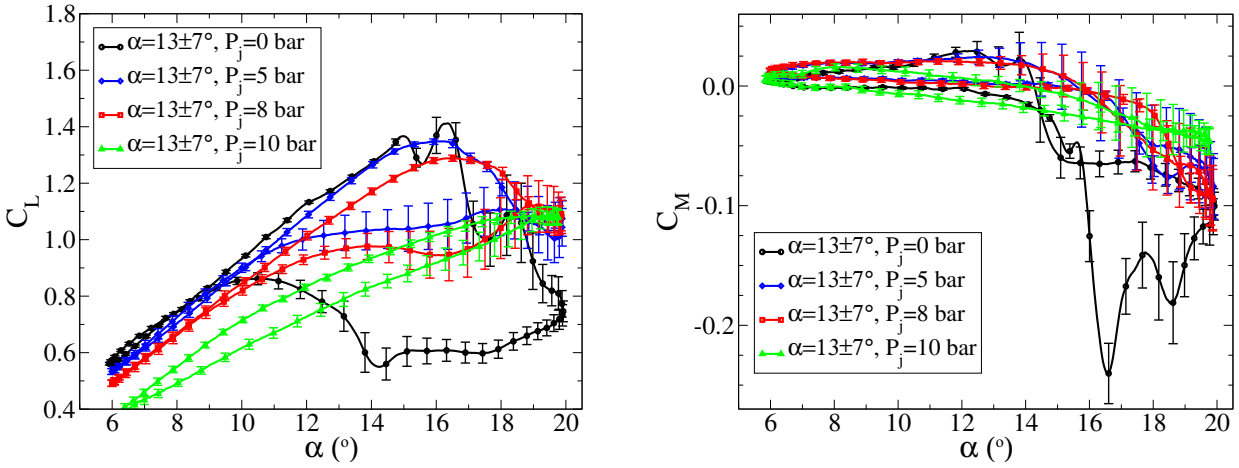

(a) C_L vs α (b) C_M vs α

Figure 4.45: Experimental comparison of forces at M=0.3, Re=575000, f=5.7 Hz (ω^*=0.11), α=13±7°, with and without constant blowing.

Re=1.15×10^6 and P_j=10 bar (C_μ=0.12, C_q=0.017), and an equivalent trailing edge dynamic stall is seen for $P_j \geq$5 bar. In Fig. 4.45, the data without blowing looks different to that at higher Reynolds number, due mainly to the pronounced kink in the lift curve at α=12°, which has been shown in other experiments in section 2.2 to be the point at which the boundary layer transition on the top of the airfoil reaches the leading edge and stops moving with angle of attack. The enhanced effect at reduced Reynolds number is probably due to the increased boundary layer thickness. The stall occurs $\Delta\alpha$=-1° lower in angle of attack than at the higher Reynolds number, and C_{L_P} is reduced by 27%. Despite these differences, C_{M_P} is of comparable size. The lift during the downstroke is reduced from that at Re=1.15×10^6, but reattachment occurs at around α=9° at both Reynolds numbers.

At P_j=5 bar (C_μ=0.12, C_q=0.019), C_{M_P} is 65% reduced from the reference case (P_j=0 bar) while C_{L_P} remains similar to the reference case and $\overline{C_L}$ increased by 16%. Both $\overline{C_L}$ and C_{M_P} are worse for both P_j=4 bar and P_j=6 bar (not shown), indicating saturation of the dynamic stall control effect at P_j=5 bar. The dynamic stall control reduces slowly in effectiveness until P_j=8 bar (C_μ=0.20, C_q=0.030), which still has a reduction in C_{M_P} of 60% and an increase in $\overline{C_L}$ of 12%. Starting at P_j=5 bar, C_{L_P} starts to reduce, until it is 9% reduced for P_j=8 bar. At higher pressures, C_{L_P} diminishes

rapidly, until at P_j=10 bar (C_μ=0.25, C_q=0.038), (Fig. 4.45(a)), C_{L_P} is reduced by 23% and there is no dynamic stall. For this case, the peak in C_M is effectively completely removed (Fig. 4.45(b)). Even though C_{L_P} is reduced, the lack of stall means $\overline{C_L}$ is only 3% lower than in the case with no blowing. As such, there are two "optimum" amounts of blowing at M=0.3 and s/c=0.067: for low dynamic loading C_μ=0.25 (C_q=0.038) and for high performance C_μ=0.12 (C_q=0.019).

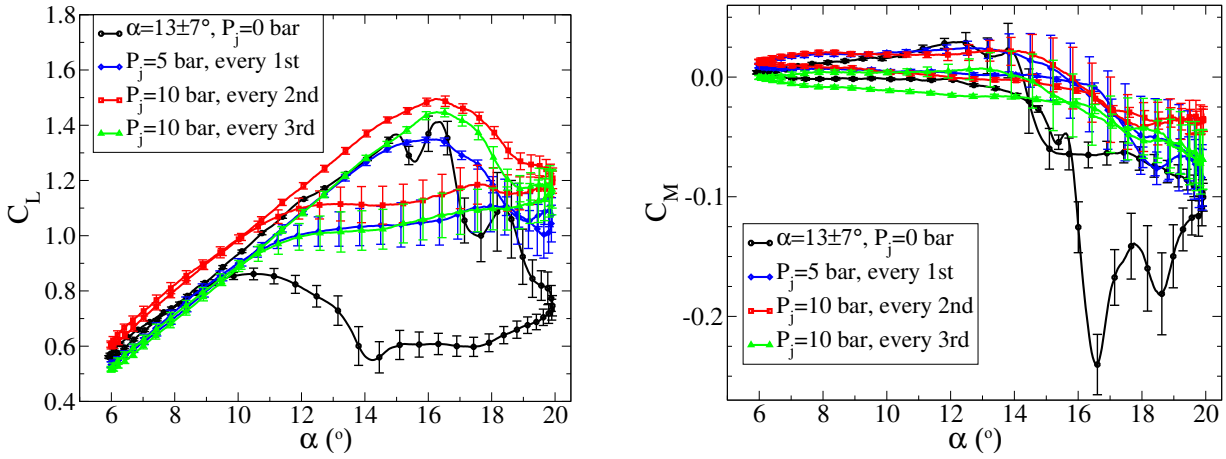

(a) C_L vs α (b) C_M vs α

Figure 4.46: Experimental effect of jet spacing with constant blowing on forces at M=0.3, Re=575000, f=5.7 Hz (ω^*=0.11), α=13±7°.

Finding the optimal spacing of the jets with constant mass flux is more difficult since the maximum mass flux is more strongly limited by the maximum 10 bar total pressure of the jet system. The jet spacing was increased from using every jet (s=6.7%c=20 mm) to using every second jet (s=13%c=40 mm) or using every third jet (s=20%c=60 mm), as shown in Fig. 4.46. No saturation of the flow control effect was found with the wider spacings, so the results at the maximum pressure of P_j=10 bar are shown. For the case using every jet, the pressure for which saturation was achieved, P_j=5 bar is shown. The data with every jet at P_j=5 bar (C_μ=0.12, C_q=0.019) has approximately the same mass flux as that with every second jet at P_j=10 bar (C_μ=0.12, C_q=0.019), but with every second jet C_{M_P} is reduced 83% as opposed to the 65% peak reduction seen for blowing with every valve. In Fig. 4.46(b) for the case using every third jet at P_j=10 bar (C_μ=0.08, C_q=0.013), the reduction in C_{M_P} is 76%, although now the first and second pitching moment peaks are joined. The increase in C_{L_P} for the case with every third jet is particularly clear in Fig. 4.46(a), although an increase is present for all three spacings, and the post-stall lift is improved by a similar amount for all three cases. All three blowing cases have trailing edge stall, with good preservation of the suction peak in front of the jets during and after stall.

The offset in C_L for the case using every second jet is significantly higher than all other cases. In Fig. 4.47(a) for attached flow at α=14° the additional lift for the case with every second jet is due to the additional height of the peak around the jet, as described in the discussion of discretization error in section 4.3.2. Likewise, when every third jet is used, the pressure peak near the jets disappears entirely in Fig. 4.47(a), which is the reason for the lower lift in the attached flow region (Fig. 4.47(a)). The reason for this is that the pressure measurement is close to the jet near the sensor in Fig. 4.33(a), which is on when every jet is used, or every second jet, but which is turned off when every third jet is used. Thus, although $\overline{C_L}$ is increased by 30% for the case with every second jet and by 19% for the case with every third jet, these values must be treated with some caution. After stall (Fig. 4.47(b)), all three jet spacings cause a pressure plateau in front of the jets which increases lift and decreases pitching moment. For the pressures available in this experiment, the optimal jet spacing was s/c=0.13

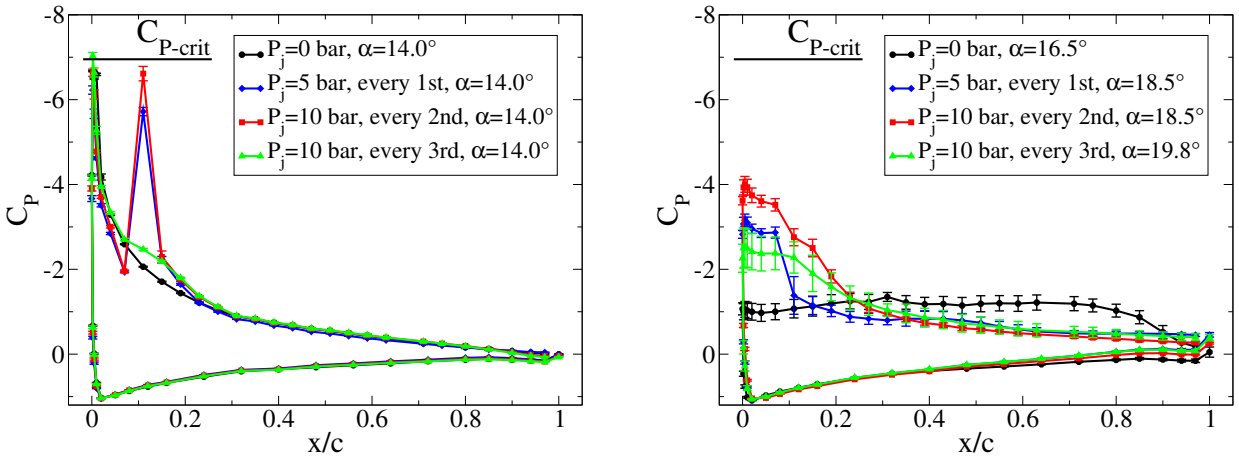

(a) α=14° before stall (b) At minimum pitching moment in the first stall peak

Figure 4.47: Experimental comparison of C_P for different jet spacings at M=0.3, Re=575000, f=5.7 Hz (ω^*=0.11), α=13±7°.

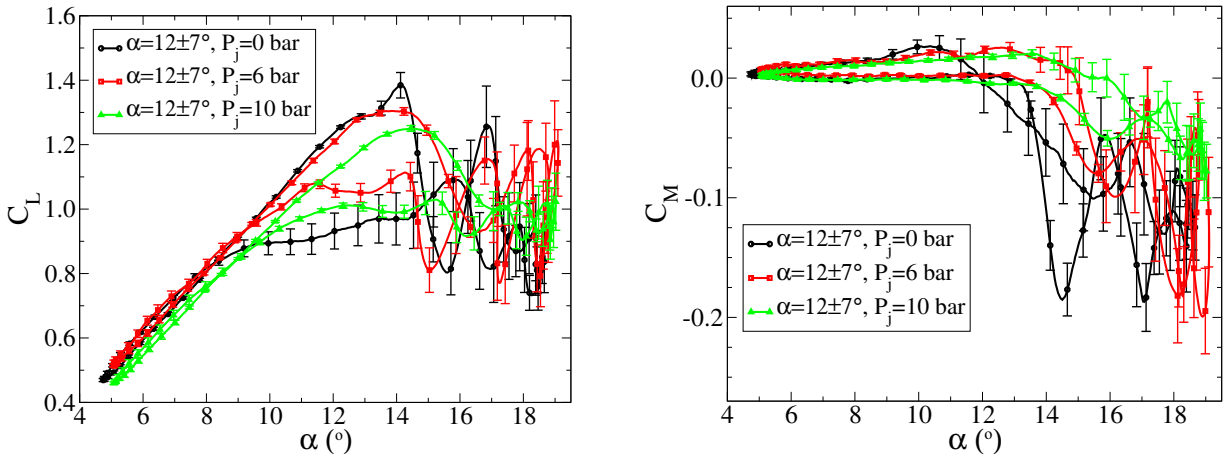

(a) C_L vs α (b) C_M vs α

Figure 4.48: Experimental comparison of forces at M=0.4, Re=1.5×10^6, f=5.7 Hz (ω^*=0.08), α=12±7°, with and without constant blowing with s/c=0.067.

(s=40 mm) for the maximum effect. Although s/c=0.20 (s=60 mm) has the most efficient use of air pressure it is assumed that this form of flow control would only be used for short periods, and thus efficiency of air use is a secondary consideration. The reduced number of portholes could result in less expensive blades.

4.3.6 Dynamic stall control at Mach 0.4

At higher Mach numbers, other flow control methods have been shown to be of varied effectiveness. The LEVoGs of Mai et al. [73] noted a control effect with slightly reduced effectiveness at M=0.4, and the vortex generator and glove approach of Martin et al. [74] showed good control at M=0.3, but was counterproductive when shocks appeared for Mach numbers between 0.4 and 0.5, depending on the pitching motion.

For the constant blowing at M=0.4 (Fig. 4.48), for the jet separation of s/c=0.067, the dynamic stall control effect is similar to that at M=0.3. At M=0.4, the mean angle of attack was reduced to

12° so that the flow at mean angle of attack was attached, aiding the adaption of the test section walls. Strong shocks appear in the flow, but analysis of the time-resolved C_P distributions indicates that the initial stall behavior remains a typical leading edge stall, similar to that seen at M=0.3. For the no blowing case, a second stall peak, similar in size to the first stall peak appears, also with typical leading edge stall. At P_j=6 bar (C_μ=0.030, C_q=0.0060), a double stall is seen, but the initial stall is trailing edge stall, followed by a stronger leading edge stall, much as at M=0.3. At P_j=10 bar (C_μ=0.050, C_q=0.010), the airfoil has only trailing edge stall, and a strong dynamic stall control effect is seen.

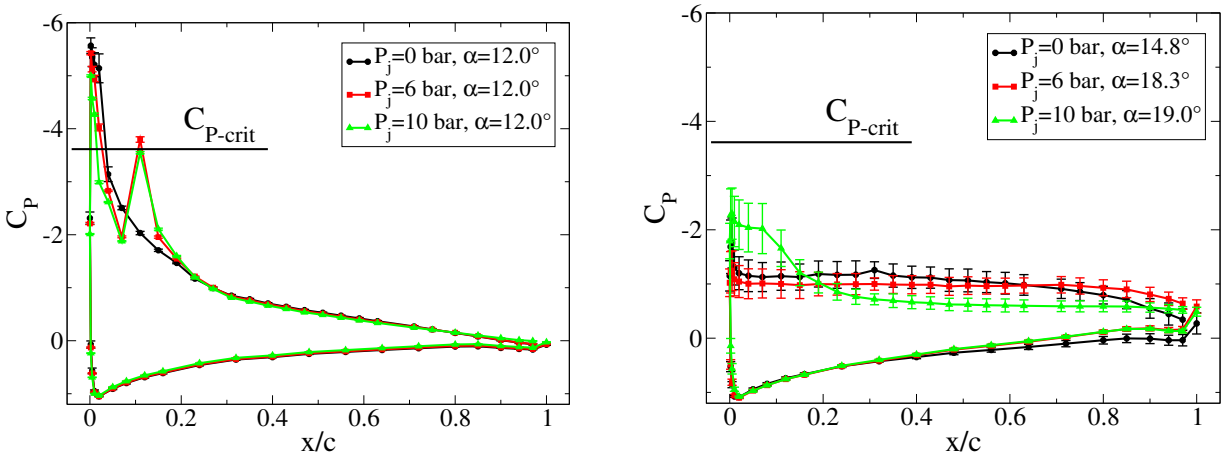

(a) α=12° before stall

(b) At peak pitching moment

Figure 4.49: Experimental comparison of C_P for different blowing pressures at M=0.4, Re=1.5×10^6, f=5.7 Hz (ω^*=0.08), α=12±7° with s/c=0.067.

In Fig. 4.48(b) for M=0.4, C_{M_P} is reduced by 56% for P_j=10 bar, while $\overline{C_L}$ is increased by 6%. C_{L_P} is reduced by 60% at this test condition. In Fig. 4.49(a), for the attached flow, the jets cause a reduction in C_L, and a change in effective angle of attack (not visible at this scale) causes a decrease in C_P on the lower side of the airfoil. For the attached flow at α=12°, the flow over the pressure sensor near the jets is now supersonic, indicating an increase in the supersonic part of the flow near the jet near the sensor in Fig. 4.33(a), compared to M=0.3, and this suction acts to increase both C_L and C_M. At the higher angle of attack where peak pitching moment occurs (Fig. 4.49(b)), a suction plateau at subsonic Mach number is maintained in front of the jets at P_j=10 bar, leading to a significantly higher C_L in the separated flow region and reducing the negative C_M of the airfoil.

The dynamic stall control effect at M=0.4 is less than at M=0.3 and, due to the limitation of the pressure system, no saturation of the dynamic stall control effect was found. Despite these shortcomings, the stall control is good, and no critical Mach number dependence was found. Thus no sudden change in the flow control effectiveness is to be expected if the jets were to be positioned sub-optimally along the radius of a rotor blade.

4.3.7 Dynamic stall at Mach 0.5

The dynamic stall of the OA209 at M=0.5 is mainly influenced by the strong shock that appears at medium angles of attack and causes a shock-induced separation of the flow on the suction side of the airfoil, starting around α=11°. It is known from the static experiment in subsection 4.3.3, that the jet portholes do not cause boundary layer transition at these Reynolds numbers, but do increase the turbulence in the boundary layer such that C_D is increased by a maximum of 10 drag counts for static points at M=0.3. The portholes do not change either the static or dynamic stall behavior. The

drag at Mach 0.7 was also checked in this reference, and found to be consistent with the drag without portholes, thus it is assumed that the effect of the portholes on the aerodynamics is also minimal at M=0.5.

The matrix of points measured at Mach 0.5 is in in Table 4.9, and example values of $\dot{m}_m$, F, C_q and C_μ are in Table 4.10 for a range of pressures. The values when using every second or every third jet can be linearly computed from the values in Table 4.10. It is a coincidence that in Table 4.10 ΔC_L=-C_μ.

Figure 4.50 shows the effect of varying amplitude for a constant pitching frequency of f=5.7 Hz (ω^*=0.06), constant Reynolds number Re=1.9×10^6 and constant mean angle of attack α=7°. As seen in Fig. 4.50(a), the lift at mean angle of attack is similar in all cases. For α=7±4°, the flow does not stall, and a small hysteresis in the lift appears. As the amplitude increases, the hysteresis becomes

Table 4.9: Dynamic airfoil data.

$\overline{\alpha}$	$\alpha_\pm$	f	P_j	C_{L_p}	$\overline{C_L}$	C_{M_p}	C_{D_p}
°	°	Hz	bar	-	-	-	-
Re=1.9×10^6, every jet on							
7	4	5.7	0	1.12	0.73	-0.003	0.053
7	5	5.7	0	1.16	0.70	-0.024	0.096
7	6	5.7	0	1.20	0.66	-0.057	0.140
7	7	5.7	0	1.23	0.62	-0.081	0.179
7	7	3	0	1.16	0.62	-0.076	0.174
Static Polar			0	1.09	-	-0.056	0.150
9	4	5.7	0	1.17	0.89	-0.056	0.139
9	4	5.7	6	1.13	0.86	0.002	0.085
7	6	5.7	0	1.20	0.66	-0.057	0.140
7	6	5.7	6	1.15	0.65	-0.002	0.086
7	7	5.7	0	1.23	0.62	-0.081	0.179
7	7	5.7	3	1.16	0.60	-0.045	0.142
7	7	5.7	6	1.16	0.60	-0.019	0.118
7	7	5.7	10	1.08	0.59	-0.004	0.112
11	7	5.7	0	1.23	0.84	-0.129	0.298
11	7	5.7	3	1.17	0.83	-0.141	0.305
11	7	5.7	6	1.17	0.82	-0.085	0.251
11	7	5.7	10	1.09	0.80	-0.054	0.212
Re=0.85×10^6, every jet on							
7	7	5.7	0	1.22	0.58	-0.103	0.189
7	7	5.7	1	1.12	0.56	-0.070	0.165
7	7	5.7	2	1.12	0.57	-0.006	0.117
7	7	5.7	3	1.10	0.57	0.000	0.111
11	7	5.7	0	1.24	0.77	-0.136	0.294
11	7	5.7	2	1.13	0.78	-0.101	0.266
11	7	5.7	4	1.07	0.77	-0.044	0.213
11	7	5.7	6	0.98	0.73	-0.050	0.208
Re=0.85×10^6, every second jet on							
11	7	5.7	6	1.19	0.83	-0.051	0.241
Re=0.85×10^6, every third jet on							
11	7	5.7	7	1.16	0.81	-0.055	0.250

Table 4.10: Example for blowing with all jets at Re=1.9×10^6.

P_j	$\dot{m}_m$	F	C_q	C_μ	ΔC_L	ΔC_M	W_j
bar	kg/s	N	-	-	-	-	kW/m
1	0.024	9.1	0.0008	0.003	-0.003	-0.0004	1.3
2	0.048	18.1	0.0016	0.006	-0.006	-0.0009	6.0
3	0.072	27.2	0.0024	0.009	-0.009	-0.0013	11.9
4	0.096	36.2	0.0033	0.012	-0.012	-0.0018	18.6
5	0.120	45.3	0.0041	0.015	-0.015	-0.0022	26.0
6	0.144	54.3	0.0049	0.018	-0.018	-0.0027	33.8
7	0.168	63.4	0.0057	0.021	-0.021	-0.0031	42.0
8	0.192	72.5	0.0065	0.024	-0.024	-0.0036	50.5
9	0.216	81.5	0.0073	0.027	-0.027	-0.0040	59.4
10	0.240	90.6	0.0081	0.030	-0.030	-0.0045	68.5

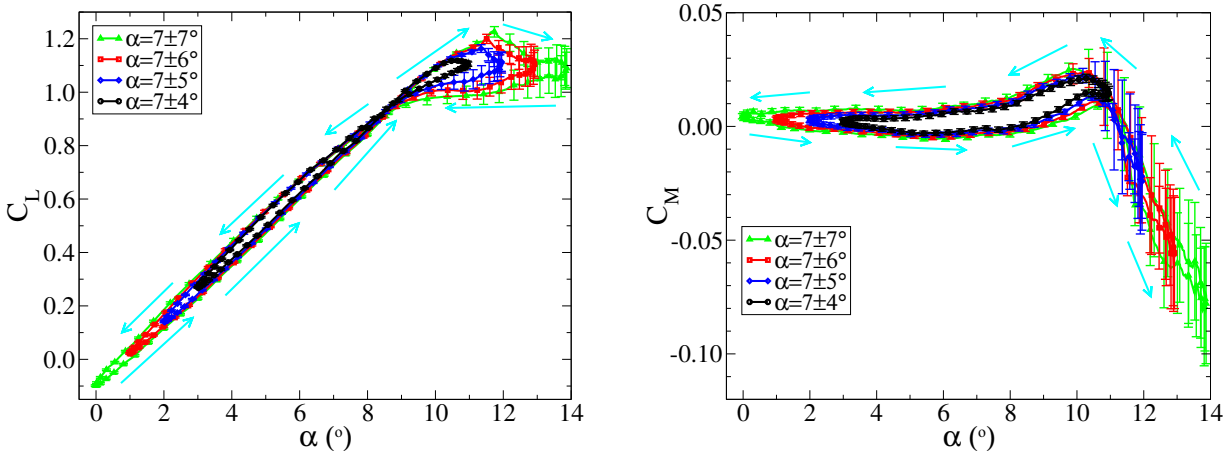

(a) C_L vs α (b) C_M vs α

Figure 4.50: Experimental comparison of forces at M=0.5, Re=1.9×10^6, f=5.7 Hz (ω^*=0.06), α=7±4-7°, without blowing.

larger and the peak lift increases, although the 6% increase in C_{L_p} between α=7±4° and α=7±7° is less than might be expected from the increase in amplitude (Table 4.9. In each case, the lift curve becomes nonlinear around α=10°, and for the two highest amplitudes ($\alpha_\pm$=6° and 7°), there is a peak in lift on the upstroke between α=11° and 12°. The flow reattaches at α=9°-10°, with later reattachment for higher amplitudes. An increased hysteresis is also visible at lower angles, and this is due to the increase in pitching angular velocity, rather than the increased maximum angle of attack.

The pitching moment in Fig. 4.50(b) has a slightly negative C_M during the pitch-up, and a kink in the positive direction around α=8° on the upstroke appears with the advent of supersonic flow and a shock. Moment stall starts around α=11°, and in contrast to the lift, the hysteresis loop in the pitching moment after stall does not become significantly wider but follows a relatively constant path as maximum angle of attack increases. On the downstroke, the pitching moment follows a qualitatively similar to the path on the upstroke, but with positive C_M. The kink in the pitching moment at α=8° is also present on the downstroke. Higher amplitudes lead to a larger hysteresis in C_M during the attached part of the cycle.

At subsonic Mach numbers [32, 85] dynamic pitching causes significant overshoots in C_L and C_M compared with steady polars, due to the formation of a dynamic stall vortex which acts on the airfoil after stall and an increase in the angle of attack of stall. Figure 4.51 illustrates the effect of varying

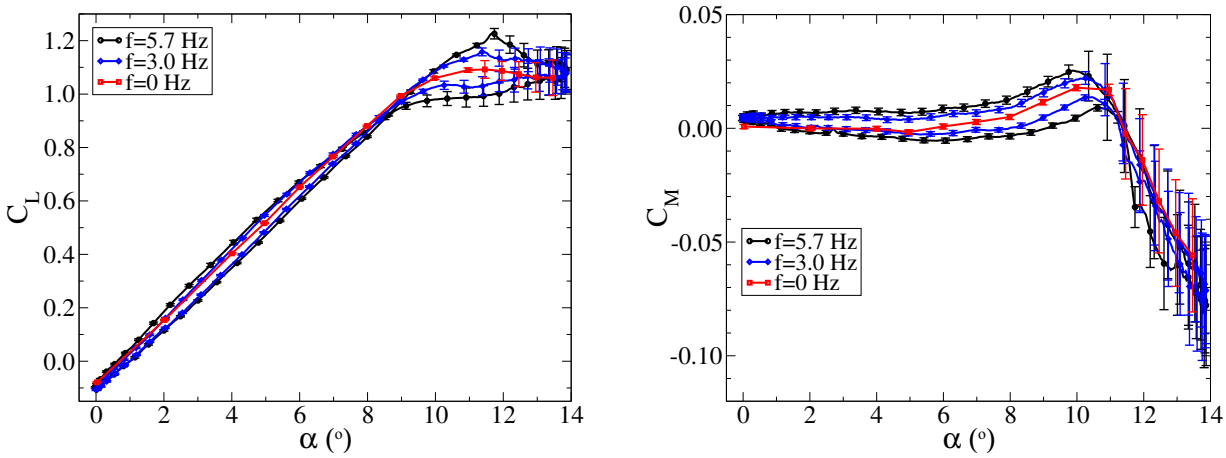

(a) C_L vs α (b) C_M vs α

Figure 4.51: Experimental comparison of forces at M=0.5, Re=1.9×10^6, f=0-5.7 Hz (ω^*=0-0.06), α=7±7°, without blowing.

frequency from a stationary polar at f=0 Hz to dynamic pitching at f=5.7 Hz. The dynamic C_L and C_M open in a hysteresis around the static polar. Figure 4.51(a) shows that maximum lift increases from C_{L_p}=1.09 to C_{L_p}=1.23 when increasing the pitching frequency from f=0 Hz and 5.7 Hz (Table 4.9). All three cases have similar pitching rates at α=13.5° and, as might be expected, C_L is similar for all three cases at that point. At low angle, the hysteresis increases with increasing pitching frequency in much the same way as for increasing amplitude.

Increasing the pitching frequency does not significantly increase the angle of attack of stall. This is most clear in Fig. 4.51(b), where the pitching moment stall is around α=11° regardless of frequency. After stall on the upstroke, C_M falls faster for higher frequencies, reaching a maximum difference in C_M of -0.03 compared with the steady polar. On the downstroke, all frequencies follow approximately the same pitching moment path. For the attached flow, the hysteresis in C_M is higher for higher pitching frequency. The kink in the pitching moment is at approximately α=8° for all three frequencies.

Figure 4.52 shows the surface C_P distributions on the model during the upstroke for M=0.5, Re=1.9×10^6, f=5.7 Hz (ω^*=0.06), α=7±7°. At α=6.0°, the flow is shockless and subsonic. As the angle of attack increases, supersonic flow appears at α=7.6°. After this, a supersonic region of low C_P grows on the front of the airfoil, as seen at α=10°. Since this supersonic region will act to increase the pitching moment, the kink in the pitching moment around α=8° is due to the appearance and disappearance of the supersonic region on the upstroke and downstroke respectively.

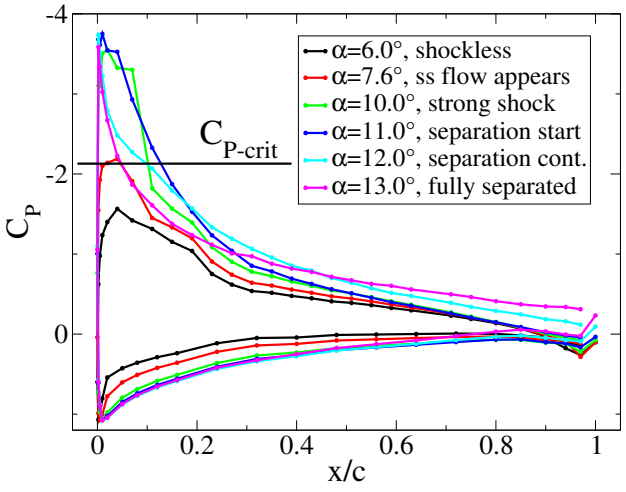

Figure 4.52: Pressure distributions on the upstroke for M=0.5, Re=1.9×10^6, f=5.7 Hz (ω^*=0.06), α=7±7°, without blowing.

At around α=11° in Fig. 4.52, the flow separation starts, and here the (isentropic) maximum Mach number on the airfoil is 1.45. At this angle of attack, the sharp com-

pression due to the shock is no longer visible on the suction side due to the sudden growth of the boundary layer separation under the shock foot and some cycle-to-cycle variation of the shock position. As the angle of attack increases, the flow separation spreads downstream, decreasing the surface C_P at the airfoil trailing edge, and upstream reducing the area of supersonic flow. Thus the airfoil has undergone shock-induced stall. Both of these changes cause a decrease in the pitching moment, as seen in Figs. 4.50 and 4.51. There is no travelling wave seen in the surface C_P, and thus no dynamic stall vortex is formed. The flow at the front of the airfoil remains supersonic after stall until after the flow reattachment, and this causes the lift to remain high even though the airfoil is stalled.

4.3.8 Stall control with constant blowing at Mach 0.5

The control of the shock-induced stall with constant blowing was first investigated using all blowing jets at Re=1.9×10^6. Figure 4.53 shows a Computational Fluid Dynamics (CFD) result for flow control with constant blowing at α=9.6° on the upstroke, to illustrate the topology of the flow with blowing. Flow is from left to right, and the white spheres are pressure sensor locations. The surface C_P is indicated with colored contours, showing that a region of low pressure appears at the front of the airfoil, which is terminated by a shock in front of the jet position at high angles of attack (in Fig. 4.53 the flow is just supercritical). A second suction peak appears at the position of the jets, which is not uniform over the spanwise direction, and which is also terminated by a shock downstream of the jet position. Volume streamlines illustrate the flow, with the white streamlines being air from the jets and dark lines air from the freestream. The jet acts as an eductor jet pump, causing a vertical acceleration of air from the freestream, leading to a local decrease in C_P in the separated region directly behind each jet. Additionally, the flow blockage between the jets causes a local decrease in C_P between the jets.

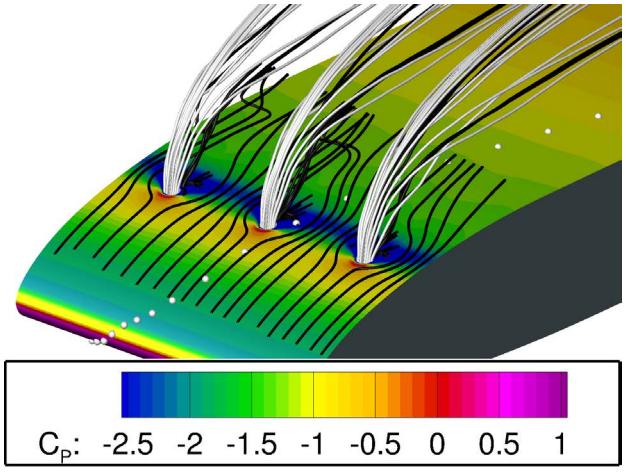

Figure 4.53: CFD result for the 3D flow. Pitching at M=0.5, Re=1.9×10^6, f=5.7 Hz (ω^*=0.06), α=11±7° with constant blowing of P_j=10 bar at α=9.6° on the upstroke.

For points in this section, the mass flux ratio (C_q) and momentum ratio (C_μ) can be found in Table 4.10. Further data on the forces can be found in Table 4.9.

During light stall, where the maximum angle of attack slightly exceeds the angle at which stall occurs, the stall can be fully controlled using constant blowing from the jets. In Fig. 4.50, at M=0.5, Re=1.9×10^6, f=5.7 Hz, no stall occurs for α=7±4°. For α=7±5°, where light stall occurs, the stall can be fully controlled by blowing through all jets at a constant P_j=3 bar (not shown). For α=7±6° full control requires P_j=6 bar. For α=7±7° no blowing condition was found where the stall was fully controlled, but the pitching moment was significantly reduced, as shown later. Thus the flow could be fully controlled only for pitching motions with a maximum angle $\alpha_{max} \leq$13°, i.e. less than 2° above the stall angle of α=11°.

Figure 4.54 shows the full control of two test cases with α_{max}=13°. The shape of both the C_L and C_M curves near α_{max} depends mainly on α_{max} and not on the amplitude. Likewise, the shape of the curves near α_{min} depends mainly on α_{min}. For these cases there is no moment stall in Fig. 4.54(b), and the pitching moment becomes slightly more positive due to the blowing, contrary to what might

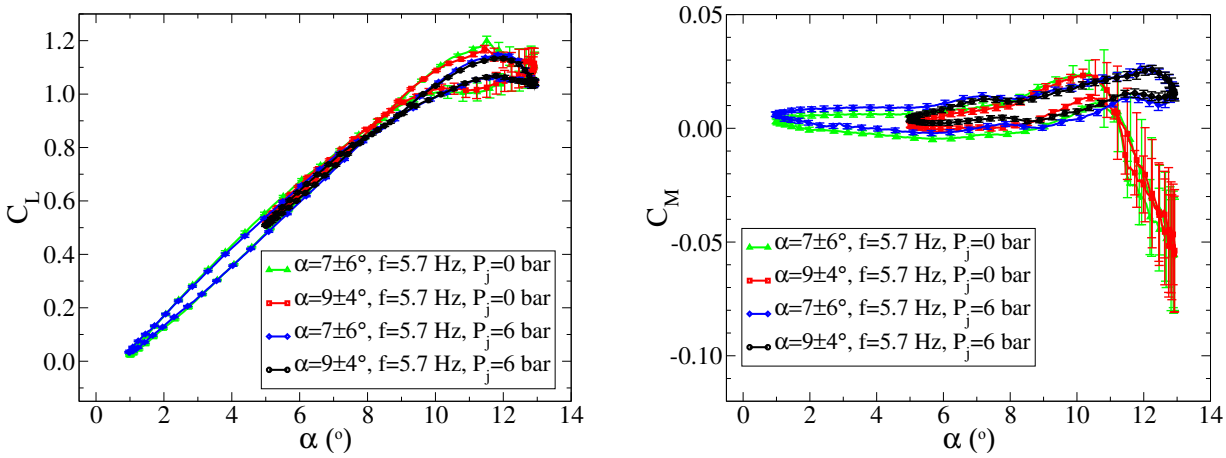

(a) C_L vs α (b) C_M vs α

Figure 4.54: Experimental comparison of forces at M=0.5, Re=1.9×10^6, f=5.7 Hz (ω^*=0.06), for test cases with full control of dynamic stall by constant blowing.

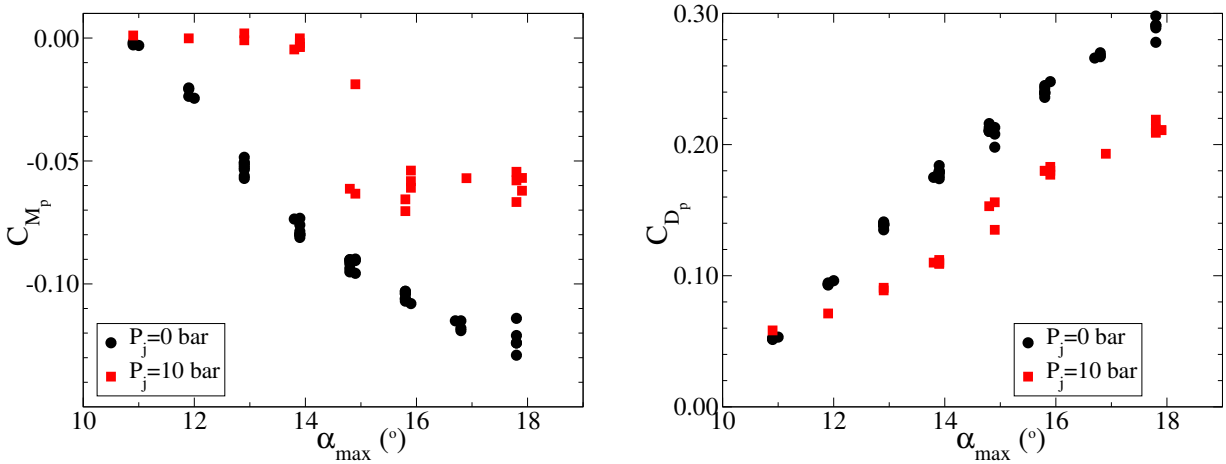

(a) C_{M_p} vs α_{max} (b) C_{D_p} vs α_{max}

Figure 4.55: Variation of peak forces with maximum angle of attack at M=0.5, Re=1.9×10^6, f=3-5.7 Hz (ω^*=0.03-0.06), α=7-11±4-7°, with and without constant blowing.

be expected due to the impulse of the jet. This is because the negative moment imparted by the jets is more than compensated by the low-pressure regions created by the jets. The lift at low angles of attack is decreased with blowing in Fig. 4.54(a), as expected, and at around α=8°, where the supersonic flow first appears when no blowing is used, there is a kink to lower lift. The maximum lift is slightly reduced, from C_{L_p}=1.20 to 1.15, but the mean lift over the pitching cycle remains relatively constant, reducing from $\overline{C_L}$=0.66 to 0.65 (Table 4.9).

The similarity in response of test cases with the same α_{max} is illustrated in Fig. 4.55, using all points measured, and not just those in Table 4.9. The peak pitching moment (C_{M_p}) is plotted against the maximum angle of attack (α_{max}) in Fig. 4.55(a) for amplitudes $\alpha_{\pm}$=4-7° and for frequencies f=3-5.7 Hz. For points without blowing, there is low scatter in the results due to the frequency and amplitude variation, with values for each α_{max} well grouped. From α_{max}=11°, where there is no stall, C_{M_p} falls at -0.024/° up to α_{max}=15° and at -0.012/° thereafter.

For blowing at P_j=10 bar, in Fig. 4.55(a), the results are also tightly grouped by α_{max}, excepting at α_{max}=15°. As discussed above, at $\alpha_{max} \leq$13° the stall is fully controlled by blowing at P_j=10 bar.

At α_{max}=14° the stall is nearly fully controlled, with a small pitching moment peak remaining, and the pitching moment peak sharply increases at α_{max}=15°. At $\alpha_{max} \geq$16°, the pitching moment peak remains constant at approximately C_{M_p}=-0.06, rather than decreasing further as for the uncontrolled flow. The pitching moment peak is thus reduced by at least 96% for $\alpha_{max} \leq$14°, 35% for α_{max}=15°, increasing to better than 50% reduction for α_{max}=18°.

The maximum drag (C_{D_p}) is plotted against α_{max} in Fig. 4.55(b), again for amplitudes $\alpha_{\pm}$=4-7° and for frequencies f=3-5.7 Hz. Blowing with P_j=10 bar causes a reduction in maximum drag, which increases with increasing α_{max}. The increase in C_{D_p} with α_{max} is 0.037/° without blowing and reduces to 0.022/° with blowing at P_j=10 bar at Re=1.9×10^6.

The maximum lift (C_{L_p}) is plotted against α_{max} in Fig. 4.56, and without blowing there is some variation in C_{L_p} at constant α_{max} due to the effect of frequency and amplitude, up to a range of ΔC_{L_p}=0.09. With blowing, C_{L_p} reduces by 0.1 on average, and the effect of variation in frequency and amplitude is reduced.

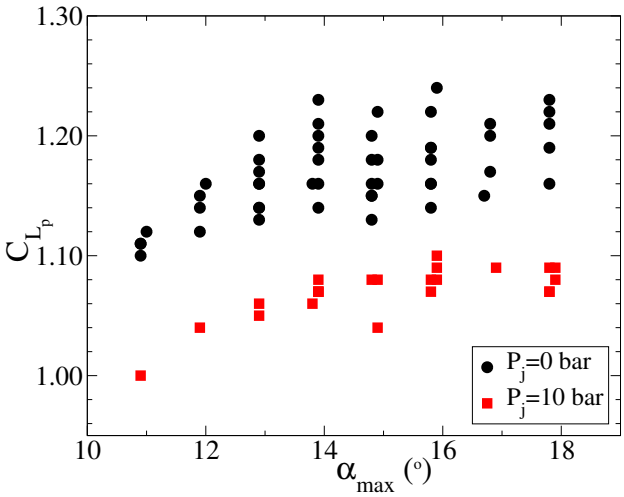

Figure 4.56: Variation of C_{L_p} with α_{max} at M=0.5, Re=1.9×10^6, f=3-5.7 Hz (ω^*=0.03-0.06), α=7-11±4-7°, with and without constant blowing.

At higher values of α_{max} the stall cannot be fully controlled by blowing, but a reduction in the pitching moment can still be found. Figure 4.57 shows the first point where full control of dynamic stall was not possible, with α=7±7° at Re=1.9×10^6 with blowing at up to P_j=10 bar, which is the maximum blowing pressure possible from the pressure system installed. The maximum lift is reduced in Fig. 4.57(a), from C_{L_p}=1.23 without blowing, to C_{L_p}=1.16 for P_j=3 bar and 6 bar, and to C_{L_p}=1.08 for P_j=10 bar (Table 4.9). Likewise blowing at P_j=10 bar reduces $\overline{C_L}$ by 6% over that without blowing. The point at which the lift encounters supersonic flow moves from α=9° to α=7° as P_j increases. The flow reattachment also moves from α=9° to α=7° as P_j increases.

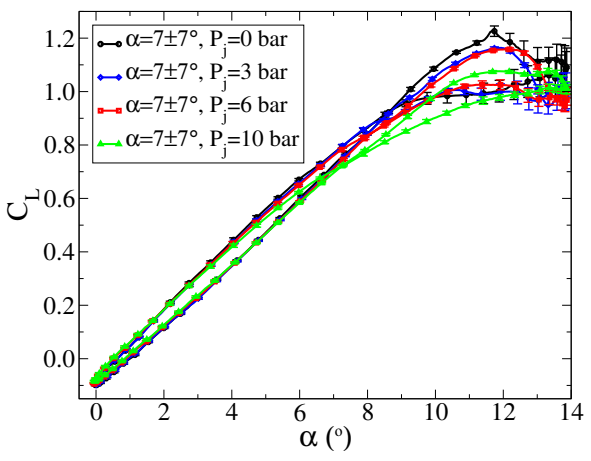

(a) C_L vs α

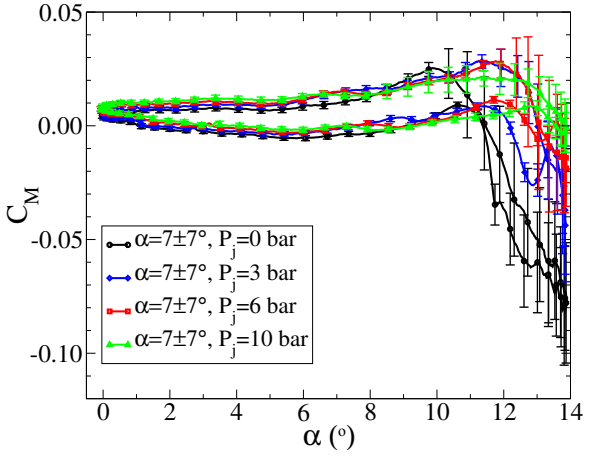

(b) C_M vs α

Figure 4.57: Experimental comparison of forces at M=0.5, Re=1.9×10^6, f=5.7 Hz (ω^*=0.06), α=7±7°, with and without constant blowing.

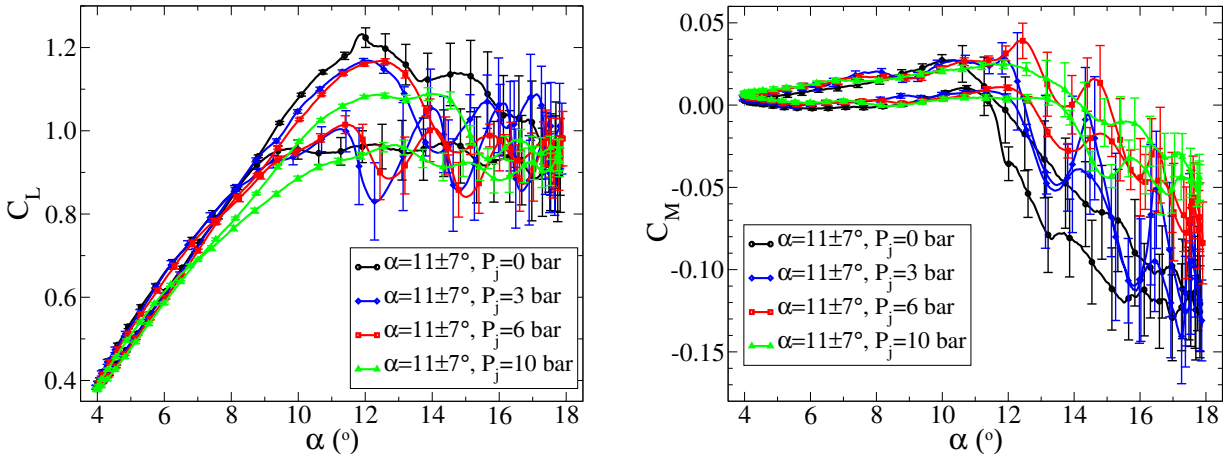

(a) C_L vs α (b) C_M vs α

Figure 4.58: Experimental comparison of forces at M=0.5, Re=1.9×10^6, f=5.7 Hz (ω^*=0.06), α=11±7°, with and without constant blowing.

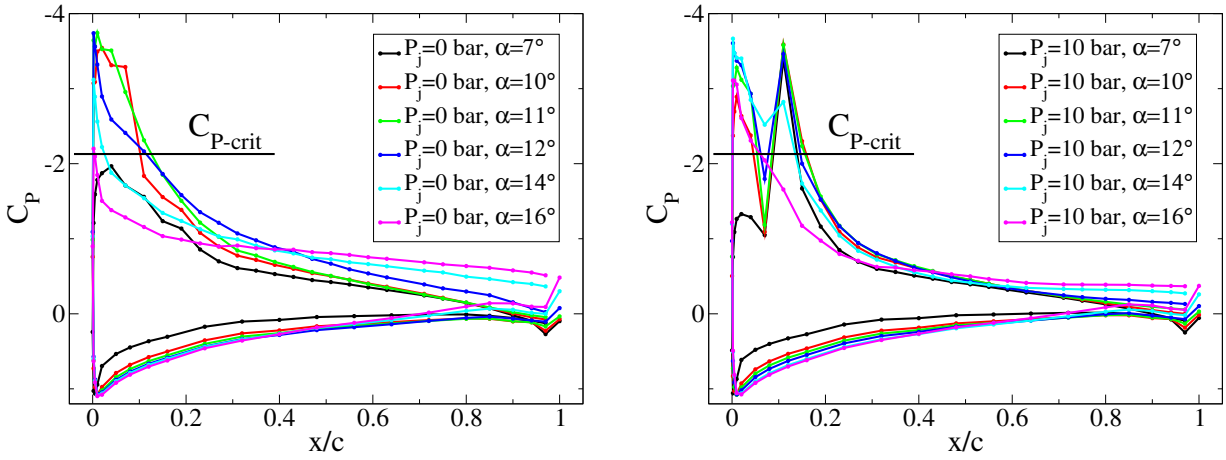

(a) P_j=0 bar (b) P_j=10 bar

Figure 4.59: Pressure distributions during stall at M=0.5, Re=1.9×10^6, f=5.7 Hz (ω^*=0.06), α=11±7°.

Figure 4.57(b) shows C_M for the same conditions. Here a monotonic improvement in C_{M_p} is observed with increasing P_j, with P_j=3 bar reducing C_{M_p} by 44%, P_j=6 bar by 77% and P_j=10 bar by 96% over the case without blowing. Additionally the stall is delayed by approximately $\Delta\alpha$=2-3° for P_j=10 bar. For this test case no saturation of the control effect is seen up to the maximum blowing rate of P_j=10 bar.

Figure 4.58 shows the deepest stall investigated. At α=11±7° the minimum pitching moment is less reduced than for α=7±7°, and blowing at P_j=3 bar does not bring any advantage, increasing C_{M_p} by 9% and adding a strong sine-wave oscillation to the forces. At higher blowing pressures a monotonic improvement in C_{M_p} occurs with increasing P_j, with P_j=6 bar reducing C_{M_p} by 34% and P_j=10 bar by 58% over the case without blowing. Similar to α=7±7° there is no saturation of the flow control effect seen up to the maximum blowing rate of P_j=10 bar. C_{L_p} reduces from 1.23 without blowing to 1.09 with P_j=10 bar, slightly less reduction than for α=7±7° (Table 4.9).

The surface C_P distributions for α=11±7° with P_j=0 bar and P_j=10 bar are examined in Fig. 4.59. The surface C_P distributions without blowing in Fig. 4.59(a) are similar to those at the same α for

α=7$\pm$7° in Fig 4.52. At α=16°, the supersonic region at the front of the airfoil has disappeared, and this correlates with the kink in C_{M_p} seen at α=15° in Fig. 4.55(a).

Figure 4.59(b) depicts the surface C_P distributions for P_j=10 bar. At α=7°, the C_P distribution is similar to that without blowing, except that there is a large suction peak due to the flow acceleration near the jets with supersonic flow and thus probably terminated by a shock. The suction peak on the front of the airfoil is lower (more positive C_P) than without blowing. The additional jet-induced suction peak results in an upward force, which almost completely offsets the downward impulse of the jet, added in the data correction procedure. The suction peak due to the jets remains approximately the same as angle of attack increases and, similar to the case without blowing, a supersonic region with terminating shock appears at the front of the suction side of the airfoil. Blowing suppresses the suction peak at the front of the airfoil and delays the appearance of the supersonic area from α=7.4° for α=11$\pm$7° with P_j=0 bar to α=8.8° for P_j=10 bar. This delay correlates with the kink in the lift curve for P_j=10 bar in Fig. 4.58(a). The pressure distribution continues to have two suction peaks as the angle of attack increases.

The airfoil without blowing stalls around α=11°, as for the motion at α=7$\pm$7° in Fig. 4.52, but the moment stall for P_j=10 bar starts around α=14°, as the two supersonic regions join in Fig. 4.59(b), and the suction peak due to the jets reduces in size. A trailing edge stall starts before this, however, at around α=12°, and this correlates with the drop in the lift slope to near zero in Figs. 4.57 and 4.58 at α=12°. By α=16° on the upstroke, the two suction peaks have fully merged, and there is supersonic flow from the start of the suction peak to the jets at x/c=0.10. This C_P distribution remains similar until approximately α=16° on the downstroke and correlates with the plateau in C_{M_p} for P_j=10 bar and $\alpha \geq$16° in Fig. 4.55(a). The reattachment behavior without blowing starts with the reappearance of the shock, the disappearance of the separation under the shock and reattachment from the shock toward the trailing edge. With blowing the reattachment is similar, but the reattachment occurs from the shock after the jet supersonic region, since the flow on the front of the airfoil remains supersonic and never separates.

4.3.9 Optimization of blowing at Mach 0.5

It is desirable to know the optimal C_q, C_μ and jet spacing (s) for this kind of flow control. Since for the data at Re=1.9$\times$10^6, the control of stall continued to improve up to P_j=10 bar (C_q=0.0081, C_μ=0.030), further increases in the normalised blowing could only be achieved by reducing the Reynolds number. Thus the optimization of blowing was investigated at Re=0.85$\times$10^6, where a saturation of the blowing effect could be achieved. Example values of $\dot{m}_m$, F, C_q and C_μ are in Table 4.11 for a range of P_j, with values for the changes to the lift (ΔC_L) and moment (ΔC_M) due to the jet momentum force F, at Re=0.85$\times$10^6, α=10° and C_L=1.0.

Figure 4.60 shows dynamic stall at α=7$\pm$7° at Re=0.85$\times$10^6 and M=0.5 with f=5.7 Hz (ω^*=0.06). Without blowing, the stall is similar to that at Re=1.9$\times$10^6, shown in Fig. 4.57, with C_{L_p} reducing by 0.5% and $\overline{C_L}$ reducing by 7% over that at high Reynolds number (Table 4.9). The pitching moment increases significantly, with the pitching moment peak at Re=0.85$\times$10^6 being 27% greater than that at Re=1.9$\times$10^6.

As at Re=1.9$\times$10^6, increasing the blowing pressure in Fig. 4.60 resulted in a reduction in peak lift, and a reduction of the pitching moment peak, however due to the reduced Reynolds number, a saturation of the flow control effect was observed with an optimum at P_j=3 bar (C_q=0.006, C_μ=0.020), completely removing the pitching moment peak. Additionally, C_{L_p} was reduced by 10% and $\overline{C_L}$ was reduced by 2% compared to the case without blowing (Table 4.9). Further increases in P_j resulted only in an undesirable reduction of lift. This optimum was less than the normalised blowing required for almost-optimum control of the dynamic stall at Re=1.9$\times$10^6, with P_j=10 bar (C_q=0.0081, C_μ=0.030). Thus higher Reynolds numbers require relatively more blowing (higher C_q, C_μ) to control the dynamic

Table 4.11: Example for blowing with all jets at Re=0.85×10^6.

P_j	$\dot{m}_m$	F	C_q	C_μ	ΔC_L	ΔC_M	W_j
bar	kg/s	N	-	-	-	-	kW/m
1	0.024	9.1	0.002	0.007	-0.007	-0.001	3.3
2	0.048	18.1	0.004	0.014	-0.013	-0.002	9.9
3	0.072	27.2	0.006	0.020	-0.020	-0.003	17.8
4	0.096	36.2	0.007	0.027	-0.027	-0.004	26.5
5	0.120	45.3	0.009	0.034	-0.033	-0.005	35.8
6	0.144	54.3	0.011	0.041	-0.040	-0.006	45.5
7	0.168	63.4	0.013	0.047	-0.047	-0.007	55.7
8	0.192	72.5	0.015	0.054	-0.053	-0.008	66.2
9	0.216	81.5	0.017	0.061	-0.060	-0.009	77.1
10	0.240	90.6	0.018	0.068	-0.067	-0.010	88.1

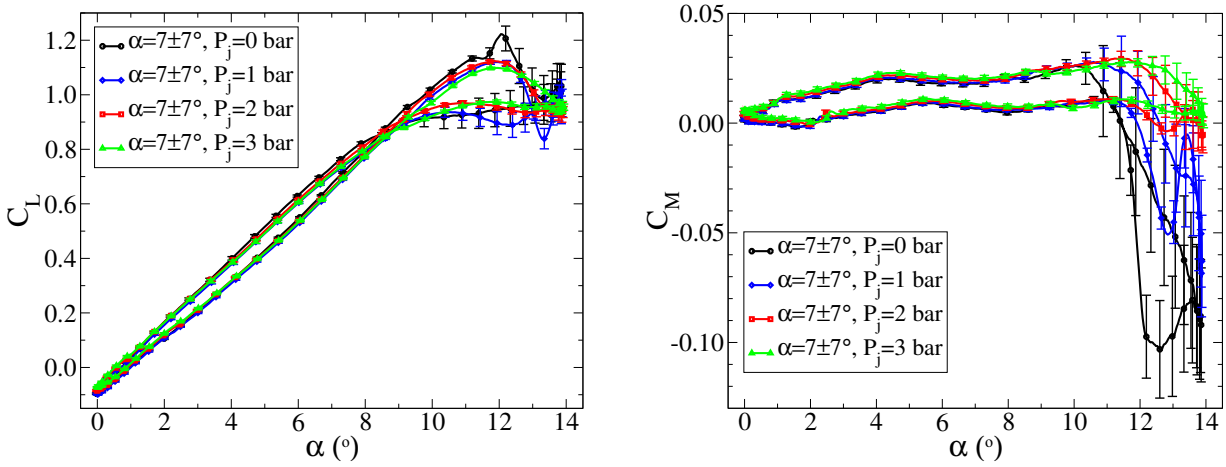

(a) C_L vs α (b) C_M vs α

Figure 4.60: Experimental comparison of forces at M=0.5, Re=0.85×10^6, f=5.7 Hz (ω^*=0.06), α=7±7°, with and without constant blowing.

stall, at least for this airfoil and movement.

At the deepest stall tested, with α=11±7°, in Fig. 4.61, the mean and peak lift without blowing are similar to those at Re=1.9×10^6, but C_{M_p} is increased by 5% (Table 4.9). A saturation of the control effect was observed, but the stall could not be fully controlled by the blowing. At P_j=4 bar (C_q=0.007, C_μ=0.027), the pitching moment peak was reduced the most with a 68% reduction over the reference case without blowing. A further increase in P_j led to a worse C_{M_p}, and a rapid decrease in C_{L_p}. For P_j=4 bar, C_{L_p} is 13% reduced, and $\overline{C_L}$ is 0.4% reduced over the case without blowing.

The spacing of the control jets was investigated by using the valves to switch on every second or every third jet only. The jet spacings of 20 mm (s/c=0.067), 40 mm (s/c=0.13) and 60 mm (s/c=0.20) are compared. For each of these cases, the optimum blowing pressure was found for α=11±7° at Re=0.85×10^6 and M=0.5 with f=5.7 Hz (ω^*=0.06), using the same method as when every blowing jet was used. The result of this optimization is shown in Fig. 4.62. When every second valve is on, the optimum is P_j=6 bar (C_q=0.006, C_μ=0.020) and when every third valve is on the optimum is P_j=7 bar (C_q=0.004, C_μ=0.016). The reduction in C_q and C_μ over the values in Table 4.11 is because fewer jets are active.

Figure 4.62(a) shows that increasing the jet spacing increased the C_{L_p} measured, with a loss of

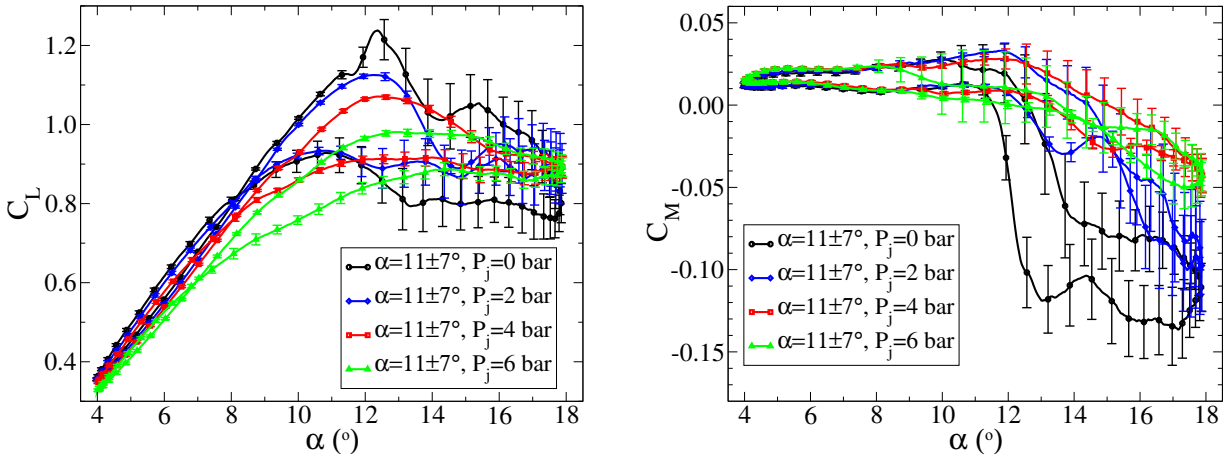

(a) C_L vs α (b) C_M vs α

Figure 4.61: Experimental comparison of forces at M=0.5, Re=0.85×10^6, f=5.7 Hz (ω^*=0.06), α=11±7°, with and without constant blowing.

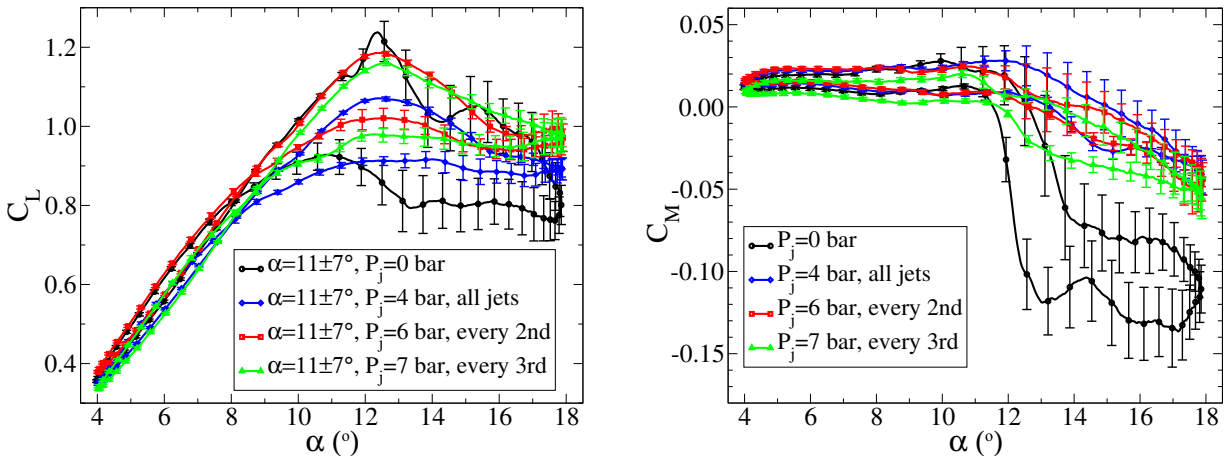

(a) C_L vs α (b) C_M vs α

Figure 4.62: Investigation of optimal jet spacing with comparison of forces at M=0.5, Re=0.85×10^6, f=5.7 Hz (ω^*=0.06), α=11±7°, with and without constant blowing with varying spacings.

only 4% in C_{L_p} compared to the reference case without blowing, and an increase of 9% in $\overline{C_L}$ when using every second jet (Table 4.9). Similarly, using every third jet results in a 6% reduction in C_{L_p} and a 5% increase in $\overline{C_L}$. The offsets in lift are due to the differences in sensor discretization error with different jet spacings. In subsection 4.3.2 the maximum offsets due to the discretization error were estimated to be ΔC_L=0.12 and ΔC_M=0.02, meaning that the experimental error is increased, but the conclusions remain unchanged. The pitching moment peak in Fig. 4.62(b) is significantly reduced for each of the three jet spacings, with a reduction in C_{M_p} of 68% using every jet, 63% using every second jet, and 60% using every third jet. Despite the reduced control in the pitching moment peak when increasing the jet spacing to 60 mm (s/c=0.20), the increase in lift and reduction of piping required for a practical installation make it an attractive option in addition to the 42% saving in compressed air mass required for the optimal control.

Each of the jet spacings investigated increased the drag at low angle of attack and decreased the drag at high angle of attack, as seen in Fig. 4.63(a). Although the drag is reduced, the energy required in compressed air to achieve this is more than the savings in drag, as shown in Fig. 4.63(b). No cases

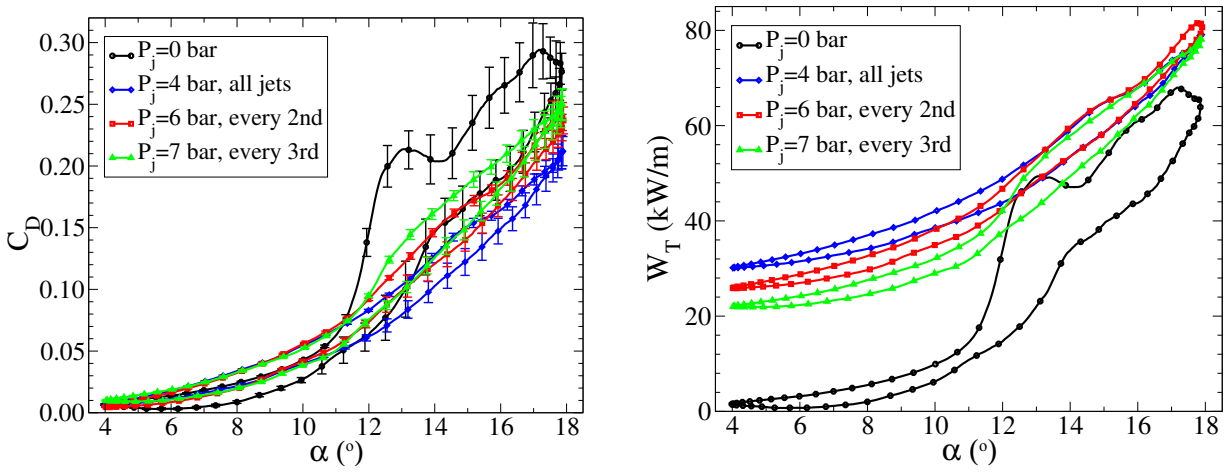

(a) C_D vs α (b) W_T vs α

Figure 4.63: Investigation of drag and energy balance at M=0.5, Re=0.85×10^6, f=5.7 Hz (ω^*=0.06), α=11±7°, with and without constant blowing with varying spacings.

were found in which flow control resulted in a reduction in total power used. Blowing at low angles of attack increases the total required power significantly with the increase proportional to the amount of compressed air used. At high angles of attack the total energy is also increased despite the reduction in drag. Thus this kind of blowing does not save power, although it will lead to a decrease in peak system power if a compressed air buffer is used. It would be desirable to switch the jets at 1/rev, so that they are only active when the flow is separated, although this would result in a considerable increase in system complexity. Cases with 1/rev switching and pulsed blowing were measured and will be reported in a later publication.

4.3.10 Aerodynamic damping at Mach 0.5

The damping coefficient D gives an indication of whether a negative damping will be too large to be counteracted by the structural damping and is computed from the theoretical and measured values of the aerodynamic damping [69]:

$$D = [-\oint C_M \, d\alpha (\alpha_\pm)^2 \pi^3 c f] / [2 v_\infty], \quad (4.7)$$

where D=1 for small oscillations with attached flow, and C_M are the phase-averaged values of the pitching moment.

Figure 4.64 illustrates that changing the blowing changes the aerodynamic damping, generally reducing it from the positive damping without blowing. With the exception of a few points with very high blowing rates, the damping D is greater than 1.0. A single point, pictured in Fig. 4.64, with P_j=9 bar and α=7±7° at Re=0.85×10^6

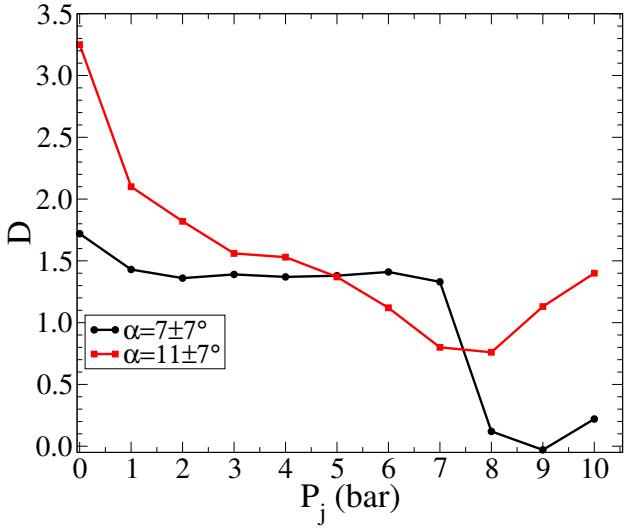

Figure 4.64: Investigation of aerodynamic damping for Re=0.85×10^6 and f=5.7 Hz (ω^*=0.06), α=11±7°, with constant blowing at varying pressure.

shows a slightly negative damping, however this point has more than double the optimal blowing and is thus unlikely to appear in a realistic configuration. Generally, the flow control with air jets is uncritical regarding the aerodynamic damping at M=0.5.

4.3.11 Conclusions

Experiments have been described, showing the dynamic stall control effect of air jets at x/c=0.10. Dynamic stall control by constant blowing from portholes was investigated on an OA209 airfoil at Mach 0.3 at Re=1.15$\times 10^6$ and Re=0.575$\times 10^6$, Mach 0.4 at Re=1.5$\times 10^6$ and Mach 0.5 at Re=1.9$\times 10^6$ and Re=0.85$\times 10^6$ with dynamic pitching motion. At Mach 0.3 and 0.4 the primary results were:

1. The effect of blowing at high pressure is to slow the stall and delay the pitching moment peak relative to the initial stall.
2. The initial stall is changed from a leading edge to a trailing edge stall, and the suction peak is maintained in front of the jets after stall. This reduces C_{M_P} and increases the lift after stall.
3. It was found that at M=0.3 the optimal blowing mass flux for the jet separation of s/c=0.067 was described by C_μ=0.25 (C_q=0.038) for low dynamic loading, with some loss in lift performance, and C_μ=0.12 (C_q=0.019) for maximum reduction in C_{M_P} without loss of lift performance. At these conditions a maximum reduction of C_{M_P} by 67% was seen, while C_{L_P} remained similar to the reference case and $\overline{C_L}$ increased by 7%.
4. As a comparison, the passive LEVoG flow control devices were attached to the model and tested without blowing, reducing C_{M_P} by 24% and increasing $\overline{C_L}$ by 4% at the same conditions.
5. Increasing the spacing of the jets resulted in an improvement in the flow control performance, with the best result found with a spacing of s/c=0.13 and blowing at C_μ=0.12 (C_q=0.019). At this condition a C_{M_P} reduction of 83% was found and $\overline{C_L}$ was increased by 30%. The dynamic stall control effect was also found to increase significantly for the few points measured with light stall, due to the stall-delaying effect of the jets.
6. At M=0.4 a reduction in C_{M_P} of 56% was achieved, for the jet separation of s/c=0.067. The pressure available for the jets was limited, so that no saturation of the control effect was found at M=0.4 and 0.5.

At Mach 0.5 the primary results were:

1. At both Reynolds numbers, the OA209 without blowing experiences shock-induced stall with a hysteresis in lift and pitching moment around the static values, rather than the overshoot in forces typically associated with a dynamic stall vortex.
2. The forces, both with and without flow control, were primarily functions of the maximum angle of attack, with pitching frequency, amplitude and mean angle of attack having minor effects.
3. Stall could be fully suppressed for lower values of α_{max}, and for higher α_{max} (in deep stall) a reduction in pitching moment peak of up to 68% was demonstrated.
4. The higher Reynolds number required relatively more blowing (higher C_q, C_μ) to control the dynamic stall.
5. Increasing the jet spacing resulted in equivalent flow control with less air use.
6. Drag was reduced for separated flow, but the energy required in compressed air to achieve this was more than the savings in drag, and no cases were found in which flow control resulted in a reduction in total power used.
7. The flow control with air jets was uncritical regarding the aerodynamic damping.

Due to the negative effects of the blowing on attached flow, it would be desirable to switch the jets at 1/rev, so that they are only active when the flow is separated. Active stall control using air jets in the manner described in this section offers a method of reducing peak loads during maneuvering flight. Since the compressed air requires significant power to supply, this would only be suitable for short bursts of use. The stall control effect does not have any critical Mach number dependence, and thus no sudden change in the flow control effectiveness is to be expected if the jets were to be positioned sub-optimally along the radius of a rotor blade.

4.4 3D effect of flow control by blowing [4]

The three-dimensional effect of flow control by blowing was investigated with pressure-sensitive paint on an OA209 airfoil, using the setup described in section 3.3. The flow generated by the blowing is strongly 3D and the error in the computation of the forces by a single line of pressure transducers is estimated to be a maximum of 8% using 3D unsteady CFD, as shown in subsection 4.3.2. Each jet was fitted with a valve [88], to switch it on and off. The blowing is characterised by C_μ, the momentum ratio between the jets and the freestream one chord length above the airfoil. The flow control system is fully described in section 4.3.

Figure 4.65 shows the force coefficients on the pitching airfoil with three different flow control settings compared to the case without flow control at M=0.3, Re=0.53×10^6, f=5.7 Hz (ω^*=0.11), α=13±7°. The flow is controlled by using every jet, every second jet or every third jet. The momentum ratio C_μ is equal for the first two cases and slightly reduced for the case using only every third jet, due to a limit on the maximum pressure in the model pressure system. It can be seen that each of the three flow control methods reduces the pitching moment during stall significantly and that each produces a qualitatively similar time-history in both lift and pitching moment with some offsets. The cycle-to-cycle differences and fluctuations (not shown) are reduced by up to a factor of 4-8 during stall on the upstroke by the blowing, but for fully stalled flow on the downstroke the fluctuations are only reduced by a factor of 2 by the blowing.

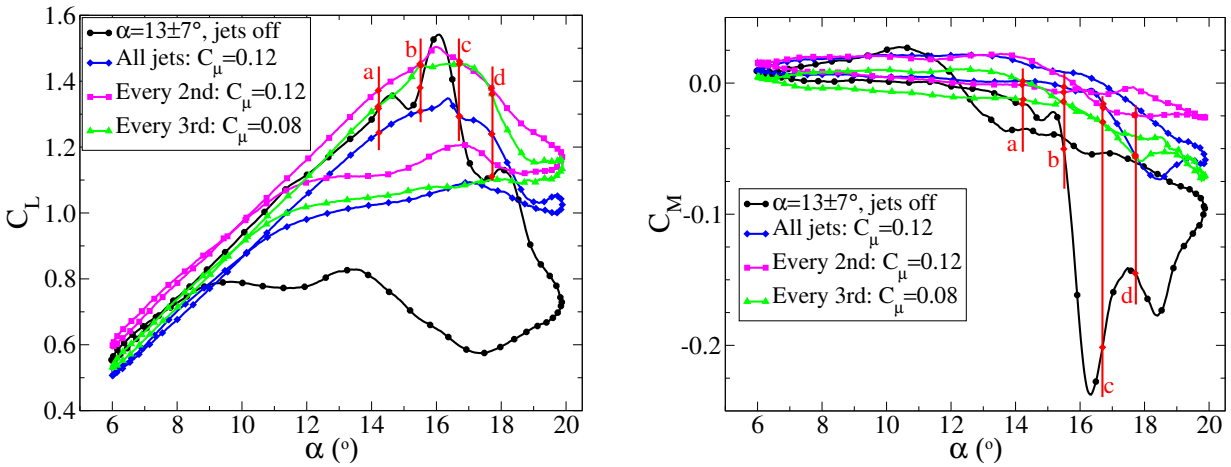

Figure 4.65: Force coefficients integrated from the pressure transducers at M=0.3, Re=0.53×10^6, f=5.7 Hz (ω^*=0.11), α=13±7° with flow control by blowing. Left: C_L Right C_M. Letters relate to the subfigures of Figs. 4.66 and 4.68.

The 3D effect of the jets and the problems for the pressure integration can be seen in Fig. 4.66. In Fig. 4.66a the attached flow before stall is seen for all 3 flow control cases and for the reference case without blowing. The pressure distributions are similar on the pressure side, and the downstream half of the suction side the airfoil and differ near the leading edge on the suction side of the airfoil. Without blowing, a standard suction peak is formed, but when all jets are turned on, a second suction peak appears at the pressure transducer which is between the jets at x/c=0.12. The pressure upstream of the jet is increased when blowing is used. When only every second jet is used, then the pressure distribution is similar, with the suction peak near the jets increased, but otherwise a similar pressure distribution. However, when only every third jet is used, the suction peak at the position of the jets is greatly reduced and this is because the jet which that pressure transducer is close to is now turned off.

[4] Text and illustrations in this section are taken from [25]: Gardner, A. D., Klein, C., Sachs, W., Henne, U. , Mai, H., Richter, K., "Investigation of three-dimensional dynamic stall on an airfoil using fast response pressure sensitive paint", , Experiments in Fluids, Volume 55, No. 9, 2014. DOI: 10.1007/s00348-014-1807-4

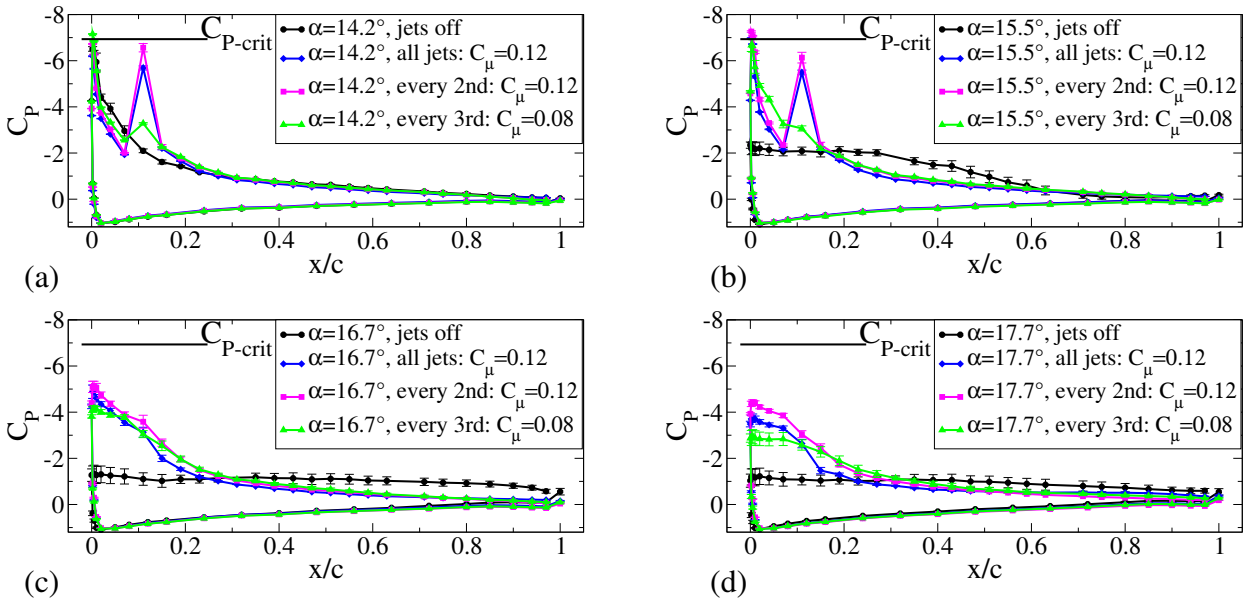

Figure 4.66: Comparison of C_P data at the pressure transducers on the upstroke at M=0.3, Re=0.53×10^6, f=5.7 Hz (ω^*=0.11), α=13±7° for different blowing types during stall, at the points illustrated in Figs. 4.65 and 4.68. (a) α=14.2° (b) α=15.5° (c) α=16.7° (d) α=17.7°

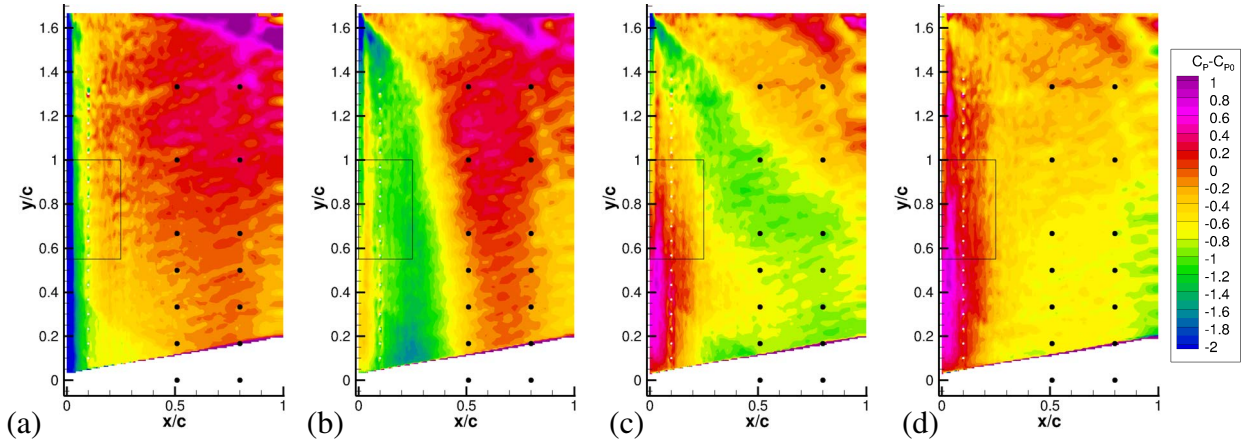

Figure 4.67: PSP pressure distributions (C_P-C_{P_0}) illustrating the 3D flow during stall for M=0.3, Re=0.53×10^6, f=5.7 Hz (ω^*=0.11), α=13±7°. (a) α=14.2° (b) α=15.5° (c) α=16.7° (d) α=17.7°. The black rectangles indicate the regions for which the C_P distributions are shown in Fig. 4.68. These are Figs. 3.34b, 3.34d, 3.34f and 3.34h.

This provides an illustration of the problem of characterizing a 3D flow using an essentially 2D line of pressure transducers. It can be seen that this problem persists in Fig. 4.66b as the stall begins, but in Figs. 4.66c and 4.66d as the flow fully stalls the localised suction peak joins the primary suction peak in all three flow control cases and it might be assumed that all flows are more 2D than before stall.

Figure 4.68 shows PSP surface C_P distributions for each of the four test cases. The time-points are shown by the red lettering and lines in Fig. 4.65 and cover points on the upstroke during the dynamic stall. The area visualised is chosen as having a relatively low error due to temperature variation and is shown by the black rectangle in Figs. 3.34b, 3.34d, 3.34f and 3.34h. Due to this low temperature variation, the C_P data could be used directly from the PSP images. The black dots illustrate the positions of the pressure transducers relative to the holes.

The pressure transducers are around y/c=0, but for illustrative purposes to understand the effect

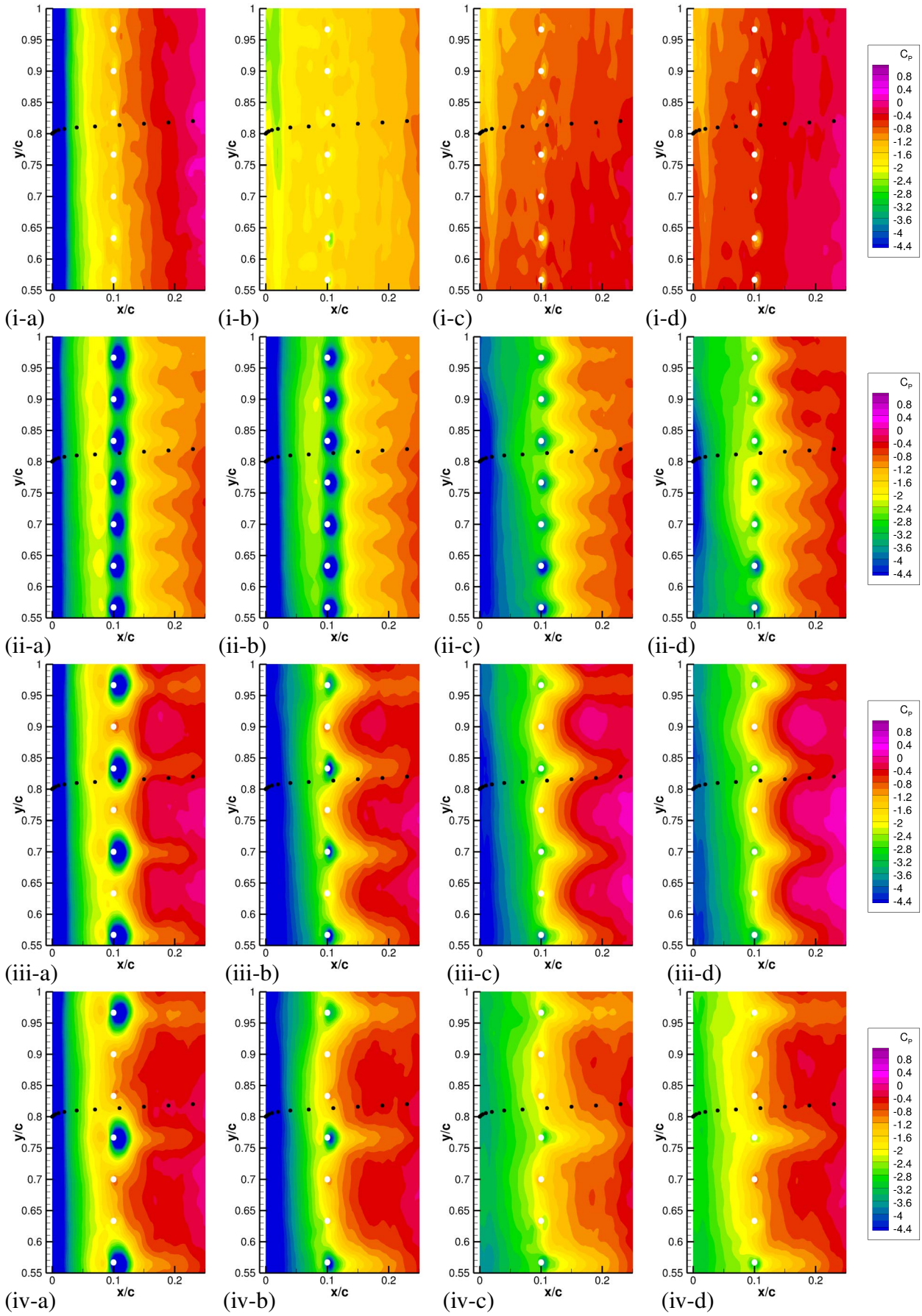

Figure 4.68: PSP pressure distributions (C_P) illustrating the 3D flow around the flow control jets at M=0.3, Re=0.53×10^6, f=5.7 Hz (ω^*=0.11), α=13±7° during stall. (a) α=14.2° (b) α=15.5° (c) α=16.7° (d) α=17.7° (i) No blowing (ii) All jets, C_μ=0.12 (iii) Every 2nd jet, C_μ=0.12 (iv) Every 3rd jet, C_μ=0.08

of the holes on the transducers, the pressure transducer positions have been shifted 12 holes in the positive y direction. Figures 4.68i-a to 4.68i-d show the flow during separation and are exactly the same data as in the rectangles in Fig. 4.67a to 4.67d, but as C_P rather than C_P-C_{P_0}. Here no flow control is active and the airfoil stalls normally. Due to the high zoom level, the passage of the vortex at stall is not visible between Figs. 4.68i-a and 4.68i-b. The pressure distribution is relatively even in the y-coordinate, both before and after stall, and thus "quasi 2D".

For the test case with flow control turned on using every jet, seen in Figs. 4.68ii-a to 4.68ii-d, each active jet is visible as a 3D suction region (in blue) created around the jet. The suction region contains material from the external flow accelerated by the flow control jet, in the same way as an eductor jet pump. In Fig. 4.68ii-a, the onflow shifts the 3D suction region to the lee of the jet. The flow between the jets is also from the onflow, accelerated in the restriction due to the jets. The jets form a unified wall of flow control at x/c=0.10, with the local effects of the jets meeting. The stall is delayed, meaning that for α=15.5° in Fig. 4.68ii-b, the flow is not stalled, in contrast to the airfoil without flow control. As the flow stalls, in Fig. 4.68ii-c, the strength of the individual 3D suction peaks greatly reduces and a unified suction area is formed which covers the area between the suction peak and the jets, as also illustrated in Fig. 4.66c. The flow does become more two-dimensional, but this effect is exaggerated in the pressure transducers, since in Fig. 4.68ii-d the 3D suction peak reduces in size and the pressure transducer at x/c=0.12 is now outside the suction peak.

For the test case using only every second jet, seen in Figs. 4.68iii-a to 4.68iii-d, the spacing of the 3D suction peaks has increased. The area of the suction regions is larger than when every jet is used, which is expected since the jet pressure is increased to have the same mass flux through half as many portholes. This increase in area could be responsible for the slight increase in the suction peak height in Fig. 4.66a, but the width of the 3D suction peak remains roughly equal. This illustrates the problems in undersampling of such a 3D region with pressure transducers.

The flow between the jets is no longer as strongly accelerated as when every jet is active, but Fig. 4.65 shows that the flow control effect to reduce the pitching moment peak is even stronger when using every second jet than when every jet is used. As the flow stalls, the suction regions around the jets again reduces in strength and joins the main suction peak, but the rearward extent of the suction peak is significantly reduced between the jets, which will lead to a reduced lift compared to the case using every jet and the lift will be overestimated when computed using the pressure transducers.

In the PSP-images where only every third jet is on, in Figs. 4.68iv-a to 4.68iv-d, the flow is similar to that using only every second jet. This is a contrast to the pressure transducer data which saw the disappearance of the pressure peak around the jets for this final condition. As seen in Fig. 4.68iv-a, the difference comes because the pressure transducer at x/c=0.12 which previously indicated the 3D suction peak is now outside the remaining suction peaks. This results in a change in the pressure integration through the pressure-cut. At stall the flow is similar to that using every second jet, but Fig. 4.68iv-d shows that although the suction peak extends to the jets, that C_P at x/c=0.05 is always higher than for either the case using all jets or every second jet, and this is further illustrated in the pressure transducer data in Fig. 4.66d. The lift will be underestimated when computed using the pressure transducers.

4.4.1 Conclusions

In total, a good illustration of both the weakness of single sensor measurement for strongly 3D flows and the potential advantages of PSP is found by the examination of the test cases with blowing, at least for the reduced view with a relatively constant temperature distribution. The results showed a that spatial undersampling with pressure transducers in the characterization of 3D flowfields could be identified and the direction of the force integration error could be identified.

4.5 Results with pulsed blowing [5]

The interest in pulsed blowing stems from a number of experiments showing a much greater effect for the same energy applied to the control for pulsed blowing as for constant blowing. Investigations on airfoils with static stall for airfoils in incompressible flow [110] and on a generic flap [89] have shown pulsed blowing to be more effective than constant blowing. Experiments using synthetic jet actuators with zero mass flux [117] showed that the control of stall on a ramping airfoil could be achieved, with a saturation in effect around C_μ=0.01. Experiments demonstrating dynamic stall control using pulsed blowing from a high pressure source [44] with $0.001 \leq C_\mu \leq 0.004$ noted that at these blowing rates pulsed blowing was more effective than constant blowing at the same C_μ. Both of these studies investigated dynamic stall with a small hysteresis and weak stall. Weaver et al. [121] investigated the control of deep dynamic stall in water tunnel experiments on a VR7 airfoil. Control was by blowing through a tangential slot located at x/c=0.25. Weaver et al. found that for their configuration and points investigated, pulsed blowing was better than steady blowing with $C_\mu \leq 0.01$, but for $C_\mu \geq 0.02$, as required for the control of deep dynamic stall, steady blowing started to become equal or better in effectiveness. Pulsed blowing frequency was varied between F^+=0-2.7, with pulsed blowing at F^+=0.9 being the most effective.

Singh et al. [113] used blowing from angled jets at M=0.13 and Re=1.1×10^6 on a pitching airfoil. The jets were located at x/c=0.12 and spaced at y/c=0.1 along the span with the jet exit pitched at 30° and skewed at 60°. They found that for constant blowing at C_μ=0.008 there was good control of dynamic stall. Further experiments by the same group [112] found that for the control of static stall that pulsed blowing at F^+=0.7 and F^+=1.3, was as effective as constant blowing with around twice the average mass flux.

In this experiment, the same setup was used as in the previous sections, with dry compressed air supplied to the pressure system of the wind tunnel model. The mass flux measurement was around 20 m from the model, and thus averaged the mass flux from the pulsed blowing with a limiting frequency lower than 1 Hz. The valves, each weighing 85 g, were developed by the DLR [88] and could be individually switched on and off, and pulsed at frequencies of up to 500 Hz. In Fig. 4.69 a drawing of the fast switching valve is shown installed in the nose of the airfoil. Flow around the airfoil model in the external freestream is from left to right, and flow through the valve is from right to left. A single 8 mm diameter magnetizable valve ball (1) is the closure element of the valve, and its only moving part. Only the pressure difference between valve inlet and valve outlet keeps the ball in the valve seat (2). To open the valve, the magnetic coil (3) generates a magnetic field, which is guided by magnetizable material in the housing of the valve. The magnetic field generates a force on the ball which rolls the ball off the valve seat (in the vertical direction in Fig. 4.69. The force acts mainly perpendicular to the valve axis. When the magnetic field is switched off, the flow carries the ball back on to the valve seat and the valve closes. The valves are not damaged by high accelerations, and are generally insensitive to acceleration and vibration. The opening status of two valves was monitored using a Kulite unsteady pressure sensor (4), and no difference in the switching behavior was noted between a static and pitching model. For all test cases reported here, the jets were switched in-phase with each other, and all jets were used, for a jet spacing of 20 mm. The actuation system was chosen for its simplicity and robustness, not for its similarity to a flyable actuation system, and thus the actuation power is disregarded in this analysis.

A list of points measured is in Table 4.12. The wind tunnel had a total pressure of P_0=30 kPa and total temperature of T_0=310±5 K for all test points

[5] Text and illustrations in this section are taken from [33]: Gardner, A. D., Richter, K., Mai, H., Neuhaus, D., "Experimental investigation of high-pressure pulsed blowing for dynamic stall control", *CEAS Aeronautical Journal*, Volume 5, Issue 2, pp. 185-198, 2014. DOI 10.1007/s13272-014-0099-y

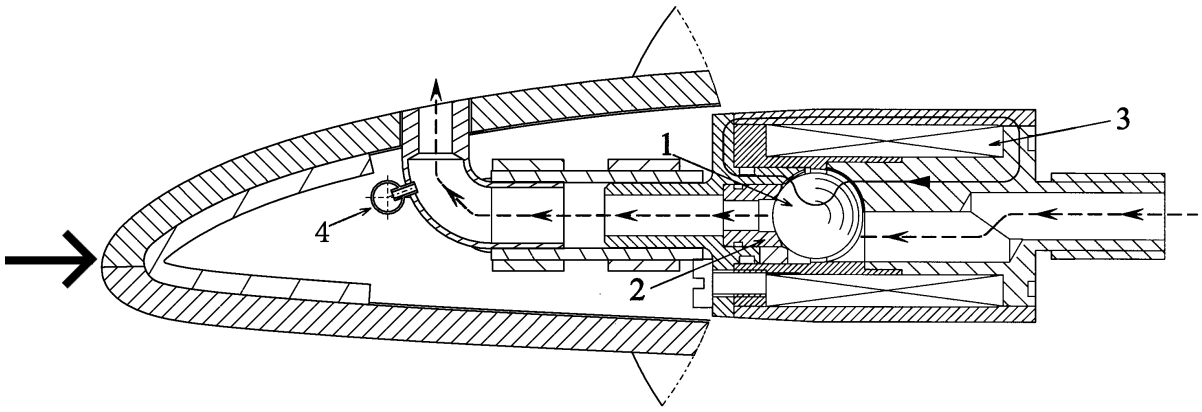

Figure 4.69: Closed fast switching valve. The solid line shows the magnetic flux, and the dashed line the gas path through the valve. Freestream flow is from the left.

Table 4.12: Dynamic airfoil data. For all cases P_0=30 kPa, T_0=310 K and f=5.7 Hz

DC	f_{pulse}	F^+	P_j	$\dot{m}_m$	$\overline{C_L}$	C_{L_p}	C_{M_p}	C_μ	C_q	W_j
%	Hz	-	bar	kg/s	-	-	-	-	-	kW/m
M=0.3, Re=530000, v_∞=109 m/s, α=13$\pm$4°, ω^*=0.10										
0	0	0.00	0	0.000	0.92	1.30	-0.186	0.000	0.000	0.0
100	0	0.00	5	0.120	1.07	1.29	-0.001	0.079	0.014	35.7
50	200	0.50	10	0.127	1.07	1.30	-0.047	0.084	0.014	46.8
50	400	0.99	10	0.127	1.08	1.30	-0.023	0.084	0.014	47.0
M=0.3, Re=530000, v_∞=109 m/s, α=13$\pm$7°, ω^*=0.10										
0	0	0.00	0	0.000	0.81	1.40	-0.229	0.000	0.000	0.0
100	0	0.00	3.5	0.075	0.92	1.37	-0.129	0.050	0.008	19.6
100	0	0.00	4	0.086	0.92	1.36	-0.127	0.057	0.010	23.7
100	0	0.00	5.5	0.125	0.91	1.32	-0.081	0.083	0.014	38.5
50	100	0.25	6	0.081	0.96	1.34	-0.168	0.054	0.009	25.7
50	200	0.50	6	0.089	0.97	1.35	-0.183	0.059	0.010	28.2
25	200	0.50	10	0.075	0.98	1.37	-0.192	0.050	0.009	27.7
50	400	0.99	6	0.079	0.94	1.36	-0.189	0.052	0.009	24.9
50	500	1.24	6	0.090	0.94	1.37	-0.129	0.059	0.010	28.4
50	100	0.25	10	0.124	0.96	1.36	-0.162	0.082	0.014	45.8
50	200	0.50	10	0.129	0.97	1.36	-0.135	0.085	0.015	47.6
50	400	0.99	10	0.129	0.94	1.35	-0.068	0.085	0.015	47.5
50	500	1.24	10	0.149	0.92	1.33	-0.080	0.098	0.017	54.8
50	5.7	0.01	-	0.086	0.91	1.35	-0.107	0.056	0.010	-
M=0.5, Re=850000, v_∞=172 m/s, α=11$\pm$7°, ω^*=0.06										
0	0	0.00	0	0.000	0.77	1.23	-0.136	0.000	0.000	0.0
100	0	0.00	4	0.098	0.77	1.07	-0.044	0.028	0.008	27.1
50	5.7	0.01	-	0.087	0.78	1.18	-0.065	0.025	0.007	-

4.5.1 Data analysis

The experimental lift (C_L), drag (C_D) and pitching moment (C_M) coefficients are integrated from a line of 49 Kulite unsteady pressure sensors (type XCQ-093), near the model centerline, and are thus

pressure-parts only of those forces. The coefficients are corrected for the momentum force F due to the air jets:

$$F = \dot{m}v = \dot{m}/L_{act}\sqrt{\frac{2\gamma RT_0}{\gamma+1}}. \tag{4.8}$$

The jet is assumed to be sonic at the surface of the model, and T_0, the total temperature, is assumed to be equal to the measured temperature of the aluminum spar in the model. Here, γ=1.4 and R=287 J/kg/K are gas constants for air. For high-frequency pulsed blowing ($f_{pulse} \geq$100Hz), the phase-averaged data is corrected using $\dot{m} = \dot{m}_m$, the mean mass flux measured by the DF12 mass flux sensor. The corrected values of C_L, C_D and C_M are computed from their uncorrected values, assuming that the jet force is directed normal to the model chord in a downward direction, at x/c=0.10. The qualitative results were not changed by these offsets.

A time-varying correction force is required when using pulsed blowing, since the impulse from the compressed air varies with time. The measured mass flux could not be directly used, since this only provided averaged values. The signal from the pressure sensor at (4) in Fig. 4.69 (P_4) was assumed to be linear to the instantaneous mass flux ($\dot{m}_{inst}$). A calibration constant K was computed for each measured point, such that:

$$\dot{m}_{inst} = K\left(P_4 - min\left(P_4\right)\right), \tag{4.9}$$

where the mean values of $\dot{m}_{inst}$ and $\dot{m}_m$ over 160 pitching cycles are equal, and the correction of forces for the jet impulse used $\dot{m}_{inst}$ in Eqn. 4.8.

The speed and form of the pulsed blowing is a function of the pressure applied. The valves are driven by a relay which applies power in a square wave based on a TTL pulse. Using more electrical power on the valves results in faster opening times, due to the fast establishment of the magnetic field, but slow closing times, since the peak magnetic field is higher. Each pulsation frequency and pressure requires a different voltage to be applied, calibrated to produce the shortest opening and closing times.

The speed of the system was tested by a calibration in which a Pitot probe, consisting

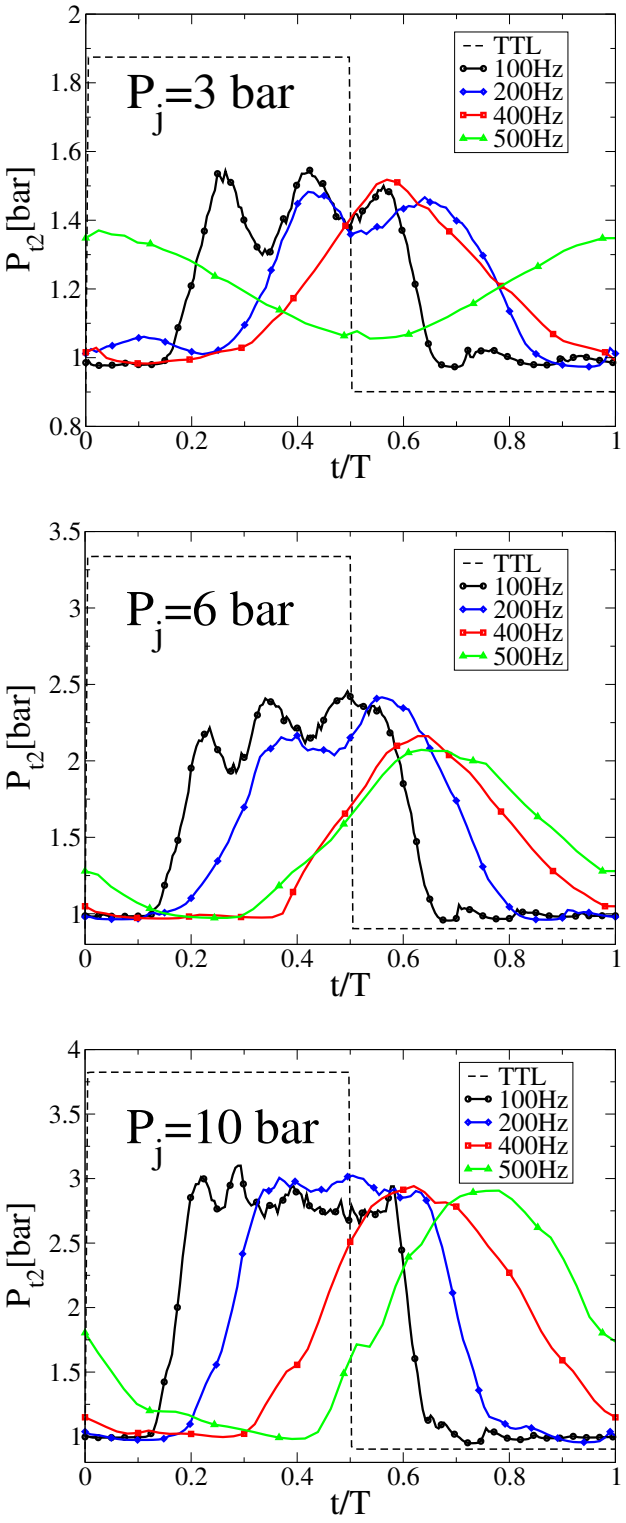

Figure 4.70: Pitot calibration data showing time-delay and rise-time for different pulsing frequencies and pressures.

of a single Kulite pressure sensor without a cavity, was situated 10 mm above the center of a jet exit. This thus measured the time for formation/stopping of the jet, including the electrical, mechanical and pneumatic parts of the system. The delay between the start of jet switching and the rise in Pitot pressure was approximately 1.3 ms. The results of this calibration are in Fig. 4.70, with the time (t) normalised to the pulsing period (T) for a duty cycle (DC) of 50%. The valves work better with higher pressures, and at P_j=3 bar three oscillations, either from bouncing of the ball element or an aerodynamic effect, can be seen after opening at f_{pulse}=100 Hz. This reduces to 2 oscillations at f_{pulse}=200 Hz and one oscillation at f_{pulse}=400 Hz, due to the reduced time for which the valve is open. At f_{pulse}=500 Hz for P_j=3 bar, the valve no longer has time to completely open and close in one pulse cycle.

For P_j=6 bar in Fig. 4.70, the oscillation is significantly reduced, and the valve now has enough time to completely open and close at f_{pulse}=500 Hz. At P_j=10 bar there are no oscillations, and a clean opening and closing is seen for all pulsation frequencies. With increasing frequency, the relative delay of the pressure signal to the TTL driving signal increases, and the rise-time of the Pitot pressure relative to (t/T) is longer, although the absolute rise-time slightly decreases with increasing frequency. The maximum frequency of the valves can be increased by using lighter valve balls than the steel balls used here, however the high reliability of the steel ball with zero creep under high load was selected because the valves are laminated inside the model and cannot be accessed for maintenance. A further investigation of the jet start process is in [122].

4.5.2 Results for pulsed blowing

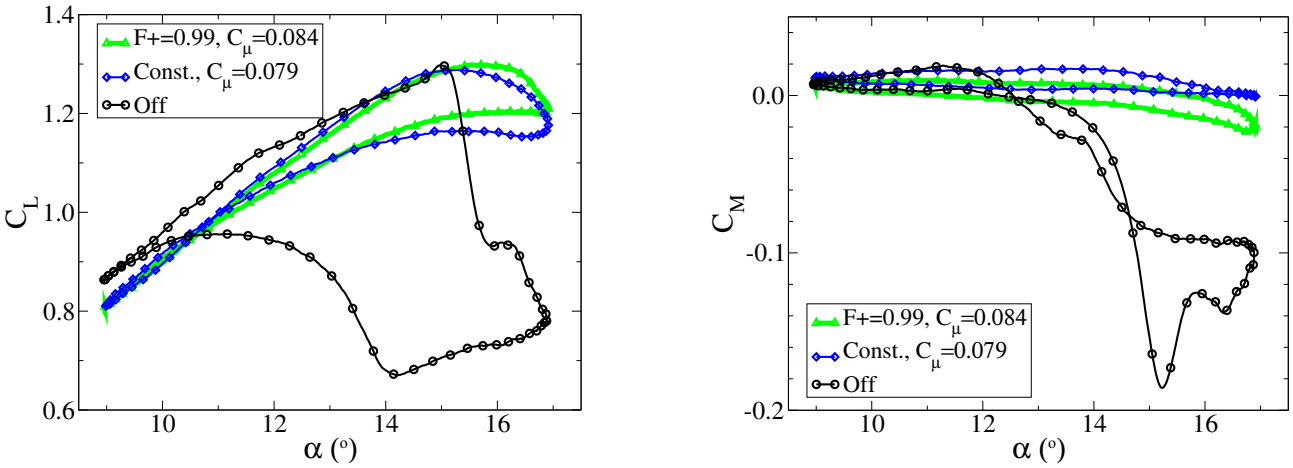

Figure 4.71: C_L (Left) and C_M (Right) for pulsed blowing at C_μ=0.08 with M=0.3, Re=530000, α=13±4°, f=5.7 Hz (ω^*=0.10) for F^+=0 and 0.99 (Constant and 400 Hz).

The OA209 airfoil was tested at M=0.3 and Re=530000, with a pitching motion of α=13±4° at f=5.7 Hz (ω^*=0.10). The valves were either operated for constant blowing, for pulsed blowing or turned off. The pulsed blowing was not a multiple of the pitching frequency, so that within the phase-averaging time of 160 cycles, the pulsed blowing was even distributed over the cycle. This allows the evaluation of the mean behavior of pulsed blowing. The force correction for the jet impulse was made using the average mass flux. Figure 4.71 shows the flow control for a test case with light stall, in terms of the lift and pitching moment. For this rather low Reynolds number, the flow without blowing shows a pronounced kink in the lift polar at α=12° during the attached flow, probably due to the boundary layer transition on the suction side of the airfoil reaching the leading edge [102, 32]. Investigation with surface hot films on a similar airfoil [102] showed a no laminar separation bubbles at M=0.3. At α=13°-14° the moment stall starts, and from α=14° the gradient of the lift curve reduces as the

dynamic stall vortex starts to be formed. By α=15° the lift stall has started and the pitching moment reaches its negative peak a short time later. The airflow remains separated while the airfoil pitches down, and reattaches shortly before the minimum angle of attack.

When constant blowing is used the lift at minimum angle of attack is reduced in Fig. 4.71, but the lift becomes more linear on the upstroke. The maximum lift is approximately the same as without blowing, but no sudden stall appears. A lift hysteresis appears on the downstroke but the pressure distributions (not shown) indicate that there is no flow separation, and the hysteresis loop closes around α=11°. The pitching moment shows no moment stall, and dynamic stall is fully suppressed by using constant blowing. For this case, C_μ=0.079 (Table 4.12), which is considerably higher than for other comparable cases in the literature. Two cases with pulsed blowing with F^+=0.50 and 0.99 (200 Hz and 400 Hz) were tested (Table 4.12), and the case with the best reduction in pitching moment peak, at F^+=0.99 is included in Fig. 4.71. For this case the mass flux of air is approximately the same as for constant blowing, C_μ=0.084, and W_j is increased by 32% due to the increased pressure required to drive the jets. For pulsed blowing the maximum lift is shifted $\Delta\alpha$=+1°, and the lift after stall is slightly higher than for constant blowing, but otherwise the lift is similar to that for constant blowing. The minimum pitching moment is lower than for fully attached flow, with 12% of the original peak remaining, and it is difficult to know whether the flow on the airfoil is stalled (usually clearly visible by unsteadiness in the surface pressure distribution), due to the highly unsteady flow generated by the pulsation.

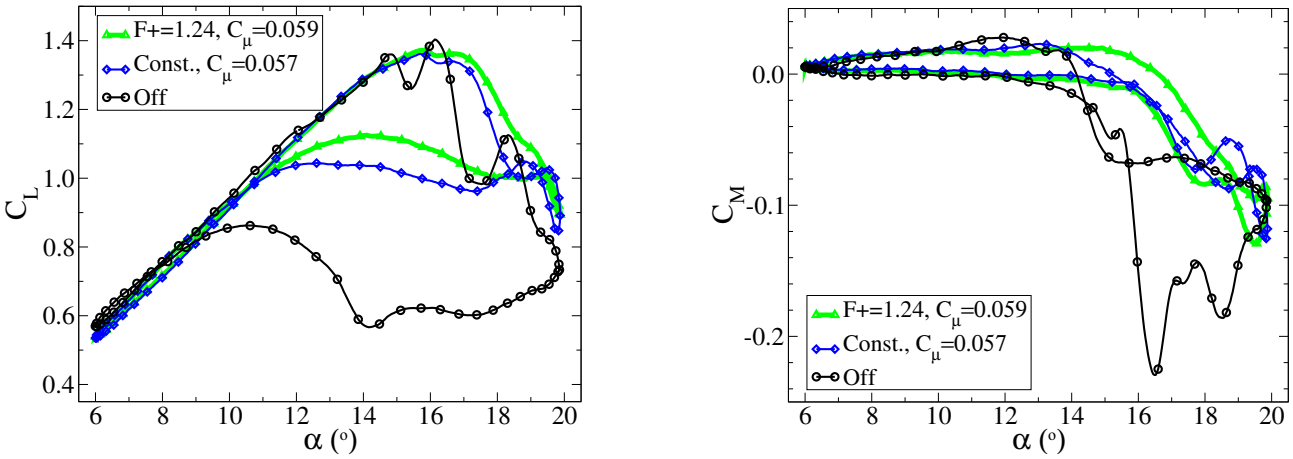

Figure 4.72: C_L (Left) and C_M (Right) for pulsed and constant blowing at C_μ=0.06 with M=0.3, Re=530000, α=13±7°, f=5.7 Hz (ω^*=0.10) for F^+=0 and 1.24 (Constant and 500 Hz).

When the amplitude is increased from α=13±4° to α=13±7°, the OA209 airfoil exhibits deep dynamic stall with the formation of a second stall peak due to the formation of a secondary vortex. Figures 4.72 to 4.75 show results for M=0.3 and Re=530000, with α=13±7° at f=5.7 Hz (ω^*=0.10). At C_μ=0.06, the best reduction in pitching moment peak was found for F^+=1.24, and for C_μ=0.08, the best reduction in pitching moment peak was for F^+=0.99, and these two test cases are compared with constant blowing in Figures 4.72 and 4.74 respectively.

In Fig. 4.72, for α=13±7°, the case without blowing shows the same kink in the lift polar on the upstroke as seen for α=13±4°. The maximum lift is higher than for α=13±4°, increasing C_{L_p} from 1.30 to 1.40. The lift drops slightly at α=15°, as the dynamic stall vortex is formed, and then rises again at α=16.5° as the fully formed vortex creates a suction on the upper side of the airfoil [48]. The second peak at α=16.5° is where the effect of the vortex is the strongest, with the vortex at around x/c=0.6 on the airfoil, and this is closely followed by the negative peak in pitching moment followed by a rise in the pitching moment as the vortex swims off from the airfoil. As the angle of attack continues to increase, a second dynamic stall vortex is formed at the leading edge of the airfoil,

leading to a further, smaller, peak in the lift and pitching moment around α=18.5°. On the downstroke the lift is lower than for α=13±4°, but reattachment in both cases is at around α=9°.

In Fig. 4.72 for constant blowing the stall is much slower than without blowing, and the pitching moment peak is reduced by 45% (Table 4.12). The lift on the downstroke is nearly double that without blowing, increasing $\overline{C_L}$ by 14%, and reattachment is around α=11° on the downstroke. When constant blowing is used, the surface pressures do not show a fully developed dynamic stall vortex, but in contrast to the full suppression of stall at α=13±4°, at α=13±7° the airfoil stalls. For the pulsed blowing at F^+=1.24 (500 Hz), the lift is again slightly higher than for constant blowing at a similar mass flux, and the pitching moment peak is approximately the same as for constant blowing.

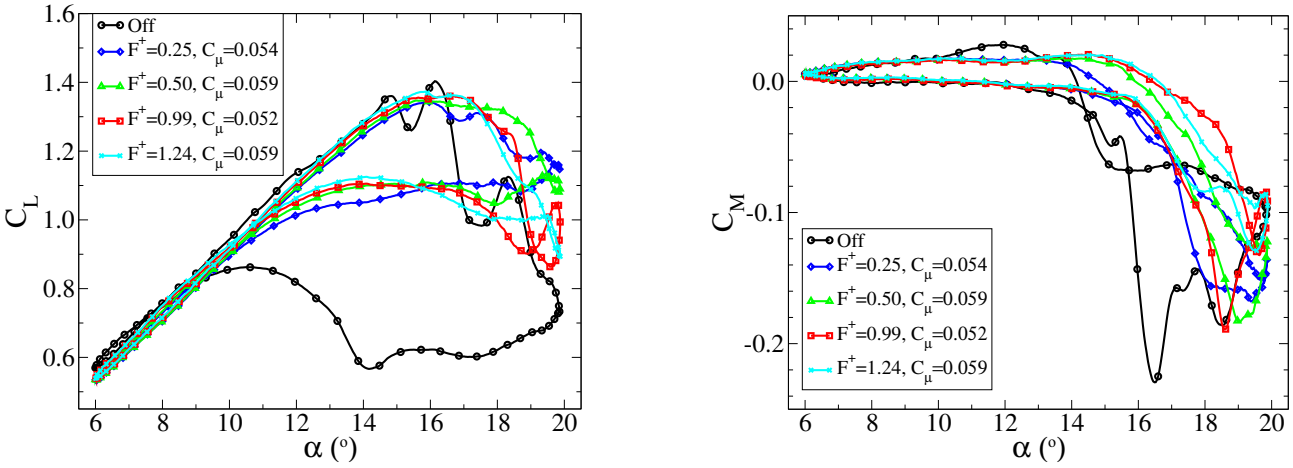

Figure 4.73: C_L (Left) and C_M (Right) for pulsed blowing at C_μ=0.06 with M=0.3, Re=530000, α=13±7°, f=5.7 Hz (ω^*=0.10) for F^+=0–1.24 (Constant to 500 Hz).

Test cases for 0.25≤ F^+ ≤1.24 (100 Hz≤ f_{pulse} ≤500 Hz) were tested at C_μ=0.06, as shown in Table 4.12 and Fig. 4.73. It can be seen that there is some variation in C_μ between the test cases (between 0.052 and 0.059). As noted above, F^+=1.24 was the best frequency with the smallest pitching moment peak after stall, and a similar lift hysteresis to the other cases with pulsed blowing. The pitching moment peak for the second best frequency, F^+=0.99 (f_{pulse}=400 Hz), only reduced the pitching moment peak by 17% from that without blowing (Table 4.12). Table 4.12 shows the power required to produce the pressurised air for these test cases, computed with Eqn. 4.4. For cases with the same average mass flux, the pressure P_j needed to be 70% higher for pulsed blowing than for constant blowing, and this results in a budget of 25% more energy to produce the compressed air for pulsed blowing at this condition than for constant blowing. Table 4.12 also shows results for testing at F^+=0.050 (f_{pulse}=200 Hz) for 25% and 50% duty cycle. The results with 25% duty cycle show that it is less efficient at reduction of the pitching moment peak than 50% duty cycle at similar mass flux.

Figure 4.74 shows results for pulsed and constant blowing at an increased C_μ=0.08. Constant blowing at C_μ=0.083 reduced the pitching moment peak by 65%, and pulsed blowing at F^+=0.99 (f_{pulse}=400 Hz) reduced the pitching moment peak by 70%. As seen in Fig. 4.75, pulsed blowing at F^+=1.24 (500 Hz) reduced the pitching moment peak by 65%, and all other frequencies reduced the pitching moment peak by less than constant blowing. Pulsed blowing at F^+=0.99 had C_μ=0.085 and W_j (as estimated by Eqn. 4.4) was increased by 23% over constant blowing. Blowing at C_μ=0.08 resulted in a lower lift during the attached part of the flow and a delay in stall of $\Delta\alpha$=+2° compared to the case without blowing. Although the pulsed blowing reduced the pitching moment peak more than constant blowing for this case, the difference is within the experimental error.

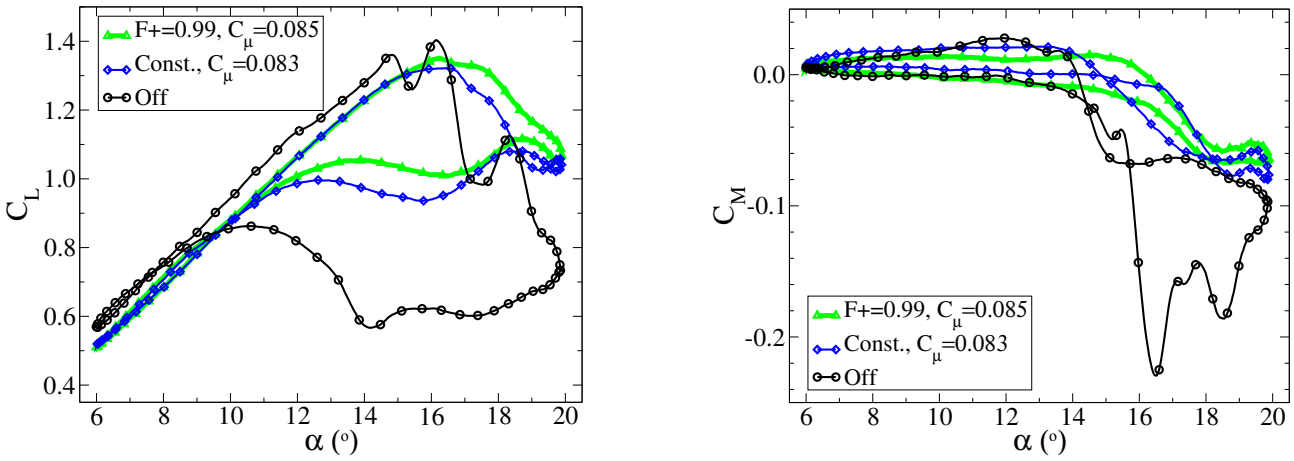

Figure 4.74: C_L (Left) and C_M (Right) for pulsed and constant blowing at C_μ=0.08 with M=0.3, Re=530000, α=13±7°, f=5.7 Hz (ω^*=0.10) for F^+=0 and 0.99 (Constant and 400 Hz).

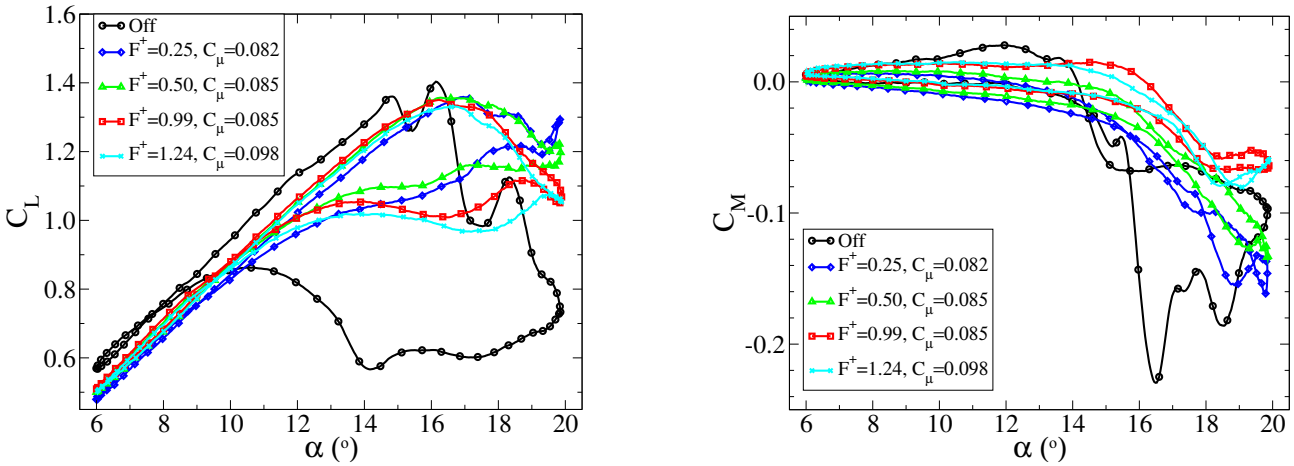

Figure 4.75: C_L (Left) and C_M (Right) for pulsed blowing at C_μ=0.08 with M=0.3, Re=530000, α=13±7°, f=5.7 Hz (ω^*=0.10) for F^+=0–1.24 (Constant to 500 Hz).

Figure 4.76 shows the pressure distributions for the flow at α=13±7° without blowing. It should be noted that for $\alpha \leq$17°, essentially identical pressure distributions are produced by the α=13±4° motion. A subsonic suction peak appears on the upstroke, seen at α=14° shortly before stall in Fig. 4.76, and this reduces sharply at stall (α=15°), with the formation of a dynamic stall vortex which moves in the flow direction. The suction peak and the low pressure area due to the dynamic stall vortex are merged at α=16° in Fig. 4.76. After stall, elevated pressures on the trailing edge and the pressure side of the airfoil produce low lift and high pitching moment, and this remains qualitatively constant until the flow reattach-

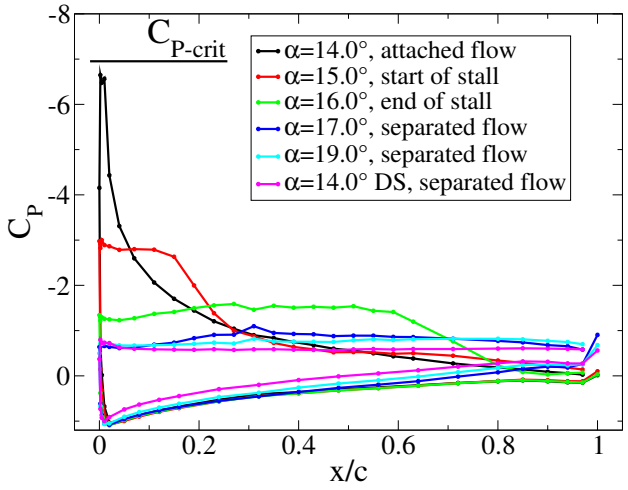

Figure 4.76: Phase-averaged pressure distributions without blowing for M=0.3, Re=530000, α=13±7°, f=5.7 Hz (ω^*=0.10).

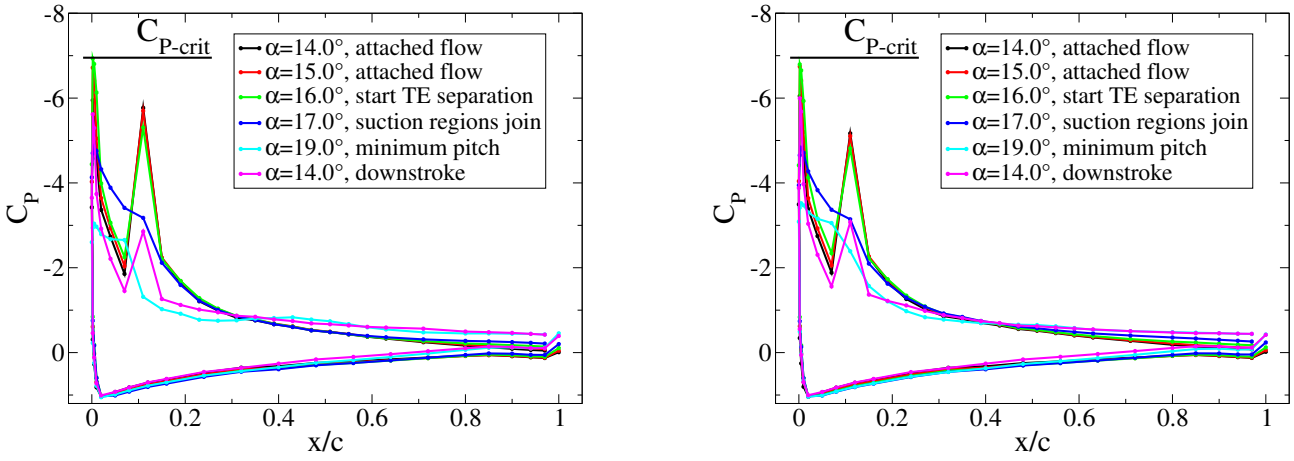

Figure 4.77: Phase-averaged pressure distributions for pulsed blowing at C_μ=0.08 with M=0.3, Re=530000, α=13±7°, f=5.7 Hz (ω^*=0.10) for F^+=0 (Left) and 0.99 (Right) (Constant and 400 Hz).

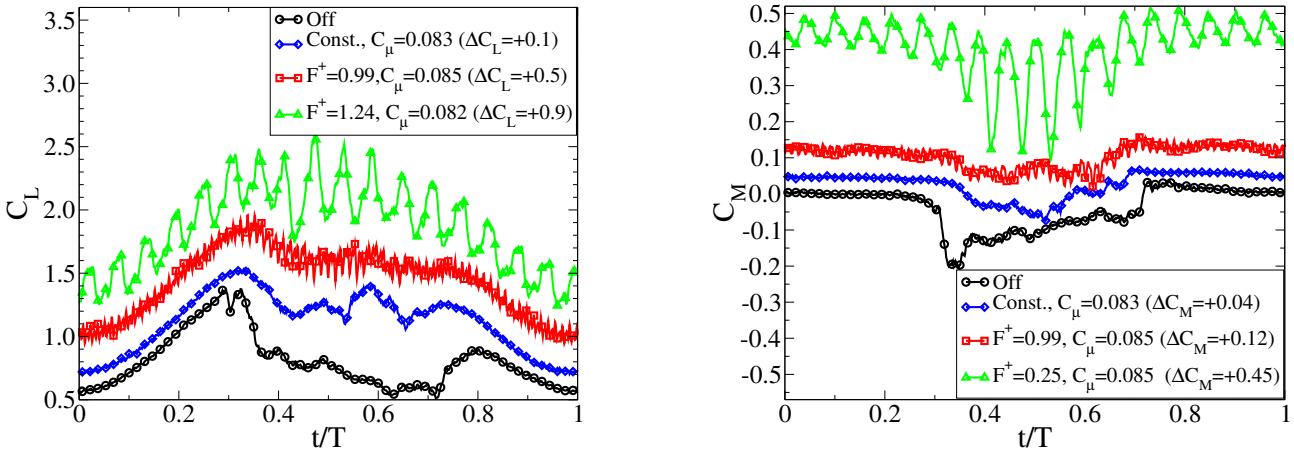

Figure 4.78: Instantaneous results for C_L (Left) and C_M (Right) for pulsed blowing at C_μ=0.08 with M=0.3, Re=530000, α=13±7°, f=5.7 Hz (ω^*=0.10). Note that the lines are offset by the C_L or C_M value in brackets in the legend, to make the unsteady effects visible.

ment on the downstroke. Figure 4.77 shows the pressure distributions with constant (Left) and pulsed (Right) blowing at C_μ=0.08. The phase-averaged pressure distributions are essentially identical for pulsed and constant blowing, and the aerodynamics is also similar. On the upstroke, the jets produce a second subsonic suction peak, push the downstream flank of the primary suction peak upstream, and reduce the suction peak size. Stall starts $\Delta\alpha$=+1° later than without blowing, and is seen as a trailing edge stall. The stall proceeds slowly and the suction regions join. Full stall occurs near the point of minimum pitching moment, and even on the downstroke after stall, a significant suction peak remains, keeping the pitching moment lower and the lift higher than without blowing.

The pulsed blowing causes an additional vibration on the airfoil, illustrated in Fig. 4.78 using data from a single pitching cycle, which is not phase-averaged. Note that the lines in Fig. 4.78 are offset by the C_L or C_M value in brackets in the legend to make the unsteady effects visible. The force correction for the jet impulse was made using the instantaneous mass flux, and the data is plotted against time normalised by the pitching period (t/T). Without blowing, the lift and pitching moment have the vibrations due to the aerodynamic loads of the dynamic stall. With constant blowing at C_μ=0.083, the peaks of these values are reduced. With blowing at C_μ=0.085 and F^+=0.99 (400 Hz), the size of this unsteady signal added to C_M increases to around 25% of C_{M_p} without blowing, and likewise the

unsteady signal added to C_L is around 20% of C_{L_p} without blowing. For blowing at C_μ=0.082 and F^+=0.25 (100 Hz), the size of the unsteady signal increases again, with an unsteady oscillation in C_M of 50-150% of C_{M_p} without blowing, and in C_L of 20-50% of C_{L_p} without blowing. The vibration added is a product of the in-phase pulsed blowing used, but can probably be significantly reduced by varying the phase of pulsation over the jet array.

For these test cases, pulsed blowing and constant blowing at the same mass flux were roughly comparable in aerodynamic effect, but the pulsed blowing required around 25% more energy for the compressed air (neglecting the actuation power), due to the higher pressure required to achieve the same mass flux. However it must be emphasised that this is a limited data set, and since other authors have found a positive effect of pulsed blowing for low mass fluxes, there must be cases where pulsed blowing is more advantageous than seen in our experiments.

4.5.3 Switching constant blowing at 1/rev

Flow control is only required for the parts of the pitching cycle where stall occurs, and switching the constant blowing on only for high angles of attack where stall occurs can also lead to a reduction in the air usage. This 1/rev switching has previously been demonstrated by Hinton [49], although C_μ was not measured. McCloud et al. [76] investigated 1/rev switching of constant blowing between C_μ=0.0003 and C_μ=0.0033, noting a halving of the compressed air required compared with constant blowing. Greenblatt et al. [42] showed control of dynamic stall on an airfoil in a low speed wind tunnel with Re=300000 and 600000, where the stall angle was exceeded by approximately 2°, using 1/rev switching of pulsed blowing with F^+=0.6 and 1.1 and C_μ=0.001 and 0.02. The flow-through pressure reducers in the strut of the OA209 model used here are not optimal for such an experiment, since the pressure inside the model increases almost linearly with time when the valves are switched off, leading to a variation of pressure of ±30% around the mean over a pitching cycle and resulting in no meaningful value of P_j. The results for 1/rev switching are corrected for the blowing force only when the jets are turned on, using $\dot{m}_{inst}$.

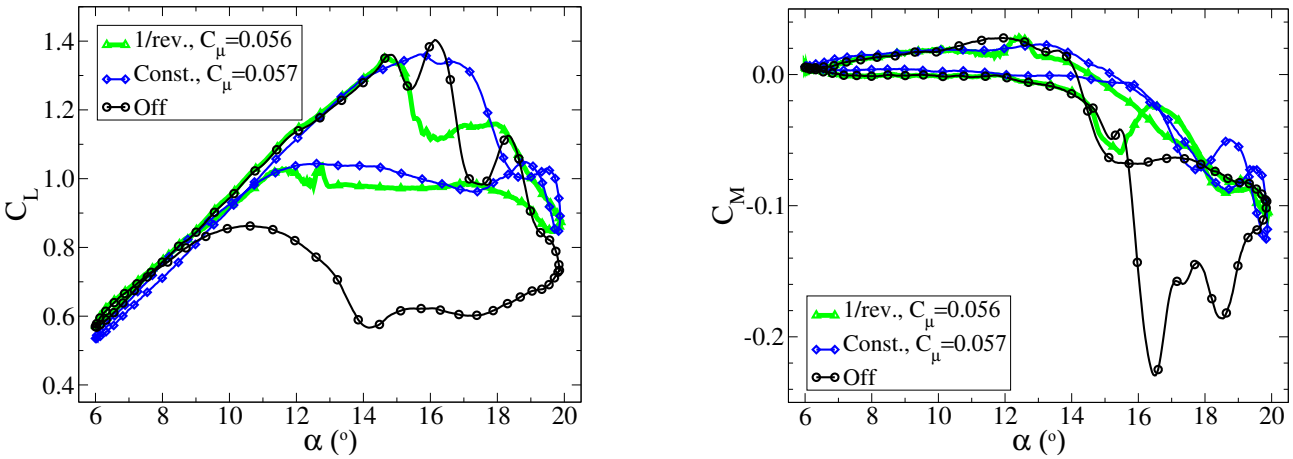

Figure 4.79: C_L (Left) and C_M (Right) for constant blowing and 1/rev switching at ϕ=0°,C_μ=0.06 M=0.3, Re=530000, α=13±7°, f=5.7 Hz (ω^*=0.10).

Figure 4.79 shows C_L and C_M against α for 1/rev switching at M=0.3 and Re=530000, with α=13±7° at f=5.7 Hz (ω^*=0.10). The blowing is switched on for 50% of the pitching cycle, and the phase ϕ was varied compared to the pitching motion, with the optimum (defined as ϕ=0°) shown in Fig. 4.79. The pressure of the blowing system could not be held constant for 1/rev switching, and thus the mean, rather than the instantaneous mass flux was used as a comparator, see values in Table 4.12. The comparison case with constant blowing was chosen for its similar C_L and C_M time

history. It can be seen that when the jets are turned on at α=15°, both the lift and moment stall are arrested and both C_L and C_M switch to follow a similar path to that seen for constant blowing. When the jets are turned off at α=13° on the downstroke, both C_L and C_M switch back to the paths without blowing. The pressure distributions for this case are as those for Figures 4.76 and 4.77 (Left).

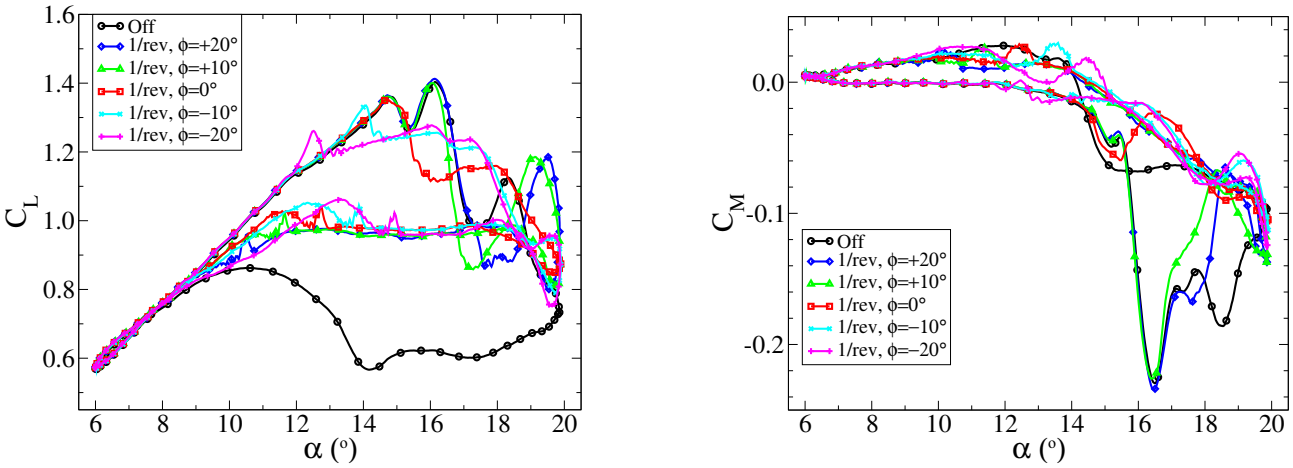

Figure 4.80: C_L (Left) and C_M (Right) for 1/rev switching at different phases ϕ for C_μ=0.06 M=0.3, Re=530000, α=13±7°, f=5.7 Hz (ω^*=0.10).

Figure 4.80 shows the variation of the phase ϕ in switching on the blowing. Since the blowing was always over 50% of the cycle, it also shows the difference caused by varying the phase of switching off the blowing. In Fig. 4.79 (Left) the lift after stall between α=16° and 18° on the upstroke is different, and as seen in Fig. 4.80 (Left) this is also the same for other phases. Particularly it can be seen that for ϕ=-20° there is a transient and then the lift lowers significantly. Since the blowing pressure is not constant, but is much higher at the moment of valve opening than the average, this range of $\Delta\alpha$=2° appears to have stronger blowing than the constant blowing case. After this initial phase, the 1/rev blowing forces are similar to those for constant blowing. It can be seen that the optimal phase is where the blowing is switched on at the moment of stall, and switching on the blowing before or after stall results in either over-control of the flow (for ϕ <0), or uncontrolled dynamic stall (for ϕ >0). Switching off the blowing appears to be less sensitive to phase than switching it on. As seen in Fig. 4.79, the reattachment is optimal for ϕ=0°, however over the phase range shown, the difference in $\overline{C_L}$ due to the phase of switching off the blowing is minimal.

At Mach 0.5, Re=850000, with α=11±7° at f=5.7 Hz (ω^*=0.06) where shock-induced separation is observed, a similar switching is shown in Fig. 4.81. The dynamic stall of the OA209 at M=0.5 without blowing is mainly influenced by the strong shock which appears at around α=8° (see subsection 4.3.7) and is preceded by a region of supersonic flow of up to around 10% chord in length, as seen in the pressure distributions in Figure 4.82 (Left). This shock causes a shock-induced separation of the flow on the suction side of the airfoil, starting around α=11°. The pitching moment has a slightly negative C_M during the pitch-up, and a kink in the positive direction around α=8° on the upstroke due to the appearance of supersonic flow and a shock. Moment stall starts around α=11°, and the hysteresis loop in the pitching moment follows a relatively constant path as maximum angle of attack increases, without the overshoots seen at Mach 0.3. In fact it appears that at Mach 0.5 no dynamic stall vortex is formed for the OA209 (see subsection 4.3.7). On the downstroke, the pitching moment follows a qualitatively similar to the path on the upstroke, but with positive C_M. The kink in the pitching moment at α=8° is also present on the downstroke, as the supersonic flow disappears.

For constant blowing in in Fig. 4.81, the lift is reduced. As seen in the pressure distributions in Figure 4.82 (Right), the suction peak produced by the jets is now supersonic, and for attached flow at high angles of attack, the supersonic region which produces lift without blowing is terminated by

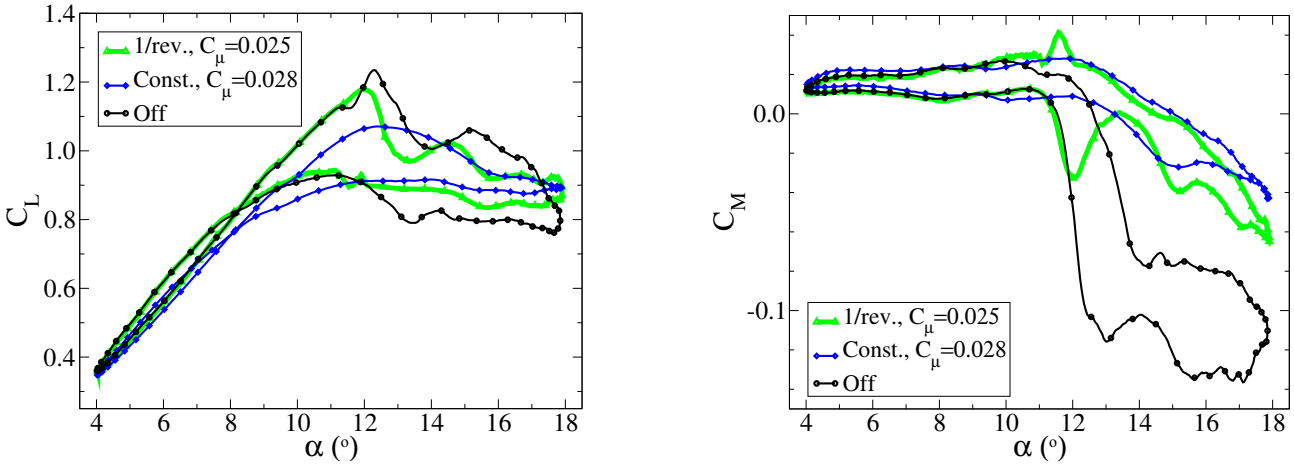

Figure 4.81: C_L (Left) and C_M (Right) for constant blowing and 1/rev switching at ϕ=0°, C_μ=0.03 with M=0.5, Re=530000, α=11±7°, f=5.7 Hz (ω^*=0.06).

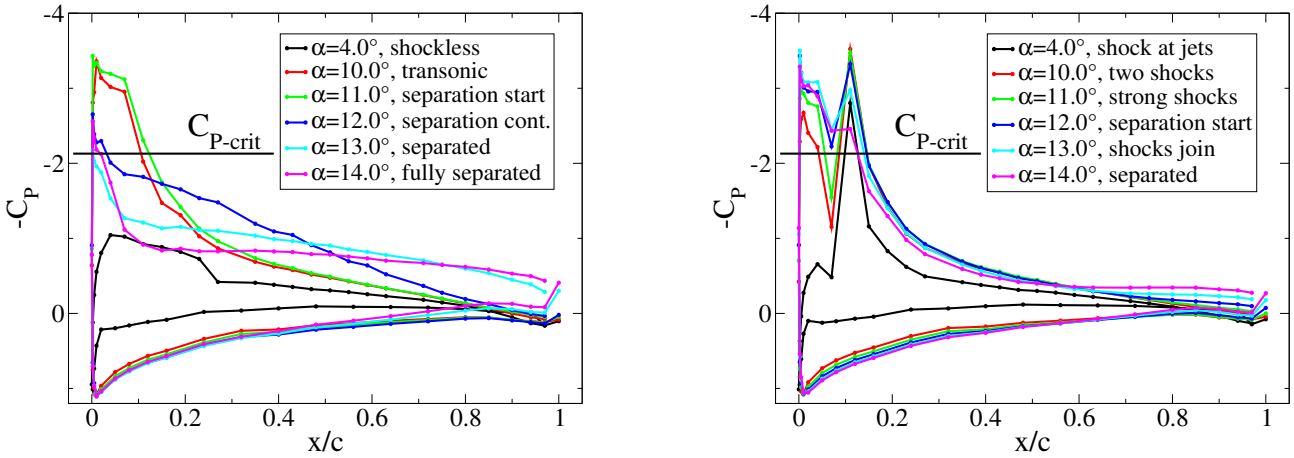

Figure 4.82: Phase-averaged pressure distributions for M=0.5, Re=530000, α=11±7°, f=5.7 Hz (ω^*=0.06) for no blowing (Left) and constant blowing at C_μ=0.03 (Right).

a shock which forms in front of the jets. The appearance of the shock on the upstroke is delayed $\Delta\alpha$=+1° compared to the case without blowing, and the jets push the position of the shock further forward, meaning that the lift is further reduced for supersonic flow, as seen in subsection 4.3.7. Moment stall is delayed $\Delta\alpha$=+2° compared to the case without blowing, and the pitching moment peak is reduced by 68% over that without blowing. Figure 4.82 (Right) shows that with blowing a trailing edge separation is formed rather than the shock-induced separation seen without blowing, and although the suction peak after stall is stronger with blowing, the pressure on the suction side of the airfoil downstream of the jets is higher, meaning that lift with stalled flow is not significantly increased over the case without blowing.

For 1/rev switched blowing in Fig. 4.81 there is a significant increase in lift during attached flow over the constant blowing, and the reduction in C_{L_p} due to constant blowing is avoided by the 1/rev switching. The effects of phase variation, shown in Fig. 4.83, are much stronger than at Mach 0.3, with switching on the blowing too early causing a significant reduction in lift, and switching on the flow too late causing full stall of the airfoil. It appears that the interaction of the blowing with the shock on the airfoil in attached flow is undesirable, but that a good control of the stalled flow can nevertheless be achieved by a well-timed switching. The phase of switching off the blowing appears to be much more critical than at Mach 0.3, with turning off the flow too early resulting in stall of the

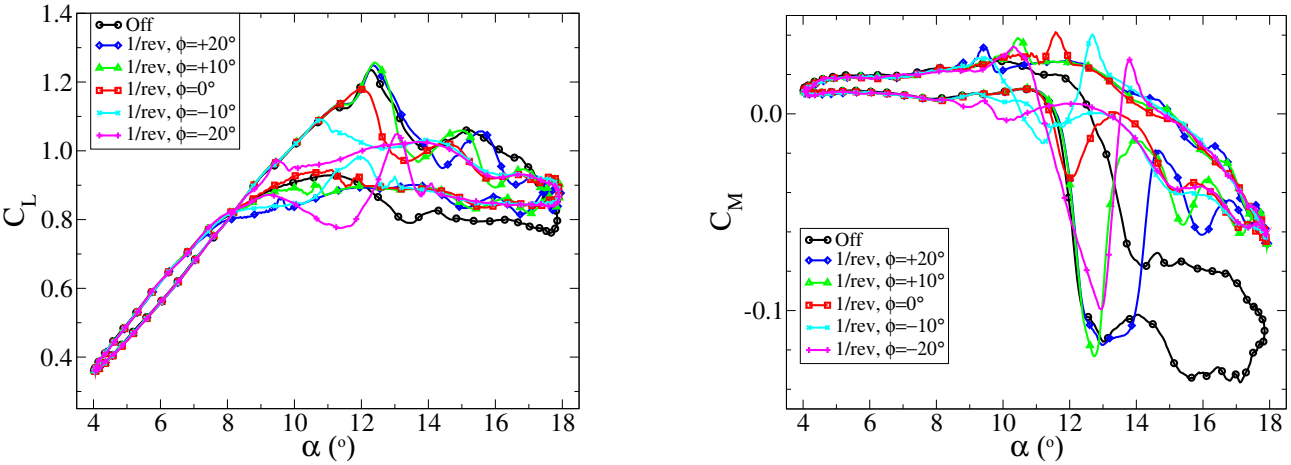

Figure 4.83: C_L (Left) and C_M (Right) for 1/rev switching at different phases ϕ for C_μ=0.03 with M=0.5, Re=530000, α=11$\pm$7°, f=5.7 Hz (ω^*=0.06).

airfoil and a pitching moment peak as high as without flow control. Switching off the blowing too late only resulted in a slight reduction in lift.

It is assumed that the negative effects of constant blowing will worsen as the Mach number increases, meaning that 1/rev switching of the jets would be very advantageous for the control of dynamic stall during fast forward flight. After stall, the positive effect of the blowing is seen, as at Mach 0.3. The 1/rev switching results in improved lift during the part of the upstroke with attached flow compared to constant blowing and a good reduction in the pitching moment peak. Within the limitations of this experimental apparatus, it appears that the 1/rev switching works and provided both the advantage of the clean airfoil in attached flow and of blowing for separated flow.

4.5.4 Conclusions

Pulsed blowing with all jets in-phase for four frequencies, two different movements and two pressures at M=0.3 was investigated for the control of dynamic stall. The pitching moment peak for deep dynamic stall could be reduced by up to 70% and the lift after stall was significantly increased. However pulsed blowing was found to be at best as effective as constant blowing with the same mass flux, for the jet configuration and test cases investigated in this section. Due to the higher blowing pressures, the power required to produce the compressed air for pulsed blowing was 25% higher than for constant blowing (ignoring the actuation power), and thus pulsed blowing always required more energy than constant blowing for the same aerodynamic effect.

Switching of constant blowing at 1/rev was achieved, within the limitations of the experimental apparatus. These initial results indicate that the 1/rev switching worked and provided both the advantage of the clean airfoil in attached flow and of blowing for separated flow. The advantages of switching off the jets while the airfoil has attached flow at transonic Mach number were demonstrated. However the pressure control was too inaccurate to show whether a saving in mass flux could be achieved by 1/rev switching.

Chapter 5

Conclusions

The dynamic stall on helicopters continues to be one of the major limitations on the operating envelope, causing strong pitch-down torsional loads on the rotor blades, and a loss of lift on parts of the rotor disc. The techniques in this habilitation thesis (amongst others) can be used to reduce or eliminate the large forces associated with dynamic stall. The most basic parameters of an aircraft are the load it can carry, flight speed, turn rate and service ceiling, and dynamic stall is the limiting factor on all four of these parameters for a modern helicopter. Reducing or eliminating dynamic stall will result in faster, and more agile helicopters, which can carry larger loads, in addition to improving the safety and fatigue lifetime of the aircraft.

Investigations into dynamic stall and dynamic stall control on airfoils were detailed using pitching airfoil experiments and numerical investigations at Mach 0.3, 0.4 and 0.5. Two-dimensional dynamic stall was investigated experimentally using an airfoil spanning the width of the adaptive-wall test section of the Transonic wind tunnel Göttingen (TWG). The 2D airfoil was pitched with forced sinusoidal oscillations using motors mounted outside the wind tunnel test section. The effects of the wind tunnel interference, and parameter variation in the wind tunnel were investigated, as well as the effect of flow control using constant blowing, pulsed blowing and leading edge vortex generators. The 2D dynamic stall was demonstrated to be significantly reduced by the flow control at all Mach numbers investigated. The effect of rotor blade rotation and the finite extent of a pitching wing on the three-dimensional stall process were investigated numerically and both effects were found to reduce the severity of the dynamic stall.

In a range of experiments and numerical investigations the following conclusions were found:

1. For a nominally 2D airfoil experiment (with aspect ratio 3.3) at static angle of attack, the gap between the airfoil and the wind-tunnel wall can have a significant effect on the three-dimensional flow topology at the intersection between airfoil and wall. However this difference is not detectable at the midline of the airfoil model. Understanding the interaction between model and sidewall is necessary to improve the accuracy of wind-tunnel airfoil testing and reduce the sidewall interference.

2. Numerical investigations of an untwisted single rotor blade with axial-only flow ("Hover") with a large cyclic pitch were compared with pitching of a finite wing and a 2D airfoil at the same flow conditions. The results show that the rotation causes the stall process to take longer at the reference section, and the axis of the dynamic stall vortex is at an angle of 20-30° trailing the blade axis. This results in a less localized stall vortex and a 25% reduction in the height of the pitching moment peak compared to the 2D case. The 3D separation in rotation appears to have a related, but different mechanism to the process of the 2D or non-rotating cases, with the dynamic stall driven by the propagation of the dynamic stall vortex towards the blade root. This resulted in a broader footprint of the vortex on the airfoil and a stronger

counter-rotating vortex for the rotating case. Without rotation, the 3D finite wing had lower lift at the reference section than for a 2D computation, and the lift overshoot classically observed for Spalart-Allmaras turbulence models during 2D dynamic stall was significantly reduced. The finite wing developed a curved dynamic stall vortex which produced qualitatively similar vortex dynamics at the reference section, but lower forces compared to the 2D test case.

3. Experimental investigations were performed on a pitching airfoil with high-speed pressure sensitive paint (PSP). Although the PSP had a high temperature sensitivity of -800 Pa/°C, which lead to a temperature error in the C_P measurement that could not be directly corrected, qualitative results could be extracted using the difference $C_P - C_{P_0}$ where C_{P_0} is the pressure distribution at the minimum angle of attack. Both the PSP and pressure transducers showed the formation of a curved 3D vortex at M=0.3, similar to that observed in the numerical investigations and other experiments with a free end from the literature. Since the numerical investigations were also with a free end, it can be stated that the wind tunnel experiments have vortex propagation much more similar to a free end than a fixed end.

4. Experimental investigations with a pitching airfoil showed that at M=0.5 the OA209 airfoil experiences shock-induced stall, with a hysteresis in lift and pitching moment around the static values which increases with increasing pitching frequency and amplitude. A 3D shock-induced stall was observed using PSP, without the formation of a dynamic stall vortex and with a wide region of constant flow in the middle of the airfoil. This is in contrast to the overshoot in forces associated with a dynamic stall vortex observed for the same airfoil at Mach 0.3.

5. Experimental investigations with pitching EDI-M109 and EDI-M112 airfoils showed that the strength of dynamic stall increased with increasing pitching amplitude and frequency. The pitching moment peak size was found to have an approximately linear correlation to the normalised mean angular velocity $\overline{\alpha'_{norm}} = \frac{\omega^*}{M} \times (\alpha_{max} - \alpha_{C_{L_{max}},static})$. Test cases where the maximum angle of attack and oscillation frequency were preserved while varying amplitude had similar dynamic stall qualities. Using a non-sinusoidal motion which combined a mixture of 1/rev and 5/rev pitching motions changed the angular velocity at the separation angle, resulting in EDI-M109 performance qualitatively similar to that for pure 1/rev pitching and quite different EDI-M112 performance.

6. A version of the Liiva-criterion was applied to the EDI-M109 and EDI-M112 airfoils, where low-amplitude, high-frequency pitching oscillations were investigated at mean angles of attack around the stall angle. It was posited that negative aerodynamic damping in these test cases would correlate with large pitching loads for dynamic stall test cases. However, no positive correlation was found between the aerodynamic damping at high-frequency, low amplitude oscillations, and the severity of dynamic stall. The damping-criterion, as applied here, is not sensitive enough to distinguish between similar airfoils of a single design family within a design process and select a better airfoil for dynamic performance.

7. An air jet blowing system to control dynamic stall was designed using RANS and URANS computations. The dynamic stall control strategies concentrated on using blowing with air jets to keep the flow attached, reduce the strength of the dynamic stall vortex and to anchor the separation of the flow and the attachment point of the dynamic stall vortex. Steady RANS computations were first used to narrow a wide field of candidates to one candidate for each flow control strategy. It was noted that configurations which increased the lift in RANS simulations of deep static stall were also successful at controlling dynamic stall. A configuration using vertical 3 mm portholes at 10% chord and 20 mm spacing was selected to be built into a wind tunnel model in preference to a tangential slot due to practical considerations. In the

computations performed during the design phase, pulsed blowing delivered less flow control than constant blowing.

8. When the air jet system was investigated experimentally on a pitching airfoil, it was noted that the effect of blowing at Mach 0.3 is to slow the stall and delay the pitching moment peak relative to the initial stall, and the initial stall is changed from a leading edge to a trailing edge stall. At Mach 0.3, 0.4 and 0.5 reductions in the pitching moment peak between 50% and 100% were achieved, depending on the test case, with a delay in the stall angle of around $\Delta\alpha$=2°. Optimal mass flux and jet spacing were found for Mach 0.3 and Mach 0.5, and depended on the test case investigated. Optima for deep stall were around C_μ=0.12 and s/c=0.13 for the maximum effect at M=0.3 and C_μ=0.02 and s/c=0.13 at M=0.5. The highly 3D flow around the air jets meant that the pressure-sensor integration to compute lift had a larger systematic error (up to 8%) with blowing than without, and this effect was quantified by CFD for different blowing schemes and angles of attack. Higher Reynolds number required relatively more blowing (higher C_q, C_μ) to control the dynamic stall and the flow control with air jets was uncritical regarding the aerodynamic damping.

9. Pulsed blowing with all jets in-phase for four frequencies, two different movements and two pressures at M = 0.3 was experimentally investigated for the control of dynamic stall. The pitching moment peak for deep dynamic stall could be reduced by up to 70% and the lift after stall was significantly increased. However, pulsed blowing was found to be at best as effective as constant blowing with the same mass flux, for the jet configuration and test cases investigated in this paper. Due to the higher blowing pressures, the power required to produce the compressed air for pulsed blowing was 25% higher than for constant blowing (ignoring the actuation power), and thus pulsed blowing always required more energy than constant blowing for the same aerodynamic effect. Switching of steady blowing at 1/rev was achieved, within the limitations of the experimental apparatus.

10. Flow control by blowing reduced drag for separated flow, but the energy required in compressed air to achieve this was more than the savings in drag, and no cases were found in which flow control resulted in a reduction in total power used. Thus the blowing control investigated cannot be used to improve the efficiency of a rotorcraft operating at high speed, but could be used to improve the aerodynamic performance of the aircraft for short periods during maneuvering flight.

Future techniques for flow control on helicopter blades need to be simple, robust and energy efficient in addition to their aerodynamic effectiveness, and developments will push the actuators in this direction to provide vertical lift technology for the future.

Bibliography

[1] www.centaursoft.com

[2] Alrefai, M., and Acharya, M., "Controlled leading-edge suction for management of unsteady separation over pitching airfoils," *AIAA Journal*, Vol. 34, No. 11, pp. 1647-1655, 1996. DOI: 10.2514/3.12155

[3] Bechert, D.W., Stanewsky, E., Hage, W., "Windkanalmessungen an einem Transsonik-Flügel mit Strömungsbeeinflussenden Massnahmen", DLR-IB 223-99-C05 (1998).

[4] Bowles, P.O., Wasikowski, M., Coleman, D.G., Corke, T.C., and Thomas, F.O., "Wind tunnel experiments on the effect of compressibility on the attributes of dynamic stall," American Helicopter Society 68th Annual Forum, Fort Worth, Texas, May 1-3, 2012.

[5] Carr, L.W., "Progress in the analysis and prediction of dynamic stall," *Journal of Aircraft*, Vol. 25, No. 1, pp. 6-17, 1988. DOI: 10.2514/3.45534

[6] Carr, L.W., Chandrashekara, M.S., Wilder, M.C., and Noonan, K.W., "The effect of compressibility on suppression of dynamic stall using a slotted airfoil," Paper 1998-332, 36th AIAA Aerospace Sciences Meeting, Reno, 12-15 January, 1998. DOI: 10.2514/6.1998-332

[7] Carr, L.W., and McAlister, K.W., "The effect of a leading-edge slat on the dynamic stall of an oscillating airfoil," Paper 1983-2533, AIAA Aircraft Design, Systems and Technology Meeting, Fort Worth, 17-19 October, 1983. DOI: 10.2514/6.1983-2533

[8] Chandrasekhara, M.S., Martin, P.B., and Tung, C., "Compressible dynamic stall performance of a variable droop leading edge airfoil with a gurney flap," Paper 2004-41, 42nd AIAA Aerospace Science Meeting and Exhibit, Reno, NV, USA, 5-8 January, 2004. DOI: 10.2514/6.2004-41

[9] Chandrasekhara, M.S., Wilder, M.C., and Carr, L.W., "Competing mechanisms of compressible dynamic stall," *AIAA Journal*, Vol. 36, No. 3, pp. 387-393, 1998. DOI: 10.2514/2.375

[10] Chandrasekhara, M.S., and Carr, L.W., "Flow visualisation studies of the Mach number effects on the dynamic stall of oscillating airfoils," *Journal of Aircraft*, Vol. 27, No. 6, 1990, pp. 516-522. DOI: 10.2514/3.25313

[11] Costes, M., Richez, F., Le Pape, A. and R. Gavériaux, "Numerical investigation of three-dimensional effects during dynamic stall", 37th European Rotorcraft Forum, Gallarate Varese, Italy, 13- 15 September 2011.

[12] Dietz, G., Mai, H., Geissler, W., "Auftriebsfläche mit verbessertem Ablöseverhalten bei stark veränderlichem Anstellwinkel", European Patent EP 1 714 869 A1 (25.10.2006).

[13] Dietz, G., Schewe, G., Mai, H., "Experiments on heave/pitch limit cycle oscillations of a supercritical airfoil close to the transonic dip", *Journal of Fluids and Structures*, Vol. 19, No. 1, pp1-16, 2004. DOI: 10.1016/j.jfluidstructs.2003.07.019

[14] DiOttavio, J., Watson, K., Cormey, J., Komerath, N., Kondor, S., "Discrete structures in the radial flow over a rotor blade in dynamic stall", AIAA Paper 2008-7344, 26th AIAA Applied Aerodynamics Conference, Honolulu Hawaii, Aug 18-21, 2008.

[15] Dumitrescu, H., Cardo, V., "Inboard stall delay due to rotation", *Journal of Aircraft*, Vol 49, No. 1, pp. 101-107, 2012. DOI: 10.2514/1.C031329.

[16] Duraisamy, K., McCroskey, W.J., Baeder, J.D., "Analysis of wind tunnel wall interference effects on subsonic unsteady airfoil flows", *Journal of Aircraft*, Vol. 44, No. 5, pp. 1683-1690, 2007. DOI: 10.2514/1.28143

[17] Edwards, J.R., Chandra, S., "Comparison of eddy viscosity-transport turbulence models for three-dimensional, shock-separated flowfields", *AIAA Journal*, Vol. 34, No. 4, 1996. pp. 756-763, DOI:10.2514/3.13137

[18] Ekaterinaris, J.A., "Numerical investigations of dynamic stall active Control for Incompressible and Compressible Flows," *Journal of Aircraft*, Vol. 39, No. 1, pp.71-78, 2002. DOI: 10.2514/2.2897

[19] Ericsson, L.E., Reding, J.P., "Dynamic stall simulation problems", *Journal of Aircraft*, Vol. 8, No. 7, pp. 579-583, 1971. DOI: 10.2514/3.59140

[20] Ewald, B.F.R. (Editor), "Wind tunnel wall correction", Agardograph 336, NATO/RTO, 1998, ISBN 92-836-1076-8.

[21] Fuchiwaki, M., Tanaka, K., "Vortex structure and scale on an unsteady airfoil", *JSME International Journal Series B Fluids and Thermal Engineering*, Vol. 49, No. 4, pp. 1056-1063, 2006. DOI: 10.1299/jsmeb.49.1056

[22] Fugelsang, P., Antoniou, I., Sørensen, N.N., and Madsen, H. Aa., "Validation of a wind tunnel testing facility for blade surface pressure measurements," Risø National Laboratory report, Risø-R-981(EN), Denmark, 1998.

[23] Gallot, J., Vingut, G., De Paul, M. V., and Thibert, J. "Blade profile for rotary wing of an aircraft," United States Patent 4325675,(20.4.1982).

[24] [1]Gardner, A.D., "Numerical investigation of air jets for dynamic stall control on the OA209 airfoil", DLR internal report: DLR-IB 224-2009 A 32, DLR Institute of Aerodynamics and Flow Technology, Göttingen, Germany, 2009.

[25] [1]Gardner, A. D., Klein, C., Sachs, W., Henne, U. , Mai, H., Richter, K., "Investigation of three-dimensional dynamic stall on an airfoil using fast response pressure sensitive paint", Experiments in Fluids, Vol. 55, No. 9, 2014. DOI: 10.1007/s00348-014-1807-4

[26] [1]Gardner, A.D., Knopp, T., Richter, K., and Rosemann, H. "Numerical investigation of pulsed air jets for dynamic stall control on the OA209 airfoil," *Notes on Numerical Fluid Mechanics and Multidisciplinary Design: New Results in Numerical and Experimental Fluid Mechanics VIII*, Springer Verlag, 2013, pp. 287-295. DOI: 10.1007/978-3-642-35680-3_35

[27] [1]Gardner, A.D., and Richter, K., "Effect of the model-sidewall connection for a static airfoil experiment," *Journal of Aircraft*, Vol. 50, No. 2, 2013, pp. 677-680. DOI: 10.2514/1.C032011

[1]Text and illustrations from these publications are used as indicated in the text

[28] [1]Gardner, A.D. and Richter K., "Influence of rotation on dynamic stall", *Journal of the American Helicopter Society*, Vol. 58, No. 3, 2013. DOI: 10.4050/JAHS.58.032001

[29] [1] A.D. Gardner, K. Richter, "Optimised pressure sensor positioning on a rotor blade airfoil model for dynamic stall experiments", STAB Mitteilung, 2012.

[30] [1]Gardner, A.D., Richter, K., Mai, H., Altmikus, A.R.M., Klein, A. and Rohardt, C.-H., "Experimental investigation of dynamic stall performance for the EDI-M109 and EDI-M112 airfoils", *Journal of the American Helicopter Society*, Vol. 58, No. 1, 2013. DOI:10.4050/JAHS.58.012005

[31] [1]Gardner, A.D., Richter K., Mai, H. and Neuhaus, D., "Experimental investigation of air jets to control shock-induced dynamic stall", *Journal of the American Helicopter Society*, Vol. 59, No. 2, 2014. DOI: 10.4050/JAHS.59.022003

[32] [1]Gardner, A.D., Richter K., Mai, H. and Neuhaus, D., "Experimental investigation of air jets for the control of compressible dynamic stall", *Journal of the American Helicopter Society*, Vol. 58, No. 4, 2013. DOI: 10.4050/JAHS.58.042001

[33] [1]Gardner, A. D., Richter, K., Mai, H., Neuhaus, D., "Experimental investigation of high-pressure pulsed blowing for dynamic stall control", *CEAS Aeronautical Journal*, Vol. 5, Issue 2, pp. 185-198, 2014. DOI 10.1007/s13272-014-0099-y

[34] [1]Gardner, A.D., Richter, K., and Rosemann, H., "Numerical investigation of air jets for dynamic stall control on the OA209 airfoil," *CEAS Aeronautical Journal*, Vol. 1, No. 1, 2011. DOI: 10.1007/s13272-011-0002-z

[35] Gardner, A.D., Richter, K., Rosemann, H., "Prediction of the wind tunnel sidewall effect for the iGREEN wing-tailplane interference experiment", In: *Notes on Numerical Fluid Mechanics and Multidisciplinary Design New Results in Numerical and Experimental Fluid Mechanics VII, Vol.112*, Springer Verlag Berlin, Heidelberg. pp. 75-82, 2010. ISBN 978-3-642-14242-0. ISSN 1612-2909

[36] Geissler, W., Dietz, G., Mai, H., Bosbach, J., Richard, H., "Dynamic stall and its passive control investigations on the OA209 airfoil section". 31st European Rotorcraft Forum, Florence, Italy, 2005.

[37] Geissler, W., Dietz, G., Mai, H., Junker, B., and Lorkowski, T., "Dynamic stall control investigations on a full size chord blade section," 30th European Rotorcraft Forum, Marseilles, 14-16 September, 2004.

[38] Geissler, W., Haselmeyer, H., "Investigation of dynamic stall on-set", *Aerospace Science and Technology*, Elsevier Masson SAS, pp. 590-600, 2006.

[39] Gerhold, T., Friedrich, O., Evans, J. and Galle, M., "Calculation of complex three-dimensional configurations employing the DLR-TAU-code", AIAA-paper 97-0167, 35th Aerospace Sciences Meeting & Exhibit, Reno, January 6-10, 1997. DOI: 10.2514/6.1997-167

[40] Glezer, A., Amitay, M., "Synthetic jets", Annual Review of Fluid Mechanics, Vol. 34, 2002. pp. 503-530. DOI: 10.1146/annurev.fluid.34.090501.094913

[41] Green, L.L., Mineck, R.R., "Wall interference assessment/correction for transonic airfoil data", *Journal of Aircraft*, Vol. 28, No. 11, pp. 774-780, 1991. DOI: 10.2514/3.46095

[1]Text and illustrations from these publications are used as indicated in the text

[42] Greenblatt, D. Neuburger, and I. Wygnanski. "Dynamic stall control by intermittent periodic excitation", *Journal of Aircraft*, Vol. 38, No. 1, 2001, pp. 188-190. DOI: 10.2514/2.2751

[43] Greenblatt, D., and Wygnanski, I., "Effect of leading edge curvature on airfoil separation control," *Journal of Aircraft*, Vol. 40, No. 3, 2003, pp. 473-481. DOI: 10.2514/2.3142

[44] Greenblatt, D., and Wygnanski, I., "Dynamic stall control by periodic excitation, Part 1: NACA0015 parametric study," *Journal of Aircraft*, Vol. 38, No. 3, pp. 430-447, 2001. DOI: 10.2514/2.2810

[45] Gregory, J.W., Sakaue, H., Liu, T. and Sullivan, J.P., "Fast pressure-sensitive paint for flow and acoustic diagnostics," *Annual Review of Fluid Mechanics*, Vol. 46, 2014, pp. 303-330. DOI: 10.1146/annurev-fluid-010313-141304

[46] Heine, B., "Passive Beeinflussung von Dynamic Stall durch Störgeneratoren", Doctoral Thesis, Leibnitz University Hannover, DLR-FB 2012-20, ISSN 1434-8454, 2012.

[47] Heine, B., Mulleners, K., Gardner, A., Mai, H., "On the effects of leading edge vortex generators on an OA209 airfoil", ODAS 2009 - 10th ONERA-DLR Aerospace Symposium, Berlin, 06-08 October, 2009

[48] Heine, B., Mulleners, K., Joubert, G., Raffel, M., "Dynamic stall control by passive disturbance generators," *AIAA Journal*, Vol. 51, No.9, 2013, pp. 2086-2097. DOI: 10.2514/1.J051525

[49] Hinton, S. H., "Application of Boundary Layer Control to Rotor Blades," *Journal of the American Helicopter Society*, Vol. 2, No. 2, 1957. DOI: 10.4050/JAHS.2.36

[50] Hird, K., Frankhouser, M.W., Gregory, J.W., Bons, J.P., "Compressible dynamic stall of an SSC-A09 airfoil subjected to coupled pitch and freestream Mach oscillations", American Helicopter Society 70th Annual Forum, Montreal, Quebec, May 20-22, 2014.

[51] Jeong, J., Hussain, F., "On the identification of a vortex", *Journal of Fluid Mechanics*, Vol. 285, pp. 69-94, 1995. DOI: 10.1017/S0022112095000462.

[52] Johnson, W., "Rotorcraft aerodynamic models for a comprehensive analysis", AHS International 54th Annual Forum Proceedings, Washington, D.C., May 20-22, 1998

[53] Joo, W., Lee, B., Yee, K., and Lee, D., "Combining passive control method for dynamic stall control," *Journal of Aircraft*, Vol. 43, No. 4, pp. 1120-1128, 2006. DOI: 10.2514/1.17957

[54] Juliano, T.J., Disotell, K.J., Gregory, J.W., Crafton, J. and Fonov, S., "Motion-deblurred, fast-response pressure-sensitive paint on a rotor in forward flight", *Measurement Science and Technology*, Vol. 23, 2012. DOI: 10.1088/0957-0233/23/4/045303

[55] Juliano, T.J., Peng, D., Jensen, C., Gregory, J.W., Liu, T., Montefort, J., Palluconi, S., Crafton, J. and Fonov, S., "PSP measurements on an oscillating NACA 0012 airfoil in compressible flow", AIAA 2011-3728, 41st AIAA Fluid Dynamics Conference and Exhibit, Honolulu, Hawaii, 27-30 June 2011. DOI: 10.2514/6.2011-3728

[56] Joubert, G., Le Pape, A., Heine, B., and Huberson, S., "Investigation of dynamic stall control by deployable vortex generator using time-resolved PIV analysis and URANS computations," *AIAA Journal*, Vol. 51, (1), 2013, pp. 240-252, January 2013. DOI: 10.2514/1.J051767

[57] Karim, M.A., and Acharya, M., "Suppression of dynamic-stall vortices over pitching airfoils by leading-edge suction," *AIAA Journal*, Vol. 32 (8), pp. 1647-1655, 1994. DOI: 10.2514/3.12155

[58] Kaufmann, K., Costes, M., Richez, F., Gardner, A.D. and Le Pape, A., "Numerical investigation of three-dimensional dynamic stall on an oscillating finite wing", American Helicopter Society 70th Annual Forum, Montréal, Québec, May 20-22, 2014.

[59] Klein, A., Richter, K., Altmikus, A., Lutz, T., Krämer, E., "Unsteady criteria for rotor blade airfoil design", 35th European Rotorcraft Forum, Hamburg, Germany, September 22-25, 2009.

[60] Klein, A., Lutz, Th., Kramer, E., Richter, K., Gardner, A.D. and Altmikus, A.R.M., "Numerical comparison of dynamic stall for two-dimensional airfoils and an airfoil model in the DNW-TWG", *Journal of the American Helicopter Society*, Vol. 57, No. 4, 2012, DOI: 10.4050/JAHS.57.042007

[61] Klein, A., Richter, K., Gardner, A.D., Altmikus, A.R.M., Lutz, T., Krämer, E., "Numerical comparison of dynamic stall for 2-D airfoils and an airfoil model in the DNW-TWG", 37th European Rotorcraft Forum, Galarate, Italy, September 3-5, 2011.

[62] Klein, C., Sachs, W. E., Henne, U. and Borbye, J., "Determination of transfer function of pressure-sensitive paint", AIAA 2010-0309, 48th AIAA Aerospace Sciences Meeting and Exhibit, Orlando, Florida, 4-7 January 2010.

[63] Knopp, T. "The actuation boundary condition for flow control in the DLR TAU code", DLR IB 224-2010 A44, 2010.

[64] Leishman, J.G., "Dynamic stall experiments on the NACA 23012 aerofoil," *Experiments in Fluids*, Vol. 9, No.1-2, 1990, pp. 49-58. DOI: 10.1007/BF00575335

[65] Leishman, G., "Principles of helicopter aerodynamics (Cambridge Aerospace Series)", Cambridge University Press, 2nd Edition, April 2006.

[66] Loendersloot, R., Freire Gomez, J., Booker, J.D., "Wind tunnel testing of a full scale helicopter blade section with an upstream active Gurney flap", 40th European Rotorcraft Forum, Southampton, England, 2-5 Sept. 2014.

[67] Le Pape, A., Costes, M., Richez, F., David, F., and Deluc, J.-M., "Experimental study of dynamic stall control using deployable leading-edge vortex generators," *AIAA Journal*, Vol. 50, No. 10, pp. 2135-2145, 2012. DOI: 10.2514/1.J051452

[68] Le Pape, A., Pailhas, G., David, F. and Deluc, J-M., "Extensive wind tunnel measurements of dynamic stall phenomenon for the OA209 airfoil including 3D effects", 33rd European Rotorcraft Forum, Kazan, Russia, September 2007.

[69] Liiva, J., "Unsteady aerodynamic and stall effects on helicopter rotor blade airfoil sections," *Journal of Aircraft*, Vol. 6, (1), 1969, pp. 46-51. DOI: 10.2514/3.44000

[70] Lim, J.W., Strawn, R.C., "Computational modeling of HART II blade-vortex interaction loading and wake system", *Journal of Aircraft*, Vol 45 (3), pp. 923-933, 2008. DOI: 10.2514/1.31081.

[71] Lorber, P.F., "Tip vortex, stall vortex, and separation observations on pitching three- dimensional wings", AIAA 93-2972, AIAA 24th Fluid Dynamics Conference, Orlando, FL, July 6-9, 1993. DOI:10.2514/6.1993-2972

[72] Lorber, P.F., Carta, F.O. and Covino, A.F. Jr., "An oscillating three-dimensional wing experiment: Compressibility, sweep, rate, waveform, and geometry effects on unsteady separation and dynamic stall", UTRO Report R92-958325-6, November 30, 1992.

[73] Mai, H., Dietz, G., Geissler, W., Richter, K., Bosbach, J., Richard, H., and de Groot, K., "Dynamic stall control by leading edge vortex generators," *Journal of the American Helicopter Society*, Vol. 53, No.1, 2008, pp. 26-36. DOI: 10.4050/JAHS.53.26

[74] Martin, P., Wilson, J., Berry, J., Wong, T., Moulton, M., and McVeigh, M., "Passive control of compressible dynamic stall," Paper 2008-7506, 26th AIAA Applied Aerodynamics Conference, 18-21 August 2008, Honolulu, Hawaii, USA. DOI: 10.2514/6.2008-7506

[75] Mavriplis, D.J., Jameson, A., Martinelli, L., "Multigrid solution of the Navier-Stokes equations on triangular meshes", ICASE-report No. 89-35, 1989.

[76] McCloud, K. L., III, Hall, L. P., and Brady, J. A., "Full-scale wind tunnel tests of blowing boundary layer control applied to a helicopter rotor," NASA TN D-335, 1960.

[77] McCroskey, W.J., McAlister, K.W, Carr, L.W., and Pucci, S.L., "An experimental study of dynamic stall on advanced airfoil sections volume 1: Summary of the experiment," NACA-TM 84245, 1982.

[78] McCroskey, W.J., "A critical assessment of wind tunnel results for the NACA 0012 airfoil", NASA Technical Memorandum 100019, 1987.

[79] Mccroskey, W.J., "The phenomenon of dynamic stall", NASA Technical Memorandum 81264, 1981.

[80] Meyer, R.K.J., "Experimentelle Untersuchungen von Rückstromklappen auf Tragflügeln zur Beeinflussung von Strömungsablösungen", Dissertation, Technische Üniversität Berlin, FB10 (2000).

[81] Min, B.-Y., Sankar, L.N., Rajmohan, N., and Prasad, J.V.R., "Computational investigation of Gurney flap effects on rotors in forward flight," *Journal of Aircraft*, Vol. 46, No. 6, pp. 1957-1964, 2009. DOI: 10.2514/1.41918

[82] Mineck, R.E., "Comparison of a two-dimensional adaptive-wall technique with analytical wall interference correction techniques", NASA Technical, Paper, 3132, 1992

[83] Mulleners, K., Henning, A., Mai, A., Raffel, M., Le Pape, A., Costes, M., "Investigation of the unsteady flow development over a pitching airfoil by means of TR-PIV", AIAA 2009-3504, 27th AIAA Applied Aerodynamics Conference, San Antonio, Texas, 22-25 June, 2009, DOI: 10.2514/6.2009-3504

[84] Mulleners, K., Raffel, M., "The onset of dynamic stall revisited", *Experiments in Fluids*, Vol. 52, No. 3, pp. 779-793, 2012. DOI 10.1007/s00348-011-1118-y.

[85] Mulleners, K., and Raffel, M., "Dynamic stall development," *Experiments in Fluids*, Vol. 54, No. 2, 2013, pp 1-9. DOI: 10.1007/s00348-013-1469-7

[86] Murthy, A.V., "Effects of aspect ratio and sidewall boundary-layer in airfoil testing", *Journal of Aircraft*, Vol. 25, No. 3, pp. 244-249, 1988. DOI: 10.2514/3.45584

[87] Neuhaus, D., "Ventil"," Deutsches Patent DE 199 22 414 (14.5.1999)

[88] Neuhaus, D., "Magnetisch betätigbares Ventil," Deutsches Patent DE 10 2005 035 878 (31.8.2006).

[89] Nishri, B., and Wygnanski, I., "Effects of periodic excitation on turbulent separation from a flap," *AIAA Journal*, Vol. 36, No. 4, 1998, pp. 547-556. DOI: 10.2514/2.428

[90] Nishino, T., Shariff, K., "Numerical study of wind-tunnel sidewall effects on circulation control airfoil flows," *AIAA Journal*, Vol. 48, No. 9, pp. 2123-2132, 2010. DOI: 10.2514/1.J050328

[91] Packard, N.O., Thake, M.P. Jr., Bonilla, C.H., Gompertz, K., and Bons, J.P., "Active control of flow separation on a laminar airfoil," *AIAA Journal*, Vol. 51, No. 5, 2013, pp. 1032-1041. DOI: 10.2514/1.J051556

[92] Piziali, R.A., "2-D and 3-D oscillating wing aerodynamics for a range of angles of attack including stall", NASA Technical Memorandum 4632, September 1994.

[93] Pope, S.B., "Turbulent flows", Cambridge University Press, 2000.

[94] Potsdam, M., Datta, A., Jayaraman, B., "Computational investigation and fundamental understanding of a slowed UH-60A rotor at high advance ratio", American Helicopter Society 68th Annual Forum Proceedings, Fort Worth, May 1-3, 2012.

[95] Potsdam, M., Jayaraman, B., "UH-60A rotor tip vortex prediction and comparison to full-scale wind tunnel measurements", American Helicopter Society 70th Annual Forum, Montreal, Quebec, May 20-22, 2014.

[96] Potsdam, M., Yeo, H., Johnson, W., "Rotor airloads prediction using loose aerodynamic/structural coupling" *Journal of Aircraft*, Vol. 43, No. 3, pp. 732-742, 2006. DOI: 10.2514/1.14006.

[97] Prince, S.A., Khodagolian V., and Singh, C., "Aerodynamic stall suppression on airfoil sections using passive air-jet vortex generators," *AIAA Journal*, Vol. 47, No. 9, pp. 2232-2242, 2009. DOI: 10.2514/1.41986

[98] Prouty, R., "Helicopter Aerodynamics", Philips Publishing, Inc, 1985.

[99] Raffel, M., Kompenhans, J., and Wernert, P., "Investigation of the unsteady flow velocity field above an airfoil pitching under deep dynamic stall conditions," *Experiments in Fluids*, Vol. 19, No. 2, 1995, pp. 103-111. DOI: 10.1007/BF00193856

[100] Ray, E.J., Hill, A.S., "CAST-10-2/DOA2 airfoil studies workshop results", NASA Conference publication 3052, 1988.

[101] Rehman, A., Kontis, K., "Synthetic jet control effectiveness on stationary and pitching airfoils", *Journal of Aircraft*, Vol. 43 No. 6, pp. 1782-1789, 2006. DOI: 10.2514/1.20333

[102] Richter, K., Koch, S., and Gardner, A.D., "Influence of oscillation amplitude and Mach number on the unsteady transition on a pitching rotor blade airfoil," American Helicopter Society 69th Annual Forum, Phoenix, Arizona, May 21-23, 2013.

[103] Richter, K., Le Pape, A., Knopp, T., Costes, M., Gleize, V., Gardner, A.D., "Improved two-dimensional dynamic stall prediction with structured and hybrid numerical methods", *Journal of the American Helicopter Society*, Vol. 56, No. 4, 2011. DOI 10.4050/JAHS.56.042007.

[104] Richter, K., Rosemann, H., "Experimental investigation of trailing-edge devices at transonic speeds", *The Aeronautical Journal*, Vol. 106(1058), pp. 185-193, 2002.

[105] Ruotolo, A., and Meseguer, J., "A low cost, low speed wind tunnel for dynamic stall measurement," European Wind Energy Conference, Warsaw, Poland, 20-23 April 2010.

[106] Sankaran, V., Potsdam, M., Wissink, A., Datta, A., Jayaraman, B., "Rotor loads prediction in level and maneuvering flight using unstructured-adaptive Cartesian CFD", American Helicopter Society 67th Annual Forum Proceedings, Virginia Beach, May 3-5, 2011.

[107] Schaeffler, N.W., Allan, B.G., Lienard, C., Le Pape, A., "Progress towards fuselage drag reduction via active flow control: A combined CFD and experimental effort" European Rotorcraft Forum, Paris, 2010.

[108] Schatzman, D.M., "A study of unsteady turbulent boundary layer separation under conditions relevant to helicopter aerodynamics," PhD Thesis, University of Notre Dame, 2011.

[109] Schwamborn, D., Gardner, A.D., von Geyr, H., Krumbein, A., Lüdeke, H., Stürmer, A., "Development of the TAU-Code for aerospace applications", 50th NAL INCAST (International Conference on Aerospace Science and Technology), Bangalore, India, 26-28 June, 2008.

[110] Seifert, A., Darabi, A., and Wygnanski, I., "Delay of airfoil stall by periodic excitation," *Journal of Aircraft*, Vol. 33, No. 4, 1996, pp. 691-698. DOI: 10.2514/3.47003

[111] Sewall, W.G., "Effects of sidewall boundary layers in two-dimensional subsonic and transonic wind tunnels", *AIAA Journal*, Vol. 20, No. 9, pp. 1253-1256, 1982. DOI: 10.2514/6.1981-1297

[112] Singh, C., Peake, D.J., Kokkalis, A., Coton, F.N. and Galbraith, R.A., "Control of rotorcraft retreating blade stall using air-jet vortex generators," 29th European Rotorcraft Forum, Friedrichshafen, Germany, 16-18 September 2003.

[113] Singh, C., Peake, D.J., Kokkalis, A., Khodagolian, V., Coton, F.N. and Galbraith, R.A., "Control of rotorcraft retreating blade stall using air-jet vortex generators," *Journal of Aircraft*, Vol. 43, No. 4, 2006, pp. 1169-1176. DOI: 10.2514/1.18333.

[114] Spalart, P. R., Allmaras, S. R., "A one-equation turbulence model for aerodynamic flows", AIAA Paper 92-0439, AIAA 30th Aerospace Sciences Meeting and Exhibit, Reno, Jan 6-9, 1992. DOI: 10.2514/6.1992-439

[115] Spentzos, A., Barakos, G., Badcock, K., Richards, B., Wernert, P., Schreck, S. and Raffel, M., "Investigation of three-dimensional dynamic stall using computational fluid dynamics", *AIAA journal* Vol. 43, No. 5, 2005, pp. 1023-1033. DOI:10.2514/1.8830

[116] Togiti, V., Ciobaca, V., Eisfeld, B., Knopp, T., "Numerical simulation of steady blowing active flow control using a differential Reynolds stress model", CEAS/KATnet II, Bremen, 2009.

[117] Traub, L.W., Miller, A., and Rediniotis, O., "Effects of synthetic jets on large-amplitude sinusoidal pitching motions," *Journal of Aircraft*, Vol. 42, No. 1, 2005, pp. 282-285. DOI: 10.2514/1.3919

[118] Van Driest, E.R., and Blumer, C.B., "Effect of roughness on transition in supersonic flow," *AGARDograph 255*, 1960.

[119] Visbal, M., Yilmaz, T.O. and Rockwell, D., "Three-dimensional vortex formation on a heaving low-aspect-ratio wing: Computations and experiments", *Journal of Fluids and Structures*, Vol. 38, 2013, pp. 58-76. DOI: 10.1016/j.jfluidstructs.2012.12.005

[120] Watkinson, J., "Introduction to helicopter dynamics", Elsevier, 2004. ISBN 0 7506 5715 4

[121] Weaver, D., McAlister, K.W., and Tso, J., "Control of VR7 dynamic stall by strong steady blowing," *Journal of Aircraft*, Vol. 41, No. 6, 2004, pp. 1404-1413. DOI: 10.2514/1.4413684-686.

[122] Wolf, C.C., Gardner, A.D., Ewers, B., Raffel, M., "The starting process of a pulsed jet as seen by schlieren measurements," *AIAA Journal*, (2014). DOI: 10.2514/1.J053198

[123] Wong, O.D., Watkins, N.A., Goodman, K.Z., Crafton, J., Forlines, A., Goss, L., Gregory, J.W. and Juliano, T.J., "Blade tip pressure measurements using pressure sensitive paint", American Helicopter Society 68th Annual Forum, Fort Worth, Texas, May 1-3, 2012.

[124] Yang, J., Ganesh, B., Komerath, N., "Radial flow measurements downstream of forced dynamic separation on a rotor blade", AIAA Paper 2006-3377, 36th AIAA Fluid Dynamics Conference and Exhibit, San Francisco, 5-8 June, 2006. DOI: 10.2514/6.2006-3377.

[125] Zanotti, A., and Gibertini, G., "Experimental investigation of the dynamic stall phenomenon on a NACA 23012 oscillating airfoil," *Proceedings of the Institution of Mechanical Engineers, Part G: Journal of Aerospace Engineering*, July 2012. DOI: 10.1177/0954410012454100

[126] Zanotti, A., Nilifard, R., Gibertini, G., Guardone, A., Quaranta, G., "Assessment of 2D/3D numerical modeling for deep dynamic stall experiments," *Journal of Fluids and Structures*, Vol. 51, pp. 97-115, 2014. DOI:10.1016/j.jfluidstructs.2014.08.004

Vita

Dr. Anthony Gardner received his B.Sc. in Physics from the University of Queensland, Australia in 1996, and the permission for further study in Physics (B.Sc. (Hons)) in 1997. He received his M.Sc. in Mechanical Engineering from the University of Queensland in 2000. During this period (1999-2000) he worked full-time managing the expansion tube laboratory and on the construction of the large expansion tube X3 under the direction of Professor Richard Morgen.

In 2000 Dr. Gardner joined the Institute of Aerodynamics and Flow Technology at the DLR Göttingen, where he first worked in the Department of Spacecraft analysing the HyShot flight experiment, Wind tunnel experiments and numerical simulations of supersonic combusting ramjet (scramjet) aerodynamics and aerothermodynamics. This work led to the award of a Ph.D. in Mechanical Engineering from the University of Queensland, Australia in 2007.

In 2004, Dr Gardner moved to the Department of High-Speed Configurations at the Institute of Aerodynamics and Flow Technology at the DLR Göttingen, where he worked as an experimental and numerical aerodynamicist on transport aircraft, helicopters, wind tunnel design and analysis, UCAVs and missiles. In particular the investigations of unsteady airfoil aerodynamics, including flutter, buzz and dynamic stall were investigated with wind tunnel experiments and CFD investigations.

Since 2010, Dr. Gardner has been in the Department of Helicopters at the Institute of Aerodynamics and Flow Technology at the DLR Göttingen, working on flow control of stalled flow, wind tunnel interference and unsteady airfoil aerodynamics.

Through Prof. Dr. Markus Raffel, Dr. Gardner has been involved since 2010 in teaching at the Uni. Hannover in the subjects “Helicopter Aerodynamics” and “Flow Measurement Techniques”. He has a “Lehrauftrag” to teach “Flow Measurement Techniques” at the Institute of Applied Mechanics, TU Clausthal since 2013. He is the first author of eleven articles in international journals and co-author of a further ten. He is author or co-author of contributions to seven technical books and of more than 30 papers at international conferences and more than 20 DLR internal reports. He is the coauthor of one German and one US patent in the subject of helicopter aerodynamics.

List of Publications

Publications from 2016

1. Gardner, A. D., Wolf, C.C., Raffel, M., "A new method of dynamic and static stall detection using infrared thermography", Experiments in Fluids, Vol. 57, No. 9, 2016. DOI: 10.1007/s00348-016-2235-4
2. Gardner, A. D., Richter, K., "Transition determination on a periodic pitching airfoil using phase averaging of pressure data", In: New Results in Numerical and Experimental Fluid Mechanics X, Notes on Numerical Fluid Mechanics and Multidisciplinary Design Volume 132, 2016, pp 291-301. DOI: 10.1007/978-3-319-27279-5_26
3. Gardner, A.D., Opitz, S., Wolf, C.C., Merz, C.B., "Experiment demonstrating reduction of dynamic stall by a back-flow flap", American Helicopter Society 72nd Annual Forum, West Palm Beach, May 17-19, 2016.
4. Gardner, A.D., Wolf, C.C., Raffel, M., "A new method of dynamic and static stall detection using infrared thermography", 42nd European Rotorcraft Forum, September 6-8, 2016, Lille, France
5. Kaufmann, K., Gardner, A. D., Costes, M., "Comparison between two-dimensional and three-dimensional dynamic stall", In: New Results in Numerical and Experimental Fluid Mechanics X, Notes on Numerical Fluid Mechanics and Multidisciplinary Design Volume 132, 2016, pp 315-325. DOI: 10.1007/978-3-319-27279-5_28
6. Kaufmann, K., Merz, C.B., Gardner, A.D., "Dynamic Stall Simulations on a Pitching Finite Wing", 34th AIAA Applied Aerodynamics conference, Washington, DC, June 13-17, 2016.
7. Raffel, M., Gardner, A.D., Schwermer, T., Merz, C.B., Weiss, A., Braukmann, J, Wolf, C.C., Ewers, B., "Differential Infrared Thermography (DIT) for Dynamic Stall Detection", 18th International Symposium on Applications of Laser Techniques to Fluid Mechanics Lisbon, Portugal, 04-07 July, 2016
8. Richter, K., Wolf, C.C., Gardner, A.D., Merz, C.B, "Detection of Unsteady Boundary Layer Transition Using Three Experimental Methods", AIAA Aviation and Aeronautics Forum and Exposition, Washington, D.C., USA, 13-17 June, 2016

Publications from 2015

1. Gardner, A.D., Richter, K., “Boundary layer transition determination for periodic and static flows using phase-averaged pressure data”, American Helicopter Society 71st Annual Forum, Virginia Beach, May 5-7, 2015.
2. Gardner, A.D., Richter, K., “Boundary layer transition determination for periodic and static flows using phase-averaged pressure data”, Experiments in Fluids, Vol. 56, No. 6, 2015. DOI: 10.1007/s00348-015-1992-9
3. Gardner, A.D., “STELAR Back-Flow Flap Experiment for Dynamic Stall Control”, DLR IB 224-2015 A108, 88 Pages, 2015.
4. Gardner, A.D., Raddatz, J., “Analysis of dynamic stall severity indicators”, DLR IB 224-2015 C183, 21 Pages, 2015.
5. Kaufmann, K., Costes, M., Richez, F., Gardner, A. D., Le Pape, A., “Numerical Investigation of Three-Dimensional Static and Dynamic Stall on a Finite Wing”, Journal of the American Helicopter Society, Volume 60, Number 3, 2014. DOI: 10.4050/JAHS.60.032004
6. Lang, W., Gardner, A.D., Mariappan, S., Klein, C., Raffel, M., “Boundary-layer transition on a rotor blade measured by temperature-sensitive paint, thermal imaging and image derotation”, Experiments in Fluids, Vol. 56, No. 6, 2015. DOI 10.1007/s00348-015-1988-5
7. Opitz, S., Gardner, A.D., Merz C.B., Wolf C.C., “Structural demonstration of an active back-flow flap under wind tunnel conditions”, 41st European Rotorcraft Forum, Munich, Germany, 1-4 Sept. 2015.
8. Opitz, S., Gardner, A.D., Merz, C.B., Wolf, C.C., “An active back-flow flap for dynamic stall control - from concept to wind tunnel”, ICAST2015: 26th International Conference on Adaptive Structures and Technologies October 14-16th, 2015, Kobe, Japan
9. Rein, M., Gardner, A.D., “Generic Lambda Wing Configuration in Compressible Flow: Effect of Highly Integrated Intakes”, Journal of Aircraft, Vol. 52, No. 3, 2015. pp. 972-980. DOI: 10.2514/1.C033177
10. Richter, K., Gardner, A.D., Mai, H., Koch, S., “Advanced rotor blade airfoil EDI-M109 - Performance measurement and analysis report”, DLR internal report: IB 224-2015 C171, DLR Institute of Aerodynamics and Flow Technology, Göttingen, Germany, 2015.
11. Richter, K., Gardner, A.D., Mai, H., “Advanced rotor blade airfoil EDI-M112 - Performance measurement and analysis report”, DLR internal report: IB 224-2015 C172, DLR Institute of Aerodynamics and Flow Technology, Göttingen, Germany, 2015.

Publications from 2014

1. Gardner, A. D., Richter, K., Mai, H., Neuhaus, D., "Experimental investigation of high-pressure pulsed blowing for dynamic stall control", *CEAS Aeronautical Journal*, Vol. 5, No. 2, pp. 185-198, 2014. DOI 10.1007/s13272-014-0099-y
2. Gardner, A. D., Richter, K., Mai, H., Neuhaus, D., "Experimental investigation of air jets to control shock-induced dynamic stall", *Journal of the American Helicopter Society*, Vol. 59, No. 2, 2014. DOI: 10.4050/JAHS.59.022003
3. Gardner, A. D., Klein, C., Sachs, W., Henne, U. , Mai, H., Richter, K., "Investigation of three-dimensional dynamic stall on an airfoil using fast response pressure sensitive paint", American Helicopter Society 70th Annual Forum, Montreal, Quebec, May 20-22, 2014.
4. Gardner, A. D., Klein, C., Sachs, W., Henne, U. , Mai, H., Richter, K., "Investigation of three-dimensional dynamic stall on an airfoil using fast response pressure sensitive paint", Experiments in Fluids, Vol. 55, No. 9, 2014. DOI: 10.1007/s00348-014-1807-4
5. Gardner, A. D., Richter, K., "Transition determination on a periodic pitching airfoil using phase averaging of pressure data", STAB 2014, Munich, 4-5 November, 2014.
6. Gardner, A. D., "User guide for cp2cl plusm v3.x: A program to provide forces and moments from airfoil pressure distributions", DLR internal report: IB 224-2014 A101, DLR Institute of Aerodynamics and Flow Technology, Göttingen, Germany, 2014.
7. Kaufmann, K., Gardner, A.D., Richter, K., "Numerical investigations of a back-flow flap for dynamic stall control", In: *New Results in Numerical and Experimental Fluid Mechanics IX, Notes on Numerical Fluid Mechanics and Multidisciplinary Design Volume 124*, 2014, pp. 255-262. DOI: 10.1007/978-3-319-03158-3_26
8. Kaufmann, K., Gardner, A. D., Costes, M., "Comparison between two-dimensional and three-dimensional dynamic stall", STAB 2014, Munich, 4-5 November, 2014.
9. Kaufmann, K., Costes, M., Richez, F., Gardner, A. D., Le Pape, A. "Numerical investigation of three-dimensional dynamic stall on an oscillating finite wing", American Helicopter Society 70th Annual Forum, Montreal, Quebec, May 20-22, 2014.
10. Mariappan, S., Gardner, A.D., Richter, K., Raffel, M. "Analysis of dynamic stall using dynamic mode decomposition technique", AIAA Journal, Vol. 52, No. 11, 2014. pp. 2427-2439. DOI: 10.2514/1.J052858
11. Opitz, S., Kaufmann, K., Gardner, A.D. "An active back-flow flap for a helicopter rotor blade", *Advances in Aircraft and Spacecraft Science*, Vol. 1, No. 1, 2014. pp. 69-91. DOI: 10.12989/aas.2014.1.1.069
12. Opitz, S., Gardner, A.D., Kaufmann, K. "Aerodynamic and structural investigation of an active back-flow flap for dynamic stall control", *CEAS Aeronaut Journal*, Vol. 5, No. 3, 2014. pp279-291. DOI 10.1007/s13272-014-0106-3
13. Richter, K., Koch, S., Gardner, A.D., Mai, H., Klein, A., Rohardt, C.-H., "Experimental investigation of unsteady transition on a pitching rotor blade airfoil", *Journal of the American Helicopter Society*, Vol. 59, No. 1, 2014. DOI: 10.4050/JAHS.59.012001
14. Richter, K., Gardner, A.D., Park, S.H., "Numerical investigation of the influence of the model installation on rotor blade airfoil measurements", In: *New Results in Numerical and Experimental Fluid Mechanics IX, Notes on Numerical Fluid Mechanics and Multidisciplinary Design Volume 124*, 2014, pp. 225-233, DOI:10.1007/978-3-319-03158-3_23
15. Surrey, S., Gardner, A.D., Mai, H., Klein, C., "Numerical investigation of aeroelastic and three dimensional effects for an airfoil in transonic flow", 40th European Rotorcraft Forum, Southampton, England, 2-5 Sept. 2014.
16. Wolf, C.C., Gardner, A.D., Ewers, B., Raffel, M., "Starting process of a pulsed jet as seen by schlieren measurements", *AIAA Journal*, (2014). DOI: 10.2514/1.J053198

Publications from 2013

1. Gardner, A.D., "STELAR-FCD experiment 1", DLR internal report: IB 224-2013 A78, DLR Institute of Aerodynamics and Flow Technology, Göttingen, Germany, 2013.
2. Gardner, A.D., Richter, K., "Influence of rotation on dynamic stall", *Journal of the American Helicopter Society*, Vol. 58, No. 3, 2013. DOI: 10.4050/JAHS.58.032001
3. Gardner, A.D., Richter K., Mai, H., Neuhaus, D., "Experimental investigation of air jets to control shock-induced dynamic stall", American Helicopter Society 69th Annual Forum, Phoenix, Arizona, May 21-23, 2013.
4. Gardner, A.D., Richter K., Mai, H., Neuhaus, D., "Experimental investigation of air jets for the control of compressible dynamic stall", *Journal of the American Helicopter Society*, Vol. 58, No. 4, 2013. DOI: 10.4050/JAHS.58.042001
5. Gardner, A.D., Knopp, T., Richter, K., Rosemann, H. "Numerical investigation of pulsed air jets for dynamic stall control on the OA209 airfoil", In: *Notes on Numerical Fluid Mechanics and Multidisciplinary Design: New Results in Numerical and Experimental Fluid Mechanics VIII*, Springer Verlag, 2013. ISBN 978-3-642-35679-7, pp. 287-295, DOI: 10.1007/978-3-642-35680-3_35
6. Gardner, A.D., Richter, K., Mai, H., Altmikus, A.R.M., Klein, A. and Rohardt, C.-H., "Experimental investigation of dynamic stall performance for the EDI-M109 and EDI-M112 airfoils", *Journal of the American Helicopter Society*, Vol. 58, No. 1, 2013. DOI:10.4050/JAHS.58.012005
7. Gardner, A.D., Richter, K., "Effect of the model-sidewall connection for a static airfoil experiment", *Journal of Aircraft*, Vol. 50, No. 2, pp. 677-680, March-April 2013. DOI: 10.2514/1.C03201
8. Junger, C., Gardner, A.D. "Numerische Untersuchung des Ein Meter Windkanals mit offener und geschlossener Messstrecke", DLR internal report: DLR-IB 224-2013 A93, DLR Institute of Aerodynamics and Flow Technology, Göttingen, Germany, 2013.
9. Kirmse, T., Gardner, A.D., Krombholz, C., "Investigation of aero-optical effects in model deformation measurements in a transonic flow", In: *Notes on Numerical Fluid Mechanics and Multidisciplinary Design: New Results in Numerical and Experimental Fluid Mechanics VIII*, Springer Verlag, 2013. ISBN 978-3-642-35679-7, pp. 665-672, DOI: 10.1007/978-3-642-35680-3_79
10. Mariappan, S., Gardner, A.D., Richter, K., Raffel, M., "Analysis of dynamic stall using dynamic mode decomposition technique", 31st AIAA Applied Aerodynamics conference, San Diego, 24-27 June 2013.
11. Opitz, S., Kaufmann, K., Gardner, A.D., "An active back-flow flap for a helicopter rotor blade", 6th ECCOMAS Conference on Smart Structures and Materials, Politecnico di Torino, 24-26 June 2013
12. Opitz, S., Gardner, A.D., Kaufmann, K., "Aerodynamic and structural investigation of an active back-flow flap for dynamic stall control", 39th European Rotorcraft Forum, Moscow, September 3-6, 2013
13. Raffel, K., Richter, K., Gardner, A.D., "Hubschrauberkonfiguration", Deutsches Patent, DE 10 2012 100 102 A1, 11 July 2013.
14. Raffel, K., Richter, K., Gardner, A.D., "Helicopter configuration", US Patent, US 2013/0175386 A1, 11 July 2013.
15. Richter, K., Koch, S., Gardner, A.D., "Influence of oscillation amplitude and Mach number on the unsteady transition on a pitching rotor blade airfoil", American Helicopter Society 69th Annual Forum, Phoenix, Arizona, May 21-23, 2013.

Publications from 2012

1. Gardner, A.D., "SIMCOS-FCD experiment 1", DLR internal report: IB 224-2012 A69, DLR Institute of Aerodynamics and Flow Technology, Göttingen, Germany, 2012.
2. Gardner, A.D., Richter K., "Influence of rotation on dynamic stall", American Helicopter Society 68th Annual Forum, Fort Worth, Texas, May 1-3, 2012.
3. Gardner, A.D., Richter K., Mai, H., Neuhaus, D., "Experimental control of compressible OA209 dynamic stall by air jets", 38th European Rotorcraft Forum, Amsterdam, 4-6 Sept, 2012.
4. Kaufmann, K., Gardner, A.D., Richter, K., "Numerical investigations of a back-flow flap for dynamic stall control", STAB 2012, Stuttgart, 6-7 November, 2012.
5. Klein, A., Lutz, Th., Kramer, E., Richter, K., Gardner, A.D., Altmikus, A.R.M., "Numerical comparison of dynamic stall for two-dimensional airfoils and an airfoil model in the DNW-TWG", *Journal of the American Helicopter Society*, Vol. 57, Issue 4, 2012, DOI: 10.4050/JAHS.57.042007
6. Rein, M., Gardner, A.D., Rütten, M., "Study of the influence of a highly integrated flow-through intake on compressible flows about the lambda wing configuration SACCON", 30th AIAA Applied Aerodynamics Conference, New Orleans, 25 - 28 June 2012.
7. Richter, K., Gardner, A.D., Park, S. H., "Numerical investigation of the influence of the model installation on rotor blade airfoil measurements", STAB 2012, Stuttgart, 6-7 November, 2012.
8. Richter, K., Koch, S., Gardner, A.D., Mai, H., Klein, A., Rohardt, C.-H., "Experimental investigation of unsteady transition on a pitching rotor blade airfoil", 38th European Rotorcraft Forum, Amsterdam, 4-6 Sept, 2012.

Publications from 2011

1. Gardner, A.D., Richter, K., Rosemann, H., "Numerical investigation of air jets for dynamic stall control on the OA209 airfoil", *CEAS Aeronautical Journal*, Vol. 1, Issue 1, pp. 69-82, 2011. DOI 10.1007/s13272-011-0002-z
2. Gardner, A.D., Richter, K., Mai, H., Altmikus, A.R.M., Klein, A. and Rohardt, C.-H., "Experimental investigation of dynamic stall performance for the EDI-M109 and EDI-M112 airfoils", 37th European Rotorcraft Forum, Gallarate, Italy, 13-15 Sept, 2011.
3. Klein, A., Richter, K., Gardner, A.D., Altmikus, A.R.M., Lutz, T., Krämer, E., "Numerical comparison of dynamic stall for 2D airfoils and an airfoil model in the DNW-TWG," 37th European Rotorcraft Forum, Gallarate, Italy, 13-15 Sept, 2011
4. Richter, K., Le Pape, A., Knopp, T., Costes, M., Gleize, V., Gardner, A.D., "Improved two-dimensional dynamic stall prediction with structured and hybrid numerical methods," *Journal of the American Helicopter Society*, Vol. 56, Issue 4, 2011. DOI: 10.4050/JAHS.56.042007

Publications from 2010

1. Gardner, A.D., Richter, K., Rosemann, H., "Prediction of the wind tunnel sidewall effect for the iGREEN wing-tailplane interference experiment" In: *Notes on Numerical Fluid Mechanics and Multidisciplinary Design New Results in Numerical and Experimental Fluid Mechanics VII, Vol.112*. Springer Verlag Berlin, Heidelberg. pp. 75-82, 2010. ISBN 978-3-642-14242-0. ISSN 1612-2909
2. Gardner, A.D., "Numerical investigation of the effect of intake integration at transonic speeds on the DLR-F17E UCAV model for the TWG", DLR internal report: DLR-IB 224 2010 A 40, 47 S.
3. Gardner, A.D., Knopp, T., Richter, K., Rosemann, H., "Numerical investigation of pulsed air jets for dynamic stall control on the OA209 airfoil", 17th DGLR-Fach-Symposium der STAB, 9-10 Nov. 2010, Berlin, Deutschland
4. Gardner, A.D., Richter, K., Rosemann, H., "Numerical investigation of air jets for dynamic stall control on the OA209 airfoil" 36th European Rotorcraft Forum, 7-9 September 2010, Paris, France.
5. Kirmse, T., Gardner, A.D., Krombholz, C., "Density effects in model deformation measurements on a NACA 0010 profile in a transonic flow" 14th International Symposium on Flow Visualization ISFV , June 21-24, 2010, Daegu, Korea.
6. Kirmse, T., Gardner, A.D., Krombholz, C., "Investigation of aero-optical effects in model deformation measurements in a transonic flow", 17th DGLR-Fach-Symposium der STAB, 09-10 Nov. 2010, Berlin, Germany.

Publications from 2009

1. Gardner, A.D. "Numerical investigation of air jets for dynamic stall control on the OA209 airfoil", DLR internal report: DLR-IB 224-2009 A 32, DLR Institute of Aerodynamics and Flow Technology, Göttingen, Germany, 2009.
2. Heine, B., Mulleners, K., Gardner, A., Mai, H., "On the effects of leading edge vortex generators on an OA209 airfoil", ODAS 2009 - 10th ONERA-DLR Aerospace Symposium, Berlin, 06-08 October, 2009
3. Le Pape, A., Richter, K., Knopp, T., Costes, M., Gleize, V., Gardner, A.D., "Validation of structured and hybrid numerical methods for improved two-dimensional dynamic stall prediction", ODAS 2009 - 10th ONERA-DLR Aerospace Symposium, Berlin, 06-08 October, 2009
4. Rein, M., Hannemann, M., Gardner, A.D., Koch, S. "Design of a generic subsonic S-duct intake for studies on the effect of boundary layer ingestion", DLR internal report:IB 224-2009 A28, DLR Institute of Aerodynamics and Flow Technology, Göttingen, Germany, 2009.
5. Richter, K., Le Pape, A., Knopp, T., Costes, M., Gleize, V., Gardner, A.D., "Improved two-dimensional dynamic stall prediction with structured and hybrid numerical methods." American Helicopter Society 65th Annual Forum, 27-29 May 2009, Grapevine, Texas (USA).

Publications from 2008

1. Gardner, A.D., "Maximum lift polars for NLF wings in Aeronext", DLR internal report: IB 224-2008 C36, DLR Institute of Aerodynamics and Flow Technology, Göttingen, Germany, 2008.
2. Gardner, A.D., "Addendum to: CFD computations for the FLIRET straight sting configuration (DLR IB 224-2007 C20)", DLR internal report: IB 224-2008 C32, DLR Institute of Aerodynamics and Flow Technology, Göttingen, Germany, 2008.
3. Gardner, A.D., "Aeronext: Report on the A320 configuration", DLR internal report: IB 224-2008 C31, DLR Institute of Aerodynamics and Flow Technology, Göttingen, Germany, 2008.
4. Gardner, A.D., "Aeronext intermediate report: Results in 2007", DLR internal report: IB 224-2008 C27, DLR Institute of Aerodynamics and Flow Technology, Göttingen, Germany, 2008.
5. Gardner, A.D., "Pre-computations for the iGreen wing-tailplane interference experiment in the TWG", DLR internal report: IB 224-2008 A19, DLR Institute of Aerodynamics and Flow Technology, Göttingen, Germany, 2008.
6. Nitzsche, J., Brouwers, K., Gardner, A.D., Mai, H., Dietz, G., Naudin, P., Leconte, P., "Investigation of unsteady control surface aerodynamics on a 2D supercritical airfoil model", Deutscher Luft- und Raumfahrtkongress, Darmstadt, 2008.
7. Schwamborn, D., Gardner, A.D., von Geyr, H., Krumbein, A., Lüdeke, H., Stürmer, A., "Development of the TAU-Code for aerospace applications", 50th NAL International Conference on Aerospace Science and Technology, Bangalore, 2008

Publications from 2007

1. Gardner, A.D., "CFD computations for the FLIRET straight sting configuration", DLR internal report: IB 224-2007 C20, DLR Institute of Aerodynamics and Flow Technology, Göttingen, Germany, 2007.
2. Gardner, A.D., "Design and optimisation of the valve contour (Conus) of the DNW-KRG for an extended Mach number range", DLR internal report: IB 224-2007 A02, DLR Institute of Aerodynamics and Flow Technology, Göttingen, Germany, 2007.
3. Gardner, A.D., "HyShot scramjet testing in the HEG". Dissertation , University of Queensland, Australia, 2007.
4. Gardner, A.D., "HyShot scramjet testing in the HEG". DLR FB 2007-14, 2007, ISSN 1434-8454, 2007.
5. Gardner, A.D., Richter, K., Rosemann, H., "Simulation of oscillating airfoils and moving flaps employing the DLR-TAU unsteady grid adaptation". In: *Notes on Numerical Fluid Mechanics and Multidisciplinary Design, Vol. 96*; C. Tropea, S. Jakirlic, H.-J. Heinemann, R. Henke, H. Hönlinger; Springer, Berlin Heidelberg New York, 2007.
6. Koch, S., Richter, K., Gardner, A.D., Rosemann, H., "HiCon airfoil flow investigation at high Reynolds number: Test campaign in the cryogenic Ludwieg-tube", DLR internal report: IB 224-2007 C19, DLR Institute of Aerodynamics and Flow Technology, Göttingen, Germany, 2007.

Publications from 1997-2006

1. Gardner, A.D., Nitzsche, J., Neumann, J., Richter, K., Rosemann, H., Voß, R., "Adaptive load redistribution using mini-TEDs", 25th International Congress of the Aeronautical Sciences, Hamburg, Germany. ISBN 0-9533991-76, 2006.
2. Gardner, A.D., "Investigation of the sting interference effect on the LFK-NG", DLR internal report: IB 224-2006 C36, DLR Institute of Aerodynamics and Flow Technology, Göttingen, Germany, 2006.
3. Gardner, A.D., "Investigation of the sting interference effect due to the TWG 15-degree, 25-degree and 45-degree rolling stings", DLR internal report: IB 224-2006 A32, DLR Institute of Aerodynamics and Flow Technology, Göttingen, Germany, 2006.
4. Gardner, A.D., Jacobs, M., "Force and moment measurements on the PRORA-USV 1:30 model in DNW-TWG January 2006: Experiment documentation and results.", DLR internal report: IB 224-2006 C24, DLR Institute of Aerodynamics and Flow Technology, Göttingen, Germany, 2006.
5. Gardner, A.D., Jacobs, M., "Force and moment measurements on the PRORA-USV 1:30 model in DNW-TWG June-July 2005: Experiment documentation and results", DLR internal report: IB 224-2005 C11, DLR Institute of Aerodynamics and Flow Technology, Göttingen, Germany, 2005.
6. Gardner, A.D., Hannemann, K., Paull, A., Steelant, J., "Ground testing of the HyShot supersonic combustion flight experiment in HEG", Paper 1341, ISSW24, Beijing, 2004.
7. Gardner, A.D., Hannemann, K., Steelant, J., Paull, A., "Ground Testing of the HyShot Supersonic Combustion Flight Experiment in HEG and Comparison with Flight Data", AIAA 2004-3345, 40th AIAA Joint Propulsion Conference, Fort Lauderdale, Florida, July 11-14, 2004.
8. Gardner, A.D., Hannemann, K., Paull, A., "Evaluation of full-engine scramjet technology", ESA Contract report: ESTEC TRP 17001/02/NL/MV, 2004.
9. Gardner, A.D., Jacobs, P.A., Hannemann, K., "End-to-end modelling and design of a new operating condition for HEG", In: *New results in experimental fluids IV:Notes on numerical fluid mechanics and multidisciplinary design v87*, editors C. Breitsamter, B. Laschka, H-.J. Heinemann, R. Hilbig , Springer-Verlag, Berlin, 2004. TL570.S65.2004.
10. Gardner, A.D., Hannemann, K., "Evaluation of full-engine scramjet technology: Executive summary", DLR internal report: IB 224-2004 A12, DLR Institute of Aerodynamics and Flow Technology, Göttingen, Germany, 2004.
11. Gardner, A.D., Hannemann, K., "Evaluation of full-engine scramjet technology", DLR internal report: IB 224-2004 A11, DLR Institute of Aerodynamics and Flow Technology, Göttingen, Germany, 2004.
12. Jacobs, P.A., Gardner, A.D., Buttsworth, D.R., Martinez, J., Karl, S., Hannemann, K., "End-to-end modelling of the HEG shock tunnel", Paper 3111, ISSW24, Beijing, 2004.
13. Gardner, A.D., "Calculation of low enthalpy conditions for the HEG", DLR internal report: IB 224-2003 A03, DLR Institute of Aerodynamics and Flow Technology, Göttingen, Germany, 2003.
14. Jacobs, P.A., Gardner, A.D., Hannemann, K., "Gas-dynamic modelling of the HEG shock tunnel", DLR internal report: IB 224-2003 A02, DLR Institute of Aerodynamics and Flow Technology, Göttingen, Germany, 2003.
15. Gardner, A.D., Paull, A., McIntyre, T.J., "Upstream injection in a 2-D scramjet model", *Shock waves*, Vol 11, No. 5, pp369-375, 2002.
16. Palma, P.C., Gardner, A.D., Beck, W.H., "Freestream velocity in a shock-tunnel nozzle flow using diode laser absorption spectroscopy", 3rd Australian Conference on Laser Diagnostics in

Fluid Mechanics and Combustion, Dec. 2-3, 2002, Brisbane.

17. Gai, S.L., Hayne, M.J., Gardner, A.D., Morgan, R.G. and Mee, D.J., 2001, "Heat transfer behind a step in high enthalpy super-orbital flow", 39th Aerospace Sciences Meeting and Exhibit, 8-11 January, Reno, Nevada, AIAA paper 2001-0509, 2001.
18. Gardner, A.D., "Upstream porthole injection in a 2-D scramjet model", MSc. Thesis. Dept. Mechanical Engineering. University of Queensland. 2000.
19. Gardner, A.D., Paull, A., McIntyre, T.J., "Intake fuel injection in a 2-D scramjet model" Paper 0610, ISSW22, 1999.
20. Morgan, R.G., Sasoh, A., McIntyre, T.J., Littleton, B., Bishop, A., McIntyre, T.J., Hoogland, J., Gardner, A.D., "Simulation of ablative mixing layers in superorbital flows" Paper 1358, ISSW22, 1999.
21. Gardner, A.D., "Development of a shadowgraph system for the observation of a 2-D scramjet model", Honours Thesis, Dept of Physics, University of Queensland, 1997.